Experimental Surface Pressure Distributions on Three Bodies of Revolution at Mach Numbers From 0.7 to 2.02

by

C. Franklyn Markarian
Aeromechanics Division
Weapons Development Department

Naval Weapons Center
CHINA LAKE, CALIFORNIA ■ AUGUST 1972

ABSTRACT

Wind tunnel tests were conducted to measure surface pressure distributions on three bodies of revolution at Mach numbers from 0.7 to 2.02 and angle of attack from 10 to -10 degrees. Tests were conducted at the Naval Ordnance Laboratory, White Oak, Silver Spring, Md. and the Naval Ship Research and Development Center, Carderock, Md. The three bodies were based on the same ogive-cylinder with one having a sharp nose and the other two being spherically tipped. Surface pressure distributions are presented, along with expressions relating the flow angle to the pressure difference across the spherical nose caps.

NWC Technical Publication 5393

Published by . . . . . Weapons Development Department
Manuscript 40/MS 72-69
Collation . . . . . Cover, 67 leaves, DD Form 1473, abstract cards
First printing . . . . . 150 unnumbered copies
Security classification . . . . . UNCLASSIFIED

UNCLASSIFIED
Security Classification

DOCUMENT CONTROL DATA - R & D

Security classification of title, body of abstract and indexing annotation must be entered when the overall report is classified

1 ORIGINATING ACTIVITY (Corporate author) Naval Weapons Center China Lake, Calif. 93555	2a. REPORT SECURITY CLASSIFICATION UNCLASSIFIED 2b. GROUP

3 REPORT TITLE

EXPERIMENTAL SURFACE PRESSURE DISTRIBUTIONS ON THREE BODIES OF REVOLUTION AT MACH NUMBERS FROM 0.7 TO 2.02

4 DESCRIPTIVE NOTES (Type of report and inclusive dates)

5 AUTHOR(S) (First name, middle initial, last name)

C. Franklyn Markarian

6 REPORT DATE August 1972	7a. TOTAL NO OF PAGES 132	7b NO OF REFS
8a. CONTRACT OR GRANT NO b. PROJECT NO AirTask A32 320/216/72F203 22205 c. d.	9a. ORIGINATOR'S REPORT NUMBER(S) NWC TP 5393 9b. OTHER REPORT NO(S) (Any other numbers that may be assigned this report)	

10 DISTRIBUTION STATEMENT

Approved for public release; distribution unlimited.

11 SUPPLEMENTARY NOTES	12 SPONSORING MILITARY ACTIVITY Naval Air Systems Command Washington, D. C. 20360

13 ABSTRACT

Wind tunnel tests were conducted to measure surface pressure distributions on three bodies of revolution at Mach numbers from 0.7 to 2.02 and angle of attack from 10 to -10 degrees. Tests were conducted at the Naval Ordnance Laboratory, White Oak, Silver Spring, Md. and the Naval Ship Research and Development Center, Carderock, Md. The three bodies were based on the same ogive-cylinder with one having a sharp nose and the other two being spherically tipped. Surface pressure distributions are presented, along with expressions relating the flow angle to the pressure difference across the spherical nose caps.

DD FORM 1 NOV 68 1473 (PAGE 1)

S/N 0101-807-6801

UNCLASSIFIED
Security Classification

14 KEY WORDS	LINK A		LINK B		LINK C	
	ROLE	WT	ROLE	WT	ROLE	WT
Pressure distributions Bodies of revolution Wind tunnel tests						

Naval Weapons Center
AN ACTIVITY OF THE NAVAL MATERIAL COMMAND
W. J. Moran, RADM, USN ..... Commander
H. G. Wilson ..... Technical Director

FOREWORD

This report describes the results of wind tunnel tests that were conducted to measure surface pressure distributions on three bodies of revolution. This work was performed as part of the Aircraft/Missile Interference Effects Program, which is an investigation of the effect of the carrying aircraft on the flow field and aerodynamic heating of airborne ordnance. The purpose of the tests was to provide reference pressure distributions for comparison with captive flight data that were obtained as part of the program.

The wind tunnel tests were conducted during 1966 and 1968, and selected results have been previously presented in publications describing the overall program. The purpose of this report is to make the entire results of the wind tunnel program available, particularly for use in checking out analytical techniques for predicting pressure distributions on bodies of revolution. The project was funded by the Naval Air Systems Command under AirTask A32 320/216/72F203 22205.

This report is released at the working level for information purposes only.

Released by
RAY W. VAN AKEN, *Head*
Aeromechanics Division
18 July 1972

Under authority of
F. H. KNEMEYER, *Head*
Weapons Development Department

CONTENTS

INTRODUCTION

Wind tunnel tests to measure pressure distributions on an ogive-cylinder have been conducted as part of the Aircraft/Missile Interference Effects Program. This is an exploratory development program to investigate the effect of the carrying aircraft on the flow field about airborne ordnance. Results have applications in the areas of aerodynamic heating, store separation, and aerodynamic loads. The major portion of the program was the captive flight testing of a store instrumented to measure surface pressure distributions. The captive flight store was of typical airborne configuration consisting of a cylindrical body with a spherically-tipped, tangent-ogive nose (Fig. 1). Tests were conducted over a broad range of subsonic and supersonic flight conditions. A description of the captive flight test program was given in a paper prepared by the author for presentation at the AIAA 6th Aerodynamic Testing Conference.[1]

The purpose of the wind tunnel tests was to provide disturbance-free, reference pressure distributions for comparison with the captive flight data in order to help identify flow interference effects. These tests were conducted using a pressure-instrumented, quarter-scale model of the captive flight store (Fig. 2). A model of the aircraft was not included in the test setup as the objective of the tests was free-stream, reference data. The wind tunnel tests were conducted at the Naval Ordnance Laboratory (NOL), White Oak, Silver Spring, Md. and the Naval Ship Research and Development Center (NSRDC), Carderock, Md. Test conditions covered nearly the full range of captive flight test conditions with data collected at Mach numbers from 0.7 to 2.02 and angles of attack from -10 to 10 degrees.

Two nose configurations in addition to the scale nose were also tested during the wind tunnel program. These noses utilized the same ogive radius as the scale nose; however, one was blunter with a larger radius spherical tip while the other was pointed (Fig. 3). The purpose of the additional nose configurations was to provide data for use in studies of the effect of nose bluntness on pressure distribution.

[1] Markarian, C. Franklyn. "External Store Pressure Distributions During Captive Flight Aboard an F-4B Aircraft," presented at the American Institute of Aeronautics and Astronautics 6th Aerodynamic Testing Conference, Albuquerque, N. M., 10-12 March 1971.

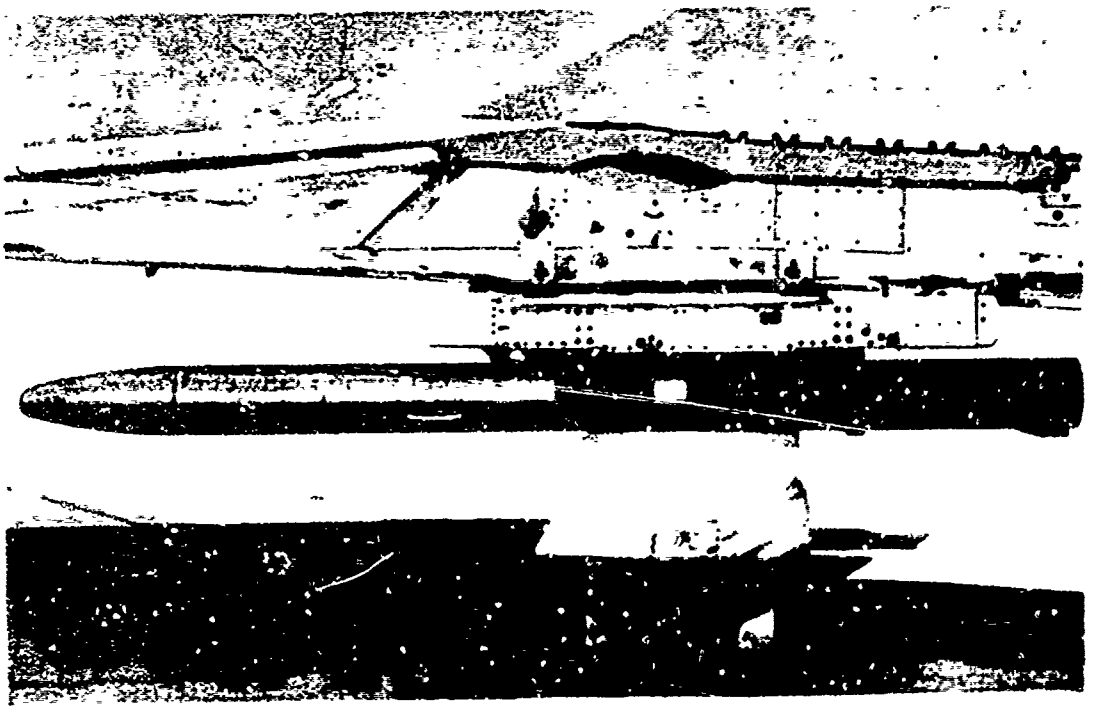

FIG. 1. Pressure-Instrumented Captive Flight Store.

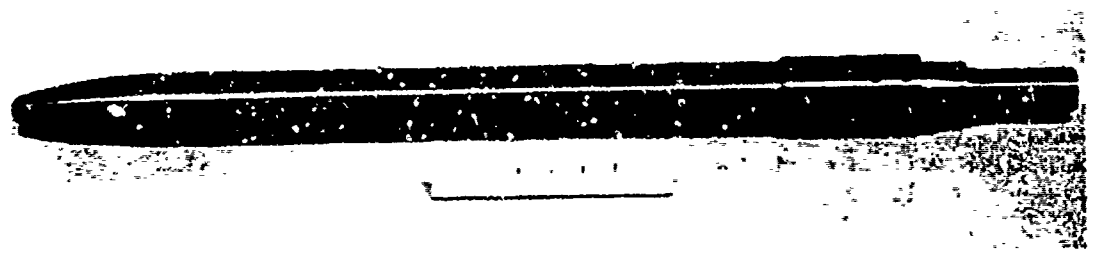

FIG. 2. Pressure Instrumented, Quarter-Scale Model of Captive Flight Store.

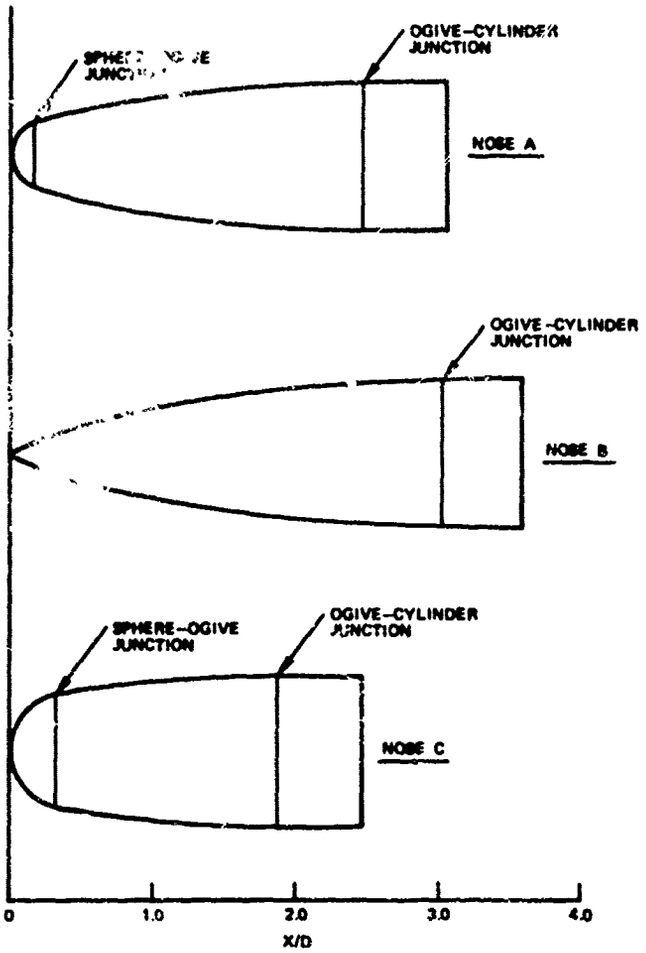

FIG. 3. Nose Configurations.

While the primary reason for conducting the wind tunnel tests was to provide reference data for the Aircraft/Missile Interference Effects Program, the results are also useful for checking analytical techniques for predicting pressure distributions on bodies of revolution. Of particular interest are the effects of the different nose configurations and angles of attack and the fact that much of the data is in the transonic Mach number range for which there is a general lack of information. No attempt at analysis of the data has been made in this report as the primary purpose is to make the results available for use in analytical investigations.

DESCRIPTION OF MODEL

For ease of construction and to allow interchangeable nose sections, the wind tunnel model is composed of four sections. The forward two sections, the nose and center body, contain the pressure taps and are constructed of mild steel. Heat-treated 4130 steel is used in the aft body and sting for additional strength. The model is 2 inches in diameter and approximately 30 inches long, depending on which of the three nose sections is installed. With Nose A, the model represents to quarter scale the pressure measurement section, or forward half, of the captive flight store. A view of the model disassembled with Nose A is shown in Fig. 4. Overall dimensions of the components and the assembled model are shown in Fig. 5.

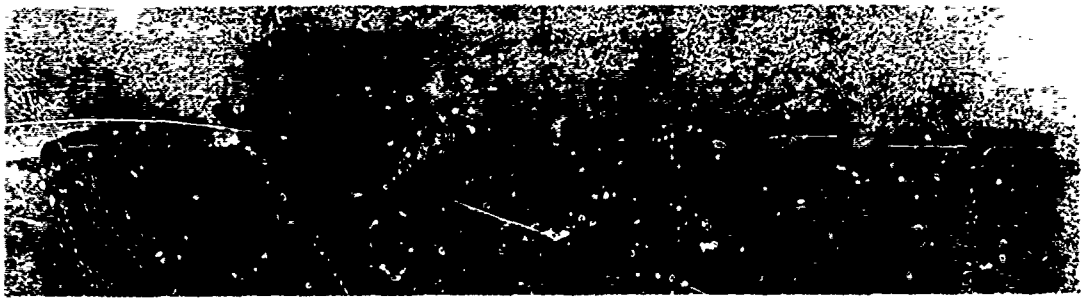

FIG. 4. Disassembled Wind Tunnel Model.

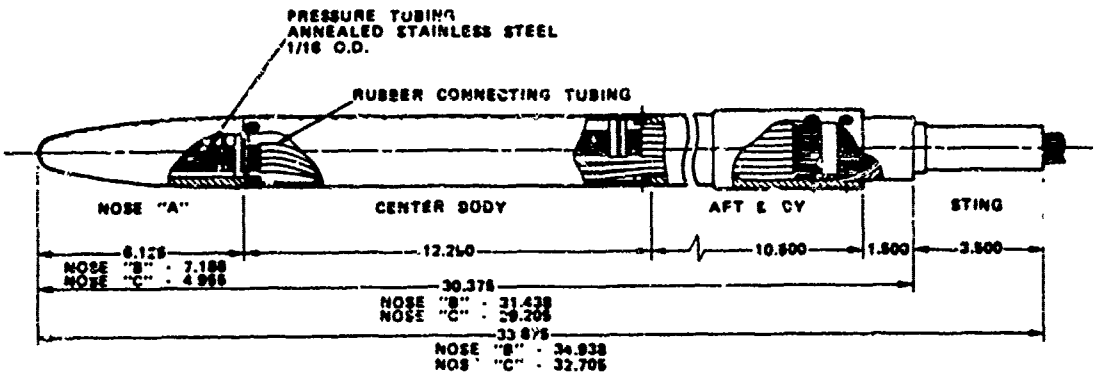

FIG. 5. Model Assembly and Dimensions.

Annealed, stainless steel tubing having an outside diameter of 0.625 inch and an inside diameter of 0.050 inch was silver-soldered to the wall of the model to form the pressure taps. Neoprene rubber tubing was used to connect the stainless steel tubing of the noses and center section to the stainless steel tubing mounted in the sting.

The three nose sections are all based on an 18.719-inch-radius tangent ogive. Nose A, the scale nose, has a 0.4375-inch-radius tangent spherical tip. Nose B has a pointed tip and Nose C, the bluntest nose, has a 0.75-inch-radius tangent spherical tip.

The majority of the pressure taps are distributed along a streamline with some taps spaced circumferentially to allow determination of flow angularity and uniformity. Pressure taps are distributed on the noses and center body as follows:

Nose A:
15 taps along streamline

3 additional taps spaced 90 deg apart circumferentially at 30-deg position on nose cap

Nose B:
14 taps along streamline

Nose C:
12 taps along streamline

3 additional taps spaced 90 deg apart circumferentially at 30- and 60-deg positions on nose cap

Center Body:
20 taps along streamline

3 additional taps spaced 90 deg apart circumferentially at fifth body tap

The model has a total of 41 pressure taps with Noses A or C installed and 37 taps with Nose B. Pertinent dimensions and pressure tap locations for the noses and the center body are given in Fig. 6, along with the tap numbering system. Exact pressure tap locations in terms of axial, radial and surface distance and surface slope are given in Table 1.

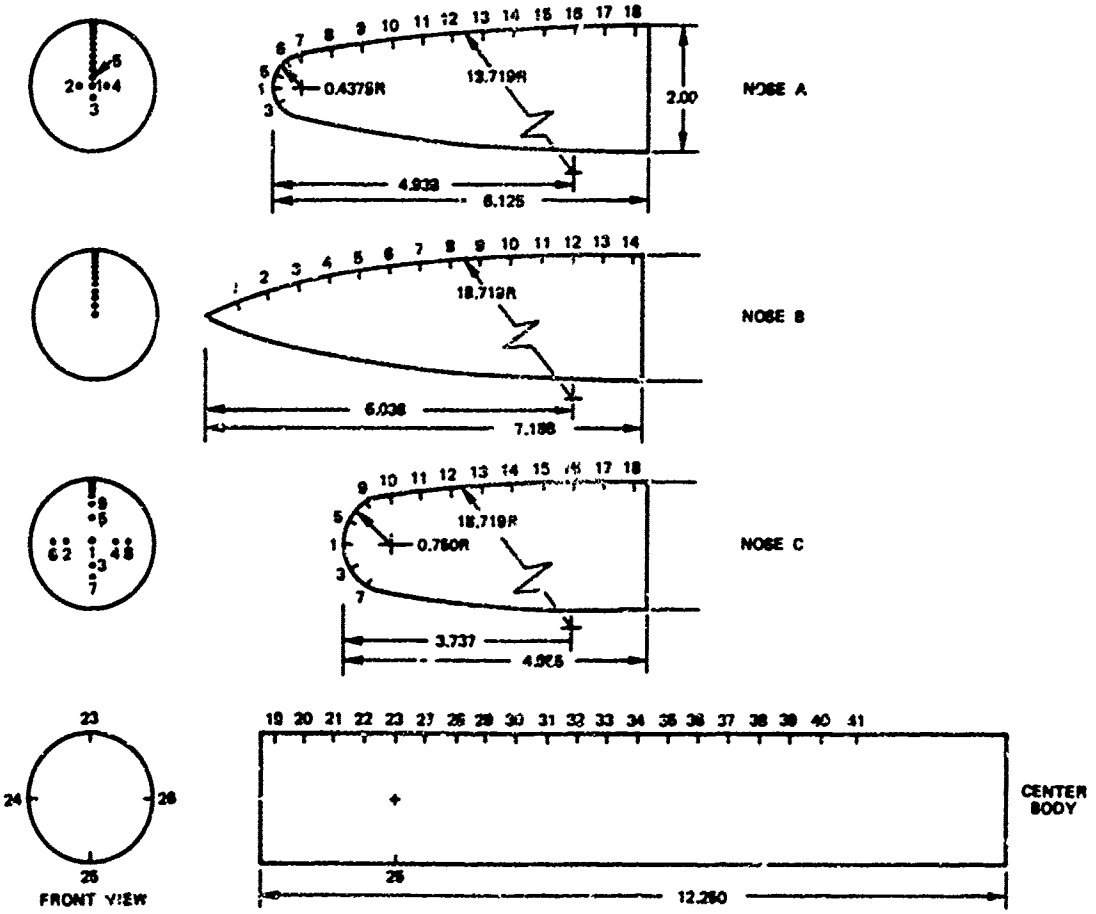

FIG. 6. Nose and Center Body Dimensions

TABLE 1. Pressure Tap Locations.

Nose configuration A							Nose configuration B							Nose configuration C						
Tap No.	Axial distance x(in.)	x/D	Surface distance s(in.)	Radial distance r(in.)	Tangent angle θ(deg)	Streamline tap No.	Tap No.	Axial distance x(in.)	x/D	Surface distance s(in.)	Radial distance r(in.)	Tangent angle θ(deg)	Streamline tap No.	Tap No.	Axial distance x(in.)	x/D	Surface distance s(in.)	Radial distance r(in.)	Tangent angle θ(deg)	Streamline tap No.
Nose taps																				
1	0.0	0.0	0.0	0.0	90.0	1	1	0.536	0.268	0.564	0.174	17.09	1	1	0.0	0.0	0.0	0.0	90.0	1
2	0.059	0.029	0.229	0.219	60.0		2	1.036	0.518	1.084	0.320	15.49	2	2	0.100	0.050	0.393	0.375	60.0	
3	0.059	0.029	0.229	0.219	60.0		3	1.536	0.768	1.601	0.451	13.91	3	3	0.100	0.050	0.393	0.375	60.0	
4	0.059	0.029	0.229	0.219	60.0		4	2.036	1.018	2.115	0.568	12.34	4	4	0.100	0.050	0.393	0.375	60.0	
5	0.059	0.029	0.229	0.219	60.0	2	5	2.536	1.268	2.625	0.670	10.78	5	5	0.100	0.050	0.393	0.375	60.0	2
6	0.219	0.109	0.458	0.379	39.0	3	6	3.036	1.518	3.133	0.758	9.22	6	6	0.375	0.188	0.785	0.650	30.0	
7	0.438	0.219	0.689	0.451	13.91	4	7	3.536	1.768	3.638	0.832	7.68	7	7	0.375	0.188	0.785	0.650	30.0	
8	0.938	0.469	1.203	0.568	12.34	5	8	4.036	2.018	4.142	0.893	6.13	8	8	0.375	0.188	0.785	0.650	30.0	
9	1.438	0.719	1.713	0.670	10.78	6	9	4.536	2.268	4.644	0.940	4.60	9	9	0.375	0.188	0.785	0.650	30.0	3
10	1.938	0.969	2.221	0.758	9.22	7	10	5.036	2.518	5.145	0.973	3.06	10	10	0.750	0.375	1.179	0.760	9.18	4
11	2.438	1.219	2.726	0.832	7.68	8	11	5.536	2.768	5.646	0.993	1.53	11	11	1.250	0.625	1.685	0.834	7.63	5
12	2.938	1.469	3.230	0.893	6.13	9	12	6.036	3.018	6.146	1.000	0.0	12	12	1.750	0.875	2.188	0.894	6.09	6
13	3.438	1.719	3.732	0.940	4.60	10	13	6.536	3.268	6.646	1.000	0.0	13	13	2.250	1.125	2.690	0.941	4.56	7
14	3.938	1.969	4.233	0.973	3.06	11	14	7.036	3.518	7.146	1.000	0.0	14	14	2.750	1.375	3.192	0.974	3.02	8
15	4.438	2.219	4.734	0.993	1.53	12								15	3.250	1.625	3.692	0.994	1.49	9
16	4.938	2.469	5.234	1.000	0.0	13								16	3.750	.875	4.132	1.000	0.0	10
17	5.438	2.719	5.734	1.000	0.0	14								17	4.250	2.125	4.692	1.000	0.0	11
18	5.938	2.969	6.234	1.000	0.0	15								18	4.750	2.375	5.192	1.000	0.0	12
Center body taps																				
19	6.375	3.188	6.671	1.000	0.0	16	19	7.438	3.719	7.548	1.000	0.0	15	19	5.205	2.602	5.647	1.000	0.0	13
20	6.875	3.438	7.171			17	20	7.938	3.969	8.048			16	20	5.705	2.852	6.147			14
21	7.375	3.688	7.671			18	21	8.438	4.219	8.548			17	21	6.205	3.102	6.647			15
22	7.875	3.938	8.171			19	22	8.938	4.469	9.048			18	22	6.705	3.352	7.147			16
23	8.375	4.188	8.671			20	23	9.438	4.719	9.548			19	23	7.205	3.602	7.647			17
24	8.375	4.188	8.671				24	9.438	4.719	9.548				24	7.205	3.602	7.647			
25	8.375	4.188	8.671				25	9.438	4.719	9.548				25	7.205	3.602	7.647			
26	8.375	4.188	8.671				26	9.438	4.719	9.548				26	7.205	3.602	7.647			
27	8.875	4.438	9.171			21	27	9.938	4.969	10.048			20	27	7.705	3.852	8.147			18
28	9.375	4.688	9.671			22	28	10.438	5.219	10.548			21	28	8.205	4.102	8.647			19
29	9.875	4.938	10.171			23	29	10.938	5.469	11.048			22	29	8.705	4.352	9.147			20
30	10.375	5.188	10.671			24	30	11.438	5.719	11.548			23	30	9.205	4.602	9.647			21
31	10.875	5.438	11.171			25	31	11.938	5.969	12.048			24	31	9.705	4.852	10.147			22
32	11.375	5.688	11.671			26	32	12.438	6.219	12.548			25	32	10.205	5.102	10.647			23
33	11.875	5.938	12.171			27	33	12.938	6.469	13.048			26	33	10.705	5.352	11.147			24
34	12.375	6.188	12.671			28	34	13.438	6.719	13.548			27	34	11.205	5.602	11.647			25
35	12.875	6.438	13.171			29	35	13.938	6.969	14.048			28	35	11.705	5.852	12.147			26
36	13.375	6.688	13.671			30	36	14.438	7.219	14.548			29	36	12.205	6.102	12.647			27
37	13.875	6.938	14.171			31	37	14.938	7.469	15.048			30	37	12.705	6.352	13.147			28
38	14.375	7.188	14.671			32	38	15.438	7.719	15.548			31	38	13.205	6.602	13.647			29
39	14.875	7.438	15.171			33	39	15.938	7.969	16.048			32	39	13.705	6.852	14.147			30
40	15.375	7.688	15.671			34	40	16.438	8.219	16.548			33	40	14.205	7.102	14.647			31
41	15.000	8.000	16.296			35	41	17.063	8.532	17.173			34	41	14.830	7.415	15.272			32

Sphere-ogive junction
x = 0.330 in., x/D = 0.165,
tangent angle = 14.25 deg
Ogive-cylinder junction
x = 4.938 in., x/D = 2.469

Ogive-cylinder junction
x = 6.036 in., x/D = 3.018

Sphere-ogive junction
x = 0.625 in., x/D = 0.312,
tangent angle = 9.6 deg
Ogive-cylinder junction
x = 3.737 in., x/D = 1.868

TEST CONDITIONS AND PROCEDURES

SUPERSONIC TESTS

Wind tunnel tests at Mach numbers of 1.52 and 2.02 were conducted in Supersonic Tunnel No. 2 of the Naval Ordnance Laboratory (NOL), White Oak during May 1966. Although this is normally a continuous flow tunnel, an oil leak problem made it necessary to conduct the tests with the tunnel operating in the blowdown mode. This resulted in a considerable reduction in the scope of the test program, which originally included a Mach number range from 0.9 to 5.0. Angle of attack was varied from 11.5 to -11.5 deg. Angle of sideslip was zero throughout the tests. Figure 7 shows the model installed in NOL Tunnel No. 2.

Complete circumferential pressure distributions were obtained with Nose A by aligning the row of streamline taps at roll angles of 0 (top), 15 (Mach 2.02 only), 30, 60, and 90 deg, and then remotely sweeping through the angle of attack range at a slow enough rate to assure pressure stabilization. It was not possible to hold at each desired angle of attack while the pressure taps were sampled, because of the relatively short blowdown run times. A similar procedure was used with Noses B and C; however, the 60- and 90-deg roll positions were not run because of time limitations. Nose A was tested at Mach numbers of 1.52 and 2.02 while Noses B and C were only tested at Mach 2.02.

Test conditions are summarized in Table 2. No attempt was made to match the wind tunnel Reynolds numbers with the captive flight values, because of the relatively small effect of Reynolds number on the pressure distribution about bodies of revolution in the angle of attack range investigated.

Each tap was monitored by an individual pressure transducer which was sampled on the order of 40 times during the sweep from 11.5 to -11.5 deg angle of attack. Pressures, expressed as pressure coefficients,[2] and corresponding angles of attack for each tap were given for each combination of nose configuration, Mach number, and roll angle. NOL provided this data in printout form and also on magnetic tape.

---

[2] Throughout this report, pressure coefficient is calculated from the relation

$$Cp = \frac{P - P_\infty}{q}$$

where

Cp = pressure coefficient
P = measured surface pressure
P_∞ = free-stream static pressure
q = dynamic pressure

TABLE 2. Wind Tunnel Test Conditions.

Wind tunnel	Mach No.	Reynolds No. per foot	Angle of attack, deg	Roll angle,[a] deg
NSRDC	0.7	3.4×10^6	0, ±2, ±4, ±6, ±8, ±10	0, 15, 30, 60, 90
NSRDC	0.8	3.6×10^6	0, ±2, ±4, ±6, ±8, ±10	0, 15, 30, 60, 90
NSRDC	0.9	3.8×10^6	0, ±2, ±4, ±6, ±8, ±10	0, 15, 30, 60, 90
NSRDC	1.0	4.0×10^6	0, ±2, ±4, ±6, ±8, ±10	0, 15, 30, 60, 90
NSRDC	1.1	4.1×10^6	0, ±2, ±4, ±6, ±8, ±10	0, 15, 30, 60, 90
NOL	1.52	4.7×10^6	11.5 to -11.5	0, 30, 60, 90
NOL	2.02	3.9×10^6	11.5 to -11.5	0, 15, 30, 60, 90

[a] Roll angle is 0 deg when the row of pressure taps is on the top of the model.

FIG. 7. Model Installed in NOL Supersonic Tunnel No. 2.

The method of least squares was used to fit a second-order polynomial to the pressure-coefficient-versus-angle-of-attack data for each tap. An example of this for a specific tap is shown in Fig. 8. The resulting pressure coefficient equations were input to a computer program which used them to calculate and plot the longitudinal pressure coefficient distributions at specified angles of attack for each run.

Some scatter occurred in the NOL data at angles of attack beyond -10 deg so that only results between 10 and -10 deg are included in this report.

TRANSONIC TESTS

Tests at Mach numbers of 0.7, 0.8, 0.9, 1.0, and 1.1 were conducted in the 7- x 10-ft transonic tunnel of the Naval Ship Research and Development Center (NSRDC) during February 1969. All three noses were tested at angles of attack from -10 to 10 deg and roll angles of 0, 15, 30, 60, and 90 deg. The NSRDC wind tunnel test conditions are also summarized in Table 2.

The procedure used in the NSRDC tests was to manually set the roll angle and remotely step the model through the angle of attack range in 2-deg increments. After this was done for each Mach number, the roll angle was changed and the process repeated. As the NSRDC transonic wind tunnel is a continuous flow tunnel, time was available to hold each angle of attack long enough to allow all pressure taps to be sampled.

Ideally it would have been desirable to roll the model while holding Mach number and angle of attack, since circumferential pressure distributions were of major interest. Unfortunately, this was not practical, because roll angle could not be set remotely. However, the repeatability of the reported Mach number and angle of attack at each roll position was such (Mach number within ±0.01, angle of attack within ±0.1 deg) that any effects caused by these minor variations were considered acceptable.

Pressures were measured by means of Scanivalve pressure scanning switches. Pressure distributions were tabulated in the form of pressure coefficient versus body station (x/D) and given, along with a heading giving test conditions, on both computer printout and magnetic tape. As with the NOL data, a program was written to give computer-generated plots of longitudinal pressure coefficient distributions.

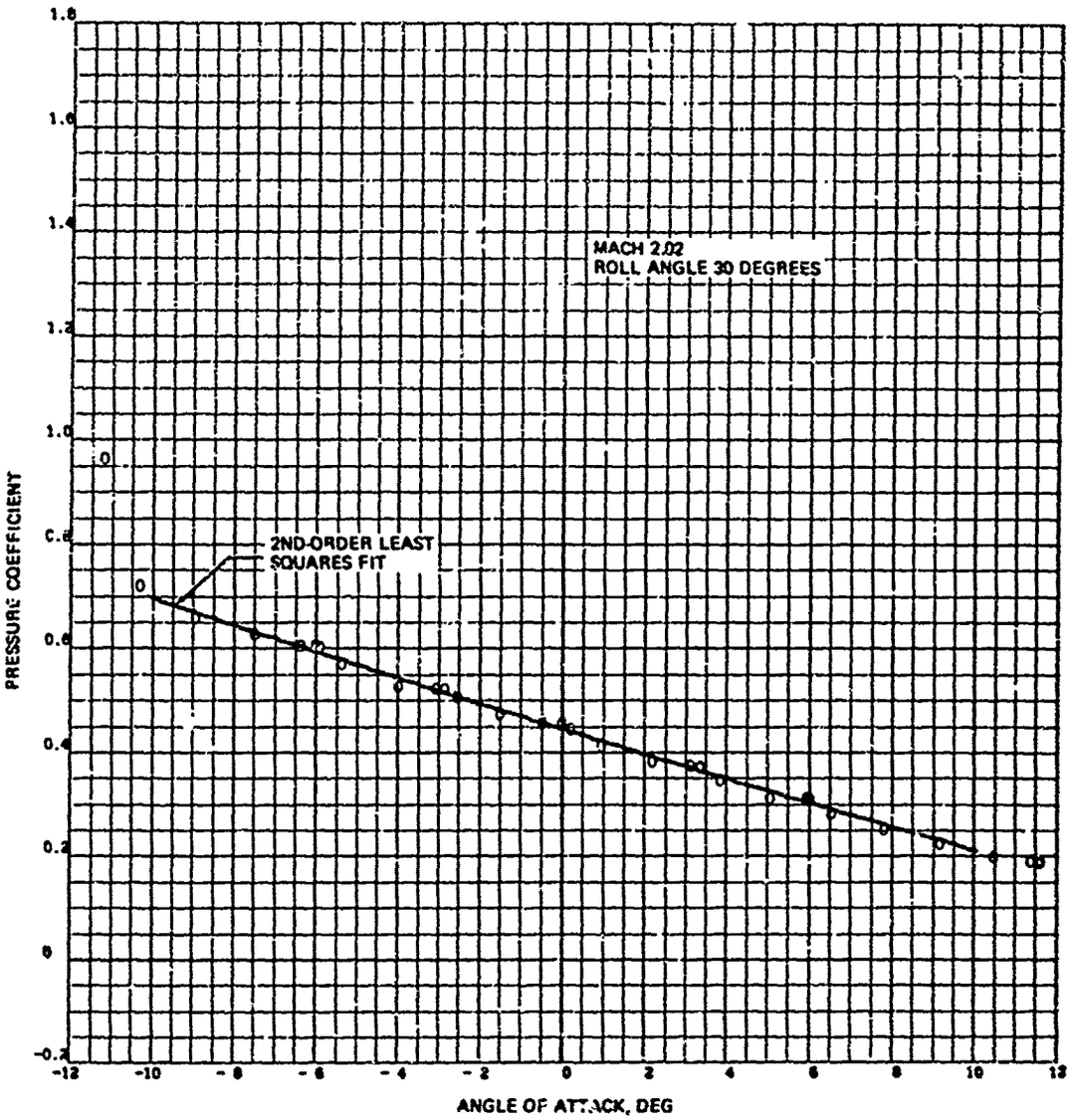

FIG. 8. Pressure Coefficient Versus Angle of Attack for Tap No. 9 of Nose C.

EVALUATION OF DATA

A systematic error analysis of the wind tunnel was not made in this program; however, various checks indicated the data to be of good quality. Published information on the NSRDC transonic tunnel[3] reports the pressure measurements to be accurate to ±1 lb/ft^2 and model angles to ±0.1 deg. Accuracy of the NOL data is felt to be of the same magnitude.

Spot checks of the data were made by calculating the Mach number from the ratio of the stagnation pressure measured by the centerline taps of Noses A and C at zero angle of attack to the free-stream static pressure. The Mach number as calculated in this manner was almost always within 0.005 of the reported Mach numbers in the NSRDC tests and was 0.03 higher for the two NOL Mach numbers.

As discussed later in the section on flow angle relationships, the pressure difference across the spherical nose caps of Noses A and C indicated a negative angle of attack bias of 0.3 to 0.5 deg for all of the data. Although this may have been caused by slight errors in the positions of the pressure taps, the same result occurred with both noses and also when the model was rolled 90 deg and a different set of nose taps was involved. The net effect on the overall pressure distribution was not felt to be significant. Differences between the pressures measured by the four taps spaced 90 deg apart circumferentially on the center body while at zero angle of attack were of the same order as the accuracy of the measurements.

Another check on the uniformity of the flow is obtained by comparing the pressure distributions at -10 and 10 deg angle of attack with the model in the 90-deg roll position. Because of symmetry, these distributions should be identical. As seen in Fig. 9 and throughout the data presented in the next section, this was nearly the case in almost all instances. The largest variation occurred over the aft portion of the body during the Mach 2.02 test with Nose A (appendix, Fig. A-34).

An indication of the repeatability of the data can be obtained by comparing the zero angle of attack pressure distribution at each roll position for a given Mach number and nose configuration. Again, as shown in Fig. 10 and the following pressure distributions, the agreement was very good.

[3] Naval Ship Research and Development Center. *The David Taylor Model Basin 7- by 10-Foot Transonic Wind Tunnel Facility*, by Walter S. Thomas. Washington, D.C., NSRDC, July 1960. (Aero Report 985)

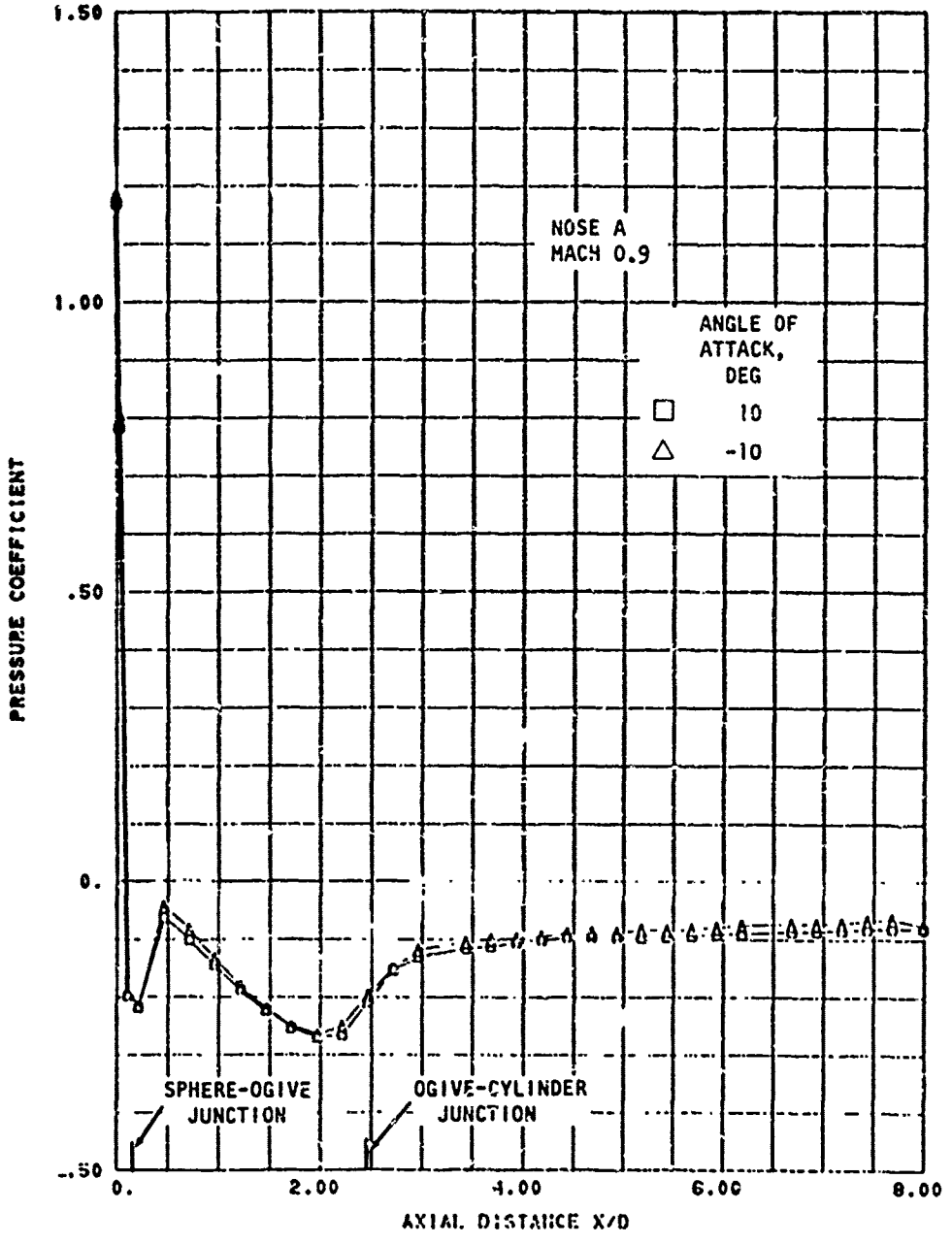

FIG. 9. Comparison of Longitudinal Pressure Distributions at 10 and -10 Degree Angles of Attack for 90 Degree Roll Angle.

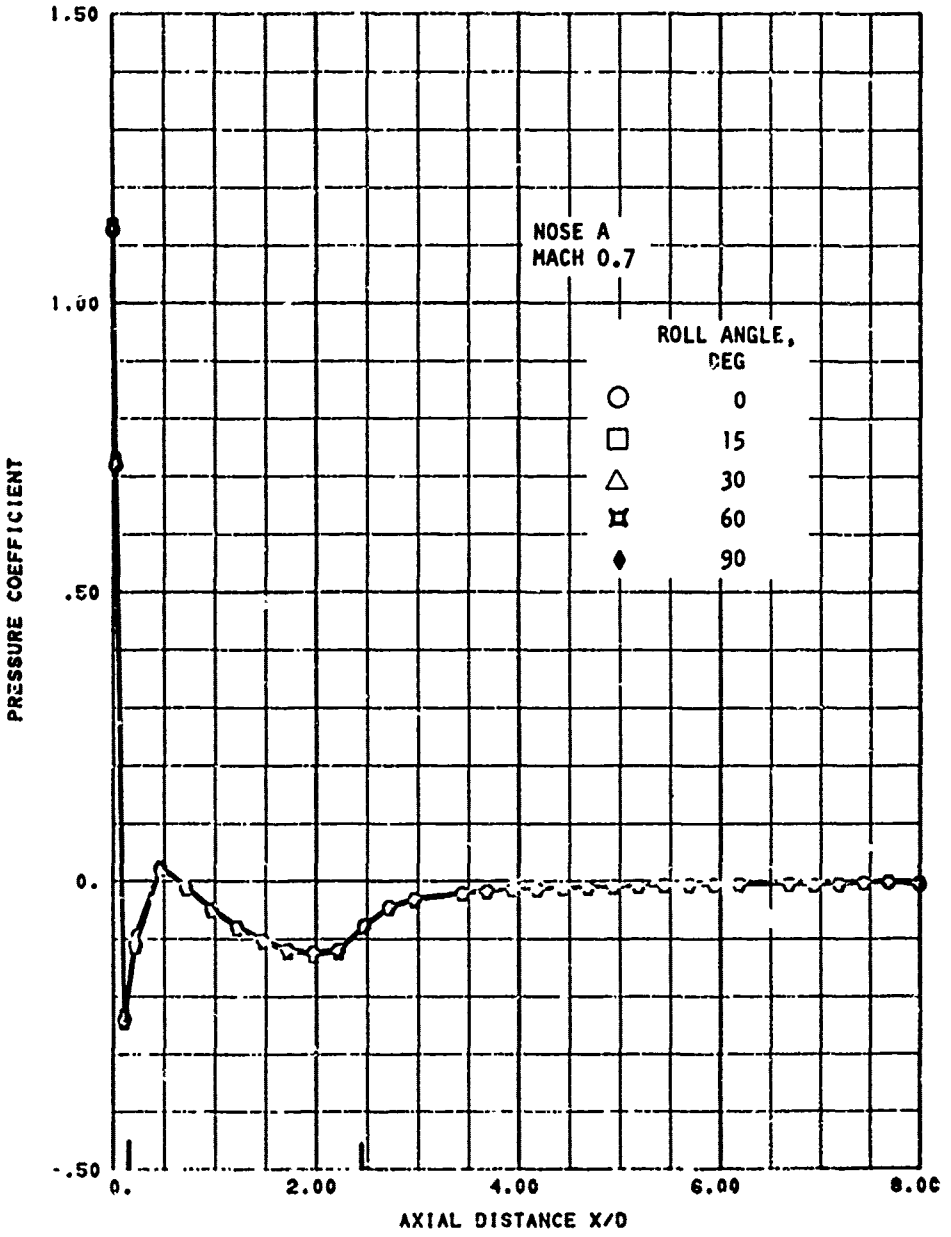

FIG. 10. Comparison of Longitudinal Pressure Distributions for all Roll Angles at Zero Angle of Attack.

RESULTS

Results of the wind tunnel tests are presented in the form of longitudinal pressure coefficient distributions in the appendix. Plots are given for each combination of nose configuration, Mach number, and roll angle. Each figure gives the pressure distributions at angles of attack of 0, 10, and -10 deg. An exception is Nose C at Mach 0.9 and zero roll (appendix, Fig A-73). The -10 deg angle of attack data was not obtained for this condition and is replaced in Fig. A-73 by the pressure distribution at -8 deg angle of attack.

The pressure distribution plots in the appendix were generated by computer and consist of the measured pressure coefficients at each station connected by straight lines. Data points were connected to aid in identifying the three different plots per figure. While connecting the data with straight lines gives a reasonably accurate fairing over most of the model because of the close tap spacing, care should be taken in interpolating between data points in regions of high pressure gradients such as the sphere-ogive junctions of Noses A and C. To aid in the interpretation of the pressure distributions, the locations of the sphere-ogive junctions and the ogive-cylinder junctions are indicated by tick marks on each plot.

Pressure distributions were examined for anomalies, and data that were obviously erroneous were eliminated. During the runs at Mach 1.0, 1.52, and 2.02 (Nose B only), the aftmost pressure taps extended out of the test section rhombus and the readings were affected. These data have been included, but are so marked on the appropriate figures.

In addition to presenting the results in the appendix, representative pressure distributions are plotted in Fig. 11 through 29 to demonstrate the effects of Mach number, roll angle, and angle of attack.

Longitudinal pressure coefficient distributions at Mach numbers of 0.7, 1.1, and 2.02 are plotted for each nose at zero roll angle (streamline taps along top of model) for angles of attack of 0, 10, and -10 deg in Fig. 11 through 19. Nose A distributions are plotted in Fig. 11, 12, and 13 for 0, 10, and -10 deg angles of attack, respectively. Figures 14, 15, and 16 give the Nose B data at angles of attack of 0, 10, and -10 deg, respectively. Pressure distributions for Nose C at the three Mach numbers are given for 0, 10, and -10 deg angles of attack in Fig. 17, 18, and 19, respectively.

Figures 20 and 21 show the effect of roll angle on Nose A at Mach 1.1 for a flow angle of 10 deg. Pressure distributions on the leeward side of the model at roll angles of 0, 15, 30, 60, and 90 deg are given in Fig. 20. Windward side pressure distributions at roll angles of 90, 120, 150, 165, and 180 deg (or 0-, 15-, 30-, 60-, and 90-deg roll angles at -10 deg angle of attack) are shown in Fig. 21.

While pressure distributions at just three angles of attack (0, 10, and -10 deg) are given in the appendix, representative results at intermediate flow angles are given in Fig. 22 through 29. Longitudinal pressure coefficient distributions for Nose A at Mach 0.7 and 0-deg roll are given for angles of attack of 0, 4, 6, 8, and 10 deg in Fig. 22, while the distributions at 0, -4, -6, -8, and -10 deg are given in Fig. 23. Results for Nose A at Mach 2.02 and 0-deg roll angle are given for the same positive and negative angles of attack in Fig. 24 and 25, respectively. The change in pressures on the nose, and in some cases the body, with angle of attack is uniform and relatively linear. This remains the case as model is rolled as shown in Fig. 26 and 27, which give the pressure distributions with Nose A at Mach 0.7 and 90-deg roll for the positive and negative angles of attack, respectively.

Distributions with Nose B at 0-deg roll angle are given for Mach 1.1 in Fig. 28 and 29 for the positive and negative angles of attack, respectively. Again, the pressure along the top of the nose increases uniformly as the model goes from positive to negative angle of attack.

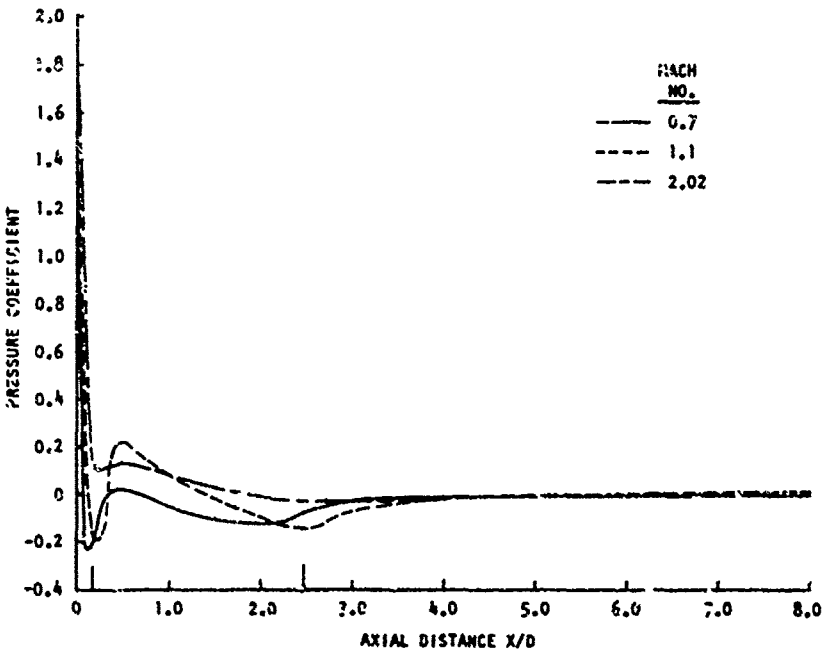

FIG. 11. Longitudinal Pressure Distributions With Nose A at Mach 0.7, 1.1, and 2.02 for Zero Roll Angle and Zero Angle of Attack.

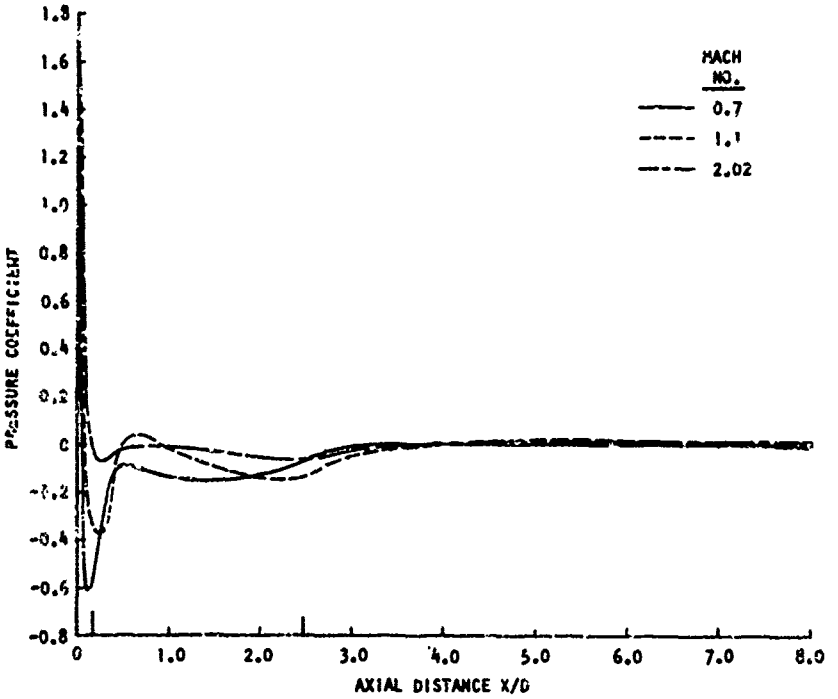

FIG. 12. Longitudinal Pressure Distributions With Nose A at Mach 0.7, 1.1, and 2.02 for Zero Roll Angle and 10 Degrees Angle of Attack.

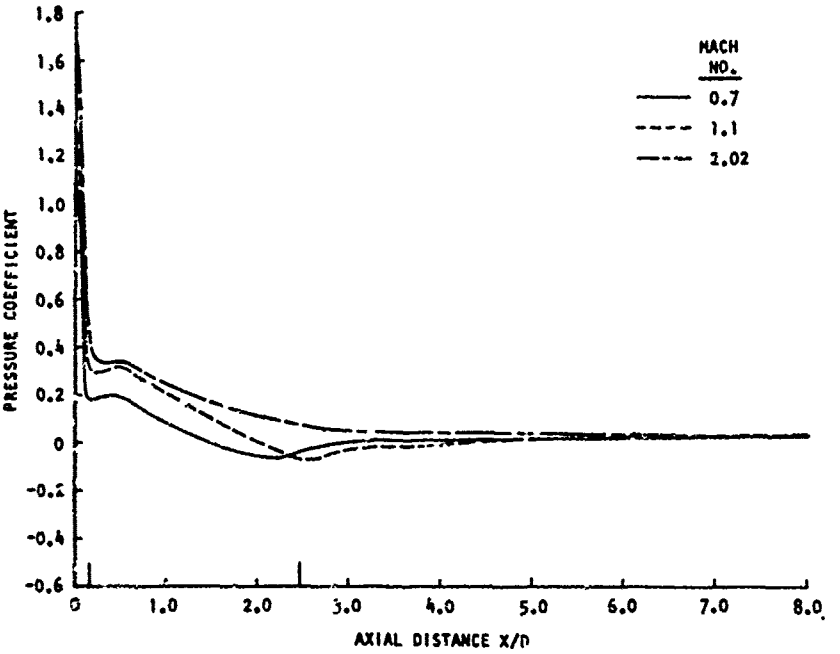

FIG. 13. Longitudinal Pressure Distributions With Nose A at Mach 0.7, 1.1, and 2.02 for Zero Roll Angle and -10 Degrees Angle of Attack.

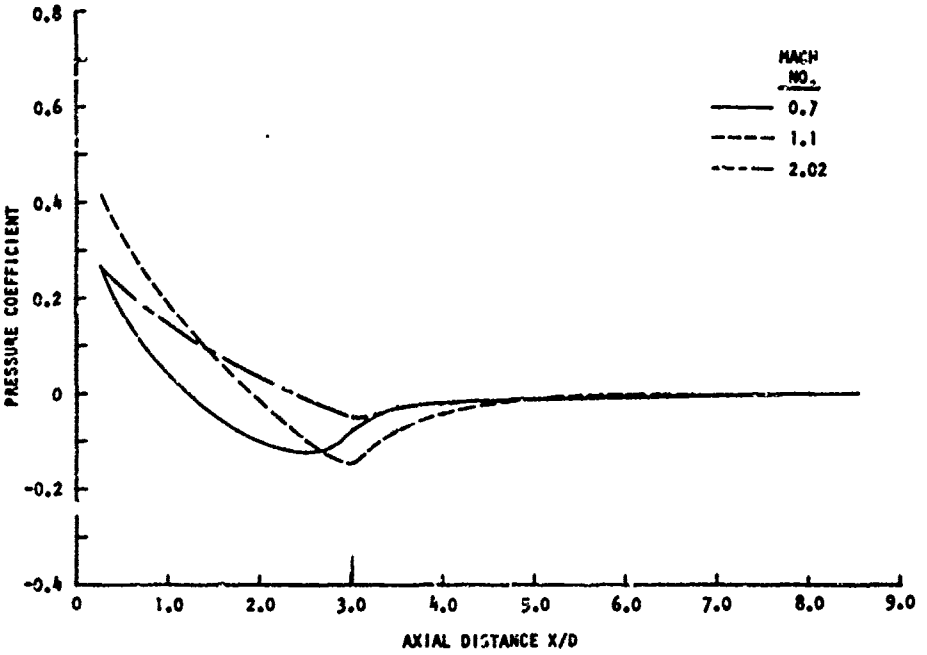

FIG. 14. Longitudinal Pressure Distributions With Nose B at Mach 0.7, 1.1, and 2.02 for Zero Roll Angle and Zero Angle of Attack.

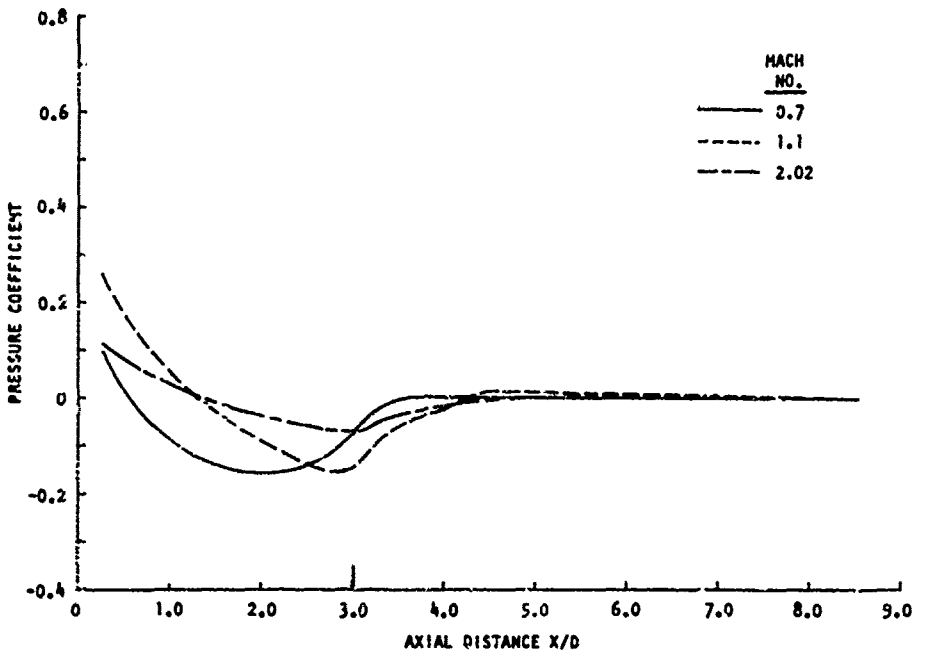

FIG. 15. Longitudinal Pressure Distributions With Nose B at Mach 0.7, 1.1, and 2.02 for Zero Roll Angle and 10 Degrees Angle of Attack.

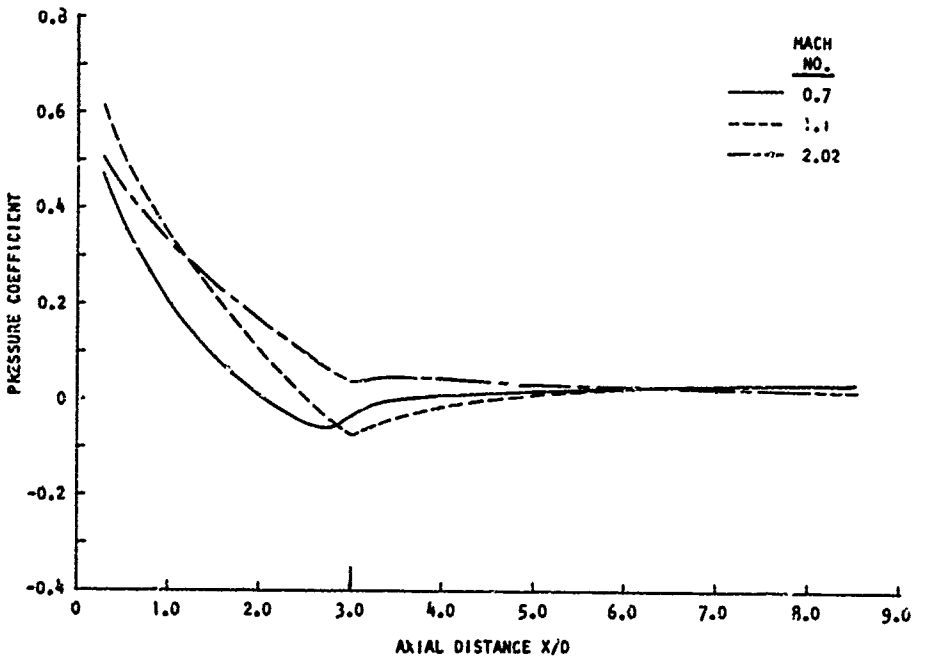

FIG. 16. Longitudinal Pressure Distributions With Nose B at Mach 0.7, 1.1, and 2.02 for Zero Roll Angle and -10 Degrees Angle of Attack.

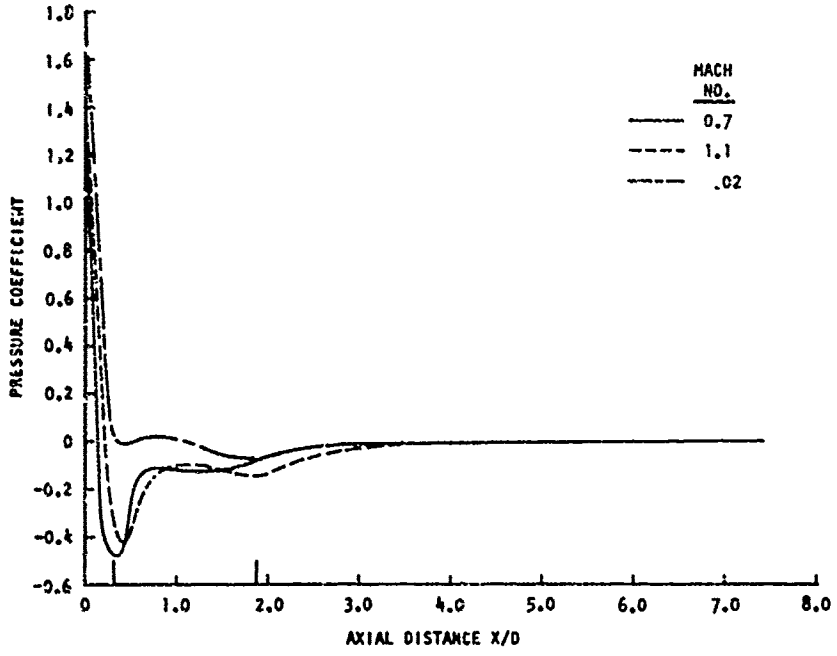

FIG. 17. Longitudinal Pressure Distributions With Nose C at Mach 0.7, 1.1, and 2.02 for Zero Roll Angle and Zero Angle of Attack.

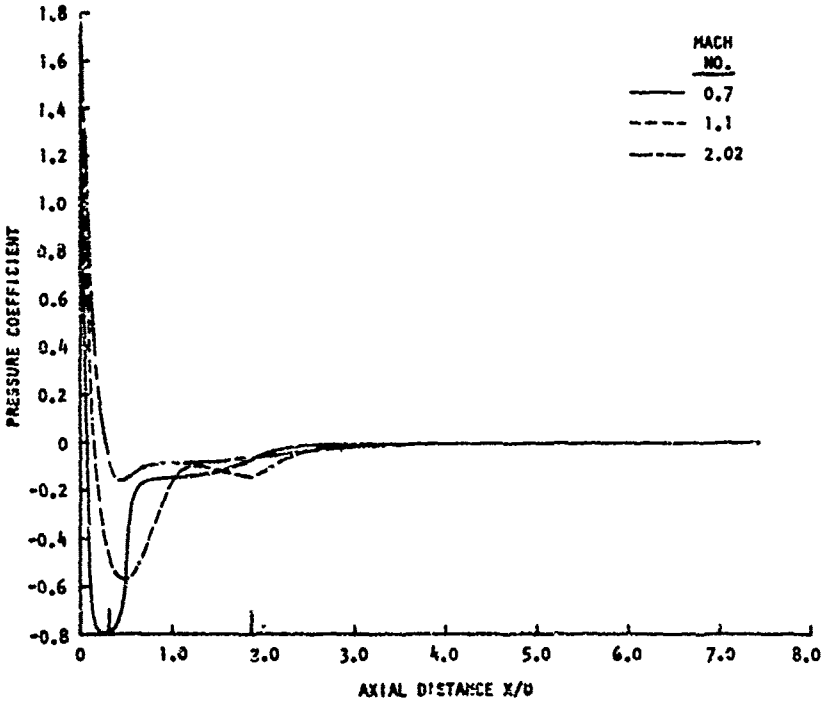

FIG. 18. Longitudinal Pressure Distributions With Nose C at Mach 0.7, 1.1, and 2.02 for Zero Roll Angle and 10 Degrees Angle of Attack.

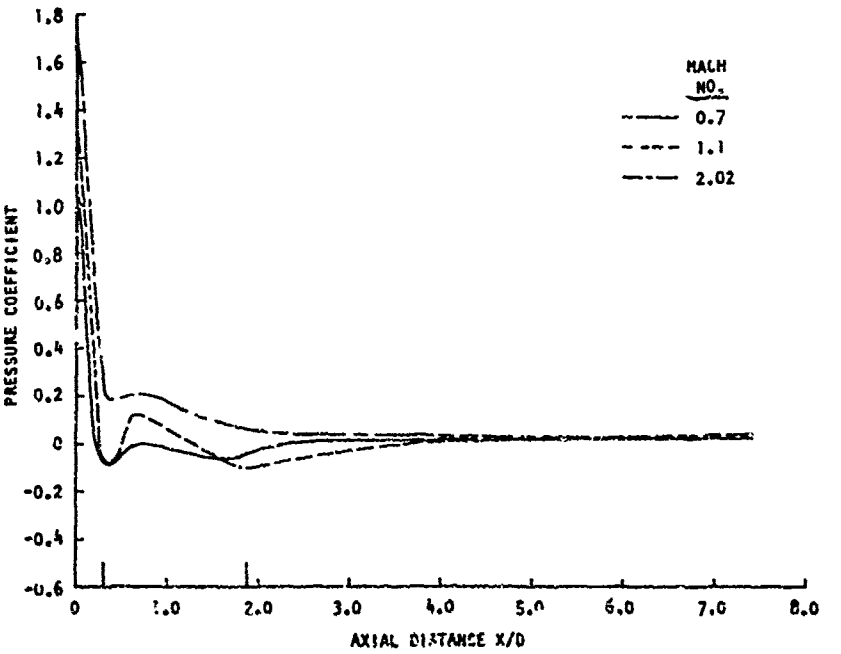

FIG. 19. Longitudinal Pressure Distributions With Nose C at Mach 0.7, 1.1, and 2.02 for Zero Roll Angle and -10 Degrees Angle of Attack.

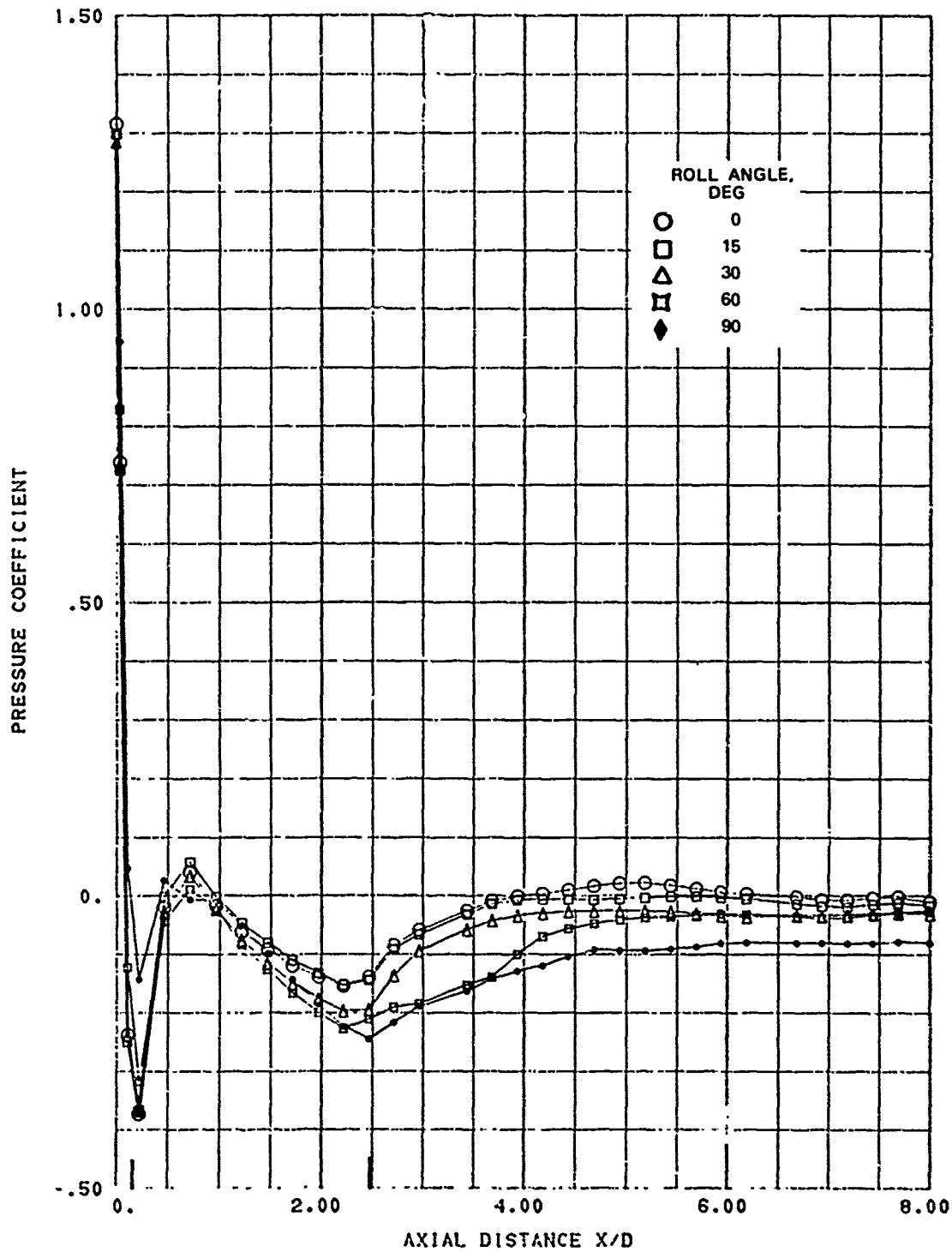

FIG. 20. Effect of Roll Angle on Nose A Pressure Distributions (Leeward Side); Mach 1.1, Flow Angle 10 Degrees.

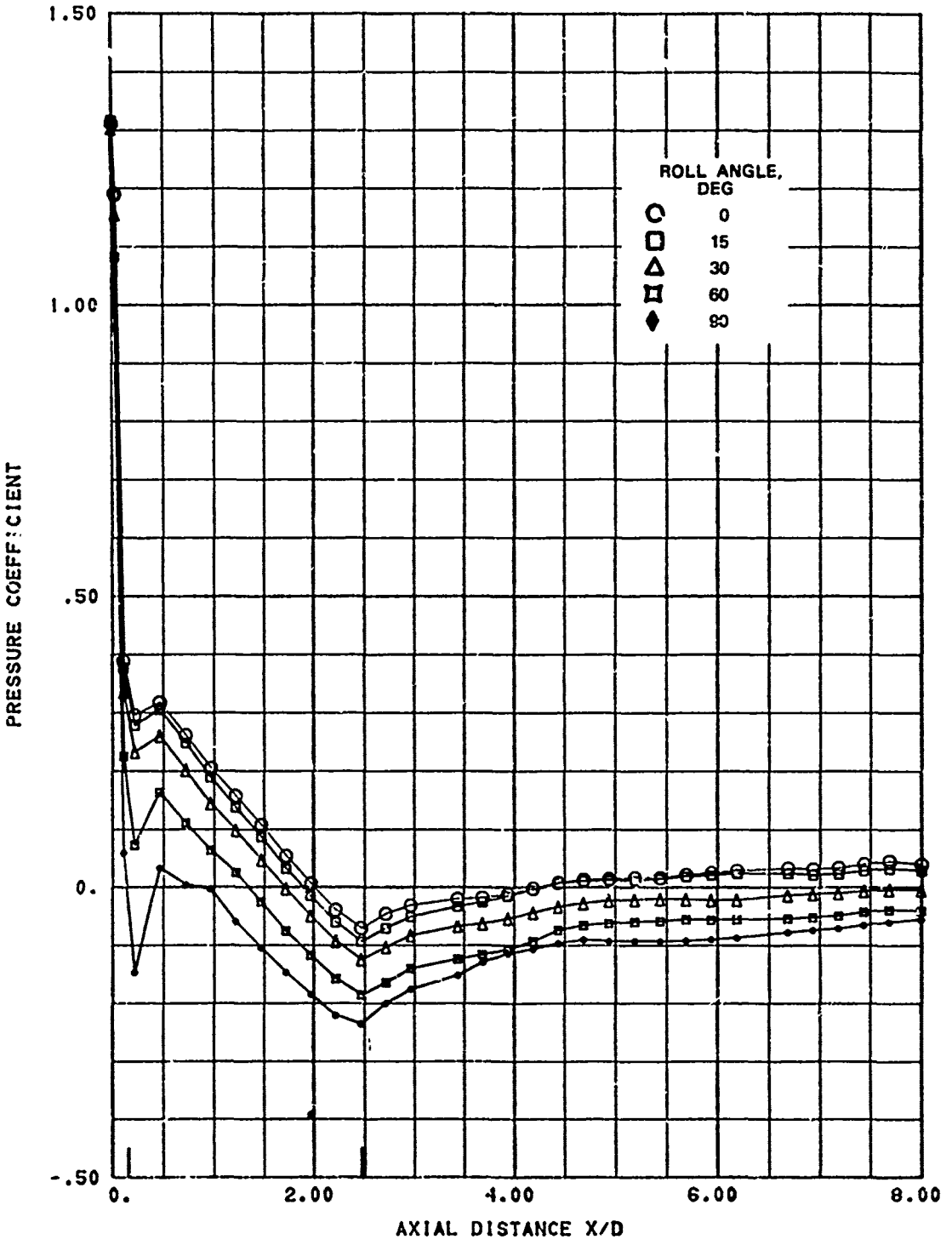

FIG. 21. Effect of Roll Angle on Nose A Pressure Distributions (Windward Side); Mach 1.1, Flow Angle 10 Degrees.

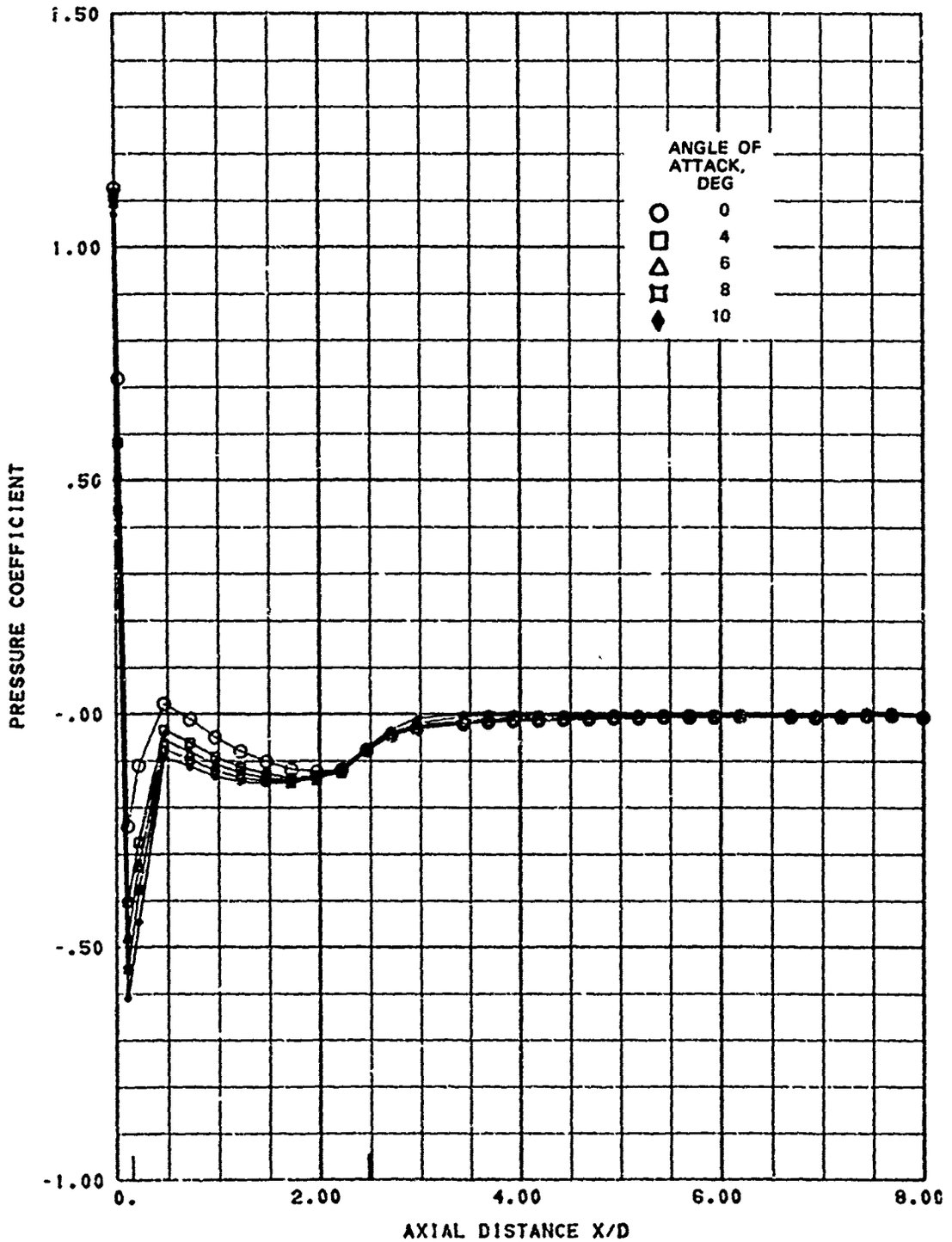

FIG. 22. Effect of Positive Angles of Attack on Nose A Pressure Distributions; Mach 0.7, Zero Roll Angle.

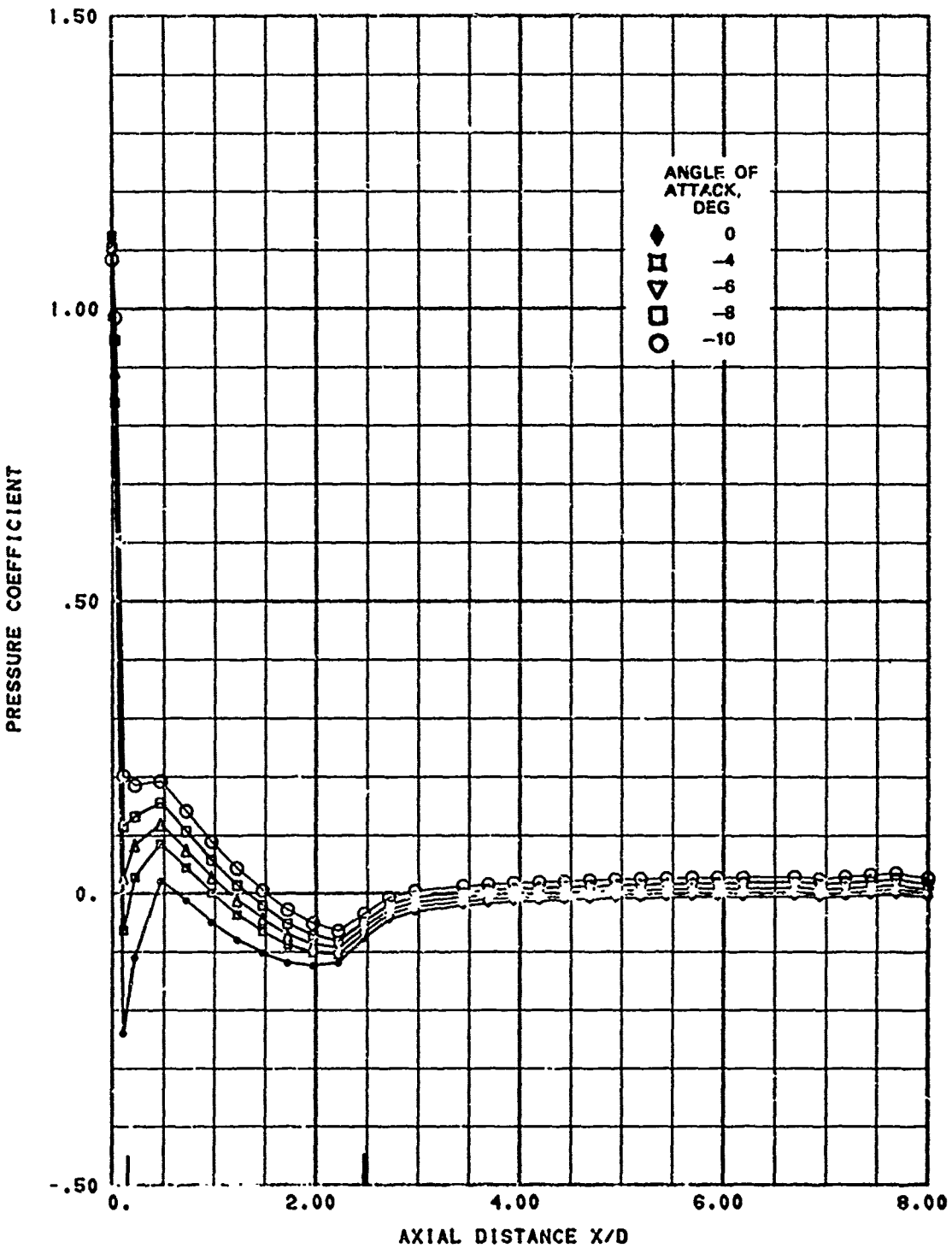

FIG. 23. Effect of Negative Angles of Attack on Nose A Pressure Distributions; Mach 0.7, Zero Roll Angle.

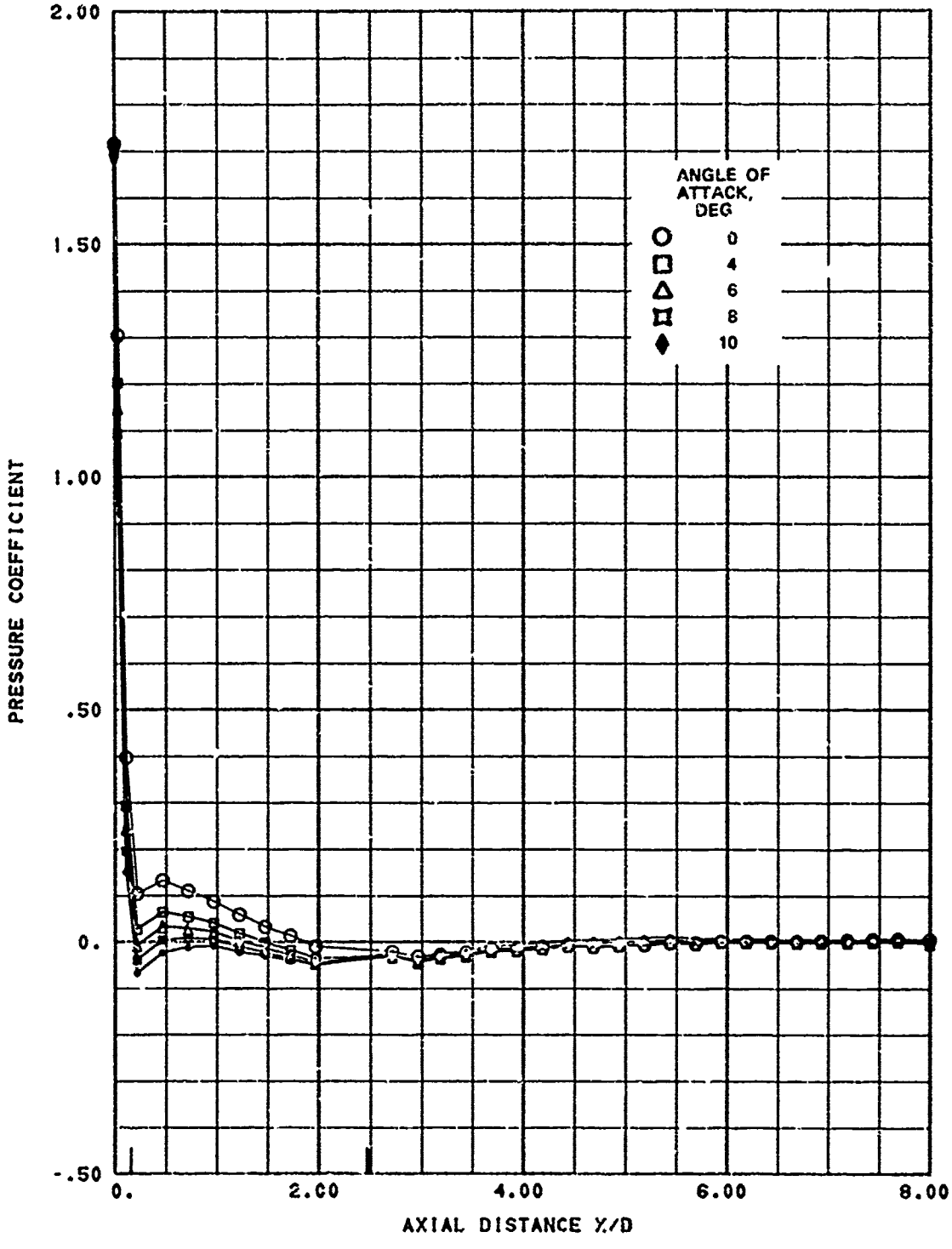

FIG. 24. Effect of Positive Angles of Attack on Nose A Pressure Distributions; Mach 2.02, Zero Roll Angle.

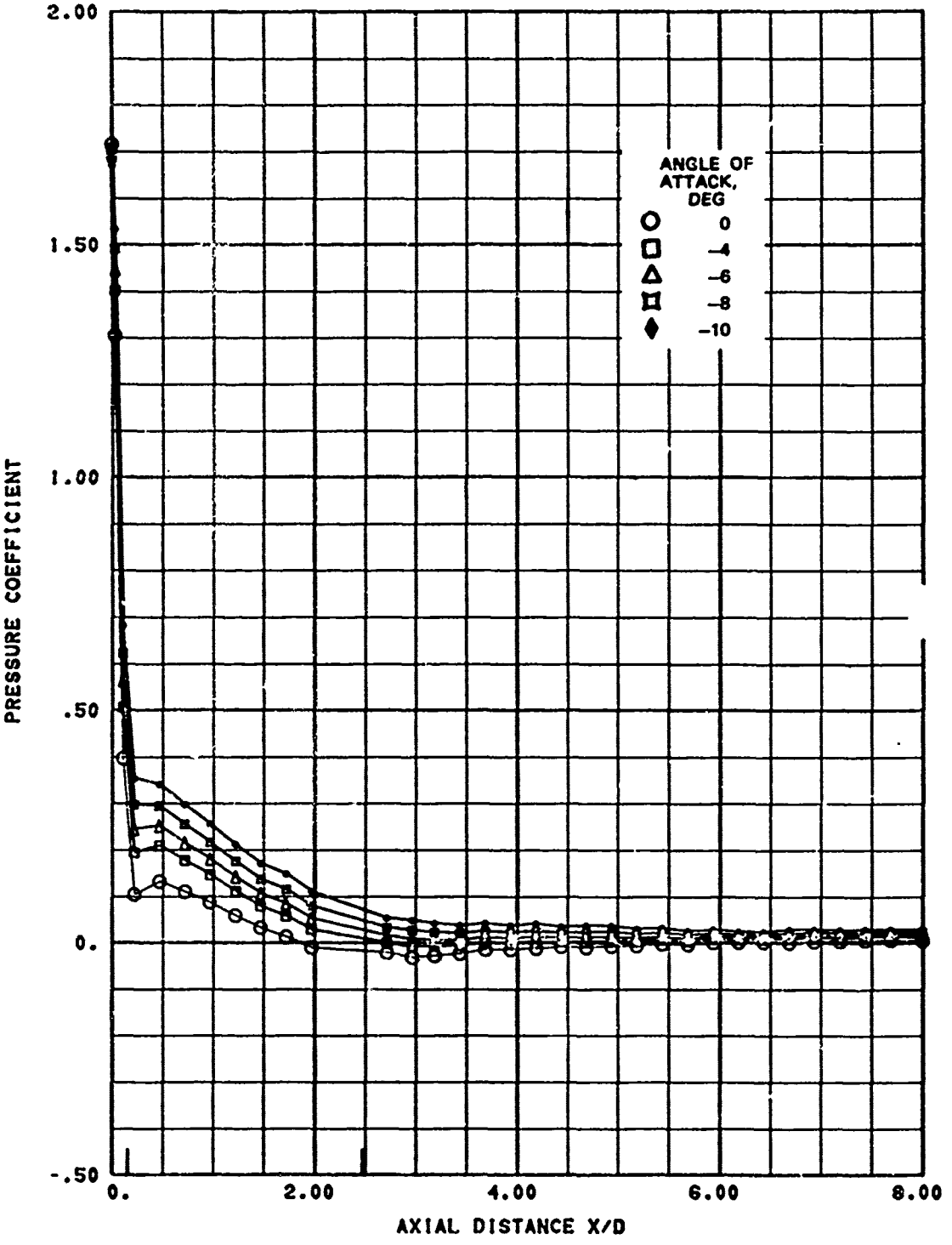

FIG. 25. Effect of Negative Angles of Attack on Nose A Pressure Distribution; Mach 2.02, Zero Roll Angle.

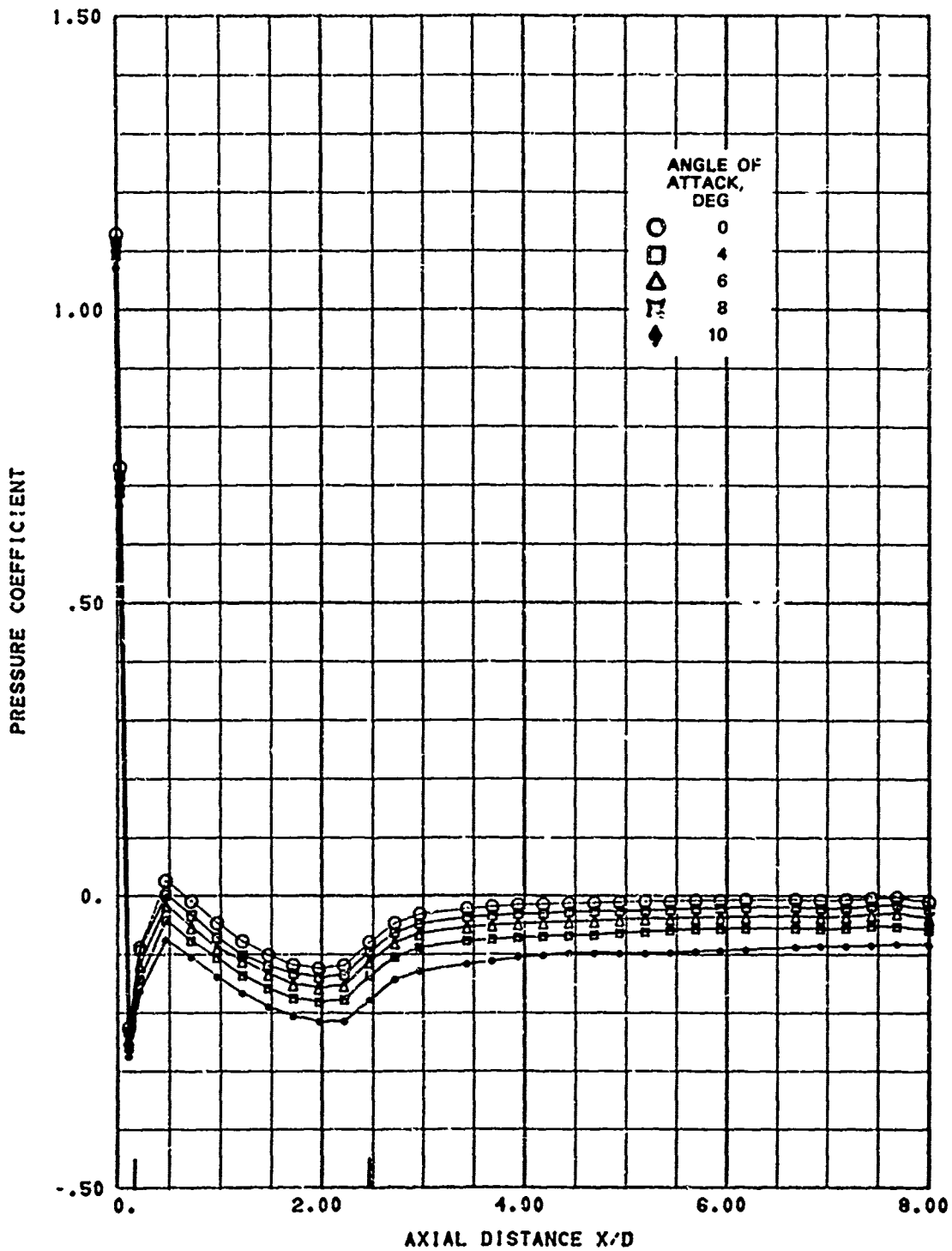

FIG. 26. Effect of Positive Angles of Attack on Nose A Pressure Distributions; Mach 0.7, 90 Degree Roll Angle.

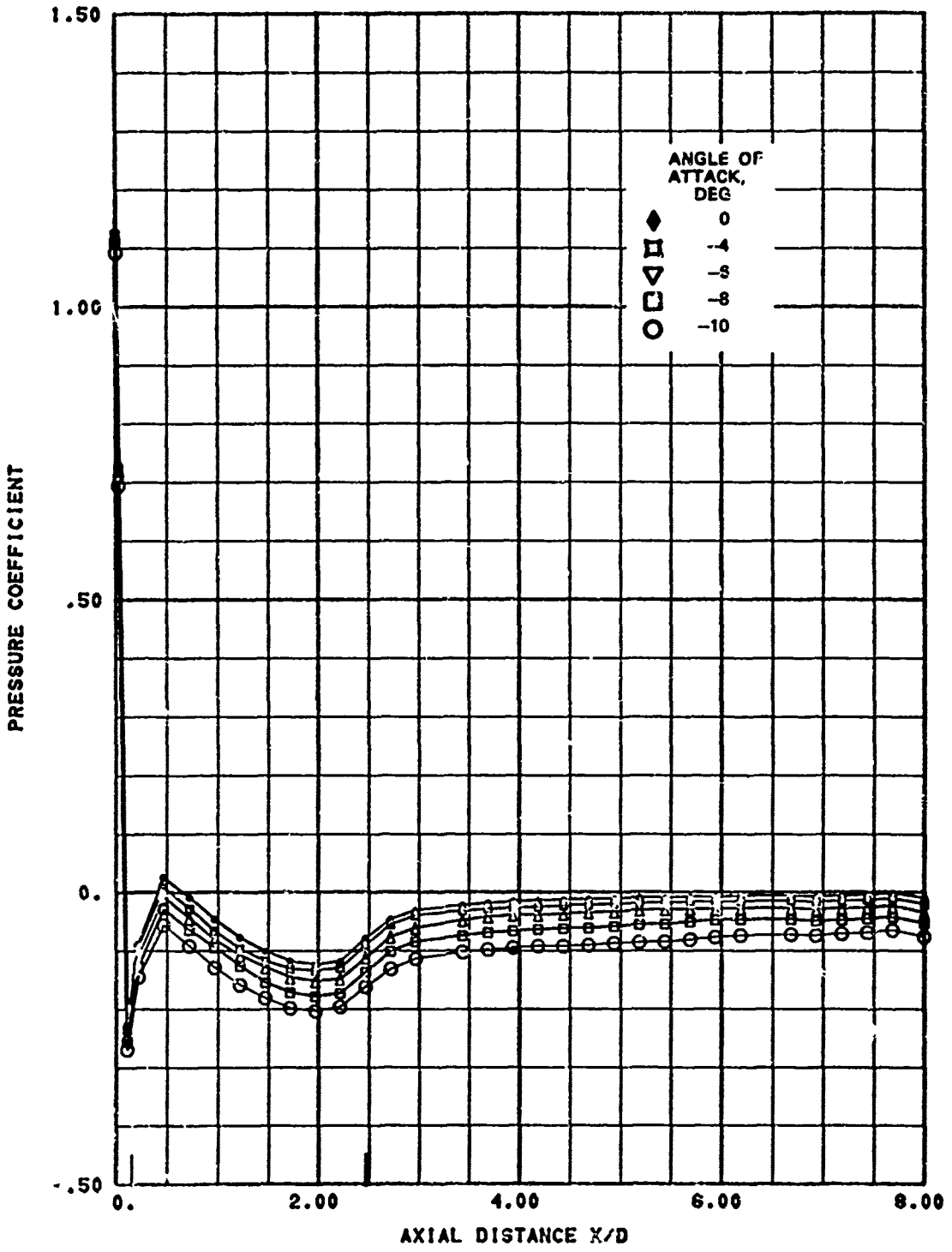

FIG. 27. Effect of Negative Angles of Attack on Nose A Pressure Distributions; Mach 0.7, 90 Degree Roll Angle.

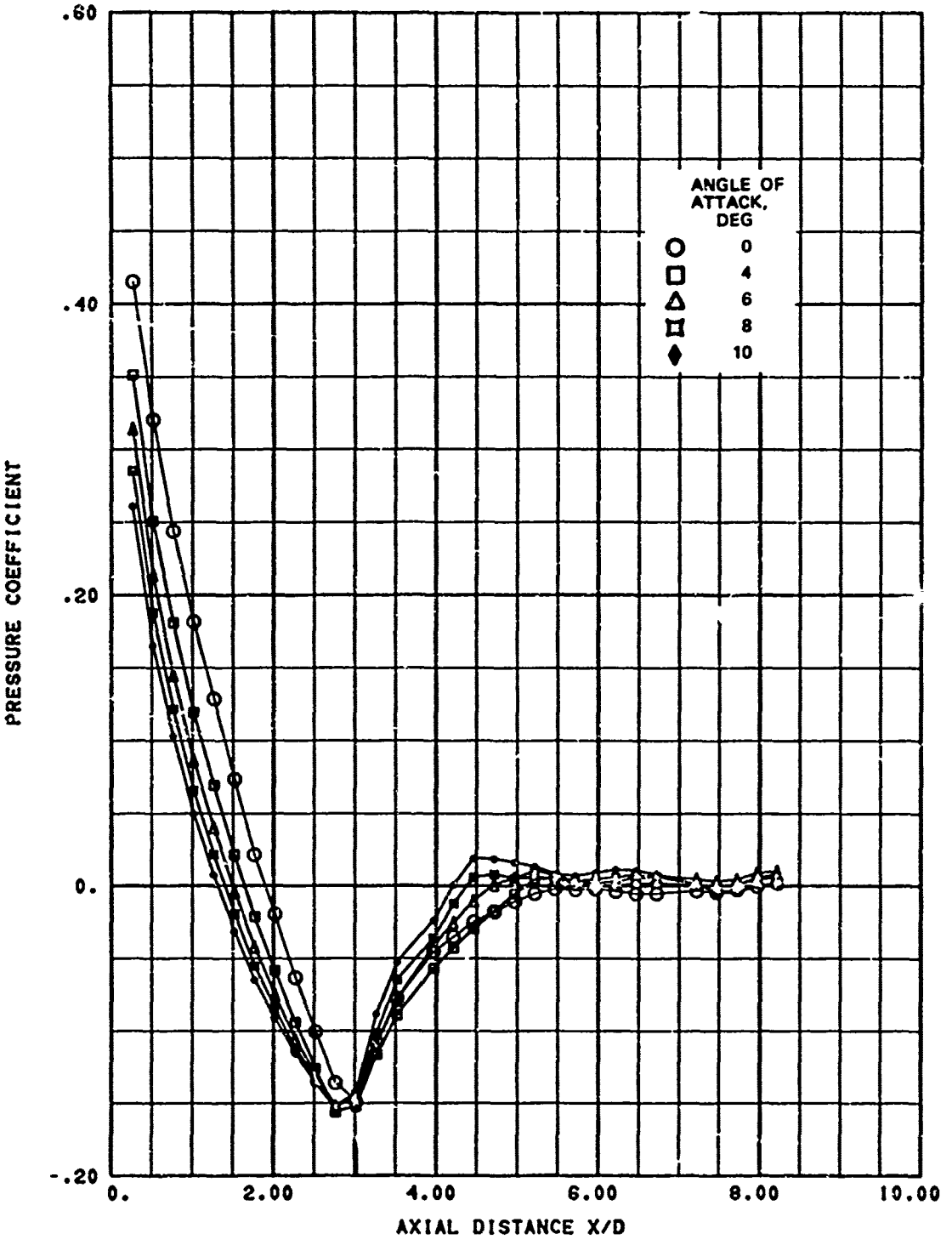

FIG. 28. Effect of Positive Angles of Attack on Nose B Pressure Distributions; Mach 1.1, Zero Roll Angle.

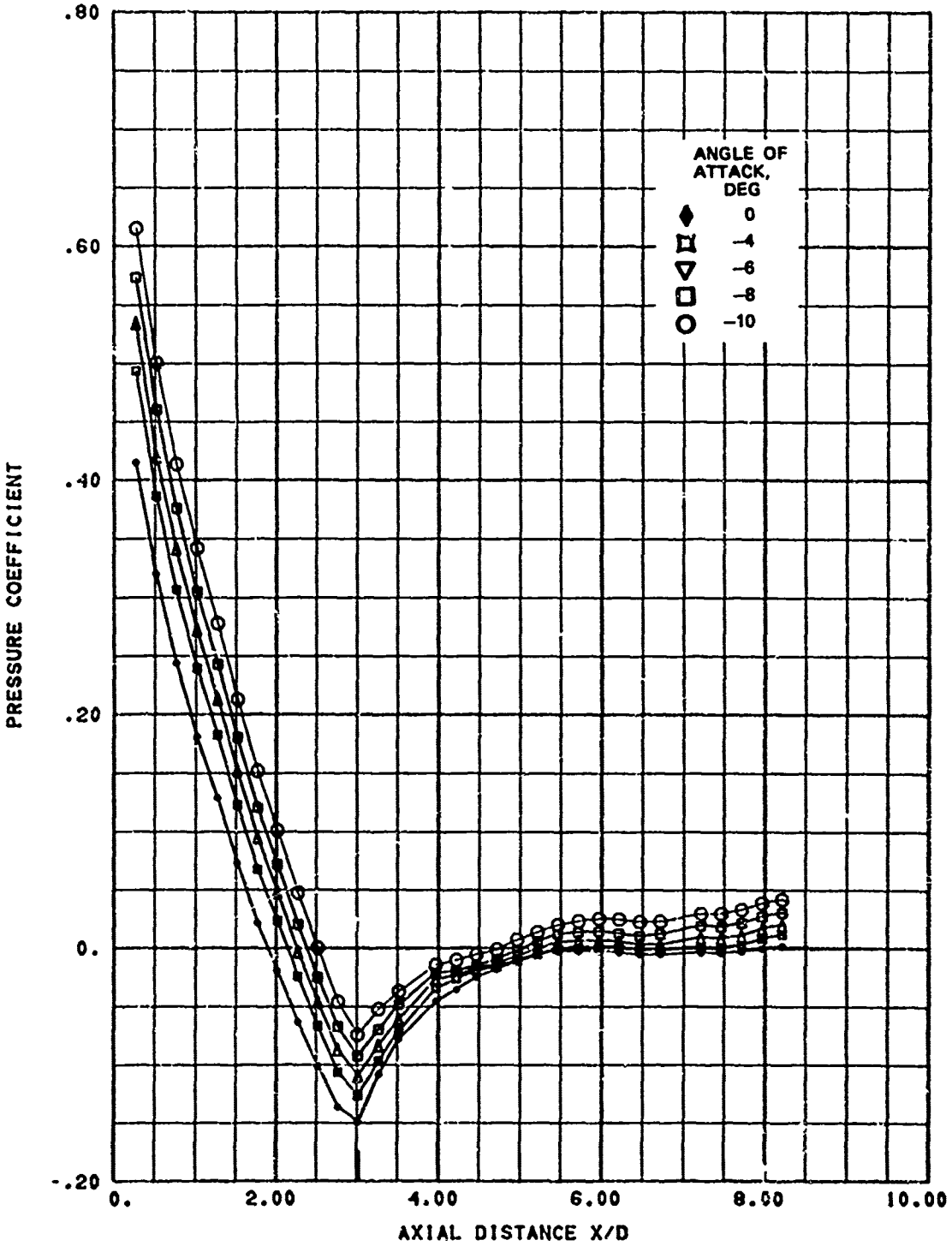

FIG. 29. Effect of Negative Angles of Attack on Nose B Pressure Distributions; Mach 1.1, Zero Roll Angle.

FLOW ANGLE RELATIONSHIPS

One of the important uses of the wind tunnel data in the Aircraft/ Missile Interference Effects Program was in estimating the flow angles (pitch and yaw) at the nose of the captive flight store. This was done by developing expressions relating the flow angle to the difference in pressure coefficient (ΔCp) across the spherical nose cap of the scale nose (Nose A). For comparison purposes, similar expressions were developed from the Nose C data.

Data from the pairs of pressure taps located 30 and 60 deg either side of the centerline of the nose cap in the pitch plane were used to develop the expressions. With Nose A, the 30-deg taps in the pitch plane were taps three and five when the model was in the 0-deg roll position and taps two and four when the model was rolled 90 deg. Since Nose A contained only one tap in the 60-deg position on the nose cap (tap six), it was necessary to use the difference in the pressure coefficients measured at corresponding positive and negative angles of attack. While this is not a preferred approach, it was considered adequate for the intended purpose because the accuracy with which the model angles were set (±0.1 deg) was greater than the accuracy sought in the captive flight flow angles (~1 degree). Nose C had two pairs of taps at both the 30-deg nose cap position (taps three and five at 0-deg roll and taps two and four at 90-deg roll) and the 60-deg position (taps seven and nine at 0-deg roll and taps six and eight at 90-deg roll).

The difference in the pressure coefficient for each pair of taps was determined at 2-deg increments over an angle of attack range from -10 to 10 deg. A first-order least squares fit was used to determine the slope and intercept of the ΔCp versus flow angle (α) data.

A typical plot of the ΔCp versus α results is given in Fig. 30 for Nose A at Mach 0.8. While the 60-deg position on the nose cap is more sensitive to the flow angle than the 30-deg position, it becomes nonlinear at the higher angles of attack. For this reason, the expressions developed from the 30-deg taps were used in estimating the flow angles about the captive flight store.

Figure 30 also demonstrates the slight negative angle of attack (~0.3-0.5 deg) at $\Delta Cp = 0$ mentioned previously. This same effect is shown in the Nose C data in Fig. 31 and 32. Since the ΔCp across the pairs of taps would be zero at a true 0-deg angle of attack (assuming correct tap location), the intercept was assumed zero when the expressions were applied to the captive flight data.

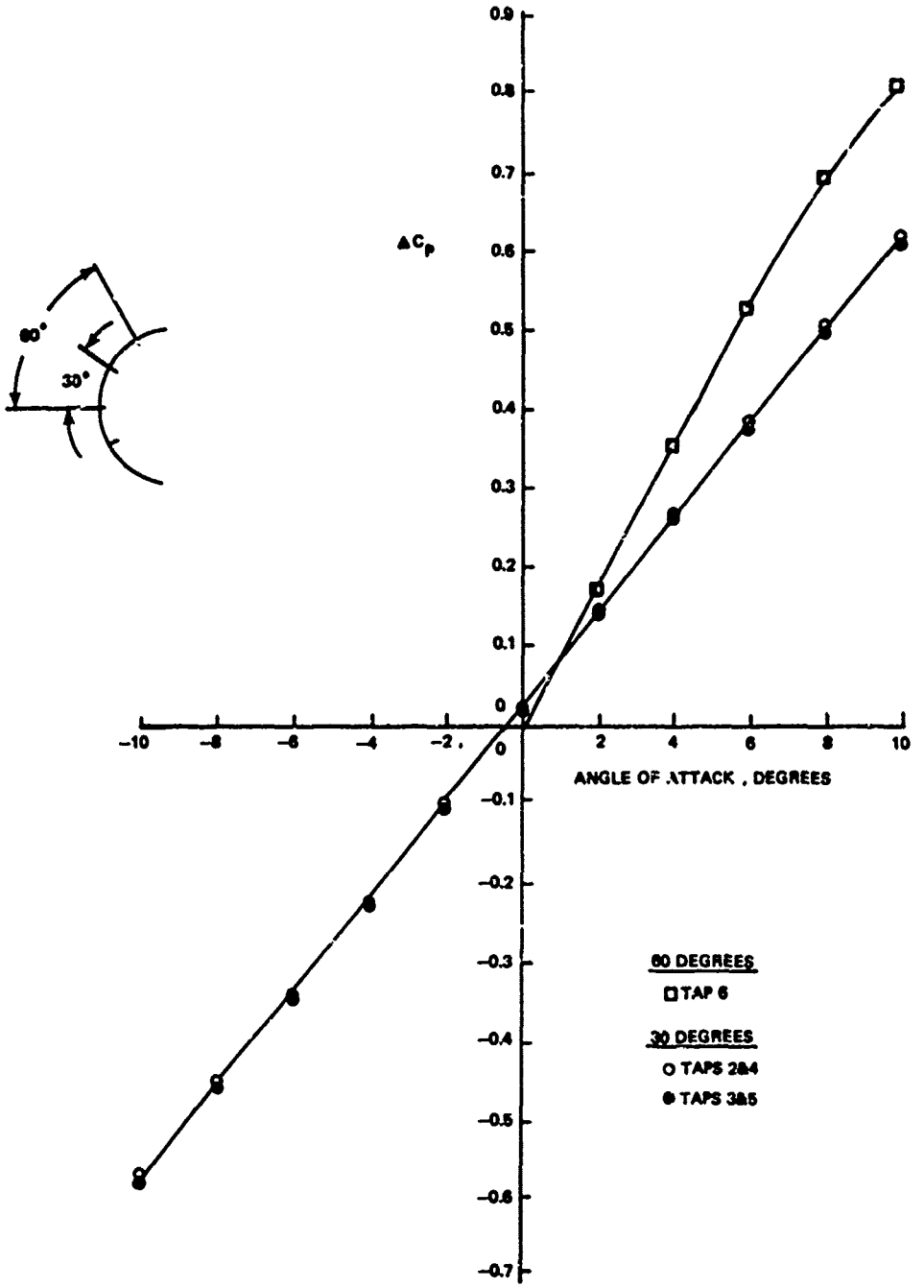

FIG. 30. Difference in Pressure Coefficient Across Nose Cap Versus Flow Angle; Nose A, Mach 0.8, 30- and 60-Degree Taps.

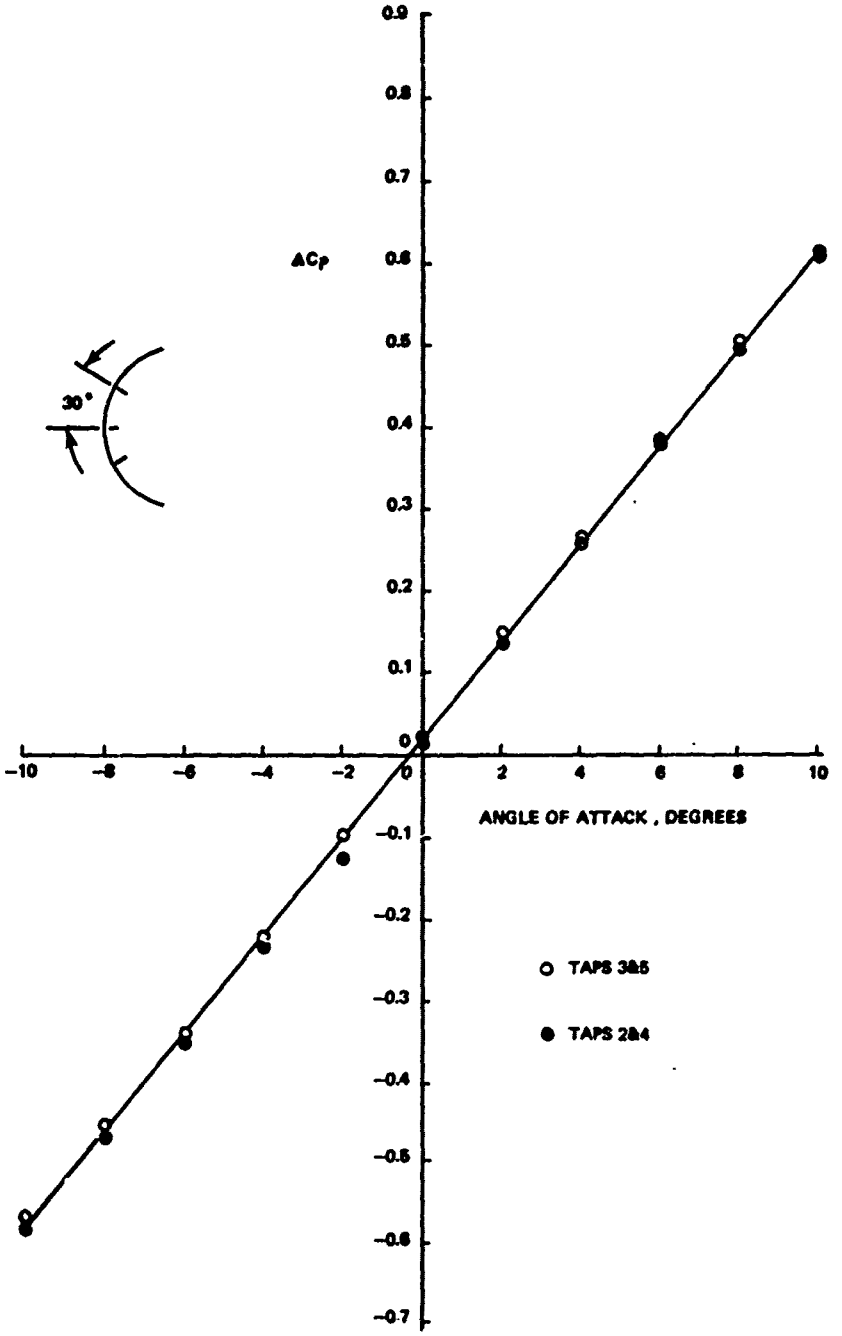

FIG. 31. Difference in Pressure Coefficient Across Nose Cap Versus Flow Angle; Nose C, Mach 0.8, 30 Degree Taps.

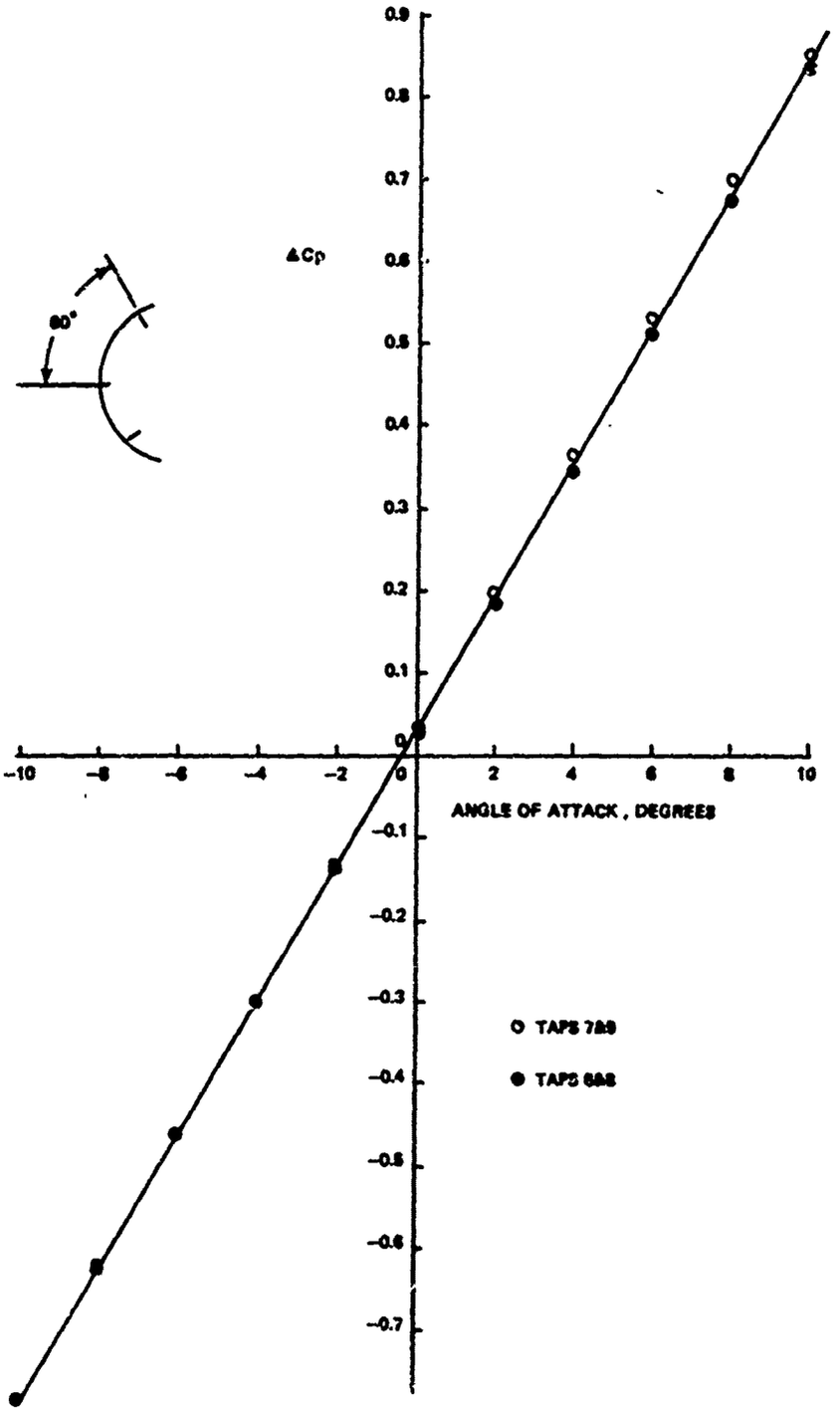

FIG. 32. Difference in Pressure Coefficient Across Nose Cap Versus Flow Angle; Nose C, Mach 0.8, 60 Degree Taps.

The ΔCp versus α slopes as obtained from the least squares fits of the data are given for Nose A at each Mach number in Fig. 33 and 34 for the 30- and 60-deg nose cap position, respectively. ΔCp versus α slopes for the 30- and 60-deg positions on Nose C are given in Fig. 35 and 36, respectively.

The expressions for the 30-deg caps of Noses A and C are quite similar up to Mach 1.1, above which Nose C becomes slightly more sensitive to the flow angle. The agreement between Noses A and C at the 60-deg position is generally not as good, possibly because this is approaching the sphere-ogive junction on Nose A (75.75 deg).

SUMMARY

Results of wind tunnel tests to measure pressure distributions on three bodies of revolution are presented. Tests were conducted at Mach numbers from 0.7 to 2.02 and angles of attack from 10 to -10 degrees. The primary purpose of the tests was to provide reference pressure distributions for comparison with captive flight data being obtained as part of a program to investigate flow interference effects between a store and its carrying aircraft. The purpose of this report is to make the wind tunnel pressure distributions available for use in checking analytical techniques for predicting pressure distributions about bodies of revolution. Included in the report are expressions developed from the data which relate the flow angles to the pressure difference across the spherical nose caps of two of the nose configurations.

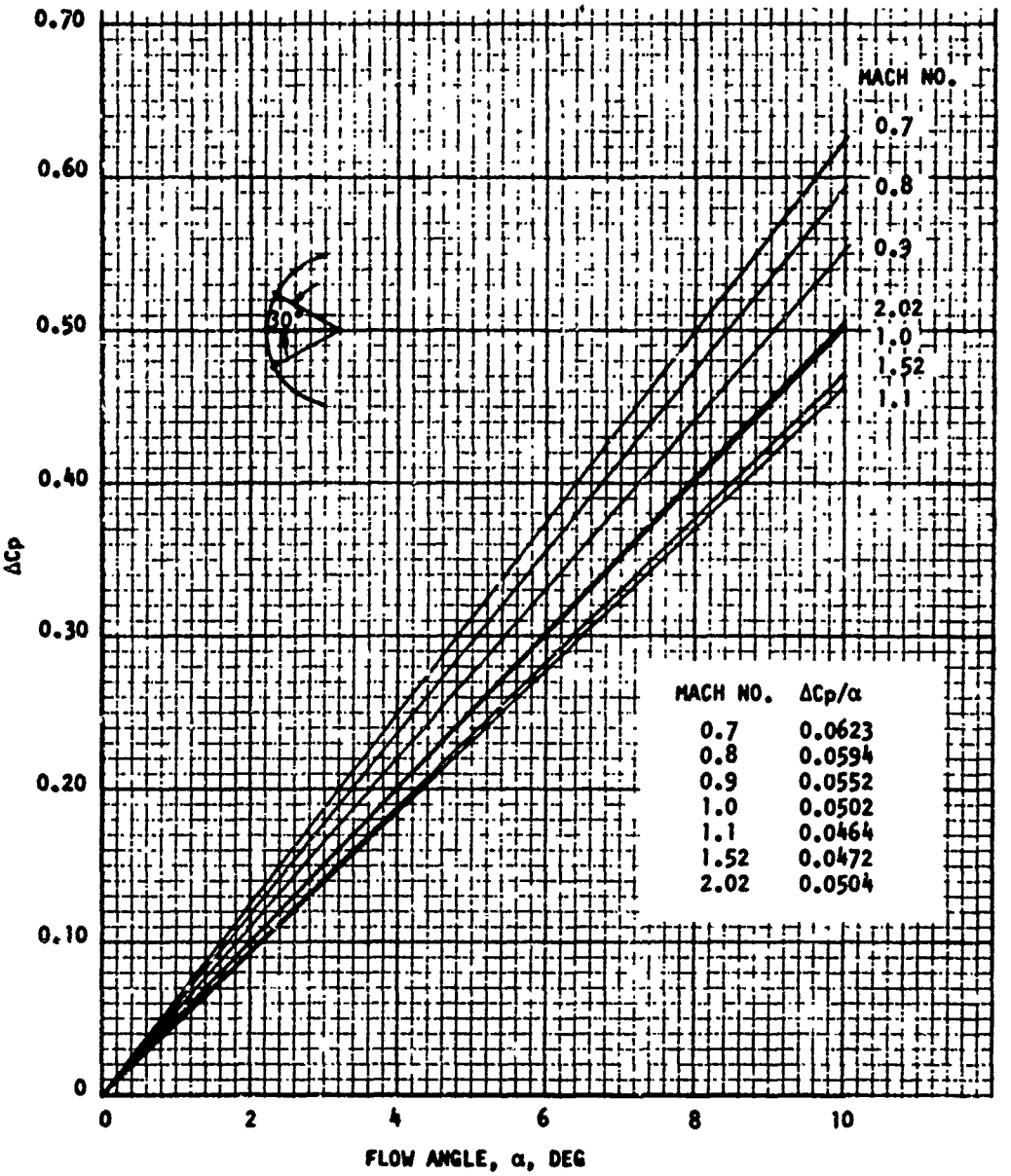

FIG. 33. ΔCp Versus Flow Angle Relationships; Nose A, 30-Degree Taps.

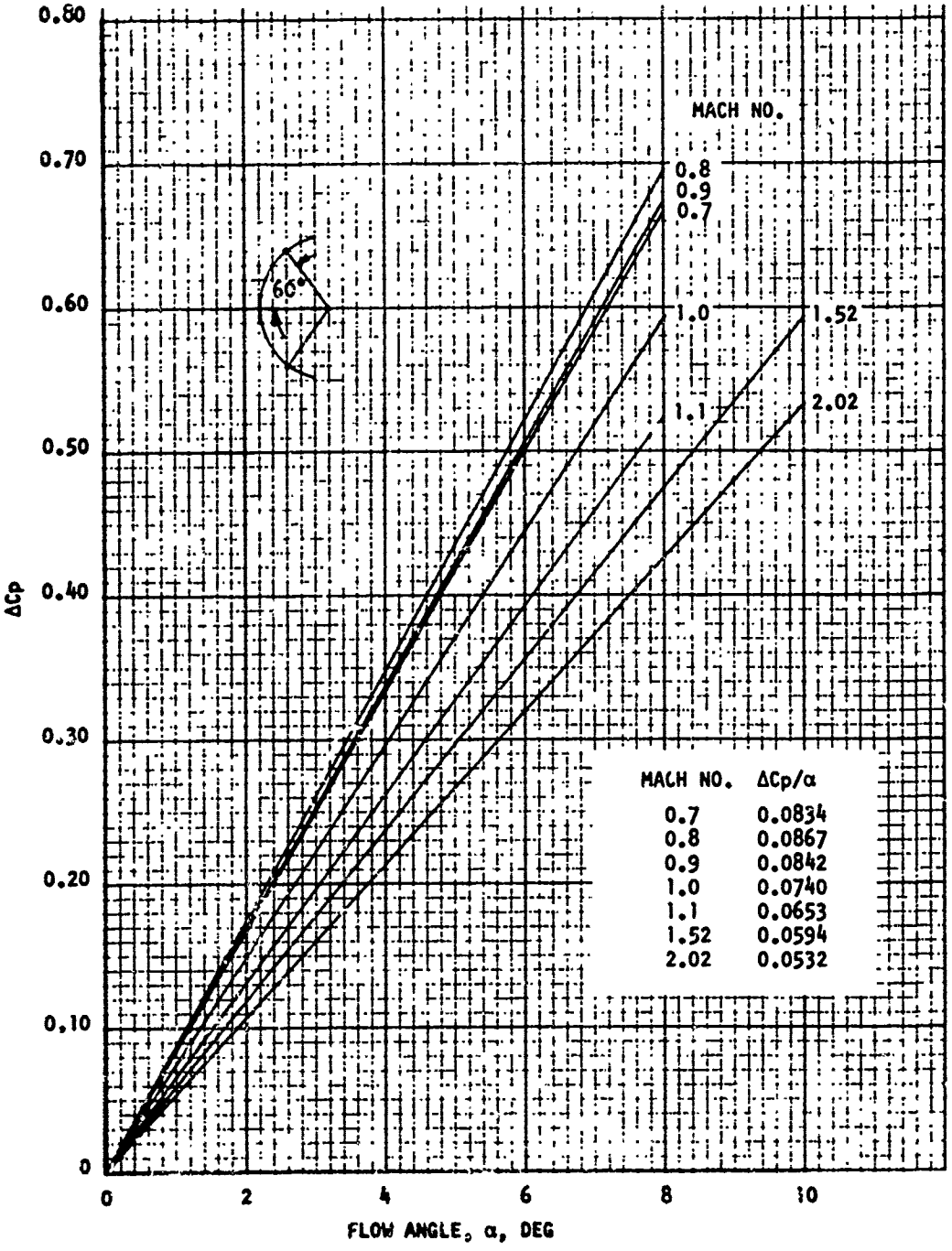

FIG. 34. ΔCp Versus Flow Angle Relationships; Nose A, 60-Degree Tape.

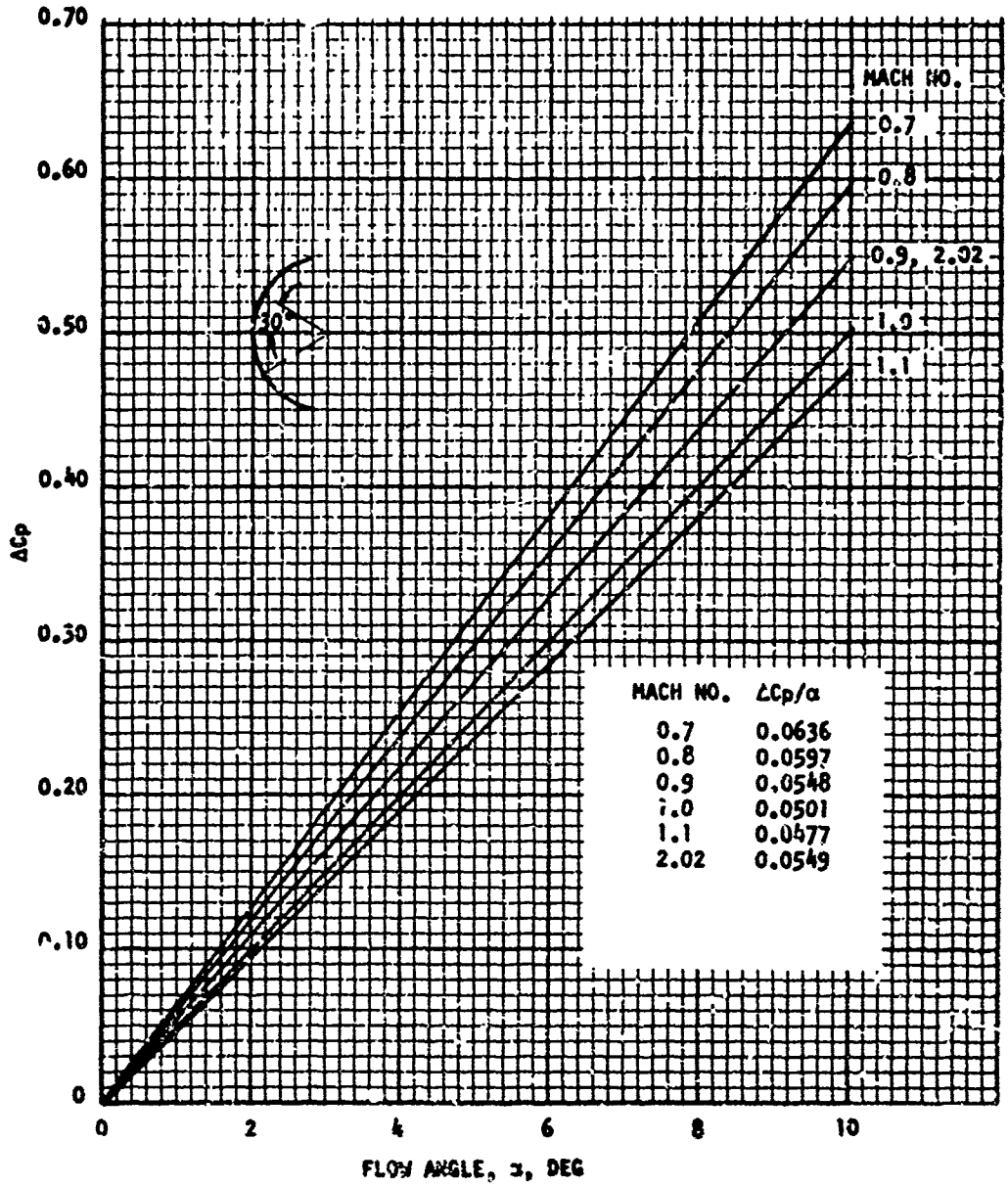

FIG. 35. ΔCp Versus Flow Angle Relationships; Nose C, 30-Degree Taps.

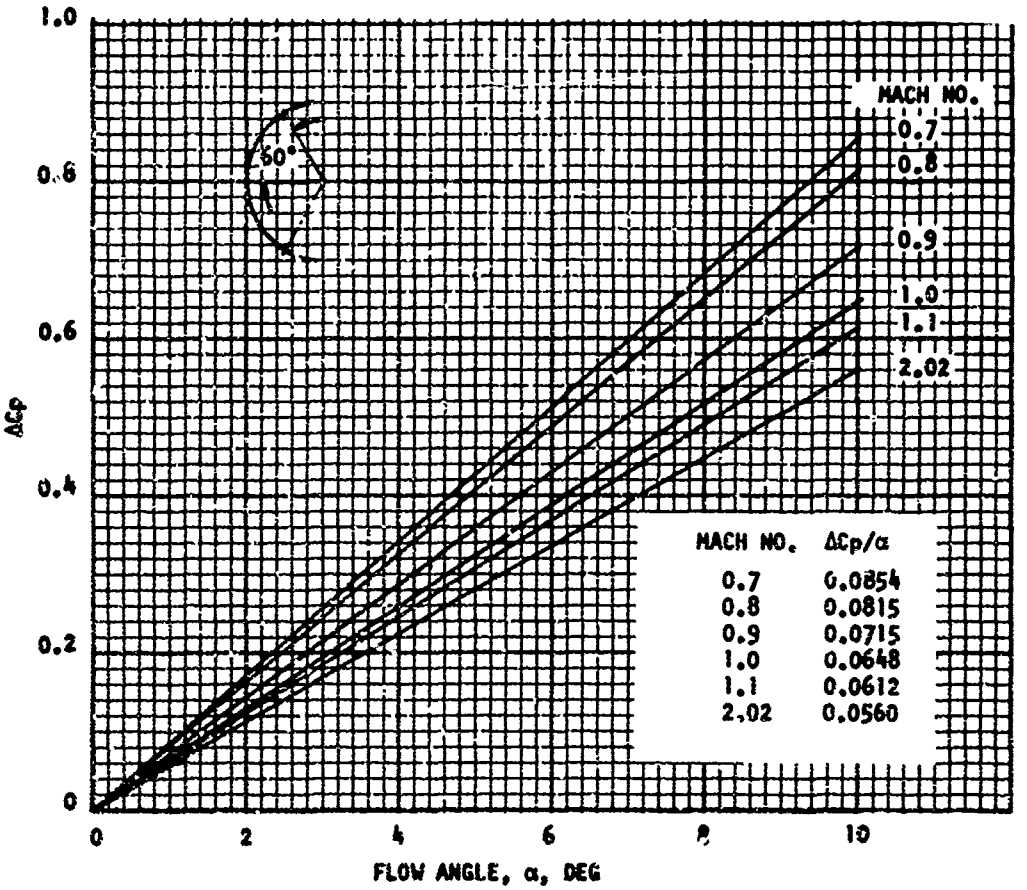

Fig. 36. ΔCp Versus Flow Angle Relationships; Nose C, 60-Degree Taps.

Appendix
LONGITUDINAL PRESSURE COEFFICIENT DISTRIBUTIONS

Preceding page blank

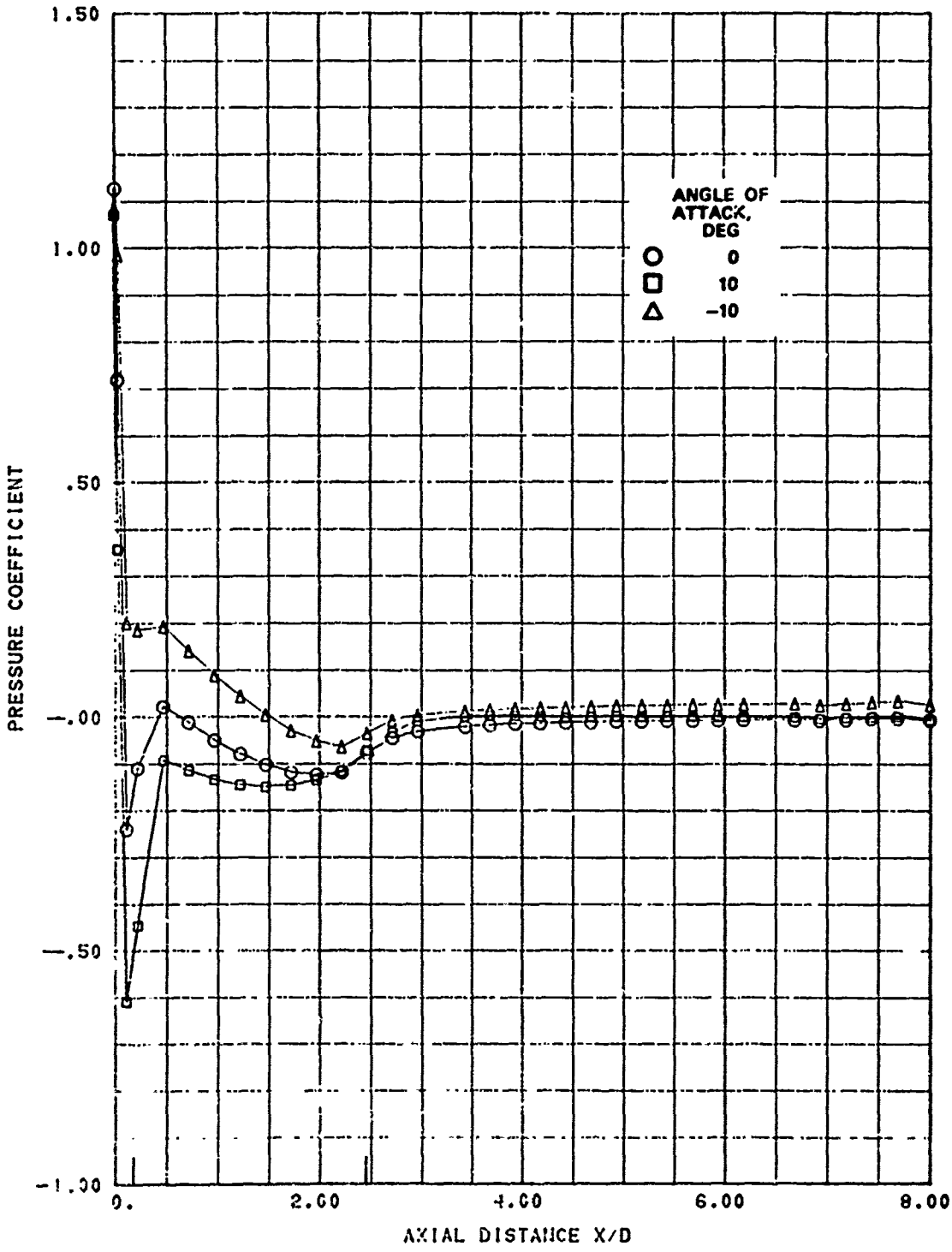

FIG. A-1. Longitudinal Pressure Distribution; Nose A, Mach 0.7, Roll Angle 0 Degrees.

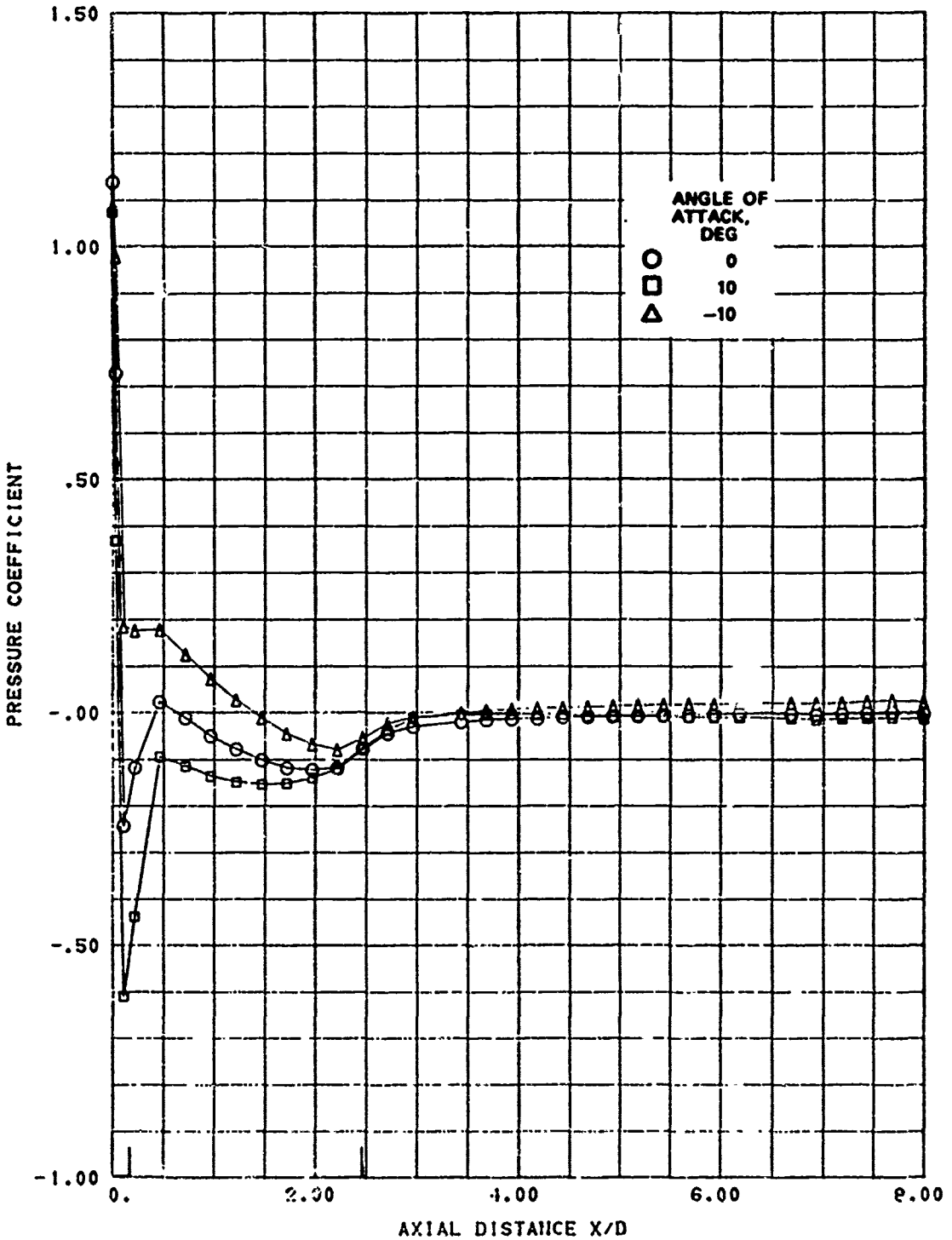

FIG. A-2. Longitudinal Pressure Distribution; Nose A, Mach 0.7, Roll Angle 15 Degrees.

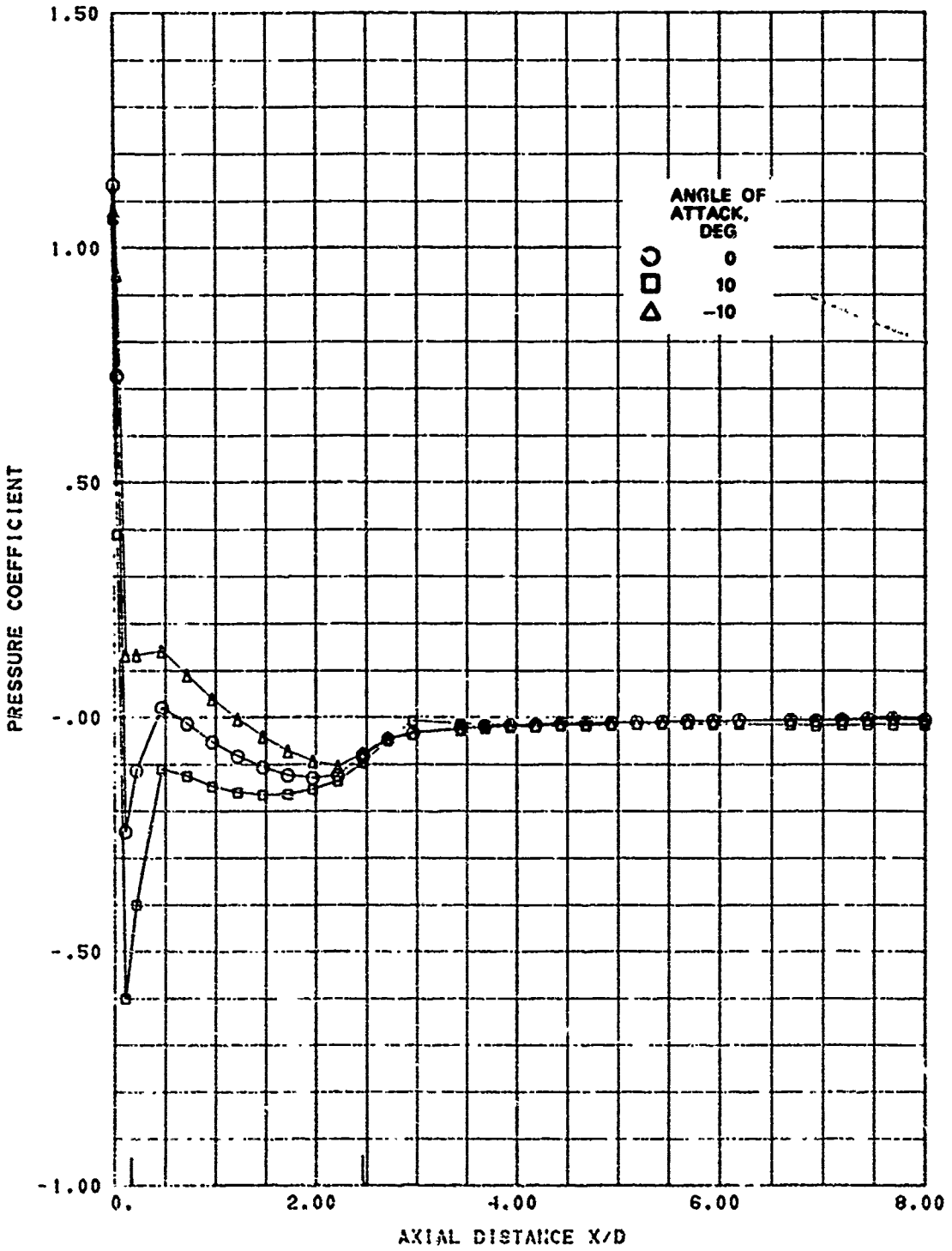

FIG. A-3. Longitudinal Pressure Distribution; Nose A, Mach 0.7, Roll Angle 30 Degrees.

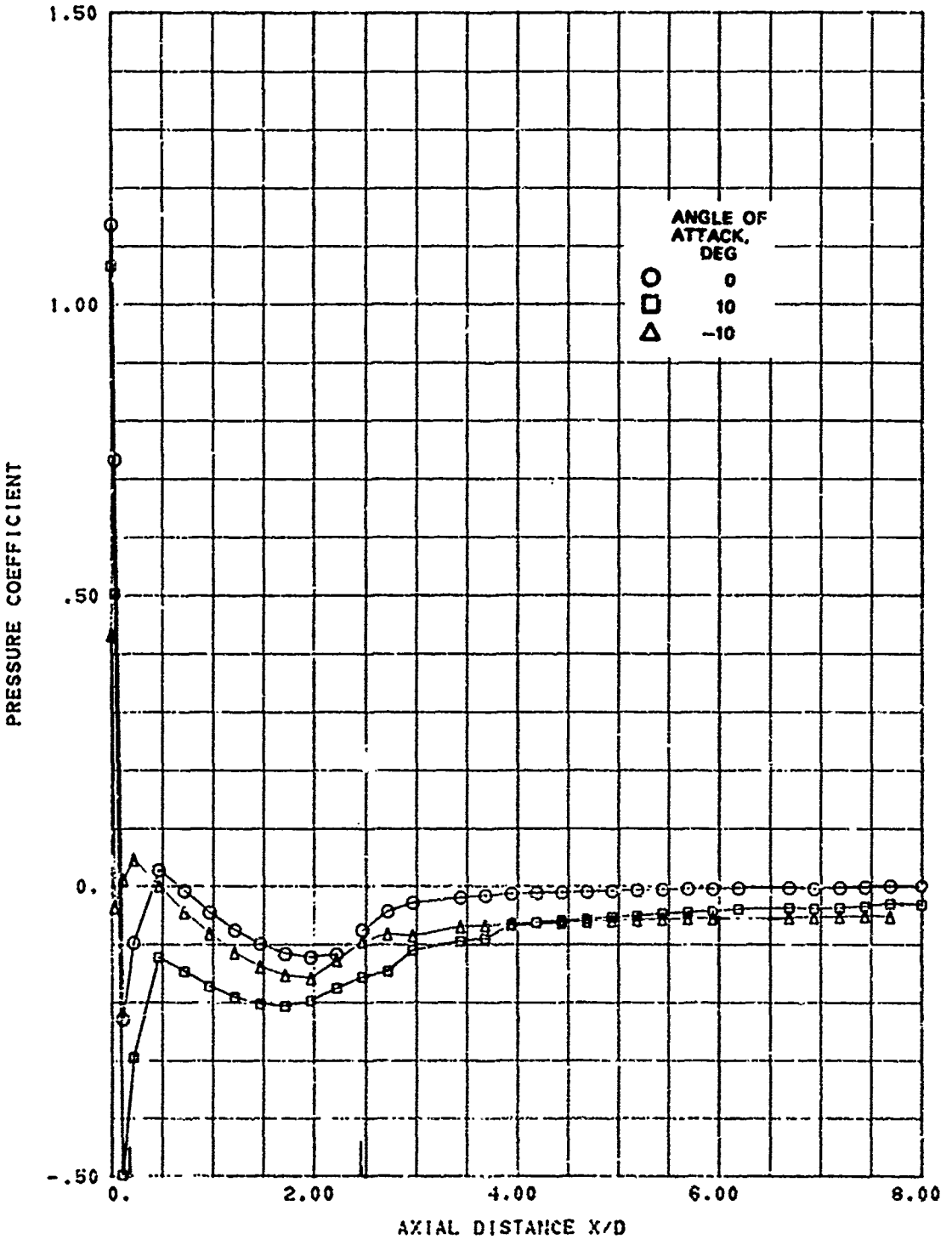

FIG. A-4. Longitudinal Pressure Distribution; Nose A, Mach 0.7, Roll Angle 60 Degrees.

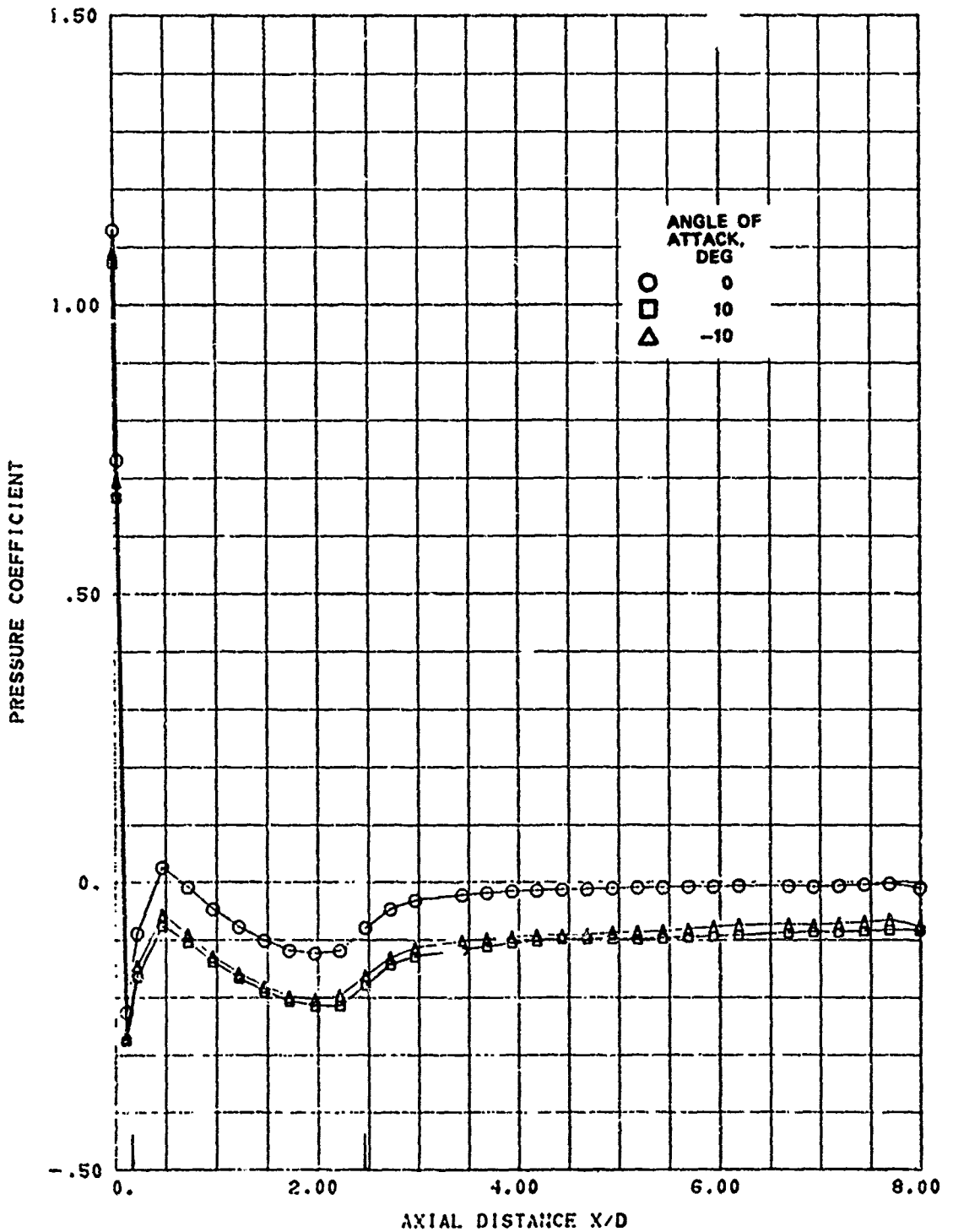

FIG. A-5. Longitudinal Pressure Distribution; Nose A, Mach 0.7, Roll Angle 90 Degrees.

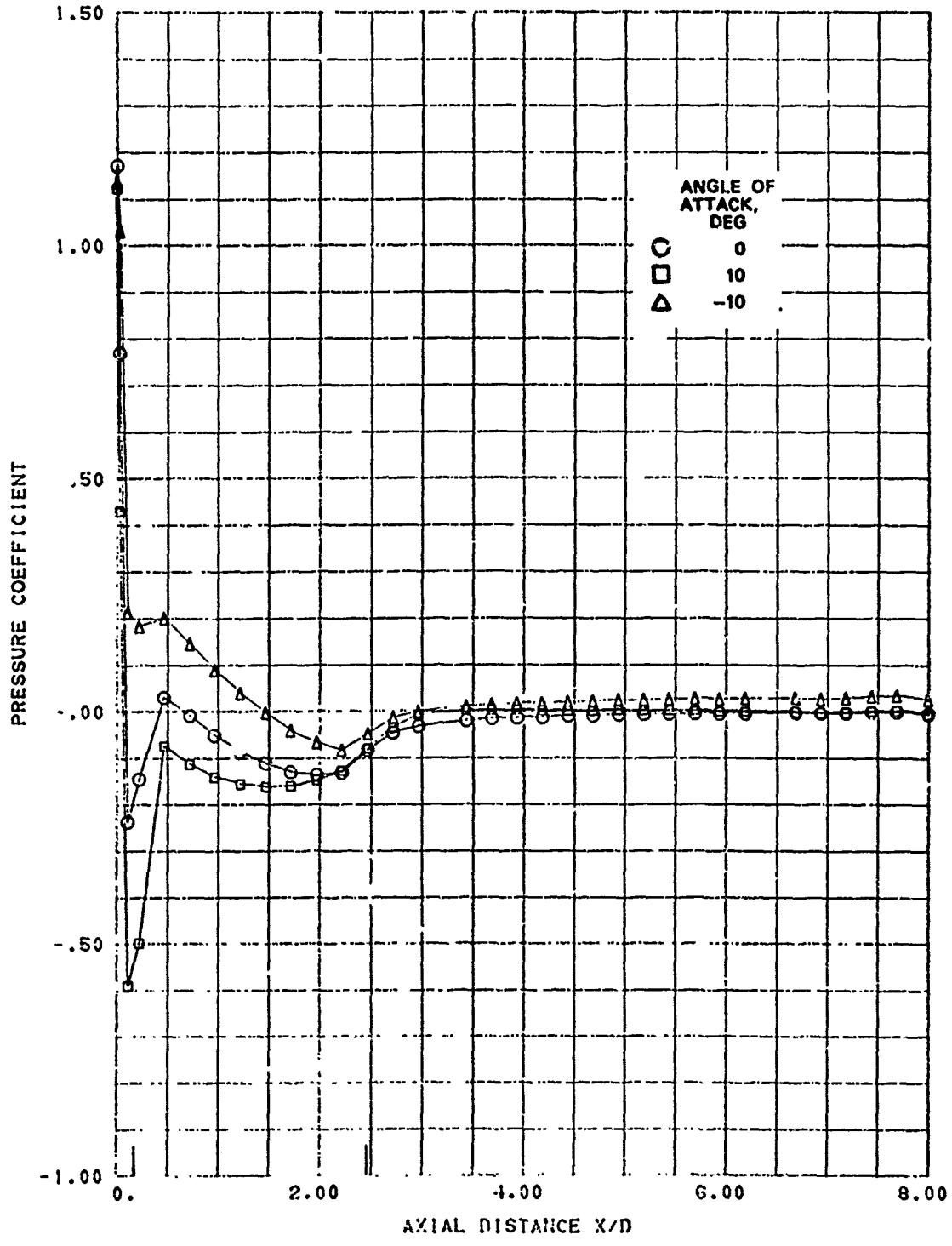

FIG. A-6. Longitudinal Pressure Distribution; Nose A, Mach 0.8, Roll Angle 0 Degrees.

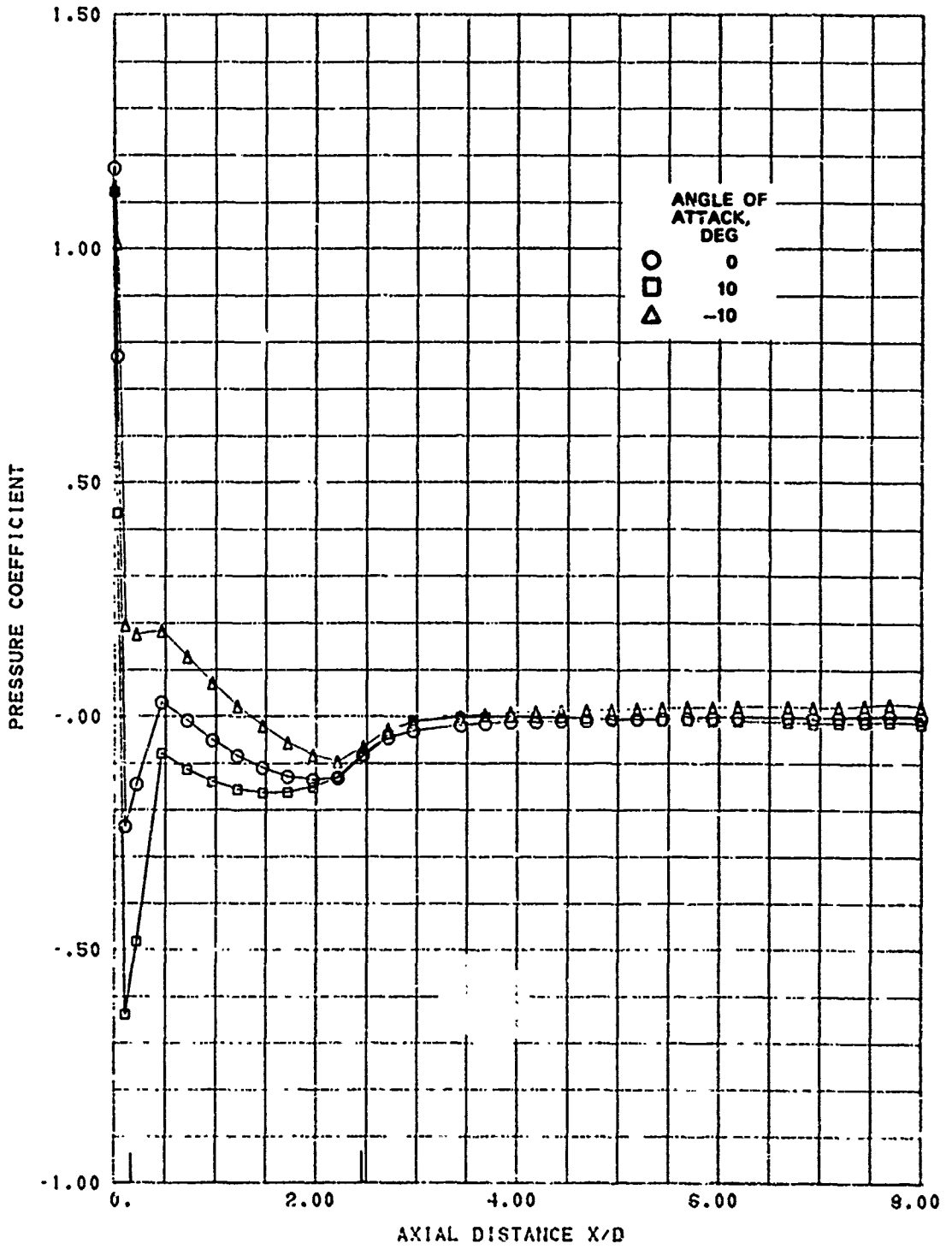

FIG. A-7. Longitudinal Pressure Distribution; Nose A, Mach 0.8, Roll Angle 15 Degrees.

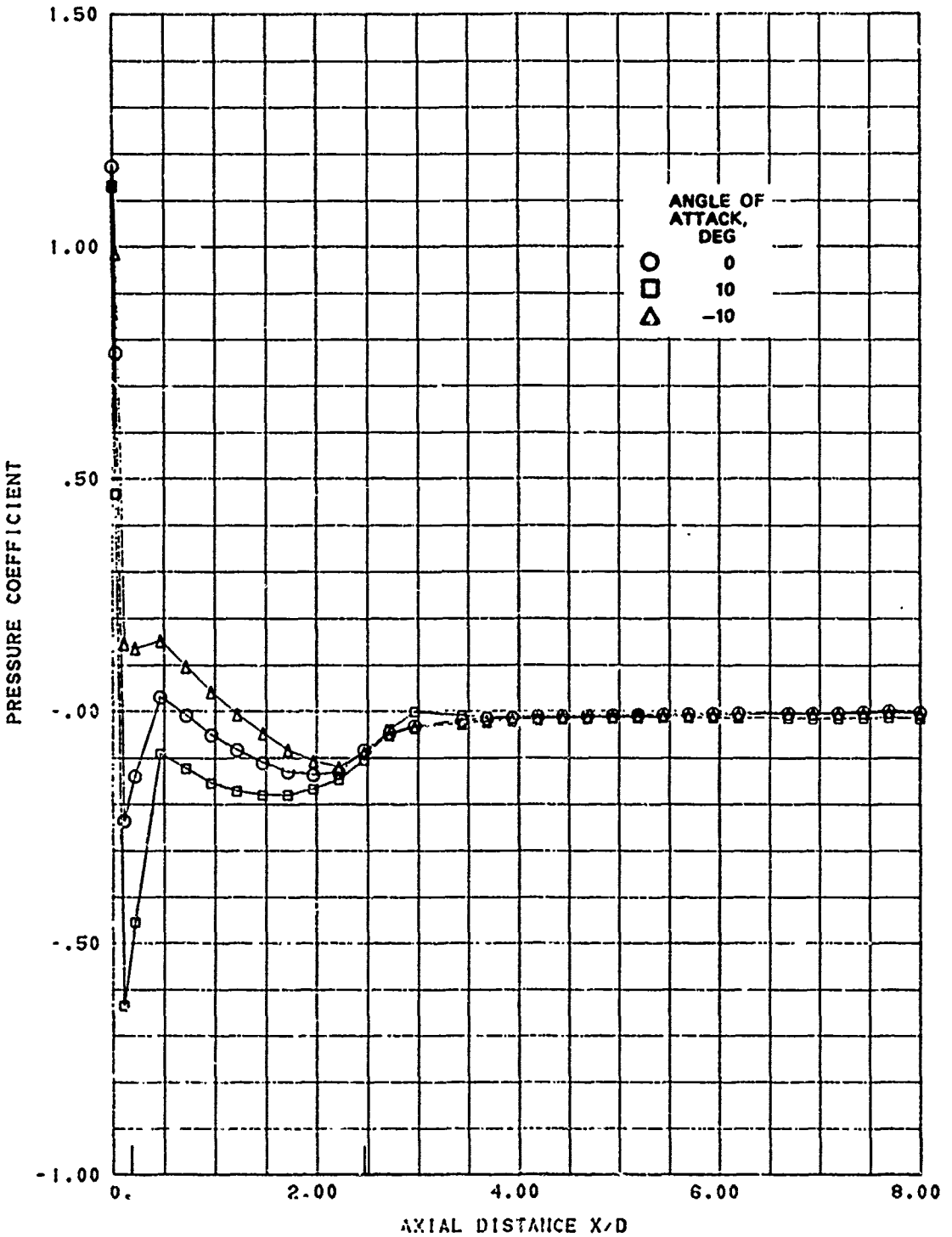

FIG. A-8. Longitudinal Pressure Distribution; Nose A, Mach 0.8, Roll Angle 30 Degrees.

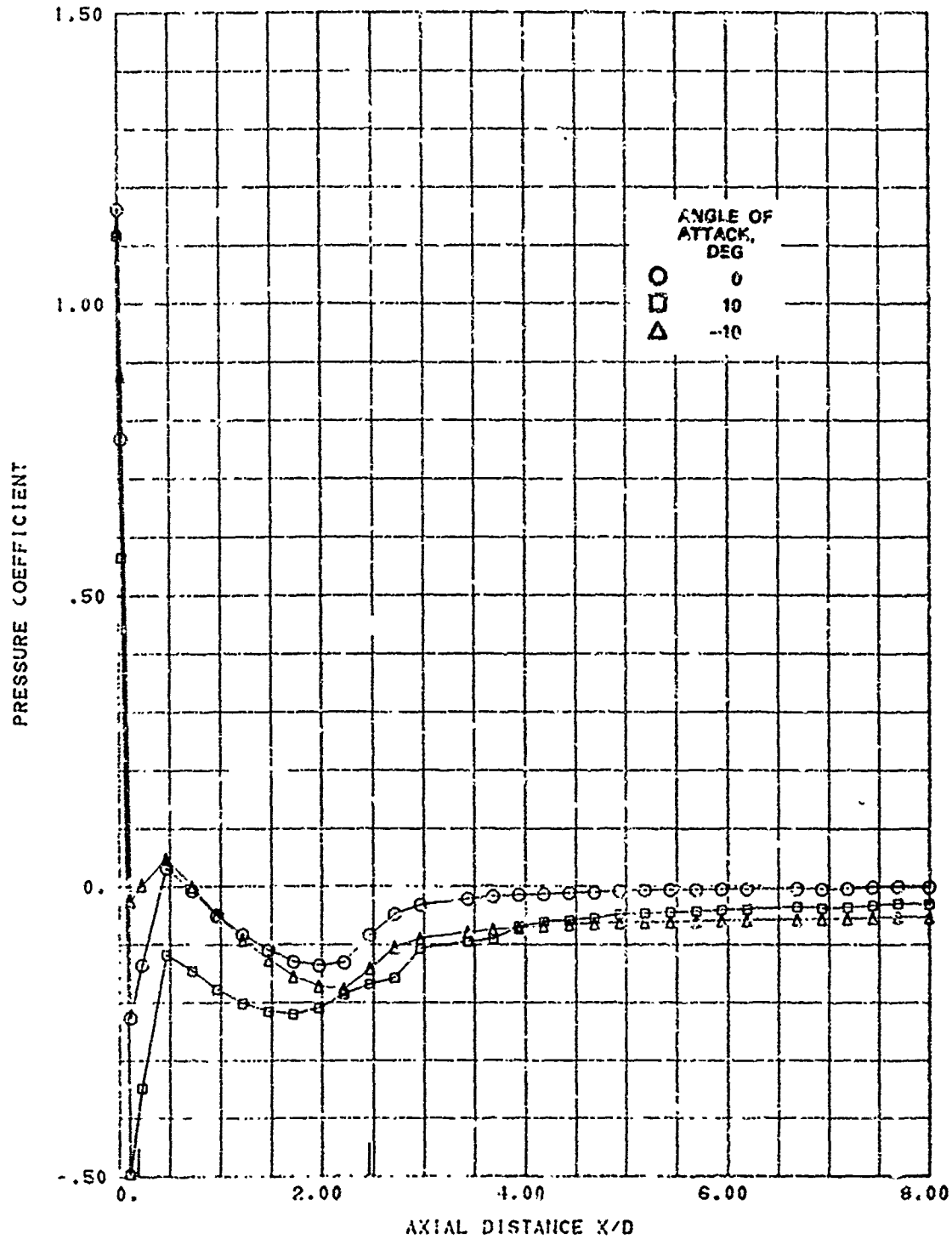

FIG. A-9. Longitudinal Pressure Distribution; Nose A, Mach 0.8, Roll Angle 60 Degrees.

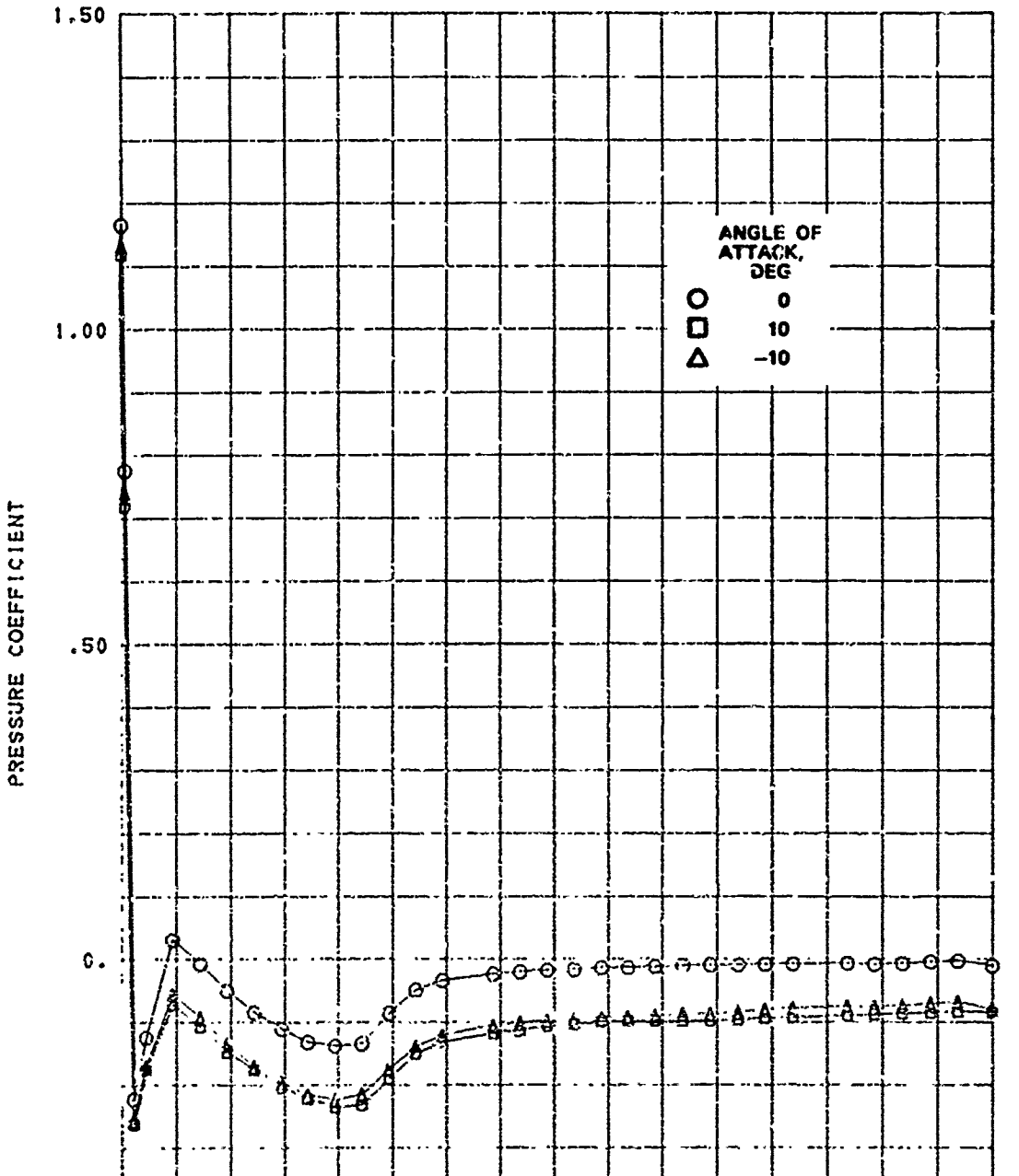

FIG. A-10. Longitudinal Pressure Distribution; Nose A, Mach 0.8, Roll Angle 90 Degrees.

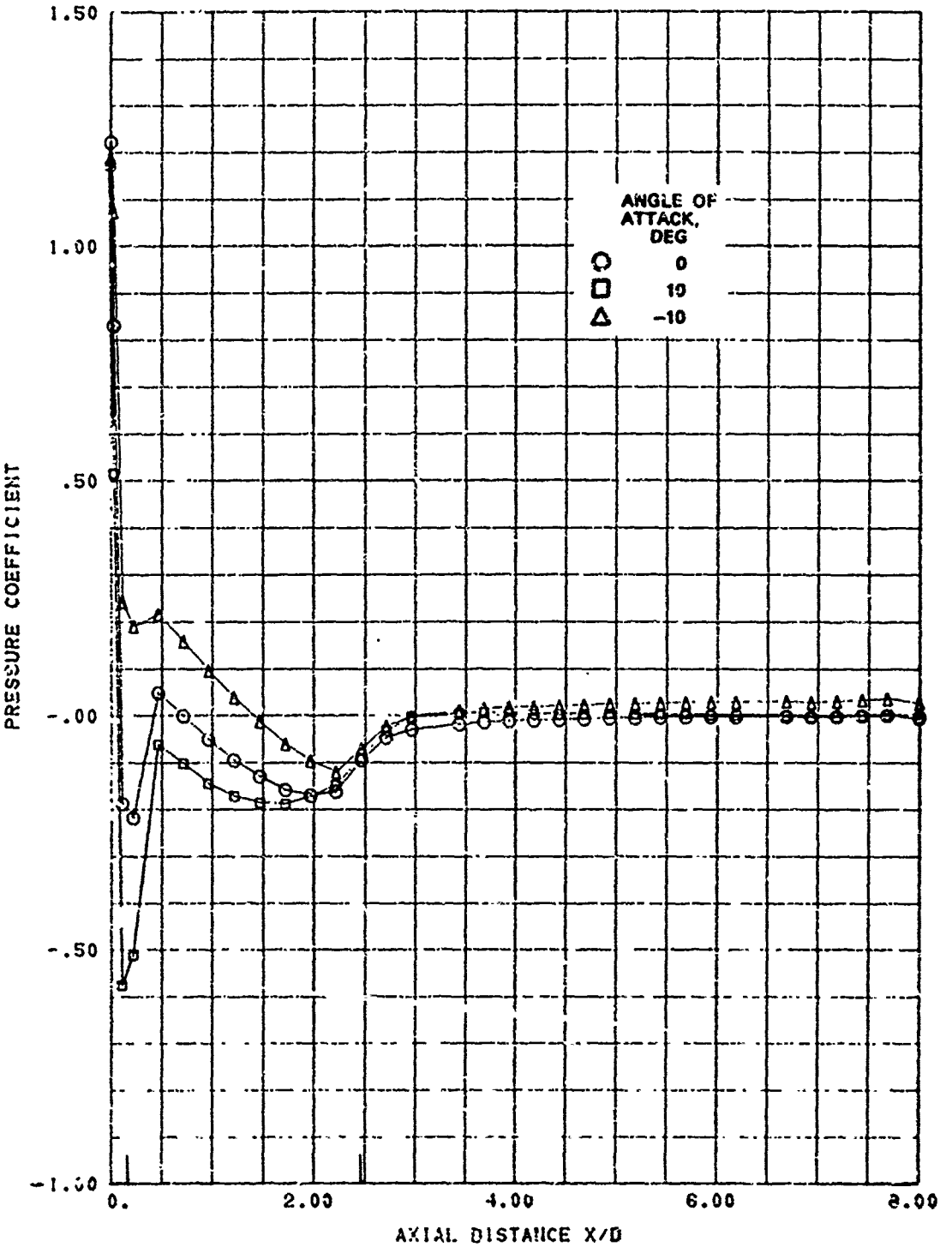

FIG. A-11. Longitudinal Pressure Distribution; Nose A, Mach 0.9, Roll Angle 0 Degrees.

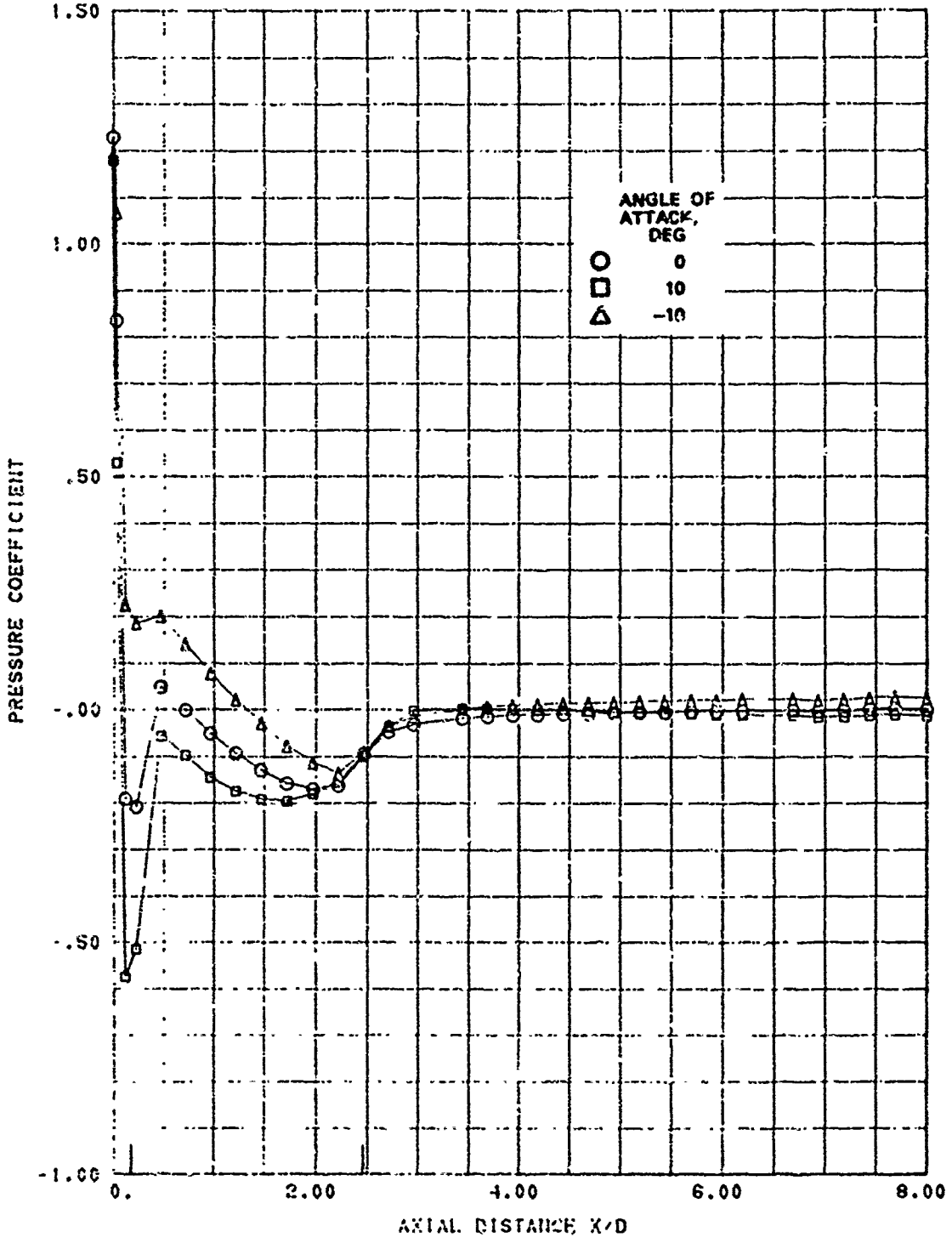

FIG. A-12. Longitudinal Pressure Distribution; Nose A, Mach 0.9, Roll Angle 15 Degrees.

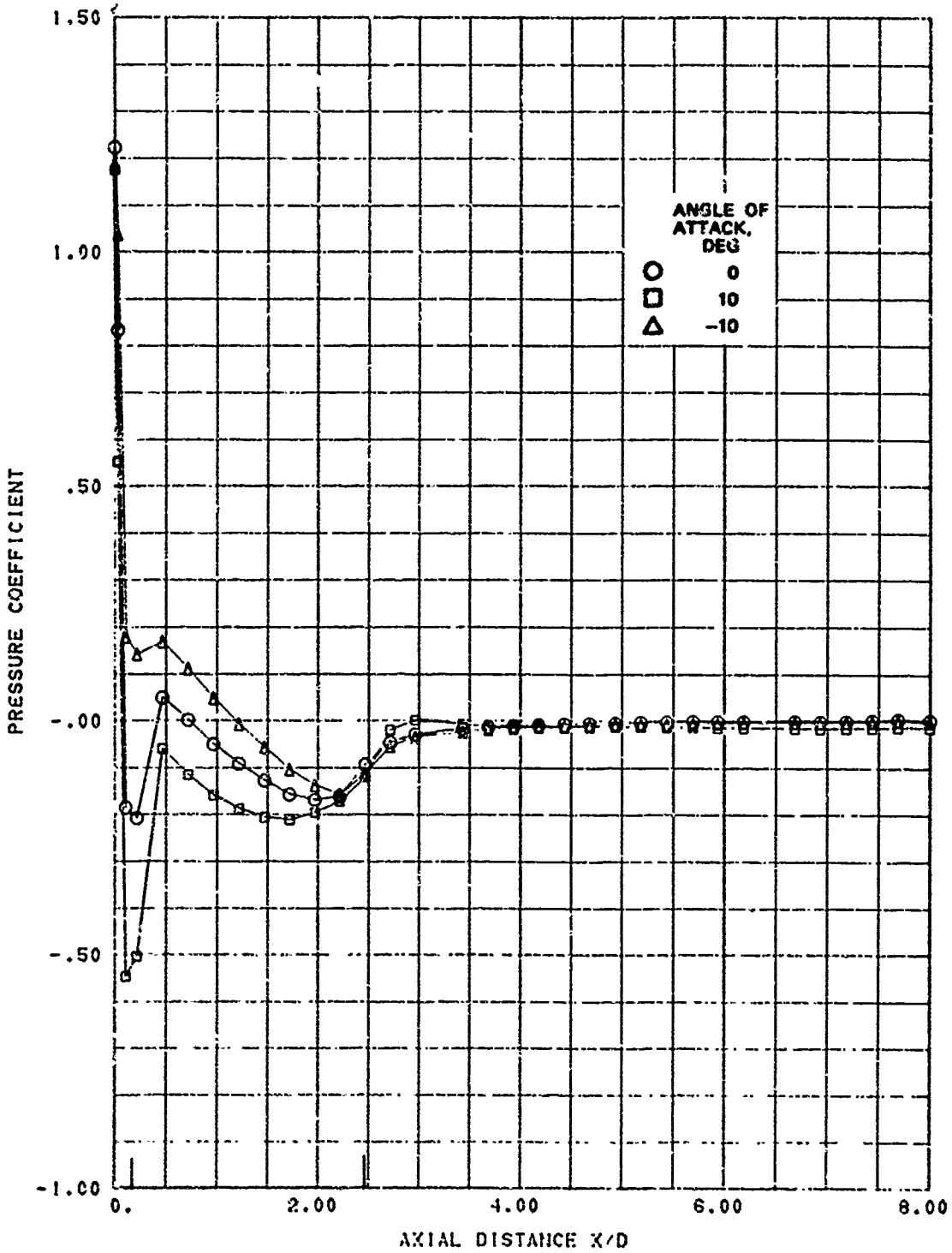

FIG. A-13. Longitudinal Pressure [illegible]ion; Nose A, Mach 0.9, Roll Angle 30 Degrees.

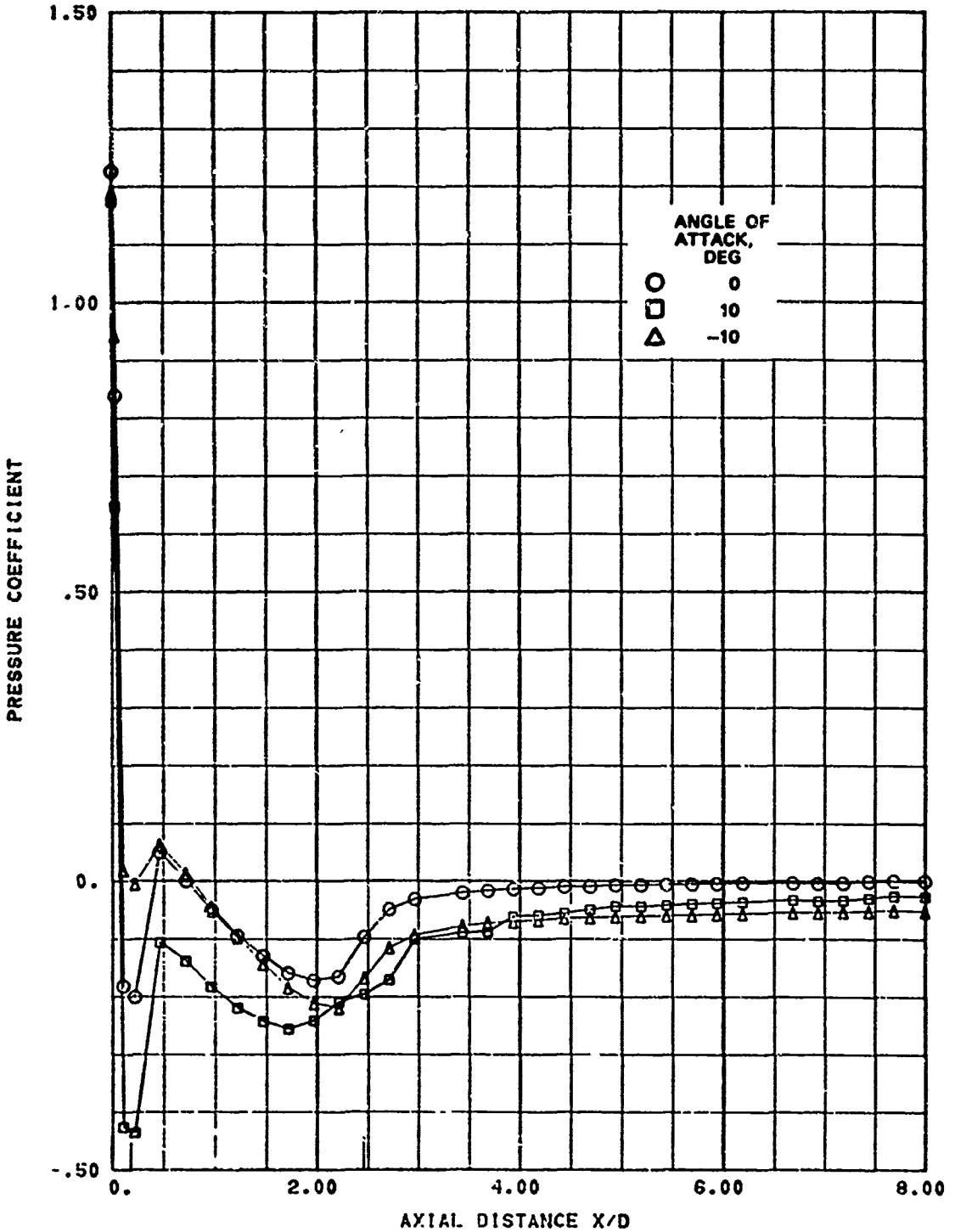

FIG. A-14. Longitudinal Pressure Distribution; Nose A, Mach 0.9, Roll Angle 60 Degrees.

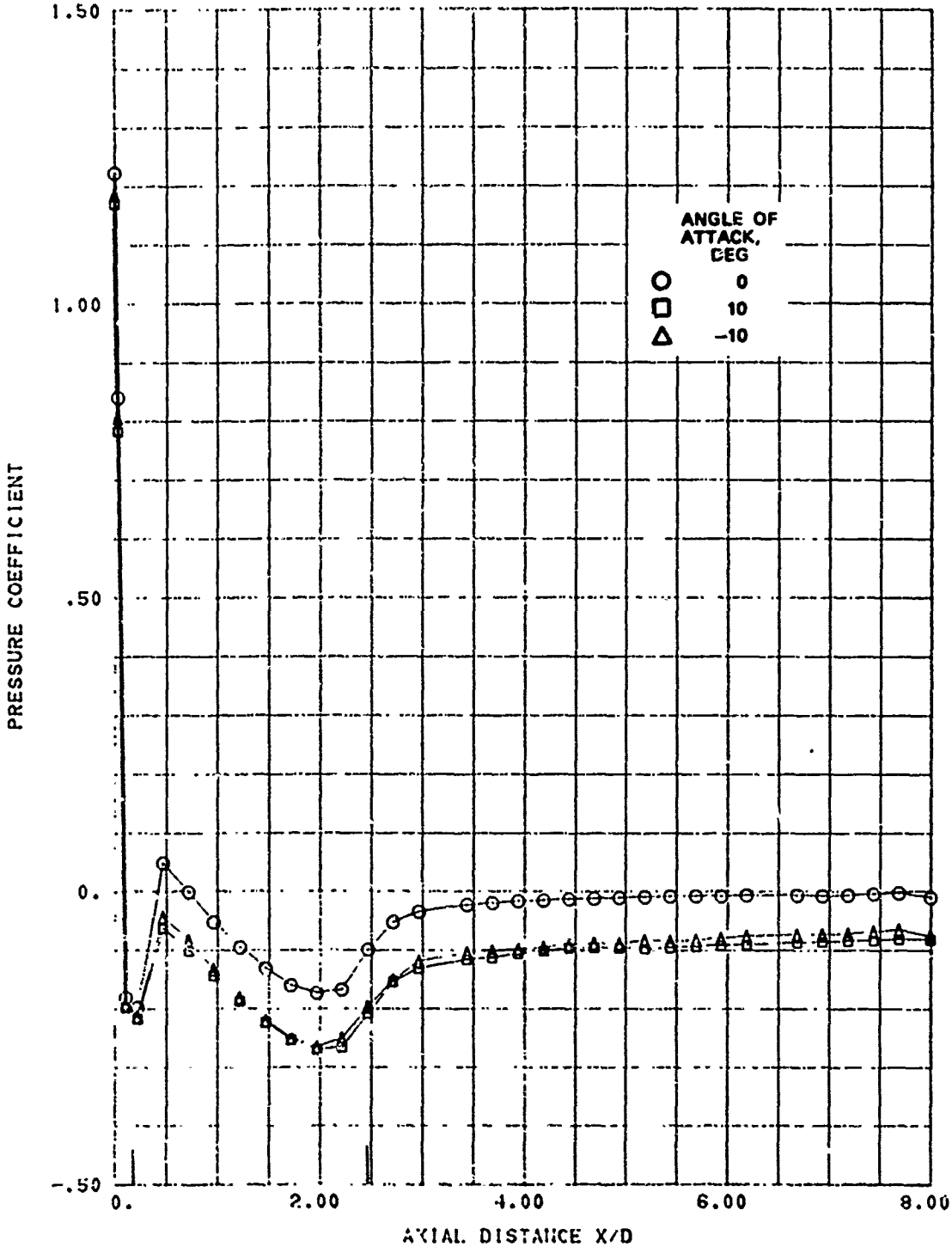

FIG. A-15. Longitudinal Pressure Distribution; Nose A, Mach 0.9, Roll Angle 90 Degrees.

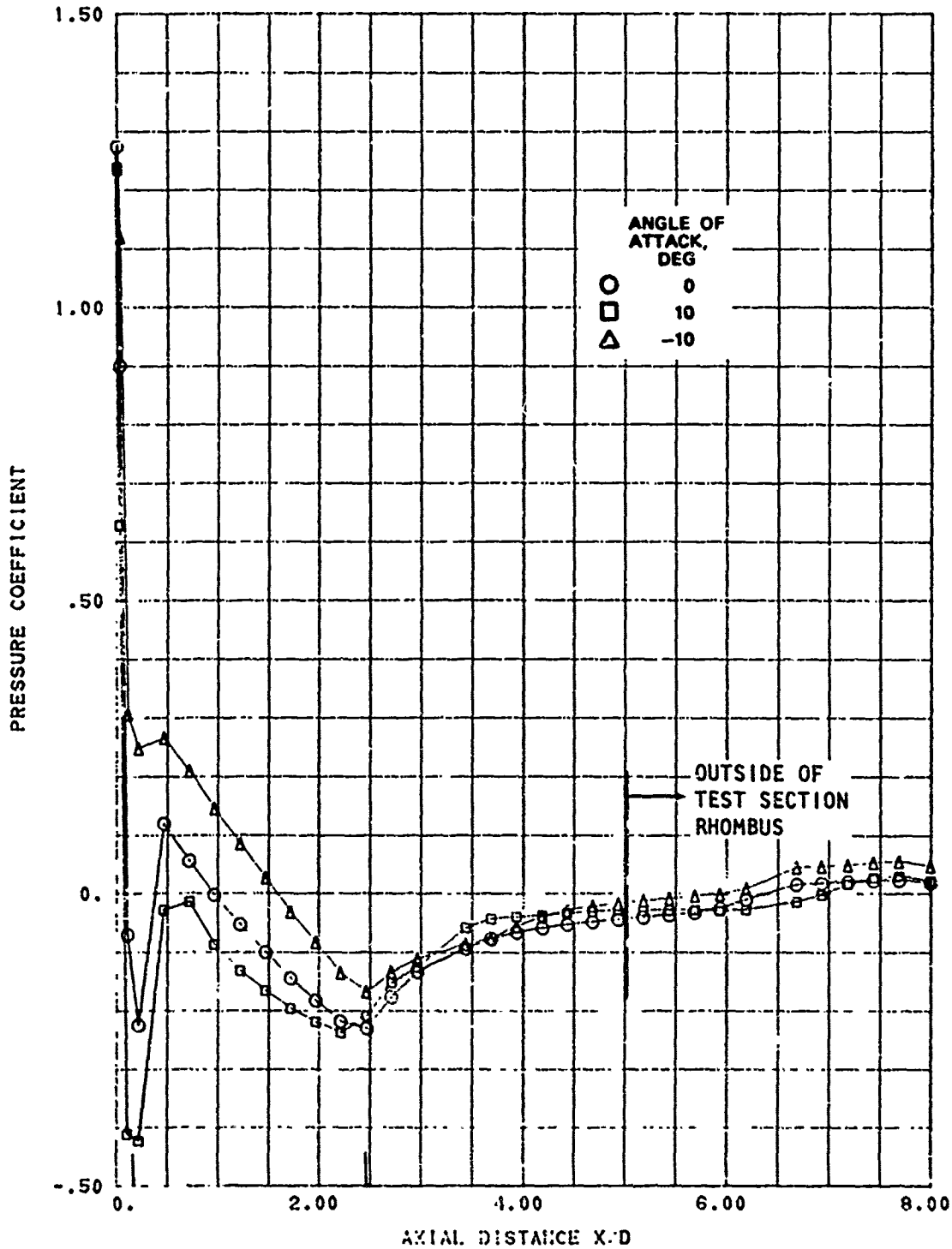

FIG. A-16. Longitudinal Pressure Distribution; Nose A, Mach 1.0, Roll Angle 0 Degrees.

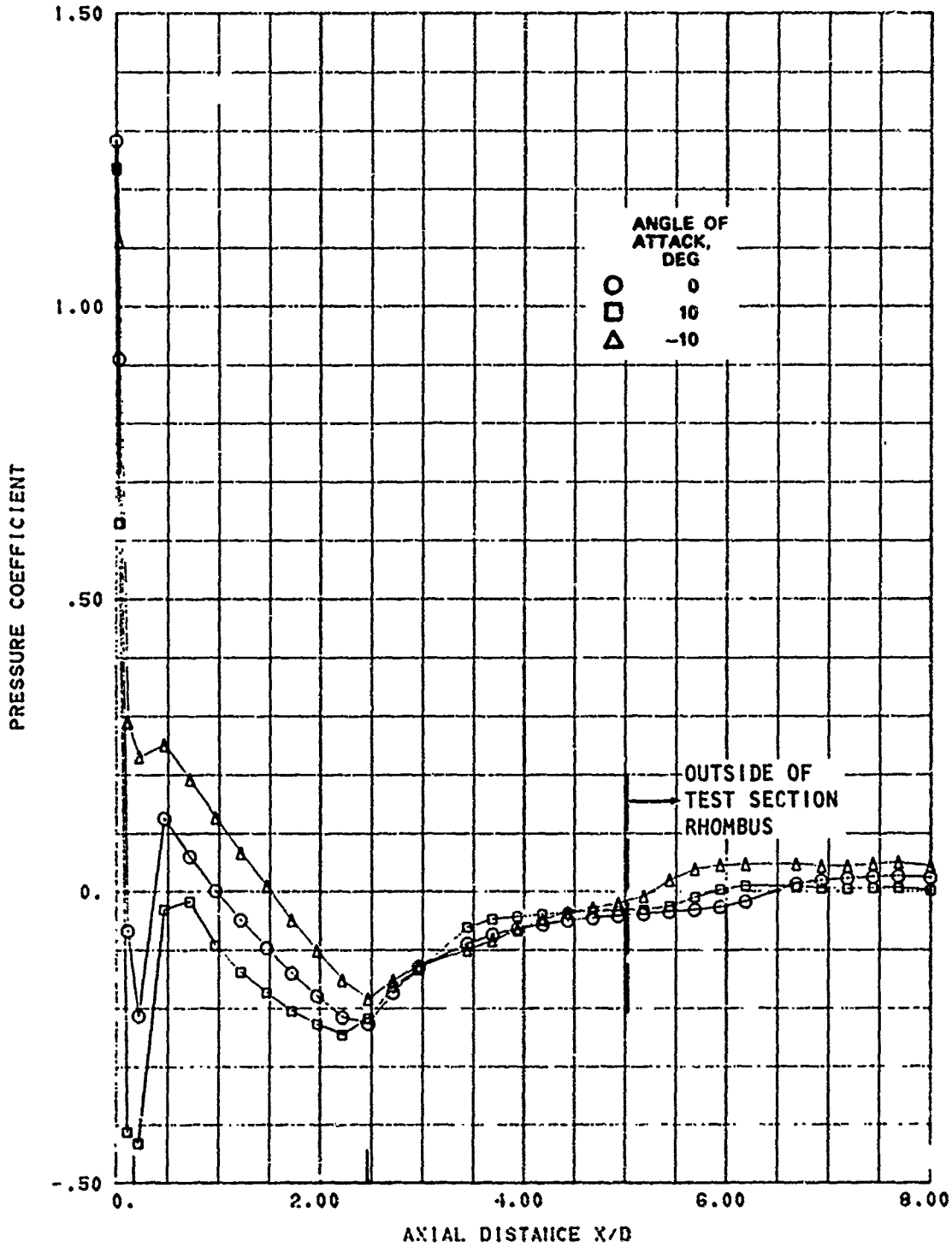

FIG. A-17. Longitudinal Pressure Distribution; Nose A, Mach 1.0, Roll Angle 15 Degrees.

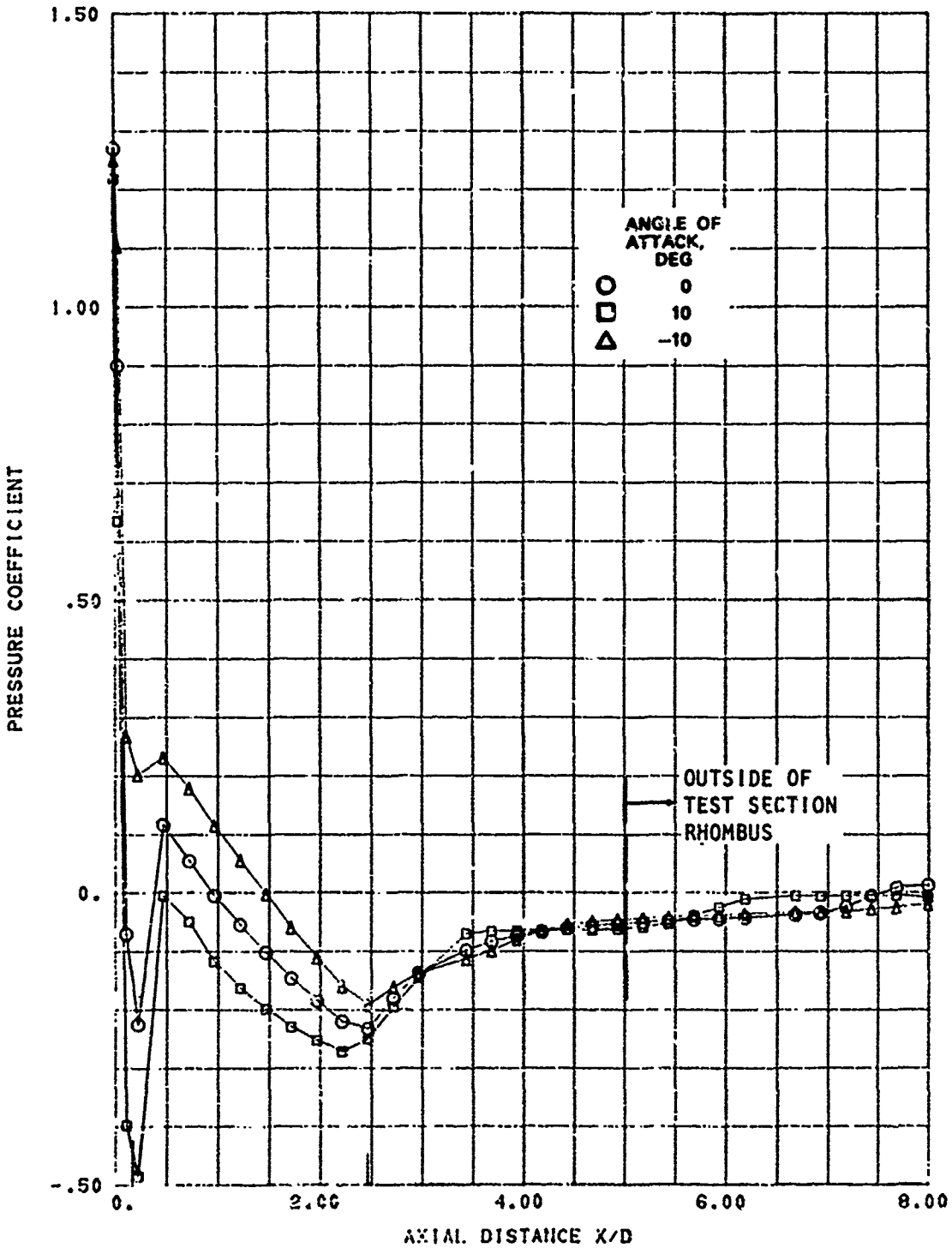

FIG. A-18. Longitudinal Pressure Distribution; Nose A, Mach 1.0, Roll Angle 30 Degrees.

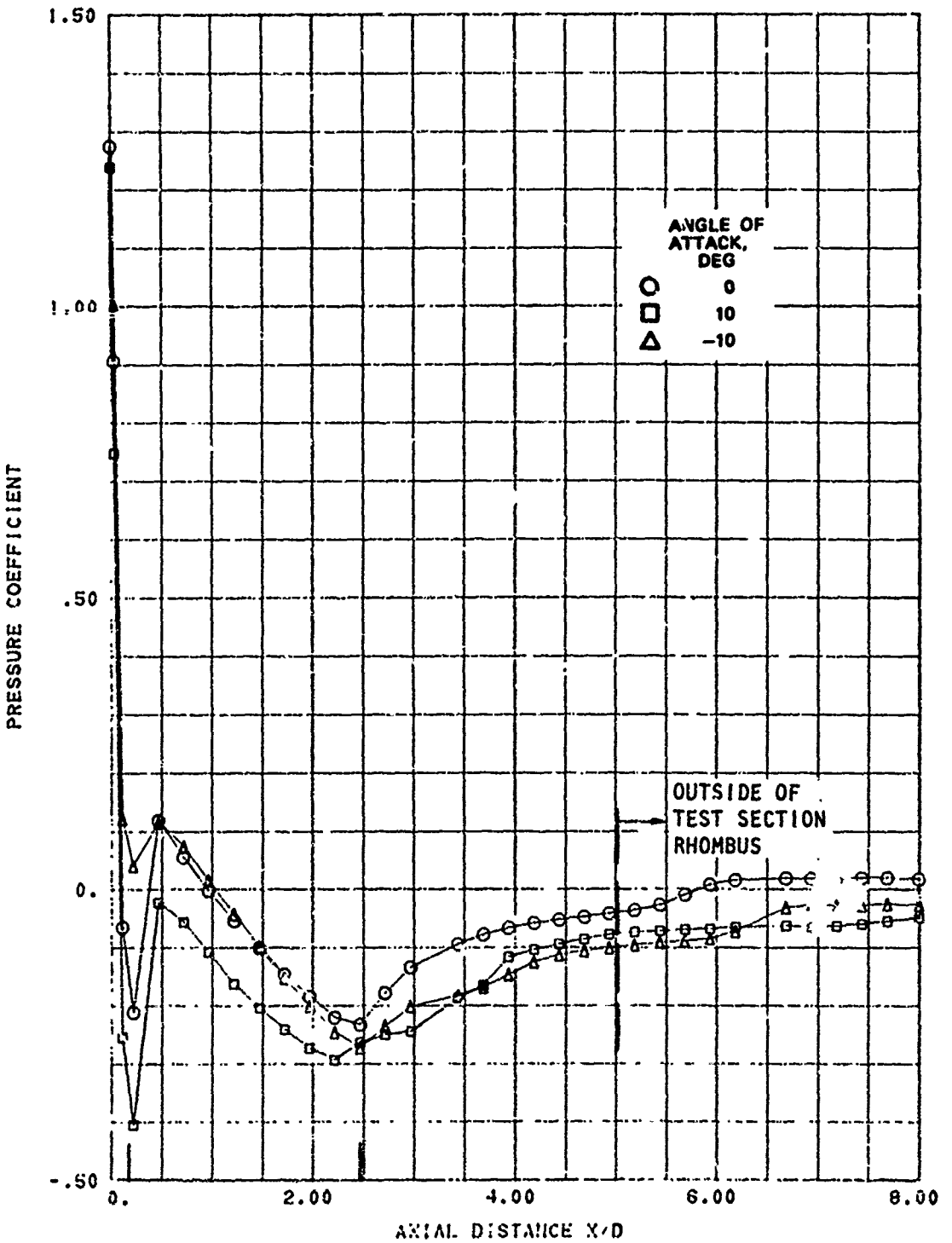

FIG. A-19. Longitudinal Pressure Distribution; Nose A, Mach 1.0, Roll Angle 60 Degrees.

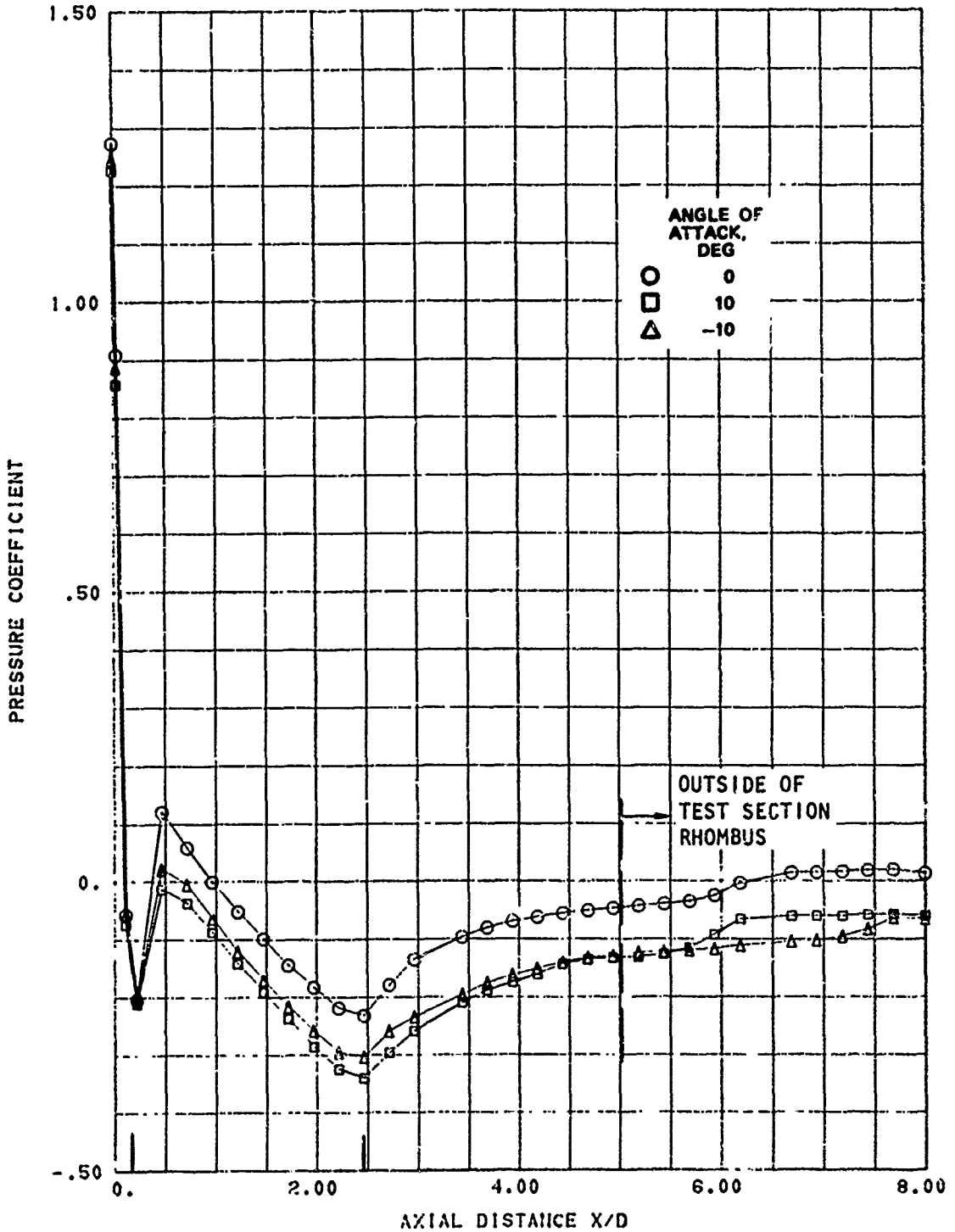

FIG. A-20. Longitudinal Pressure Distribution; Nose A, Mach 1.0, Roll Angle 90 Degrees.

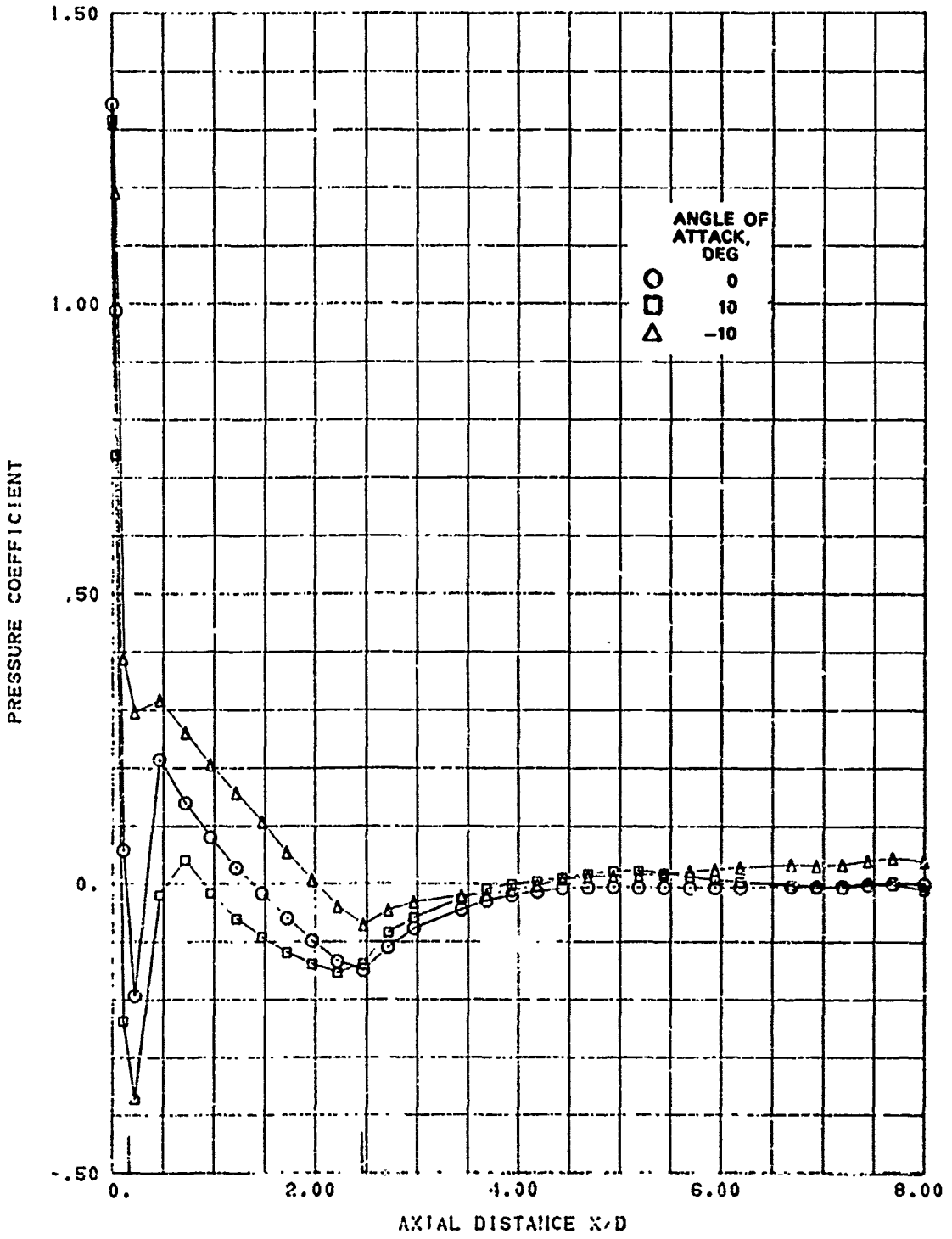

FIG. A-21. Longitudinal Pressure Distribution; Nose A, Mach 1.1, Roll Angle 0 Degrees.

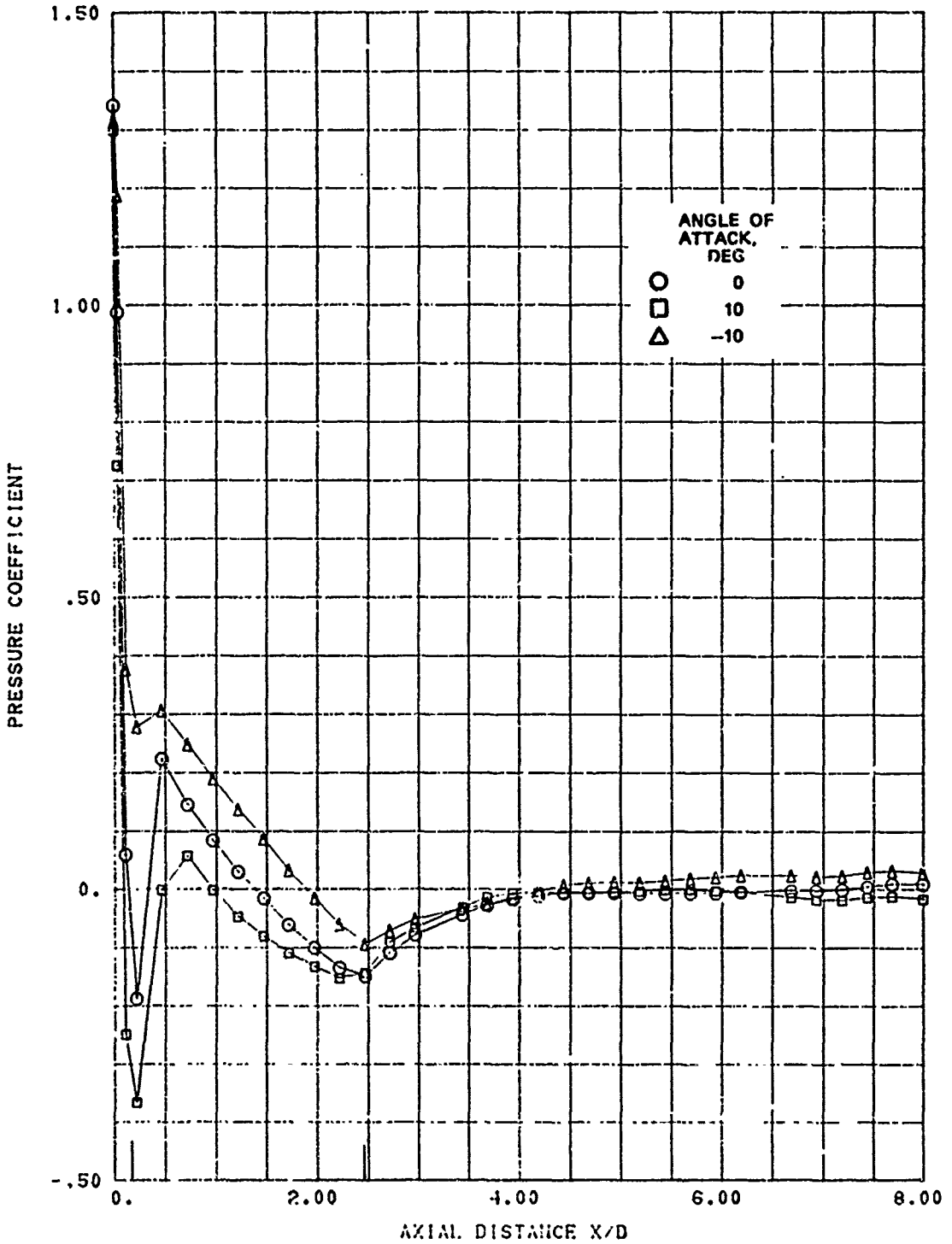

FIG. A-22. Longitudinal Pressure Distribution; Nose A, Mach 1.1, Roll Angle 15 Degrees.

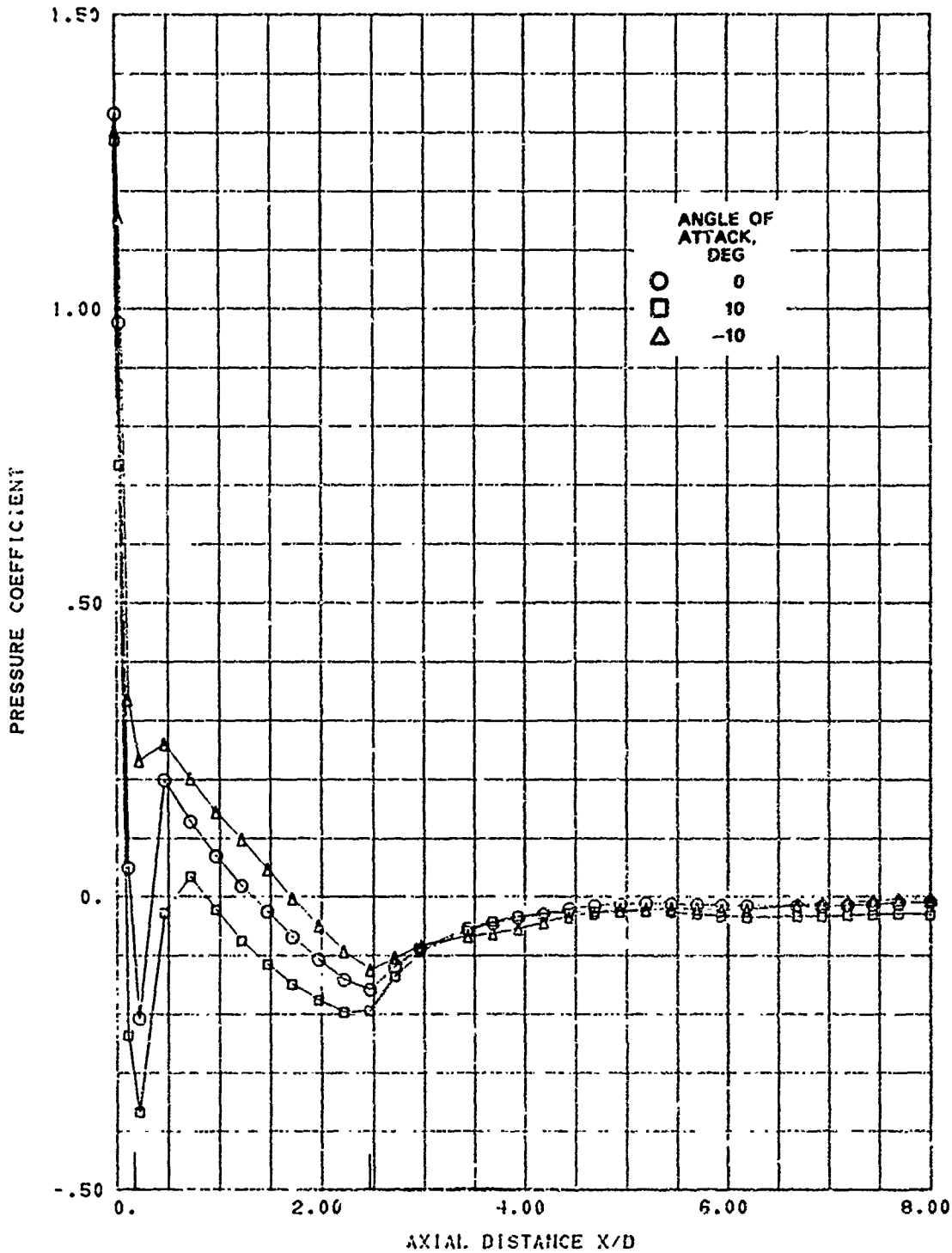

FIG. A-23. Longitudinal Pressure Distribution; Nose A, Mach 1.1, Roll Angle 30 Degrees.

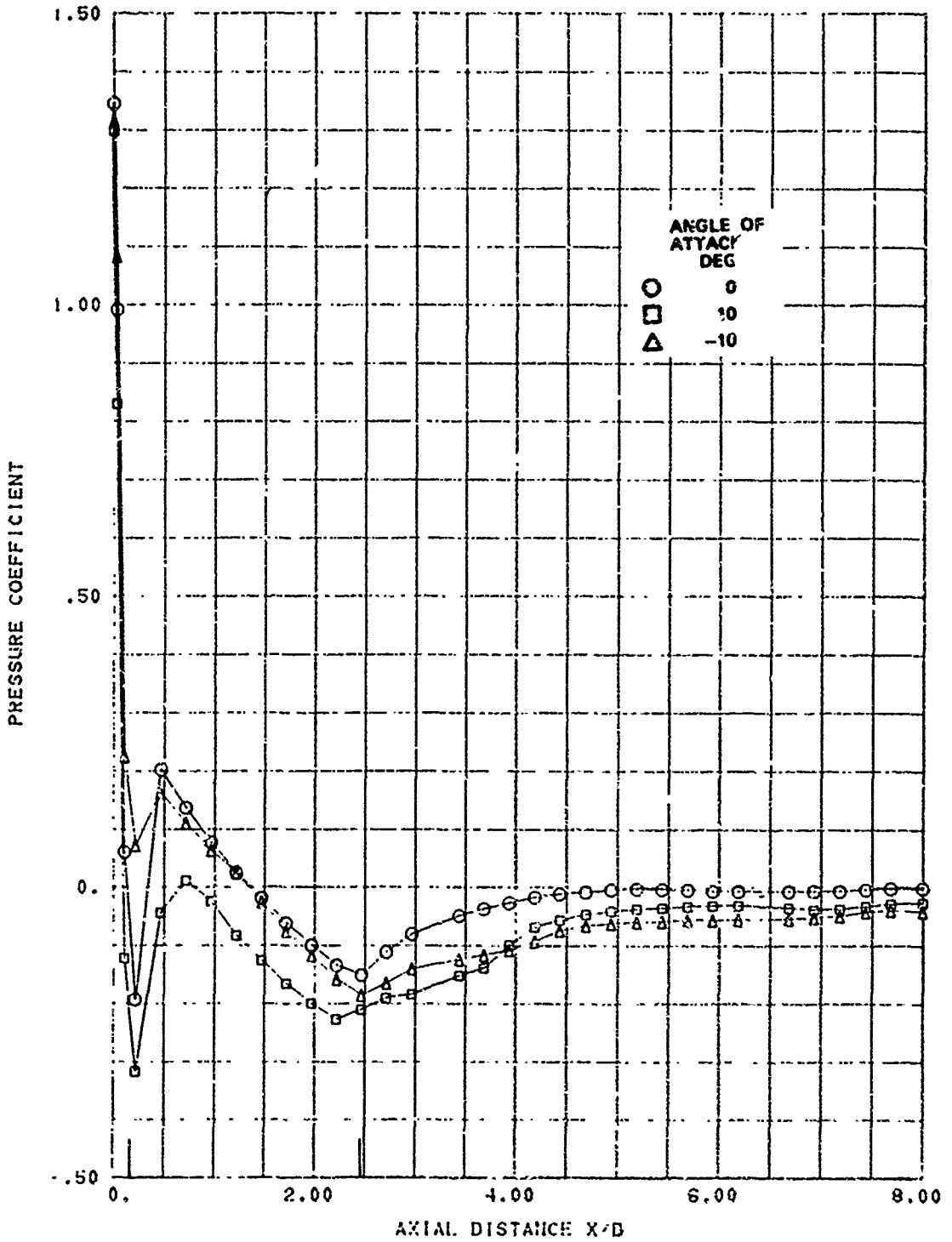

FIG. A-24. Longitudinal Pressure Distribution; Nose A, Mach 1.1, Roll Angle 60 Degrees.

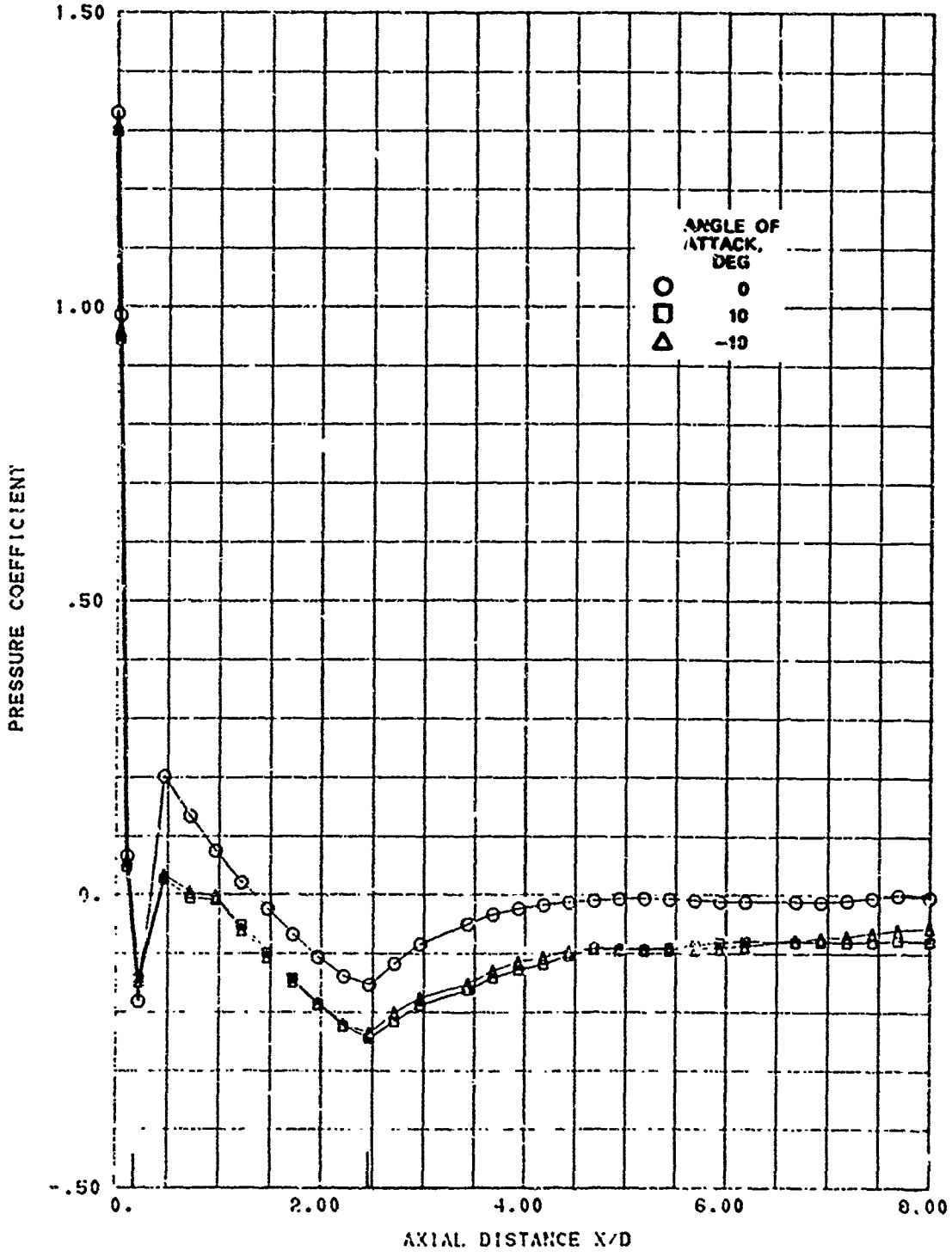

FIG. A-25. Longitudinal Pressure Distribution; Nose A, Mach 1.1, Roll Angle 90 Degrees.

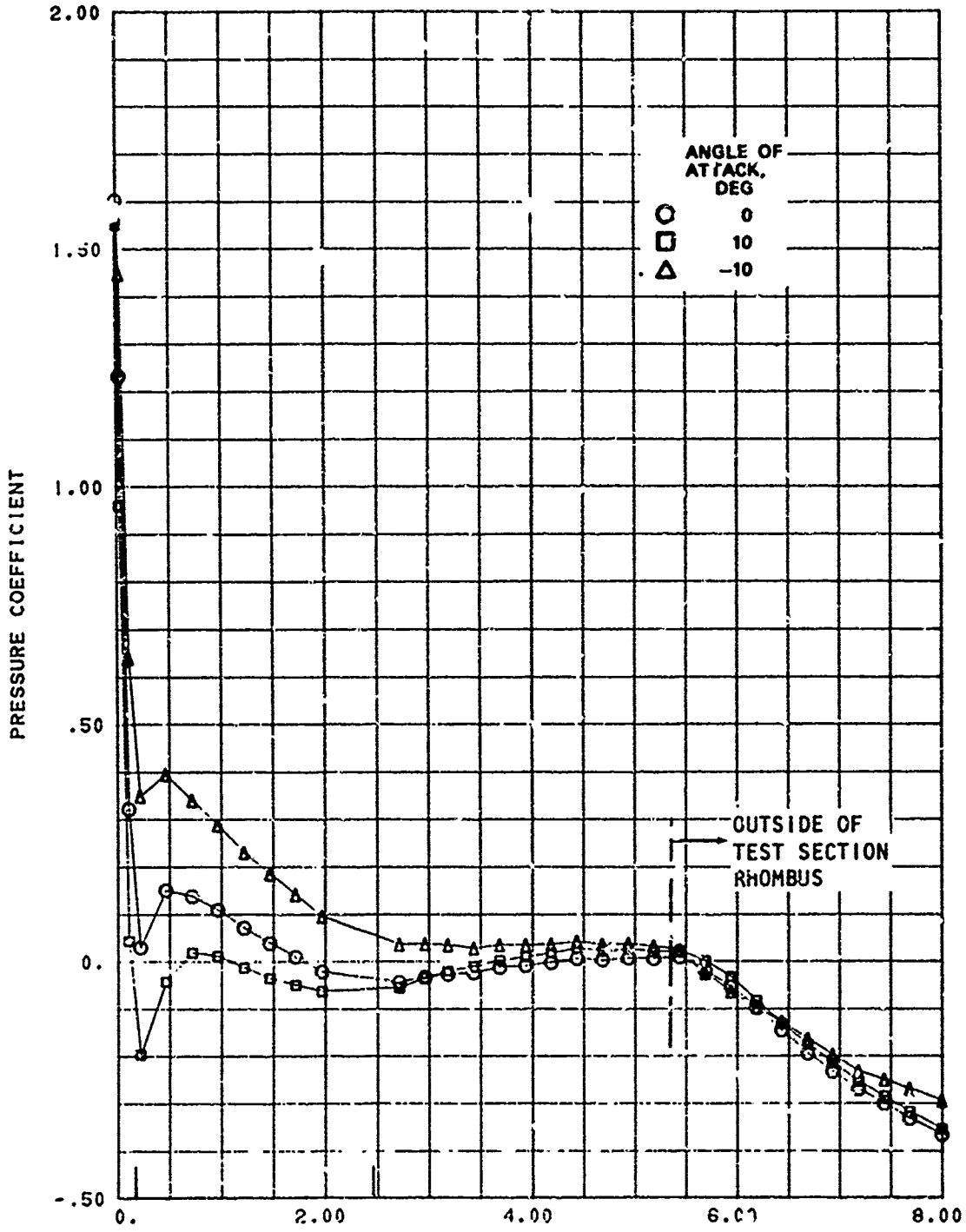

FIG. A-26. Longitudinal Pressure Distribution; Nose A, Mach 1.52, Roll Angle 0 Degrees.

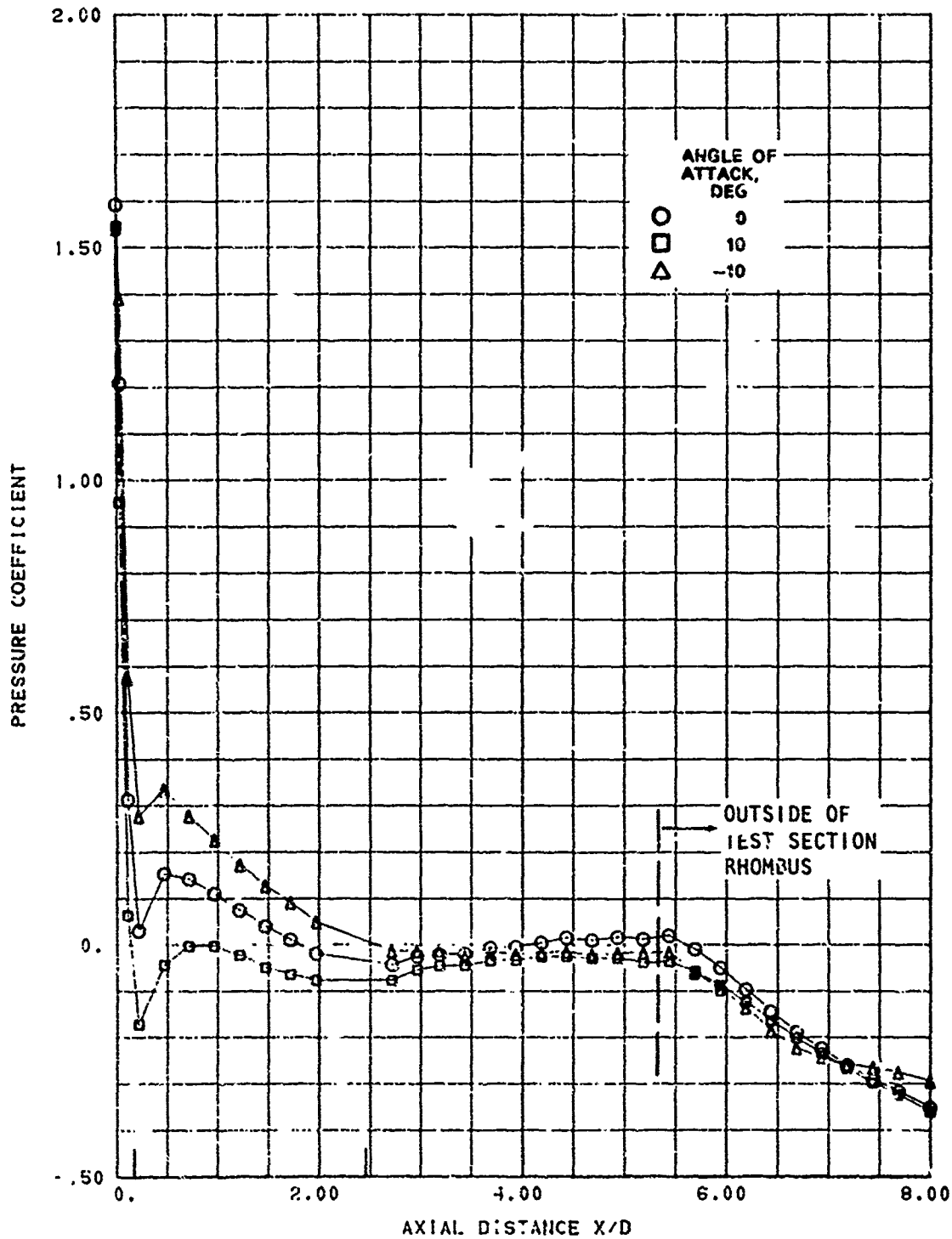

FIG. A-27. Longitudinal Pressure Distribution; Nose A, Mach 1.52, Roll Angle 30 Degrees.

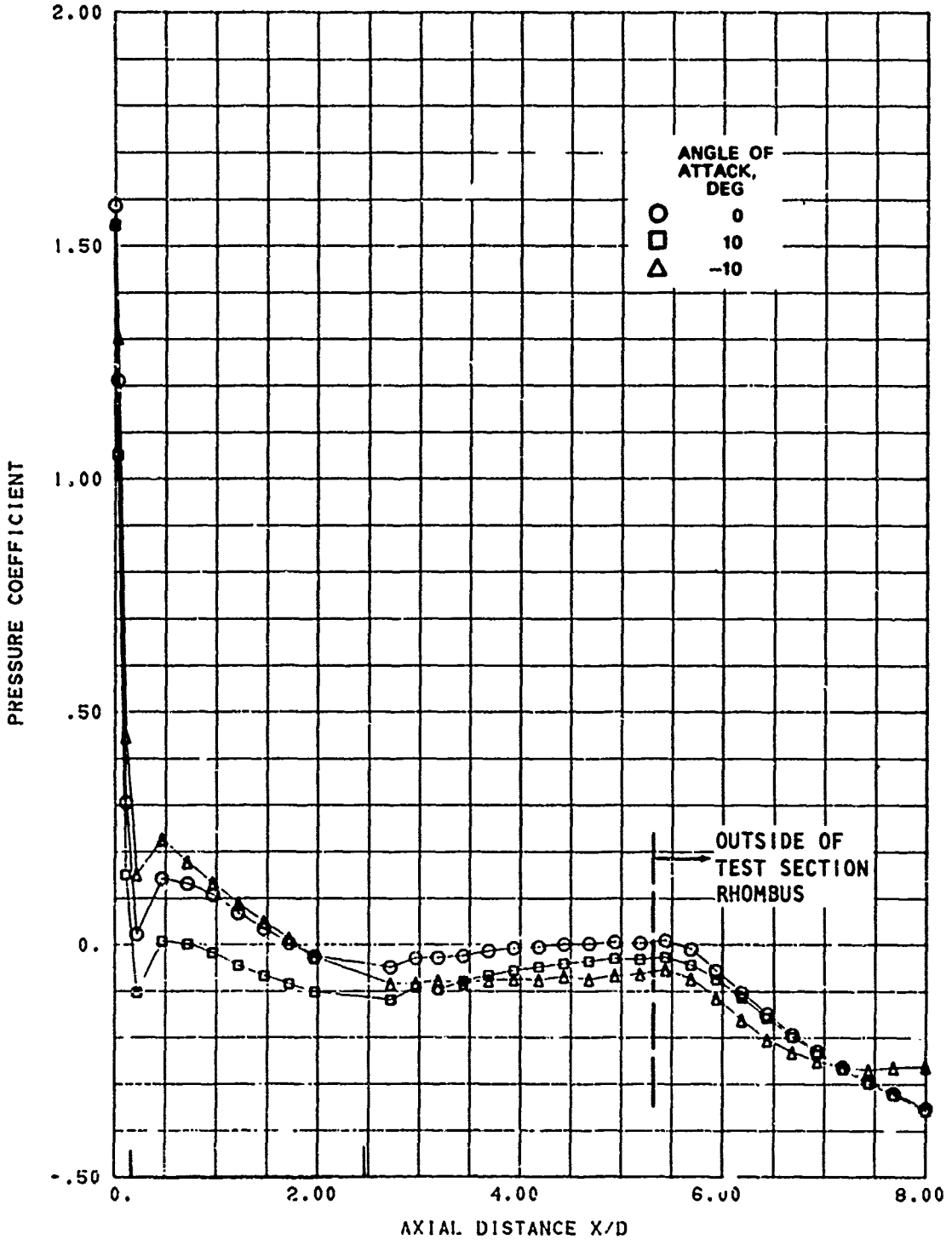

FIG. A-28. Longitudinal Pressure Distribution; Nose A, Mach 1.52, Roll Angle 60 Degrees.

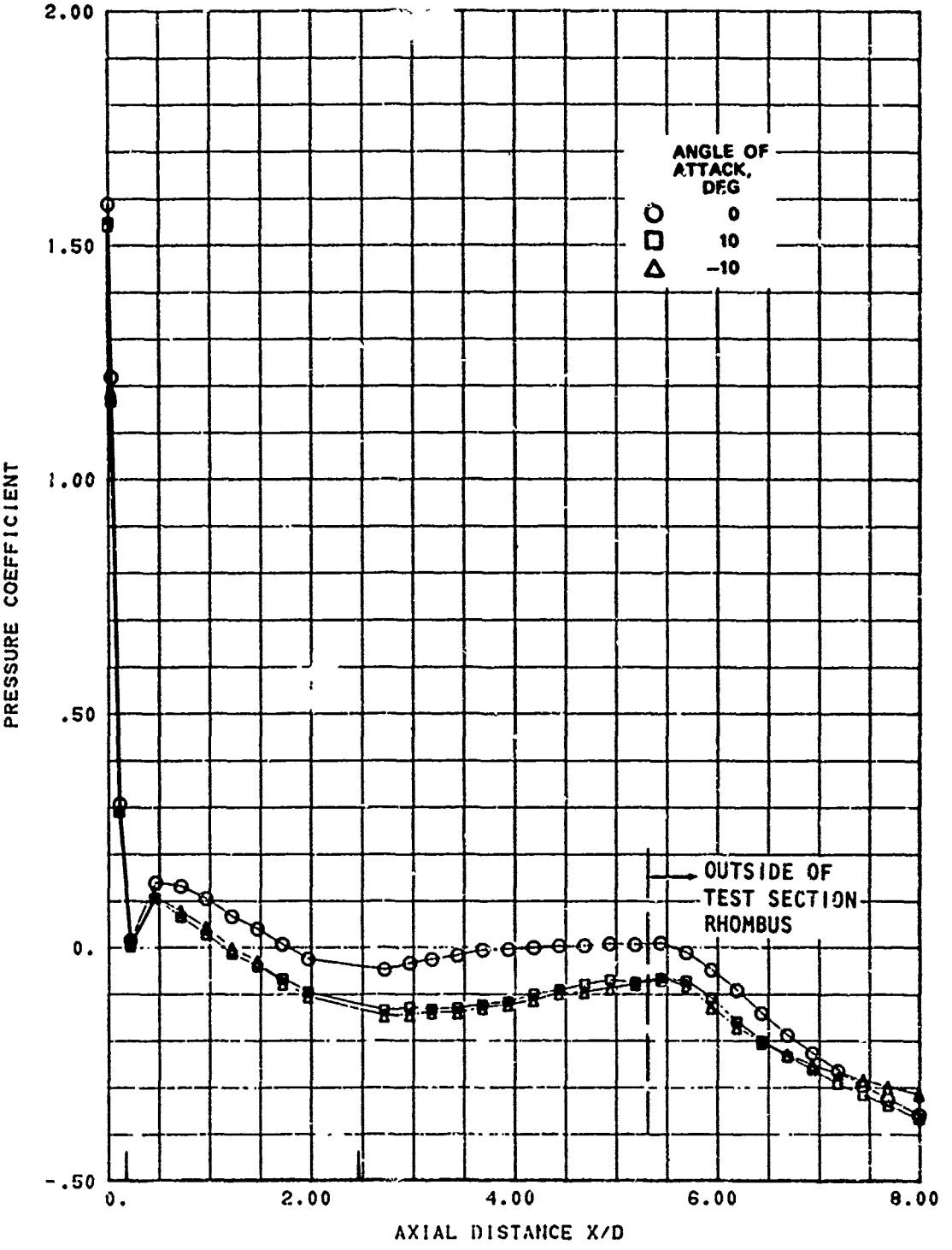

FIG. A-29. Longitudinal Pressure Distribution; Nose A, Mach 1.52, Roll Angle 90 Degrees.

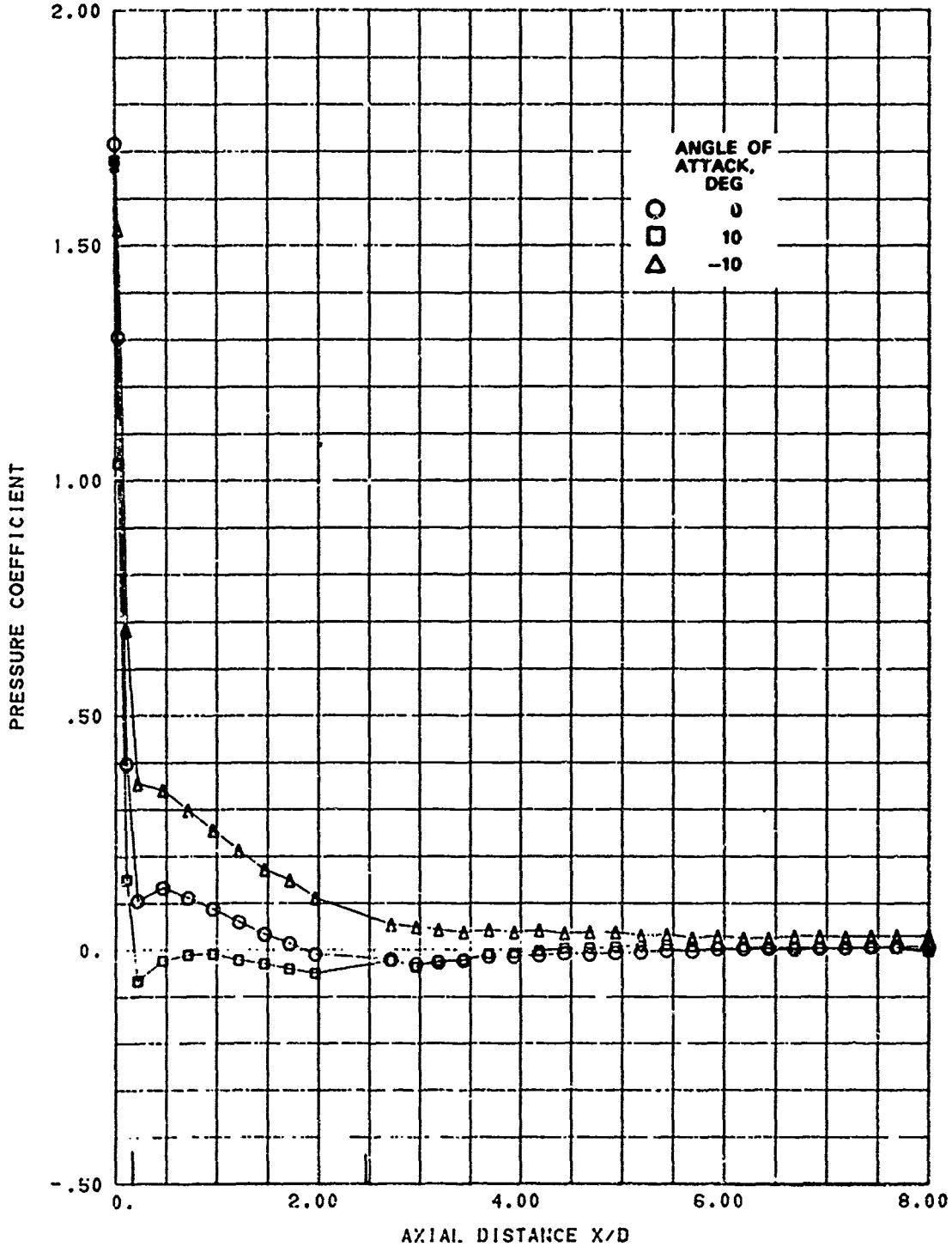

FIG. A-30. Longitudinal Pressure Distribution; Nose A, Mach 2.02, Roll Angle 0 Degrees.

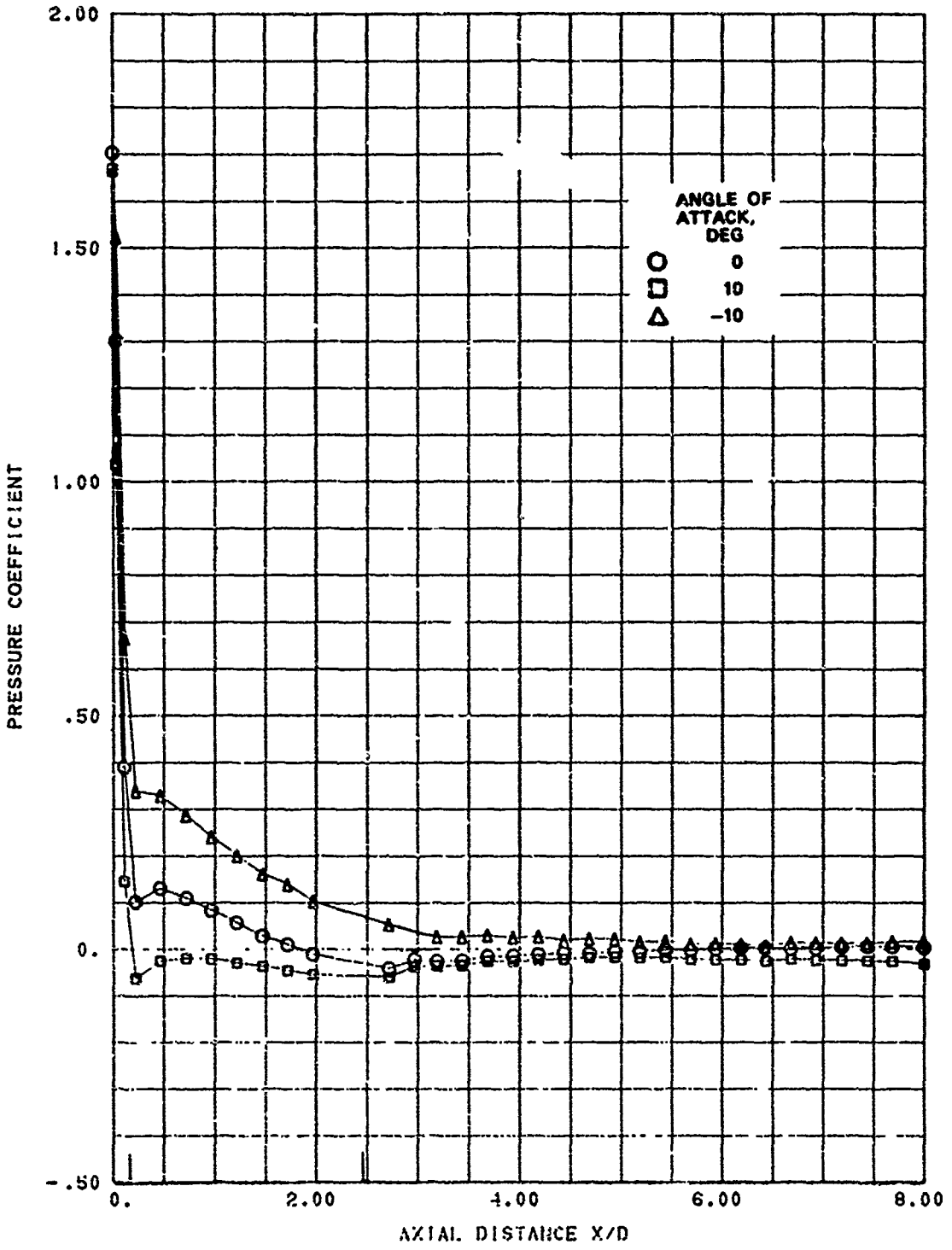

FIG. A-31. Longitudinal Pressure Distribution; Nose A, Mach 2.02, Roll Angle 15 Degrees.

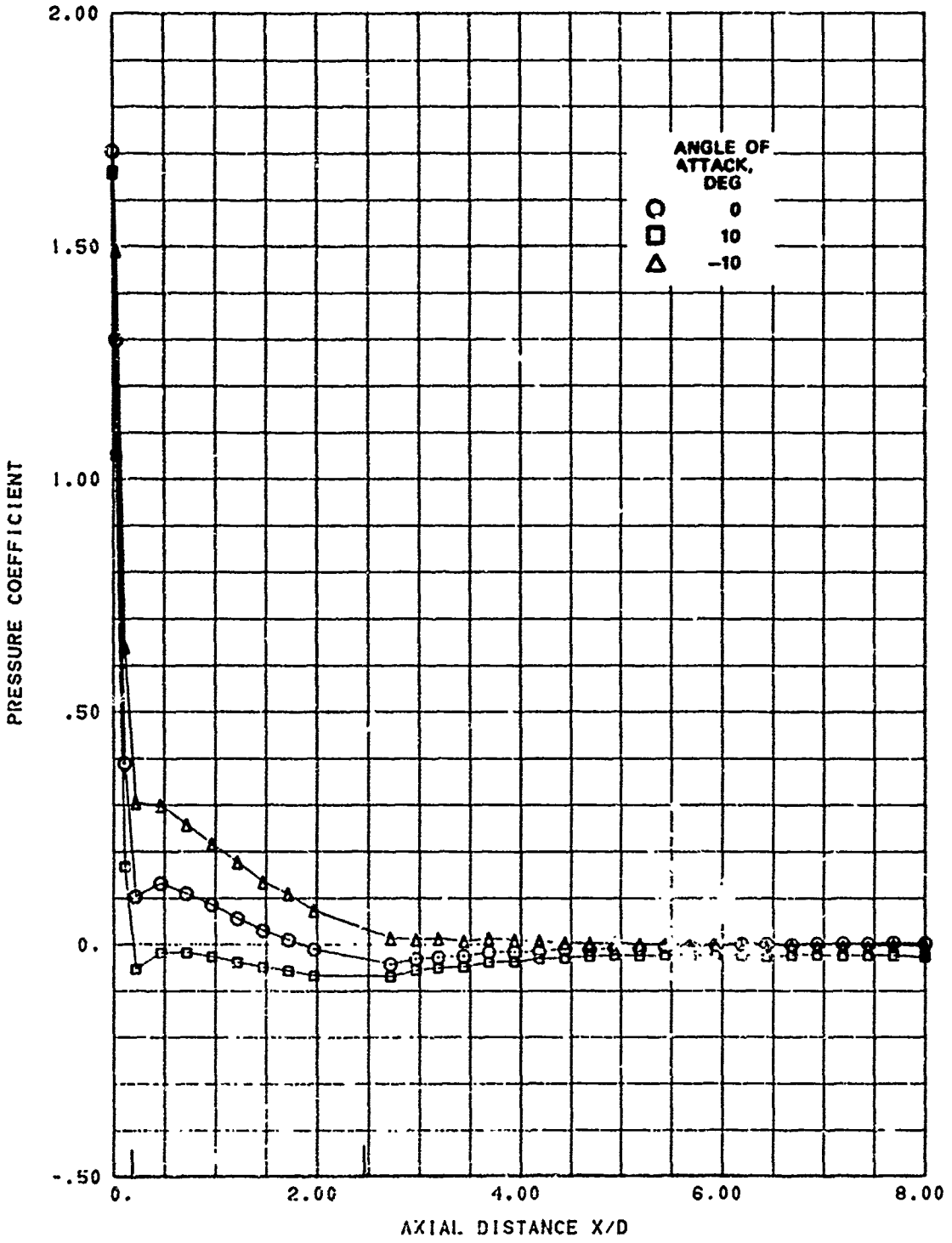

FIG. A-32. Longitudinal Pressure Distribution; Nose A, Mach 2.02, Roll Angle 30 Degrees.

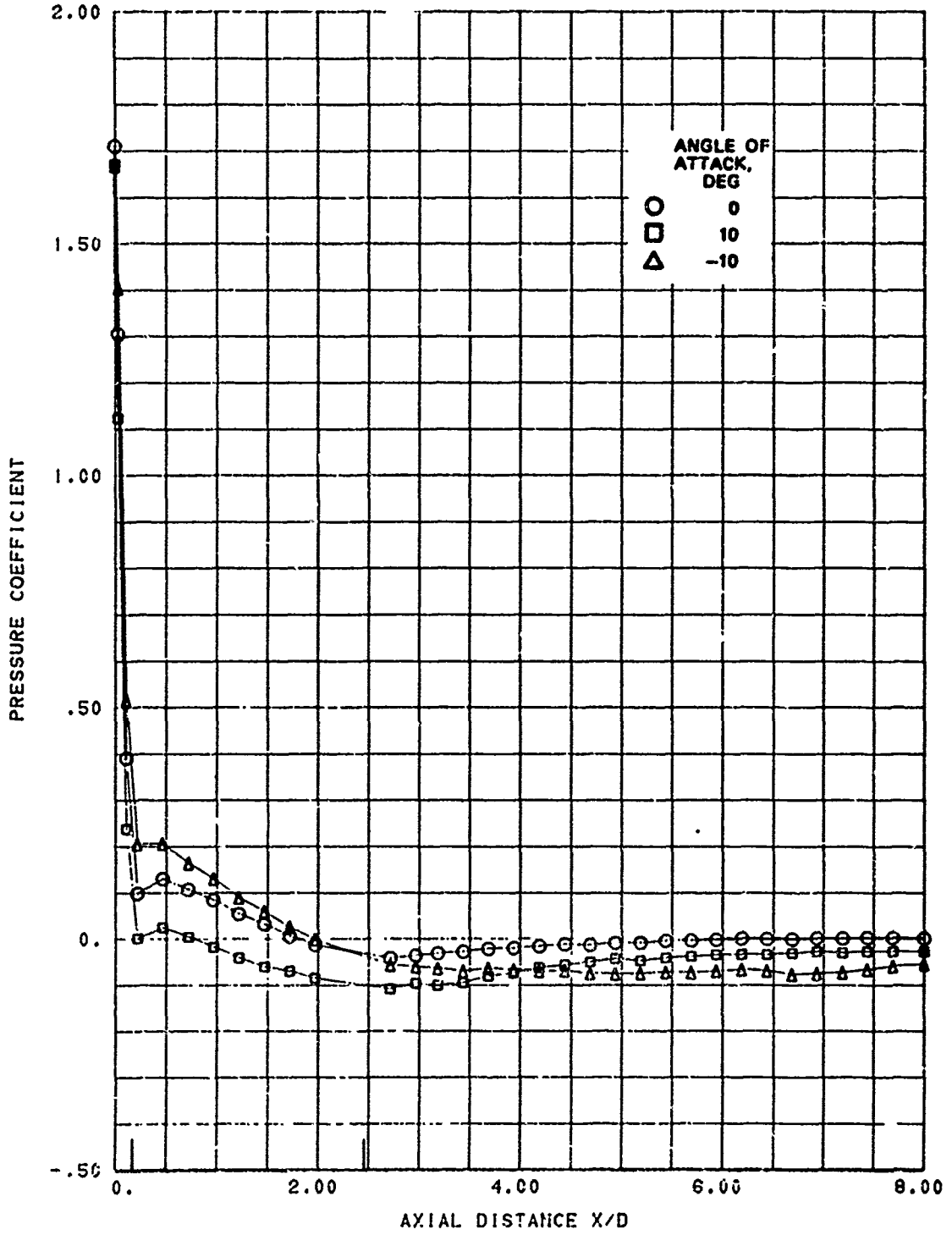

FIG. A-33. Longitudinal Pressure Distribution; Nose A, Mach 2.02, Roll Angle 60 Degrees.

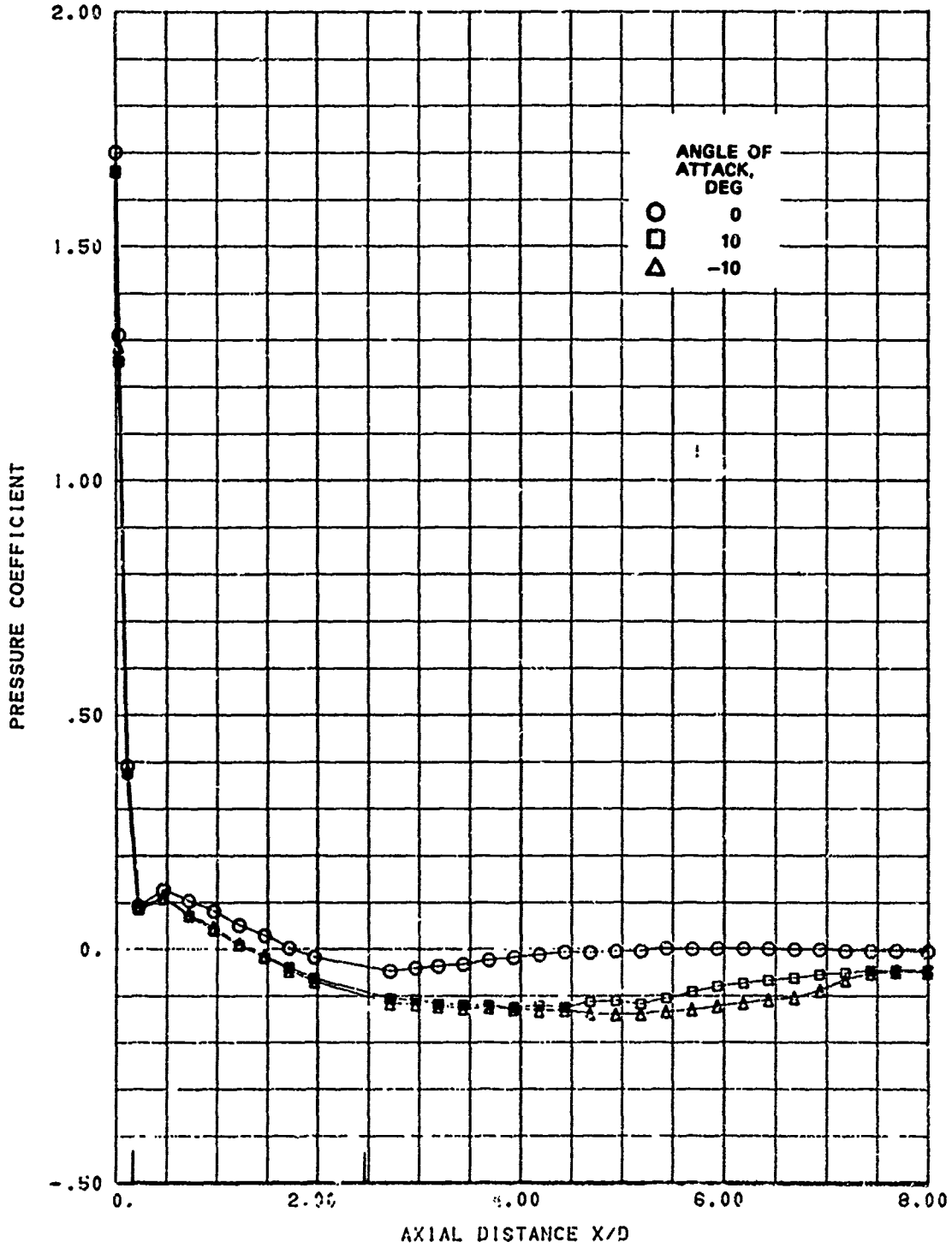

FIG. A-34. Longitudinal Pressure Distribution; Nose A, Mach 2.02, Roll Angle 90 Degrees.

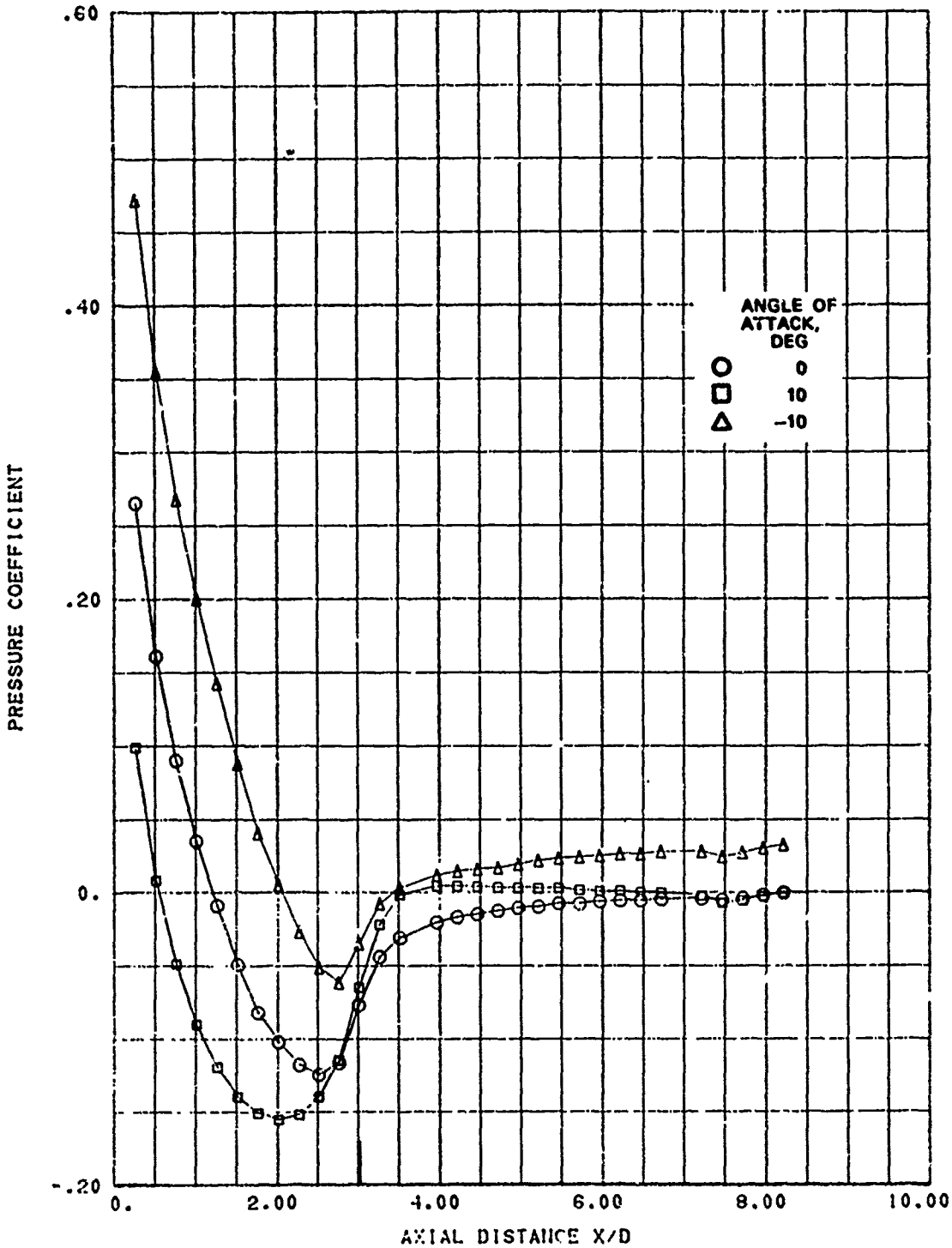

FIG. A-35. Longitudinal Pressure Distribution; Nose B, Mach 0.7, Roll Angle 0 Degrees.

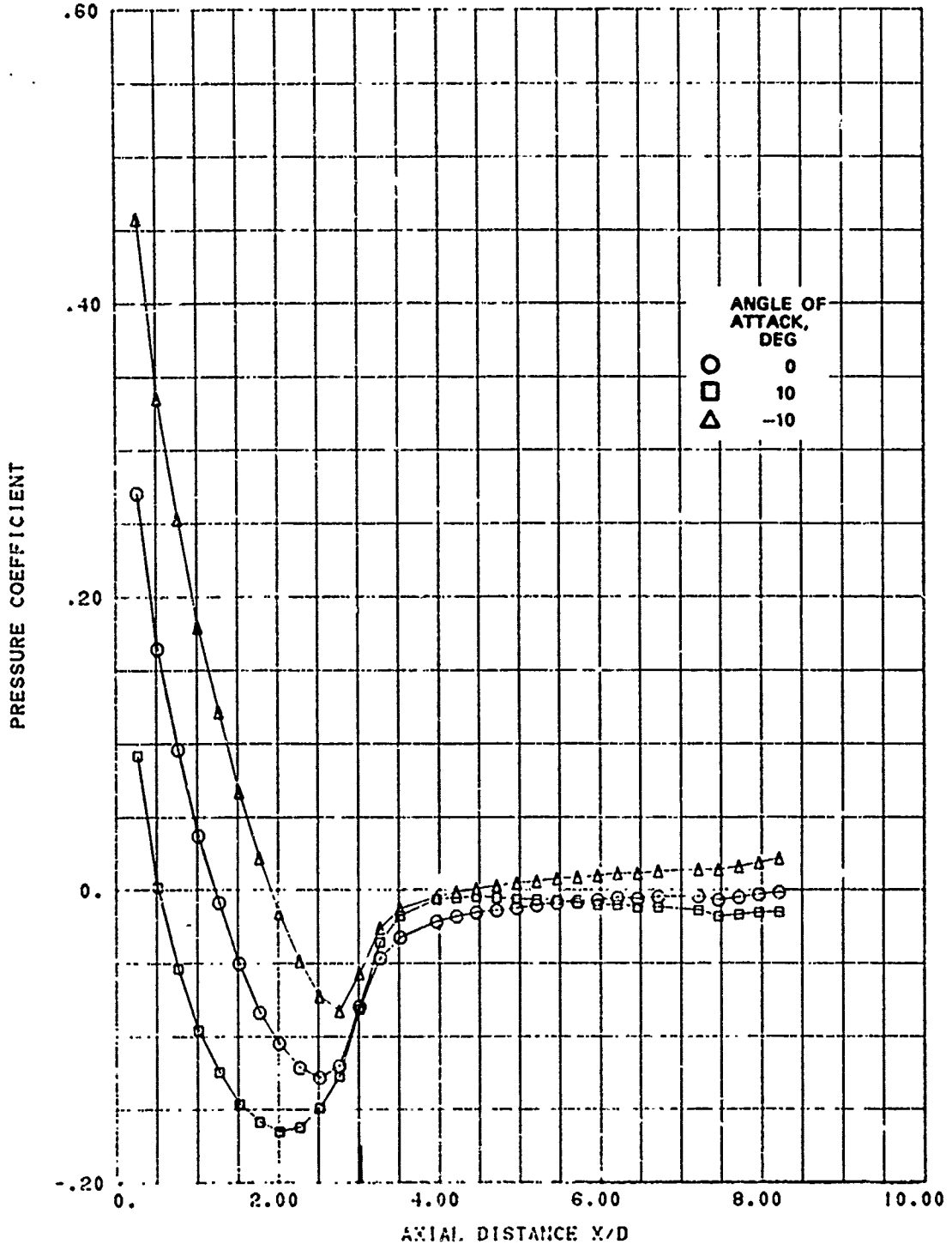

FIG. A-36. Longitudinal Pressure Distribution; Nose B, Mach 0.7, Roll Angle 15 Degrees.

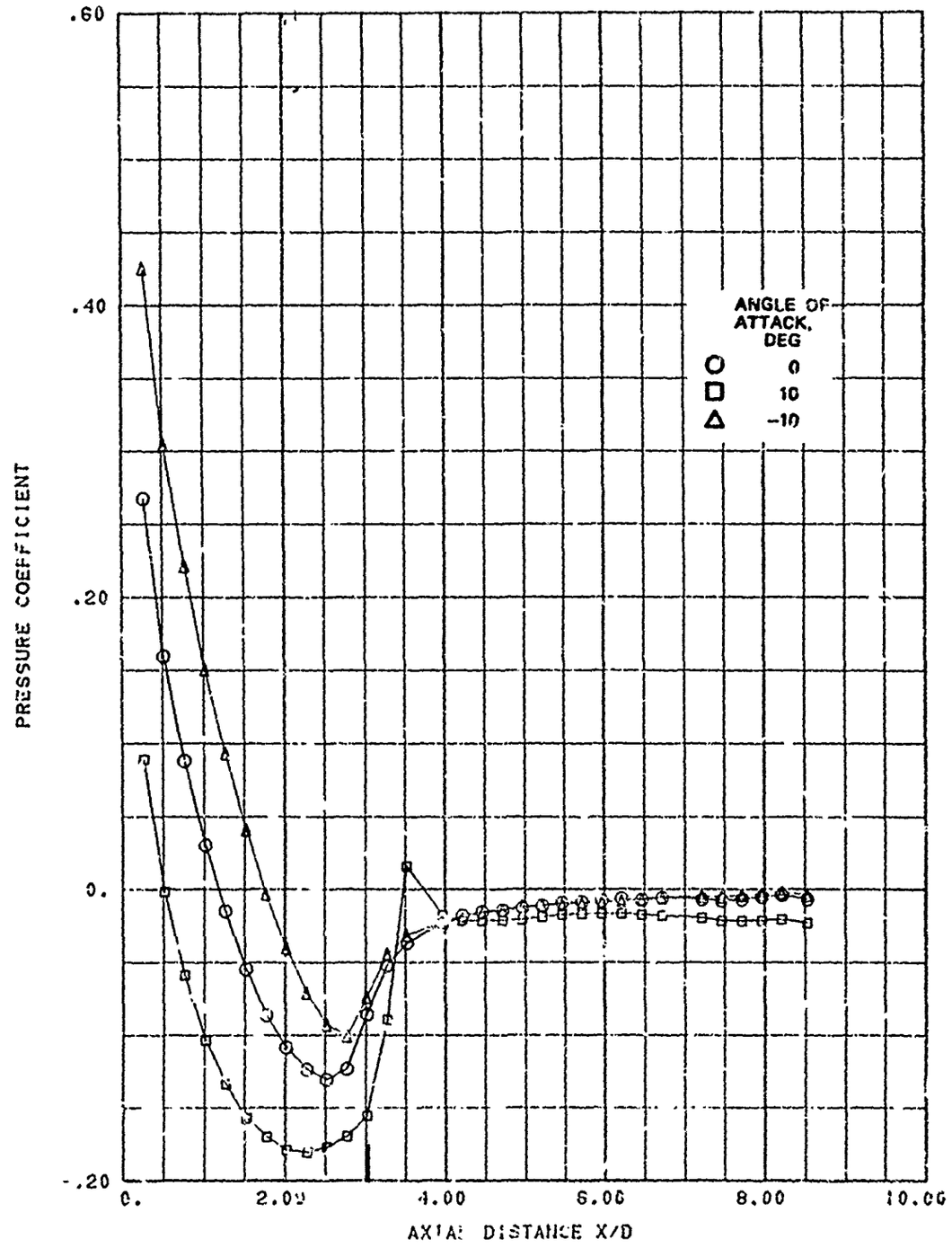

FIG. A-37 Longitudinal Pressure Distribution; Nose B, Mach 0.7, Roll Angle 30 Degrees.

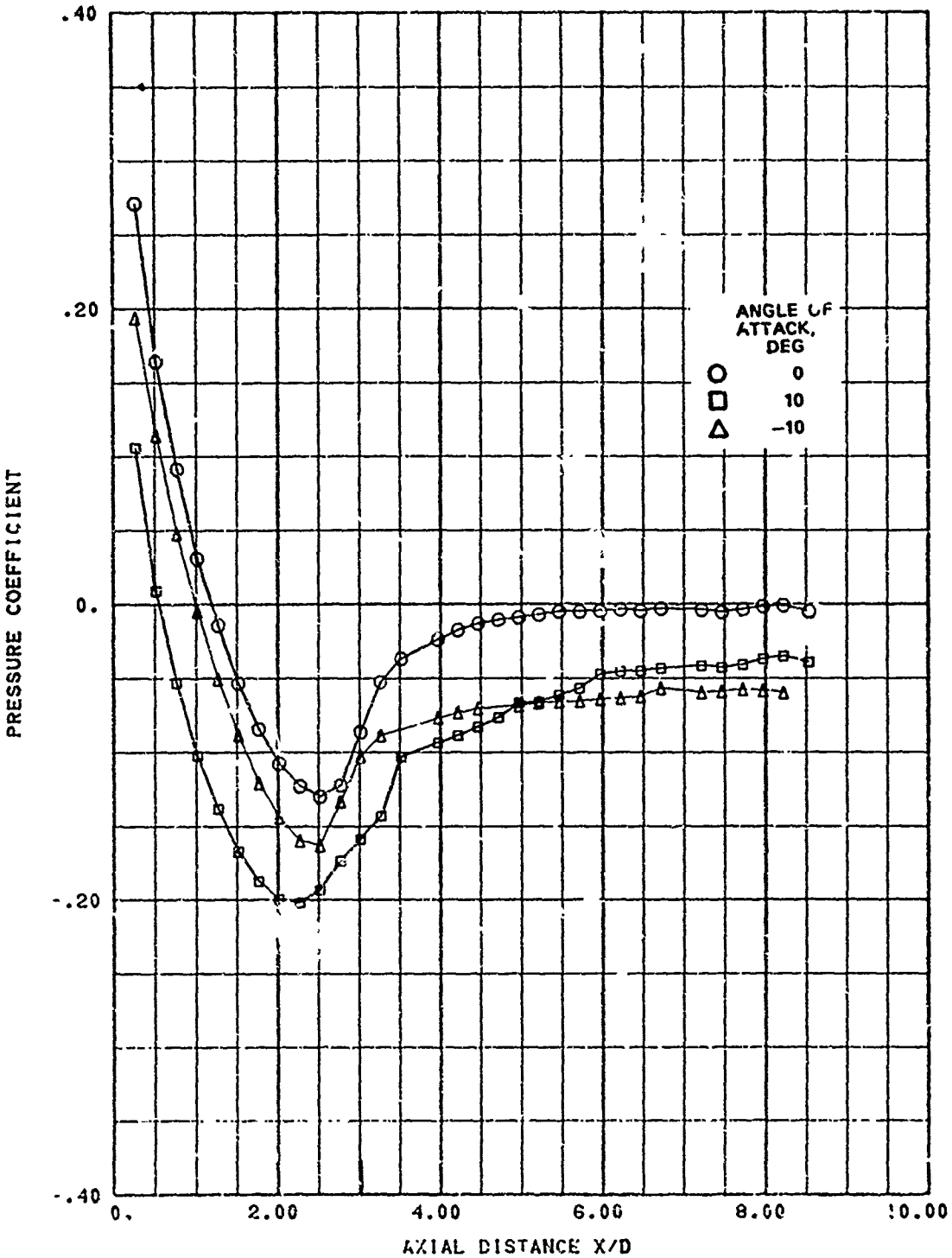

FIG. A-38. Longitudinal Pressure Distribution; Nose B, Mach 0.7, Roll Angle 60 Degrees.

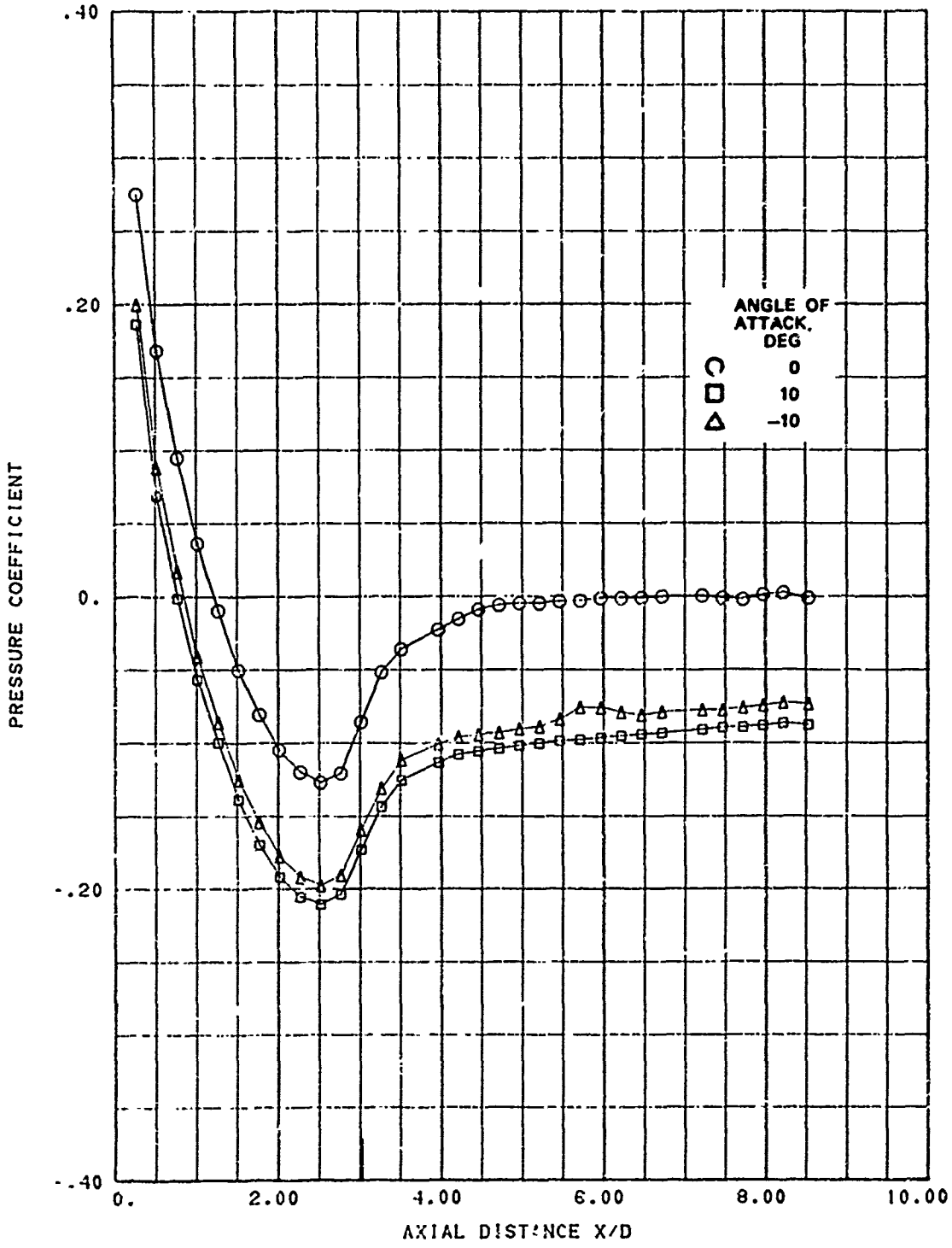

FIG. A-39. Longitudinal Pressure Distribution; Nose B, Mach 0.7, Roll Angle 90 Degrees.

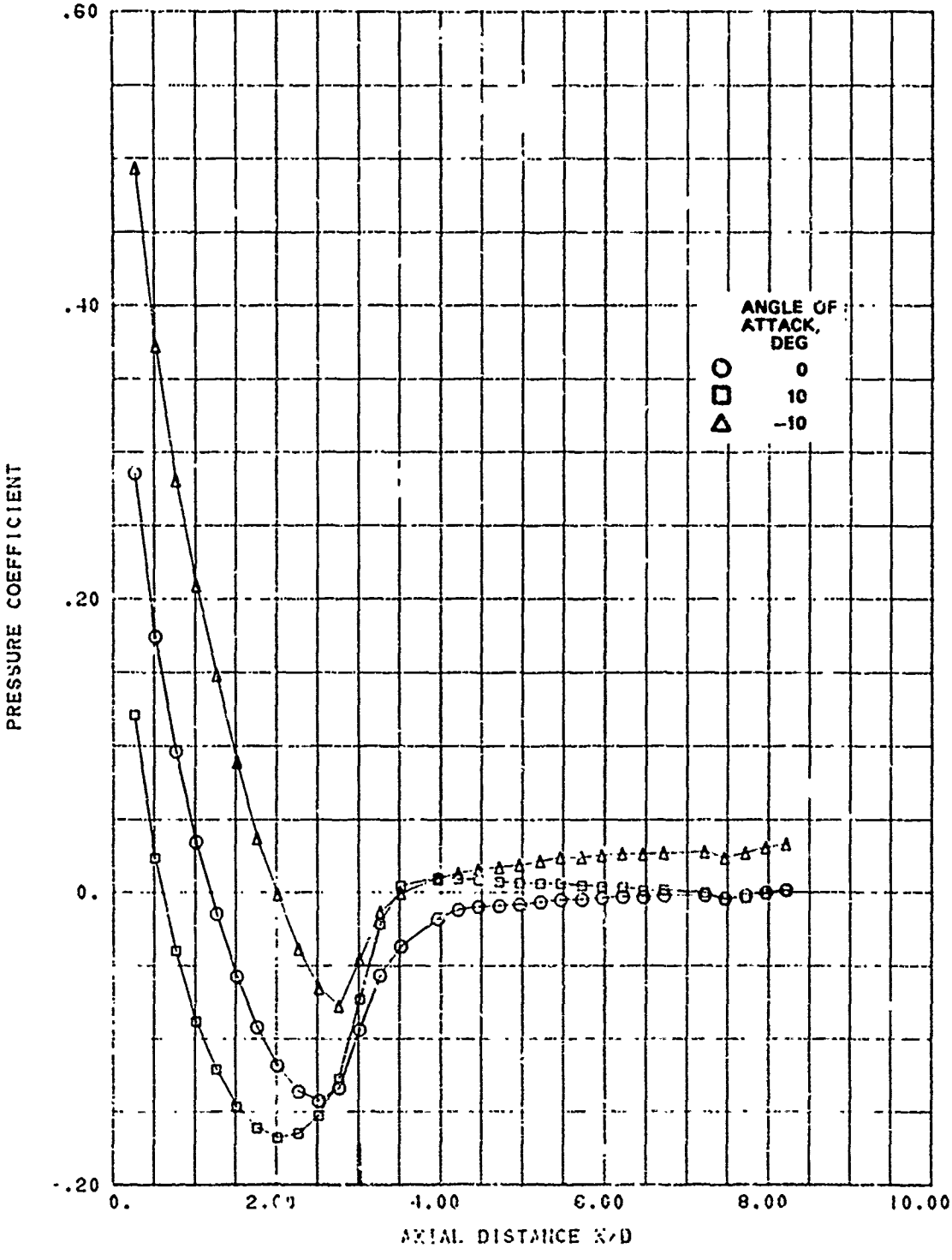

FIG. A-30. Longitudinal Pressure Distribution; Nose B, Mach 0.8, Roll Angle 0 Degrees.

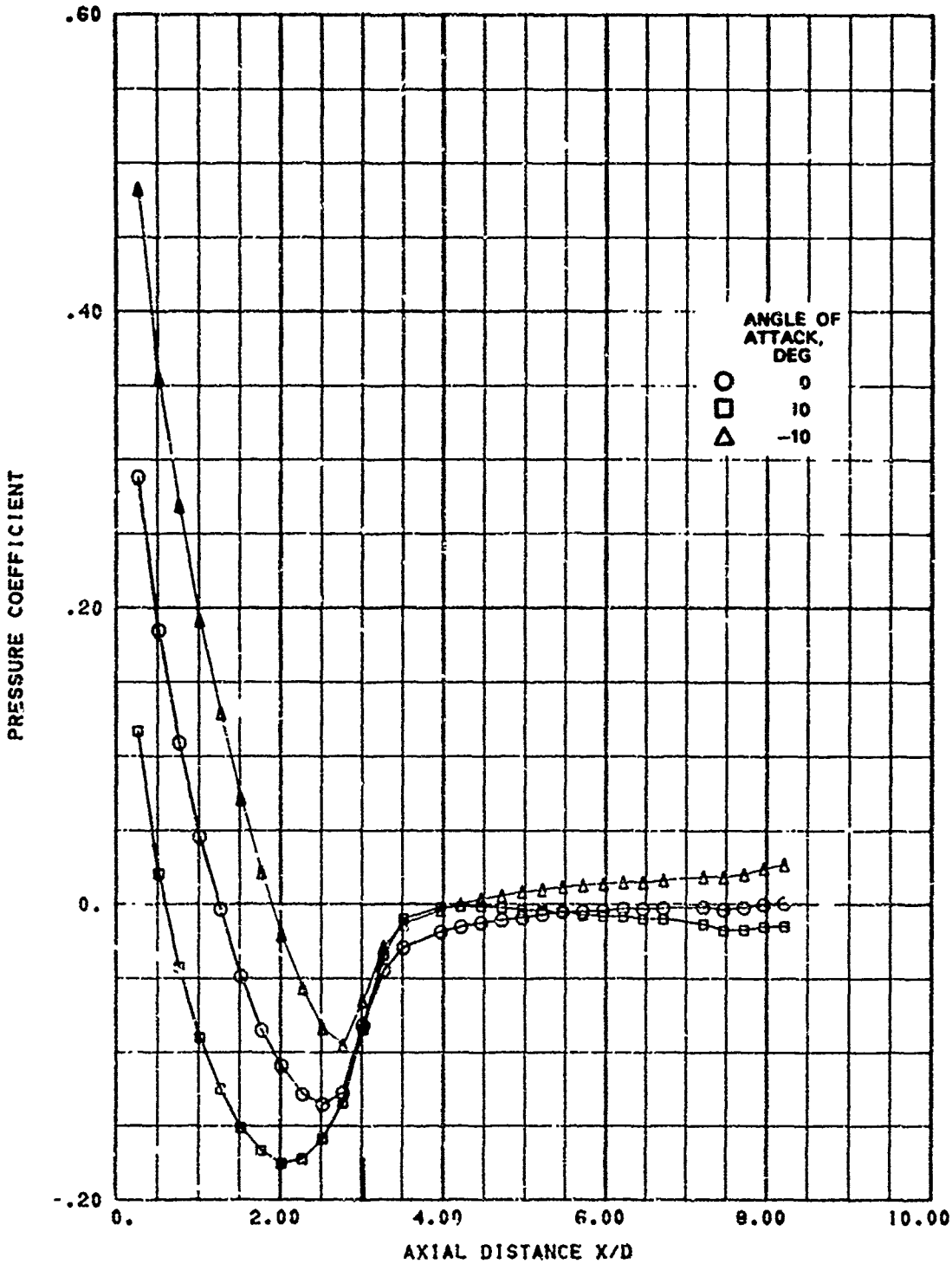

FIG. A-41. Longitudinal Pressure Distribution; Nose B, Mach 0.8, Roll Angle 15 Degrees.

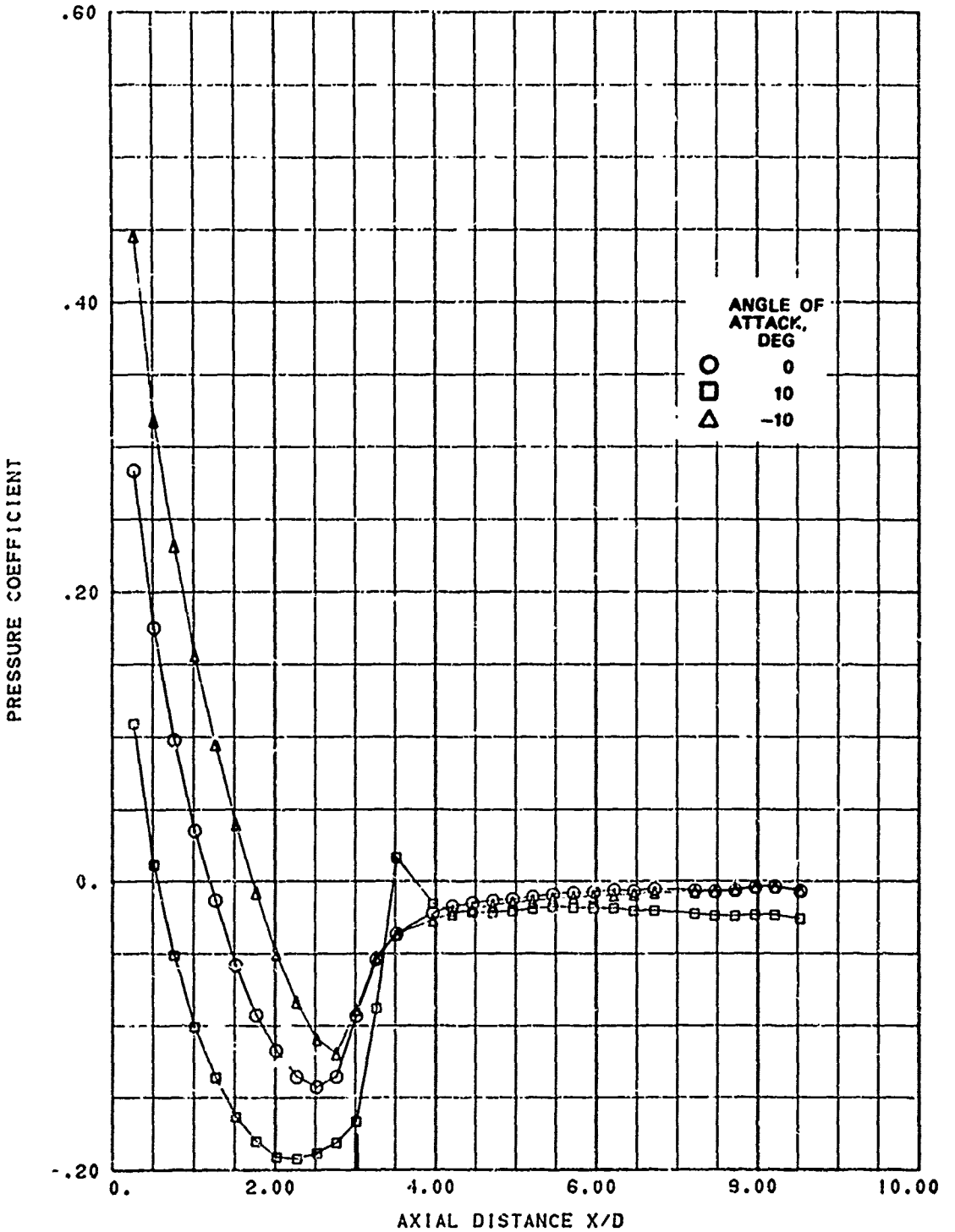

FIG. A-42. Longitudinal Pressure Distribution; Nose B, Mach 0.8, Roll Angle 30 Degrees.

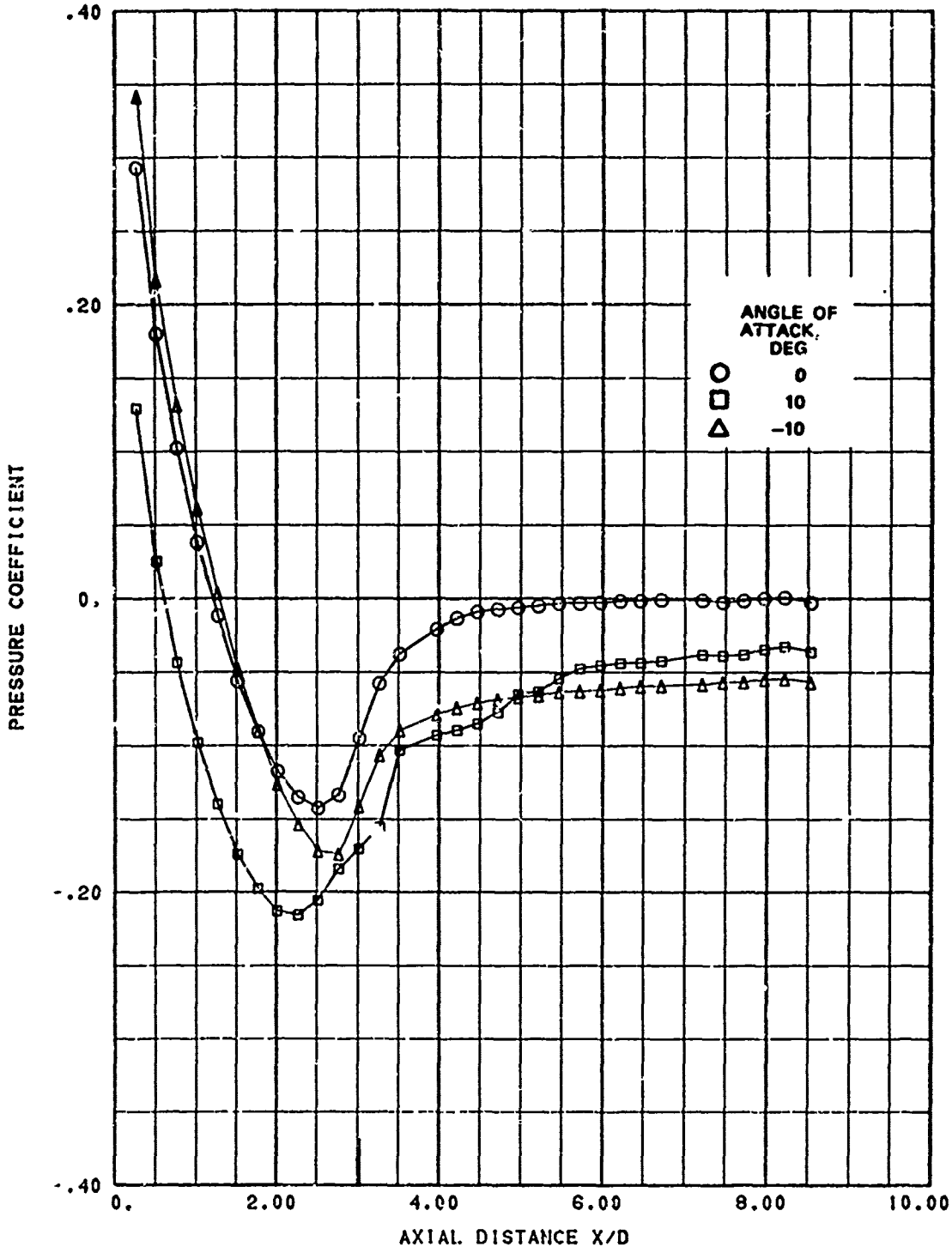

FIG. A-43. Longitudinal Pressure Distribution; Nose B, Mach 0.8, Roll Angle 60 Degrees.

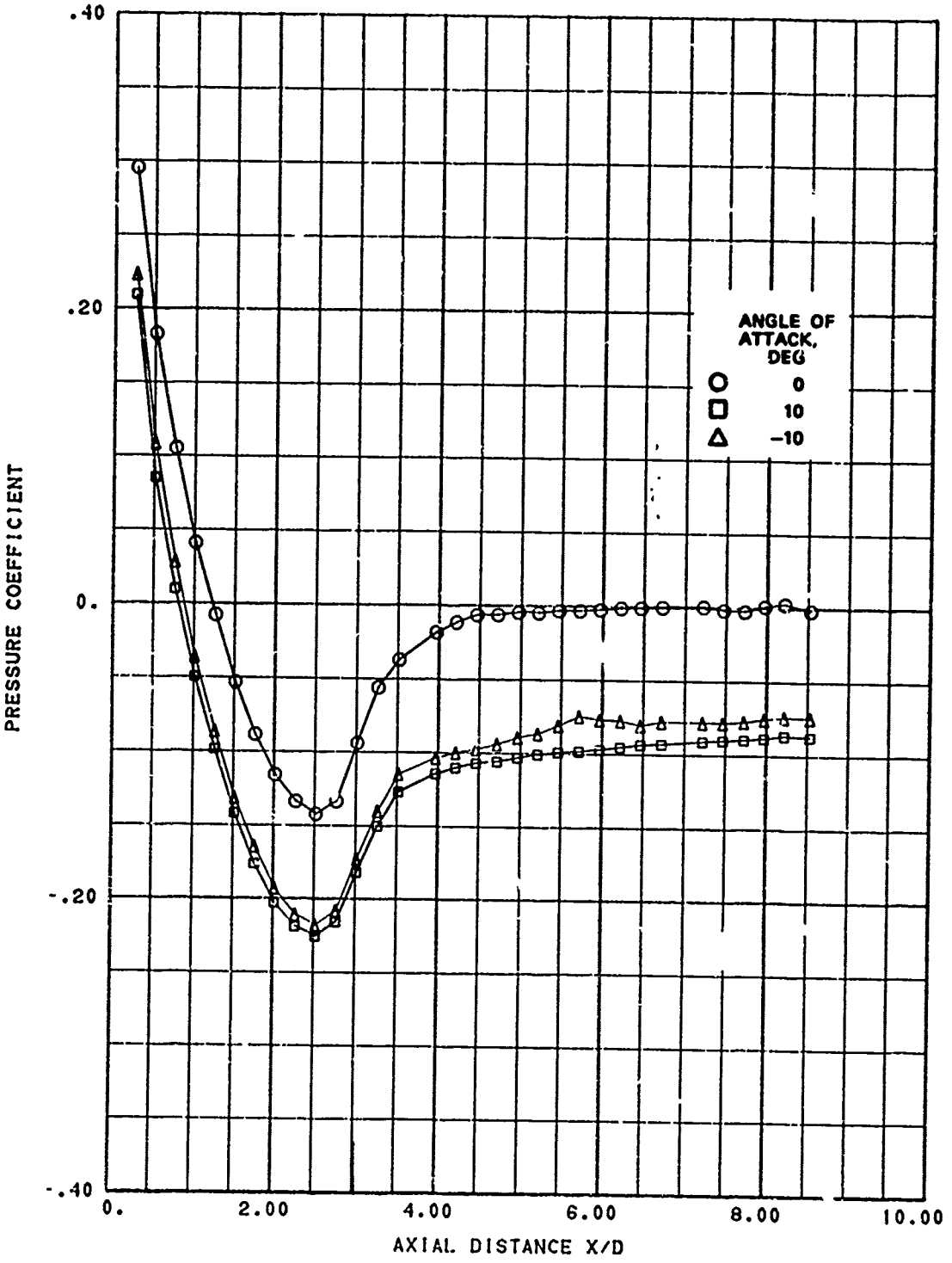

FIG. A-41. Longitudinal Pressure Distribution; Nose B, Mach 0.8, Roll Angle 90 Degrees.

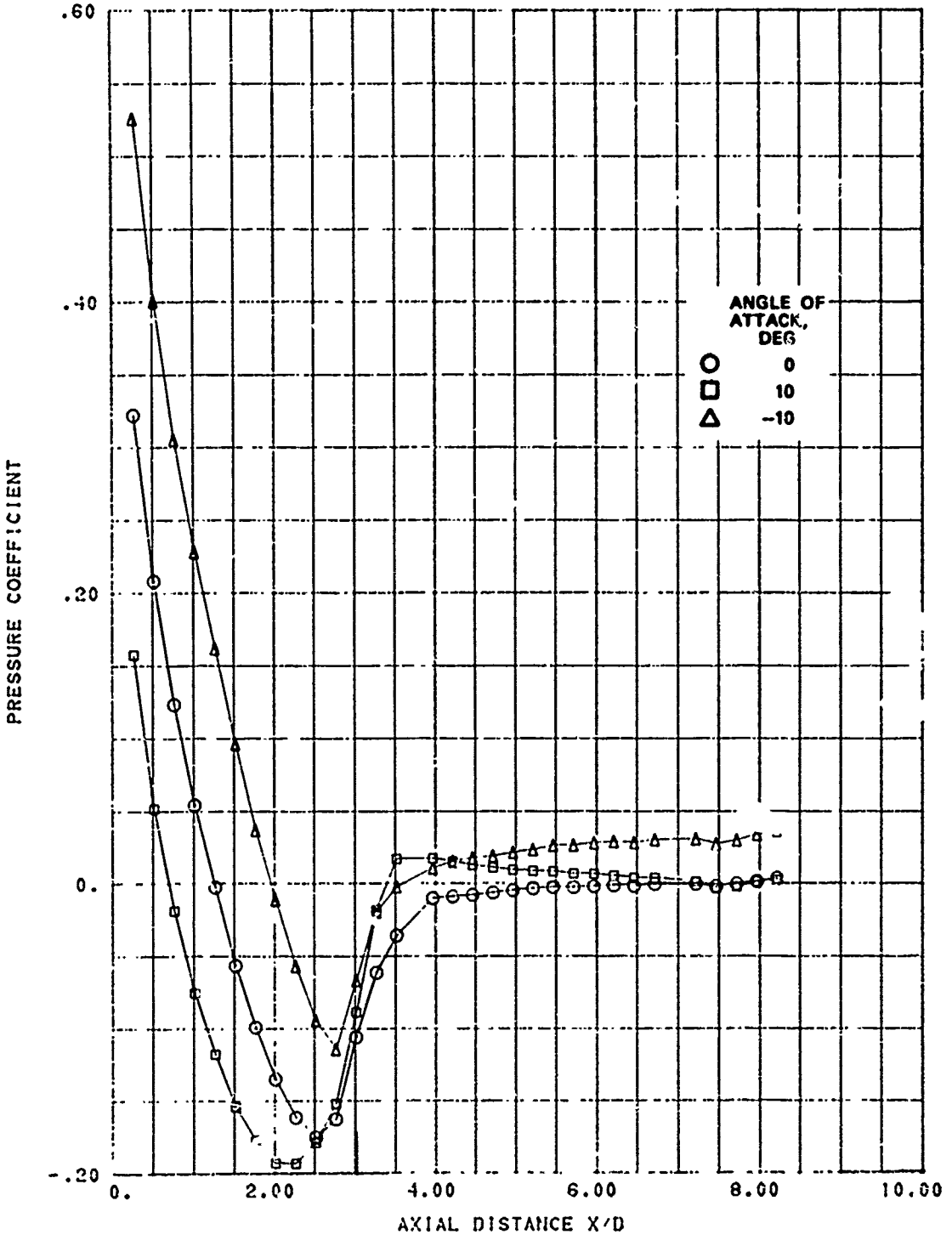

FIG. A-45. Longitudinal Pressure Distribution; Nose B, Mach 0.9, Roll Angle 0 Degrees.

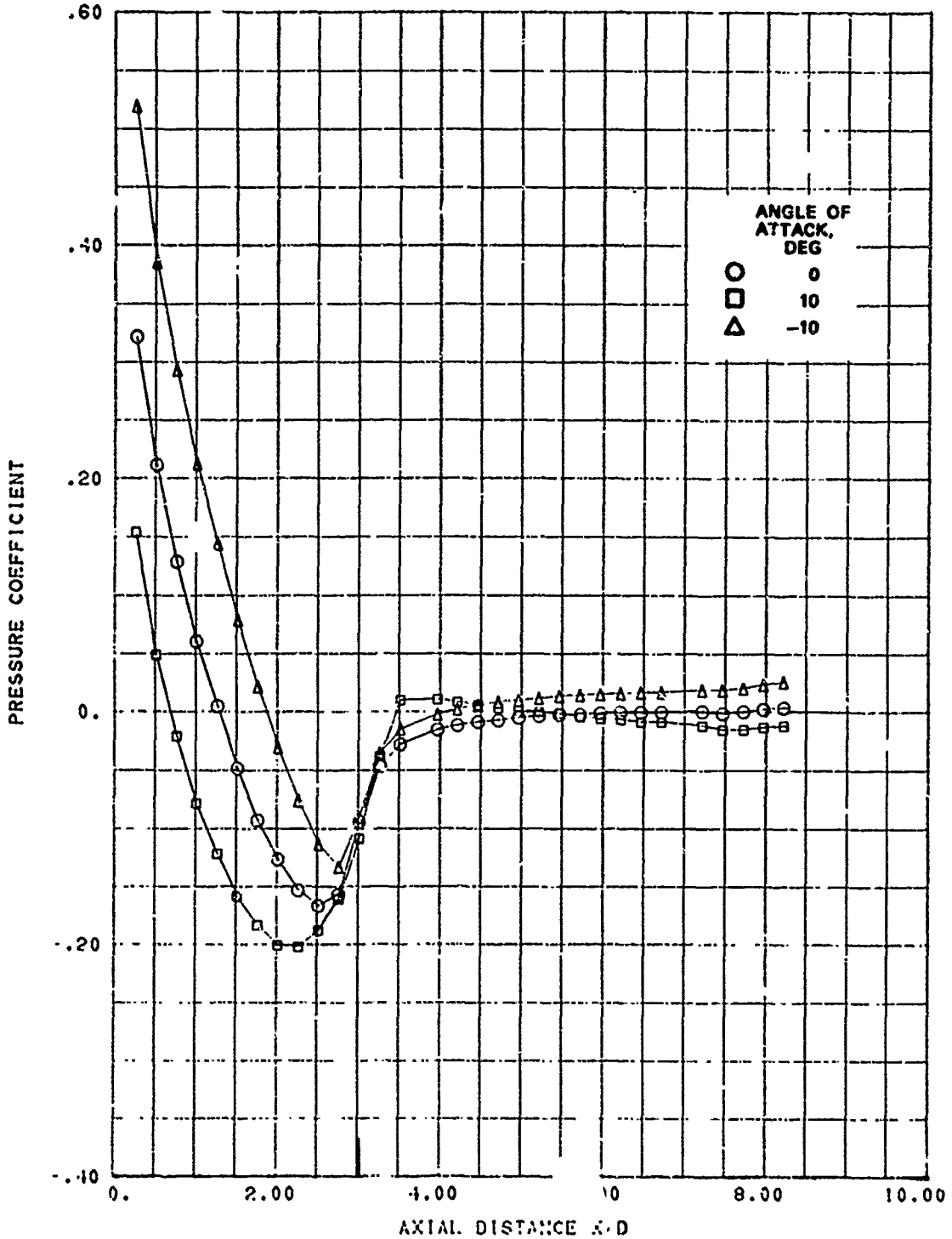

FIG. A-46. Longitudinal Pressure Distribution; Nose B, Mach 0.9, Roll Angle 15 Degrees.

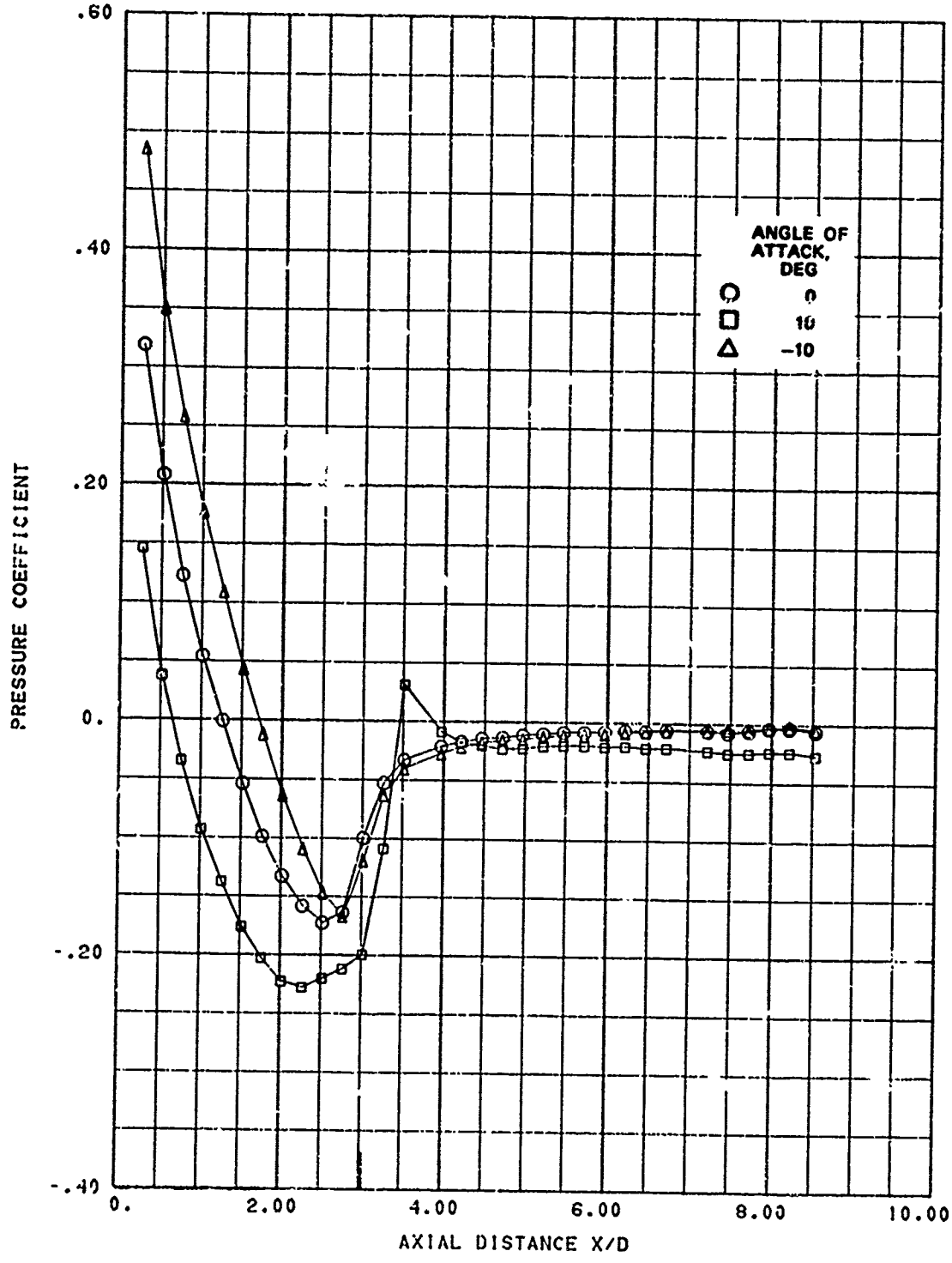

FIG. A-47. Longitudinal Pressure Distribution; Nose B, Mach 0.9, Roll Angle 30 Degrees.

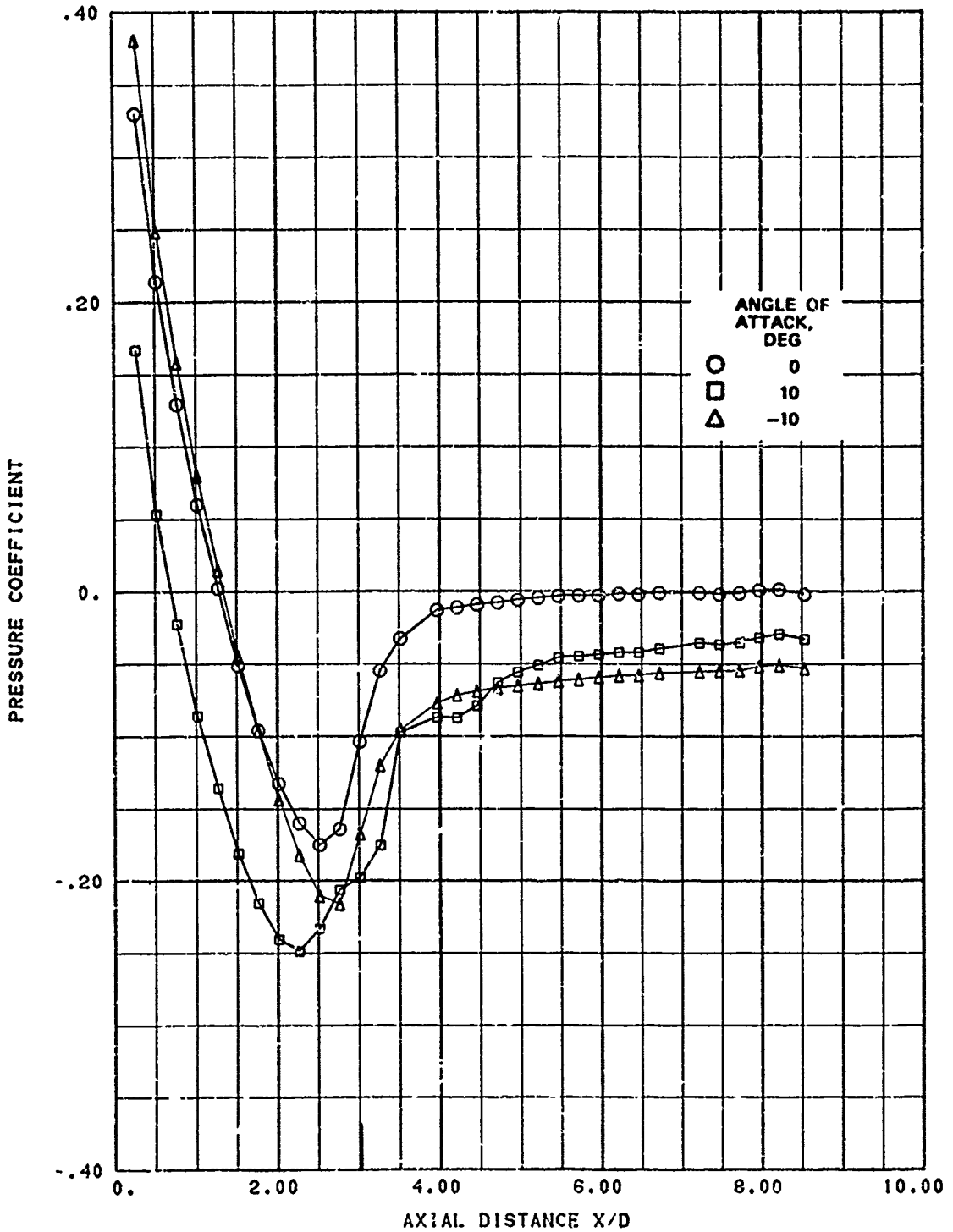

FIG. A-48. Longitudinal Pressure Distribution; Nose B, Mach 0.9, Roll Angle 60 Degrees.

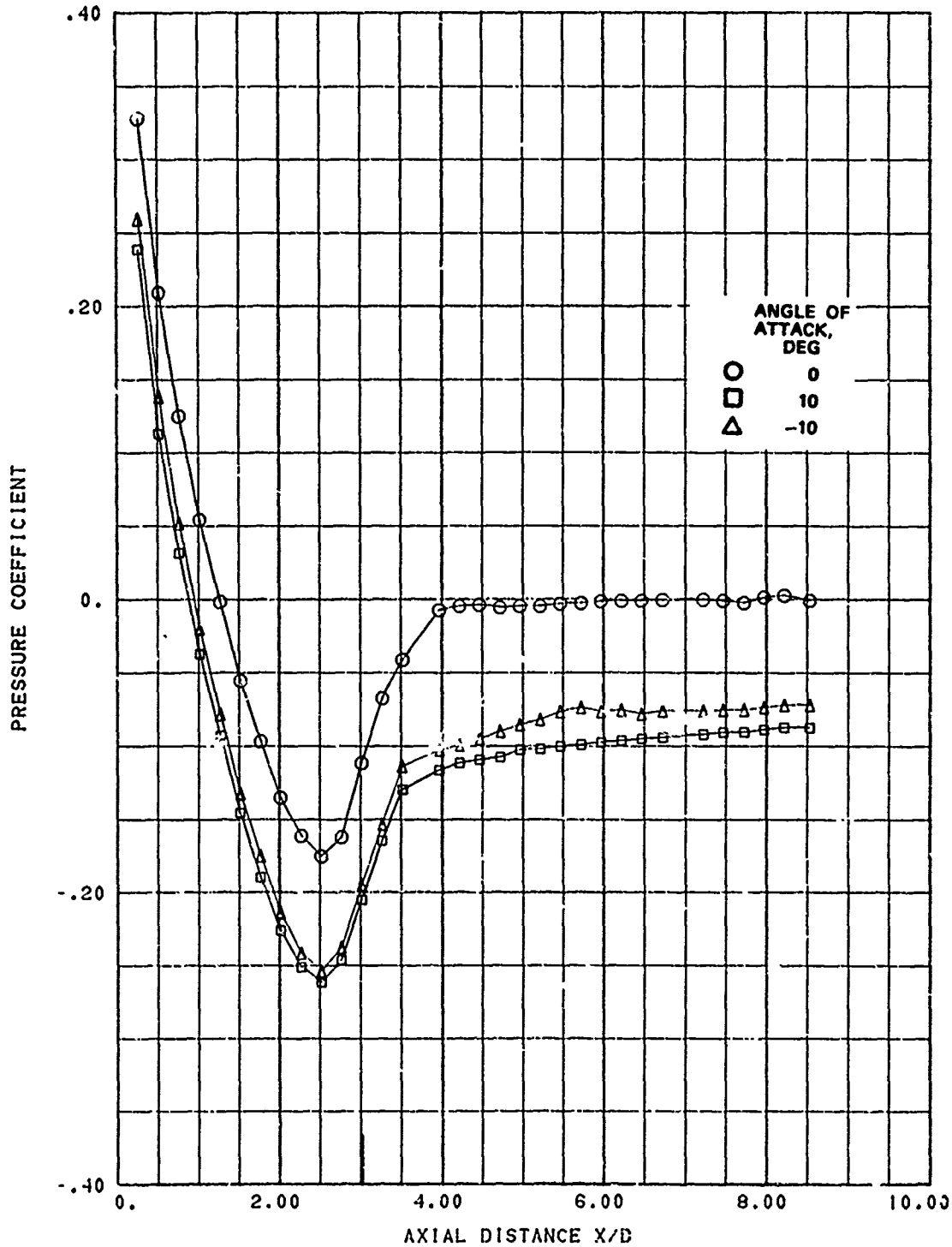

FIG. A-49. Longitudinal Pressure Distribution; Nose B, Mach 0.9, Roll Angle 90 Degrees.

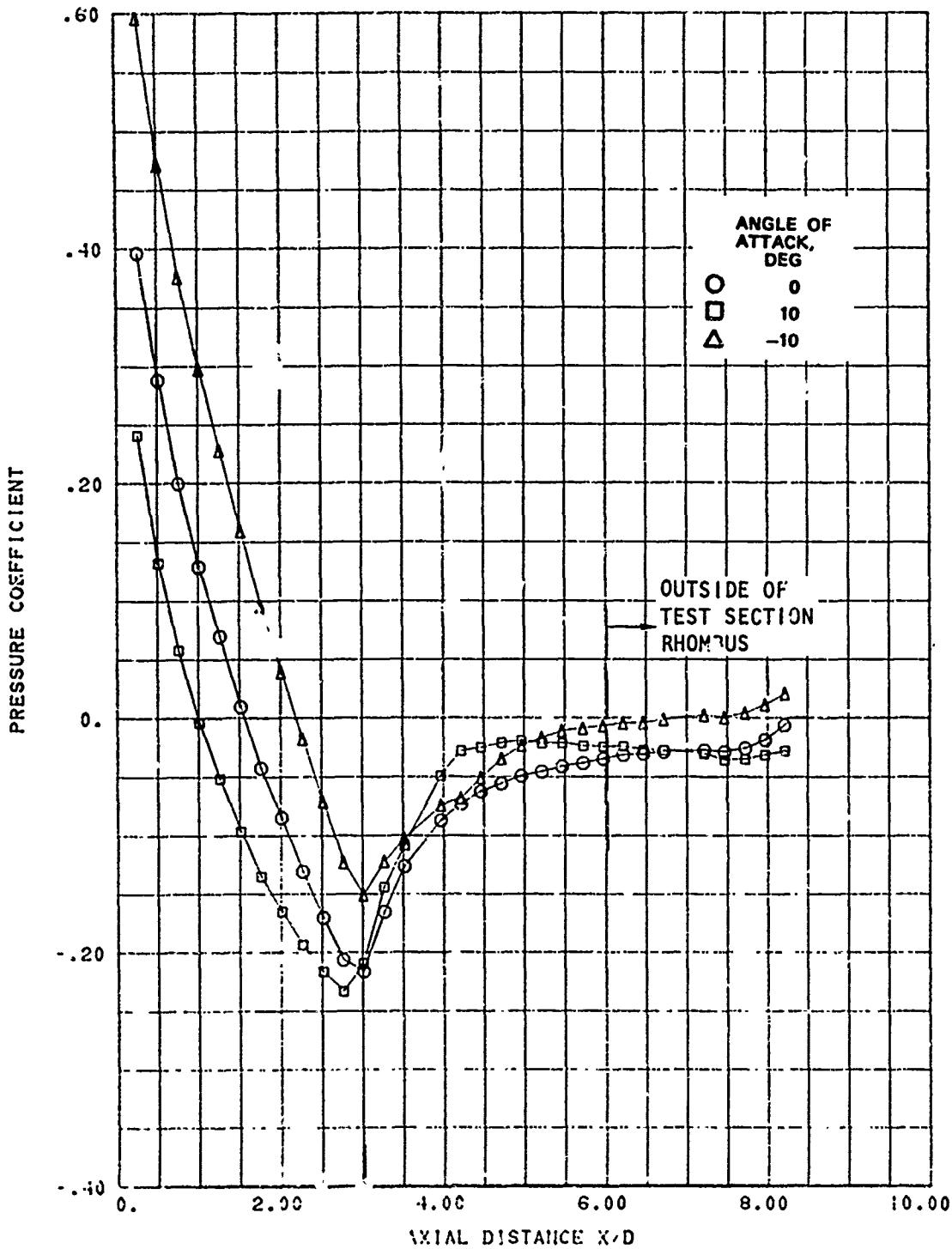

FIG. A-50. Longitudinal Pressure Distribution; Nose B, Mach 1.0, Roll Angle 0 Degrees.

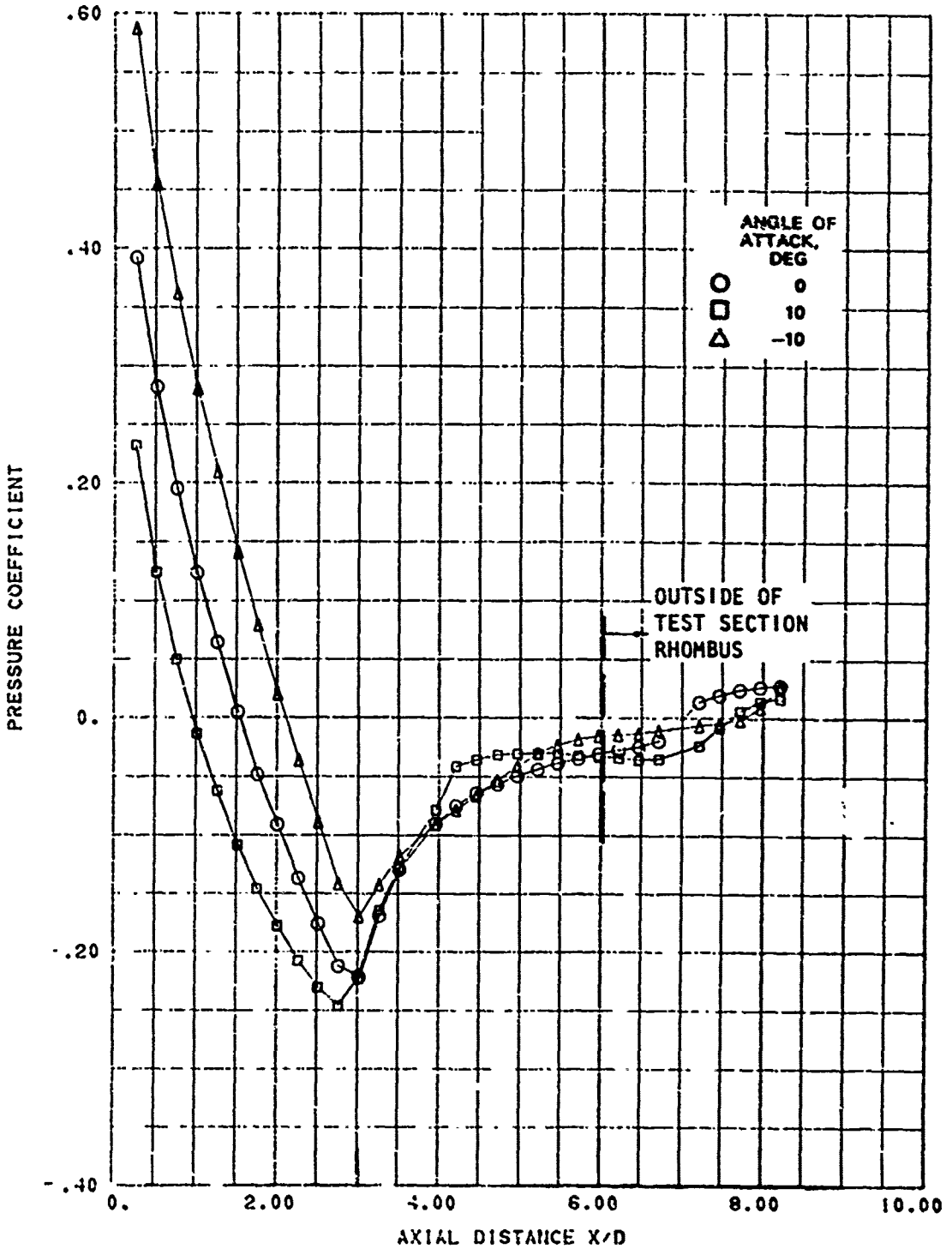

FIG. A-51. Longitudinal Pressure Distribution; Nose B, Mach 1.0, Roll Angle 15 Degrees.

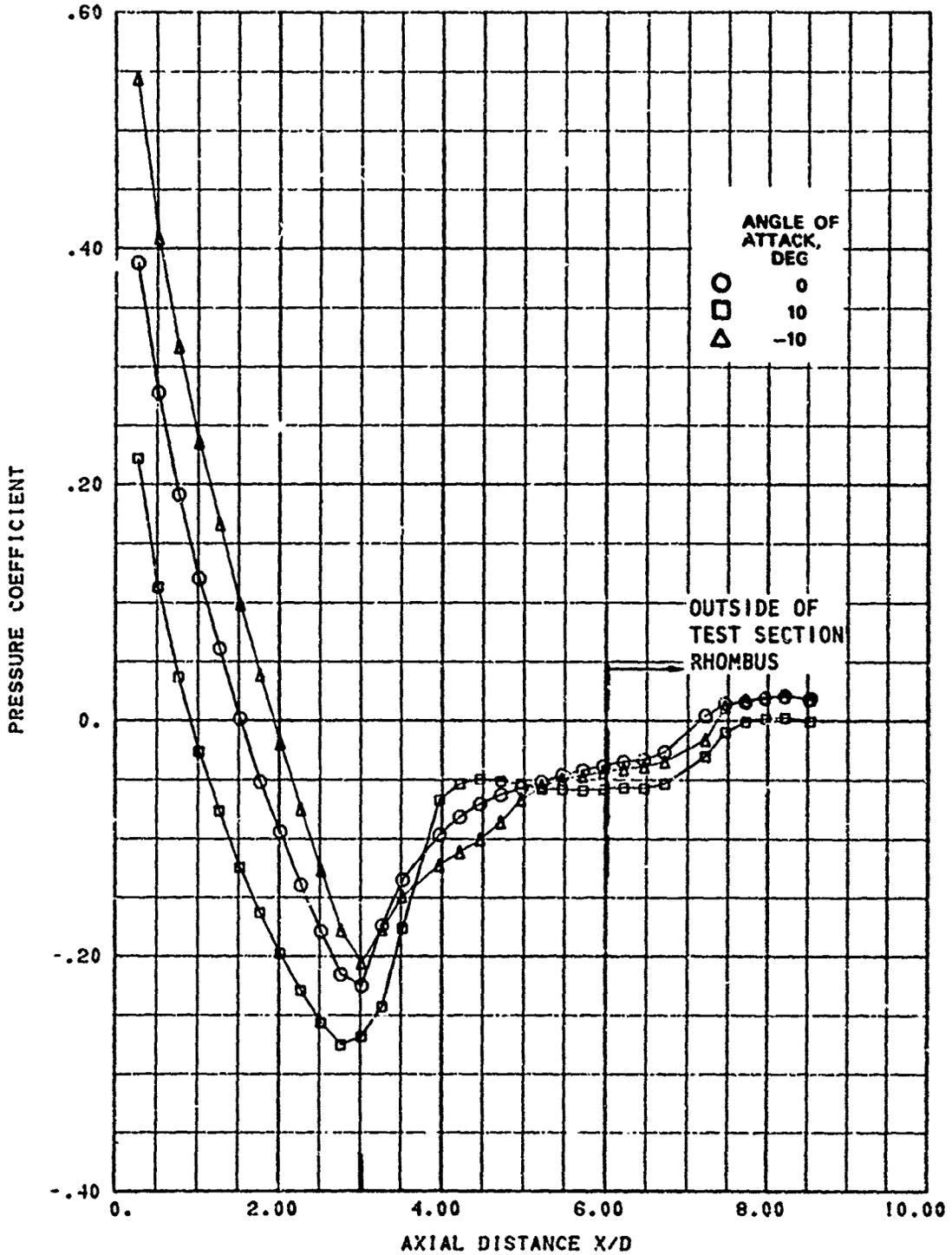

FIG. A-52. Longitudinal Pressure Distribution; Nose B, Mach 1.0, Roll Angle 30 Degrees.

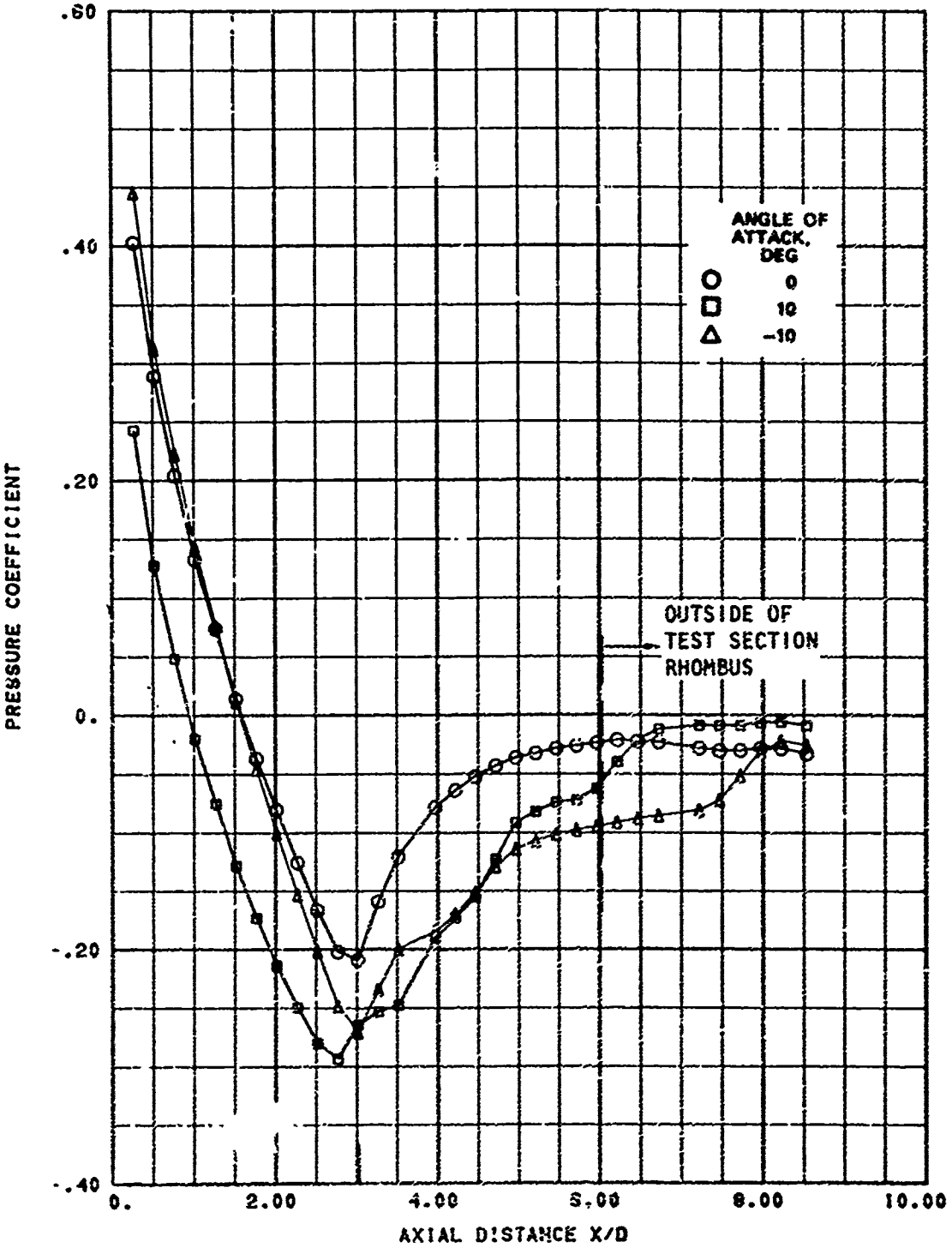

FIG. A-53. Longitudinal Pressure Distribution; Nose B, Mach 1.0, Roll Angle 60 Degrees.

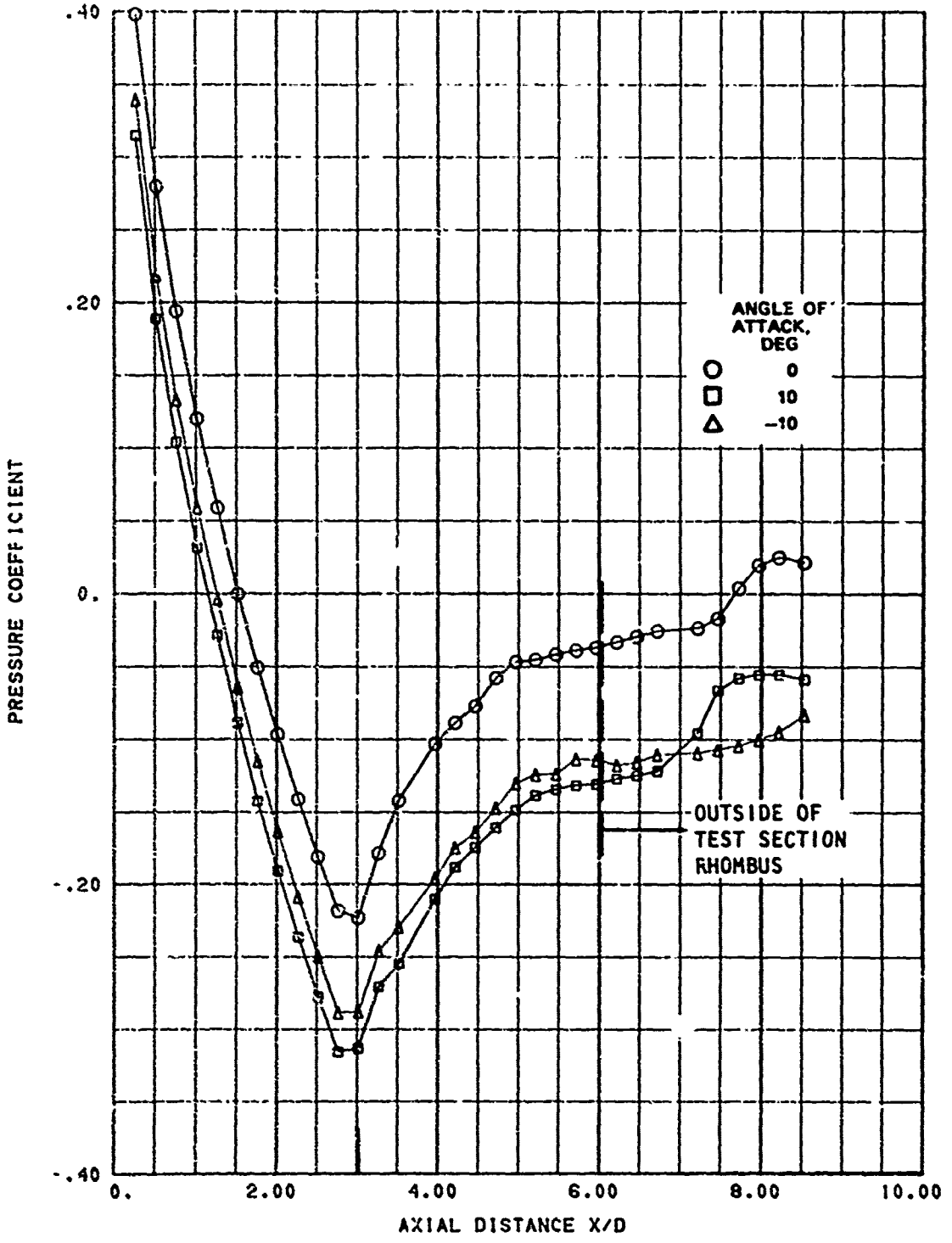

FIG. A-54. Longitudinal Pressure Distribution; Nose B, Mach 1.0, Roll Angle 90 Degrees.

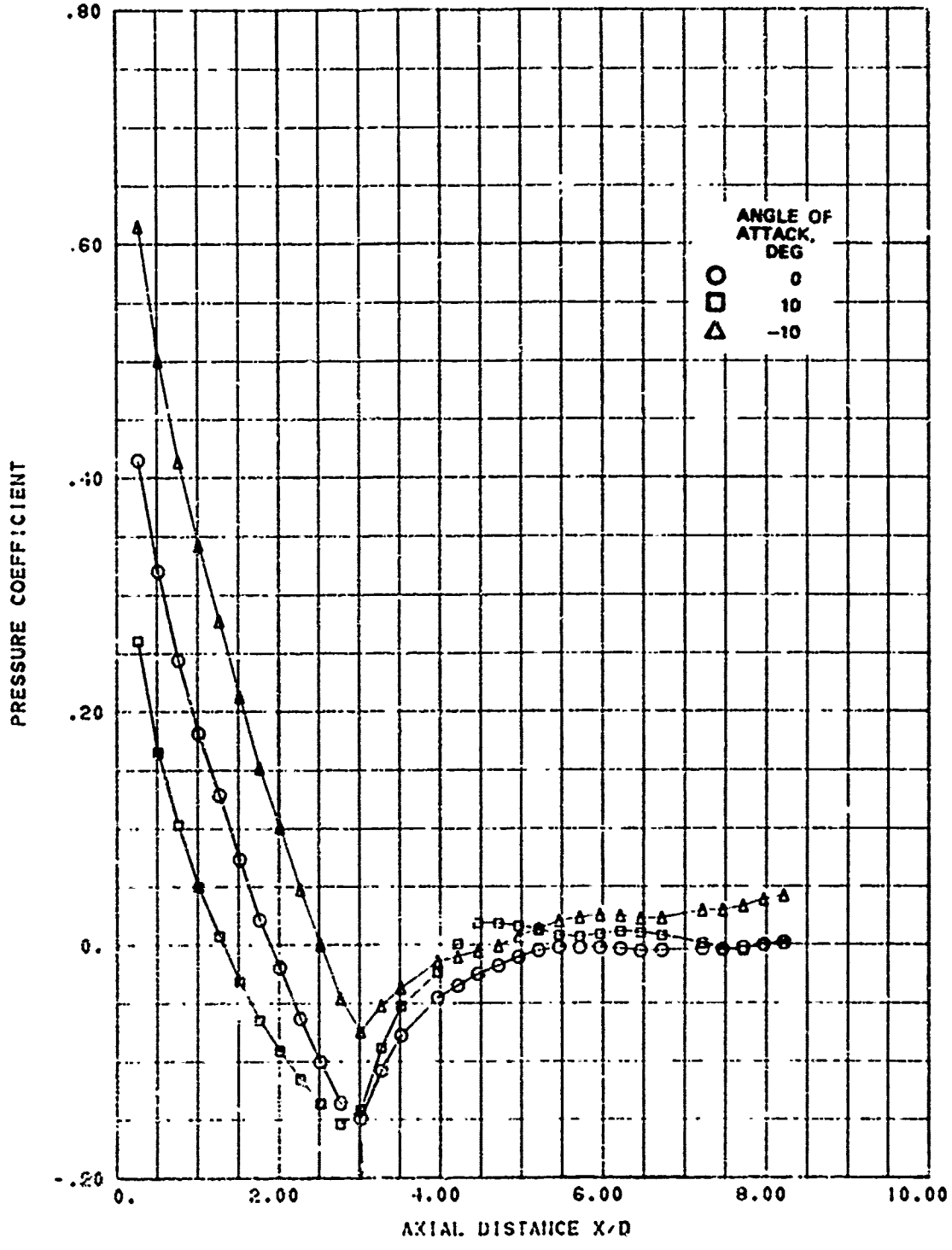

FIG. A-55. Longitudinal Pressure Distribution; Nose B, Mach 1.1, Roll Angle 0 Degrees.

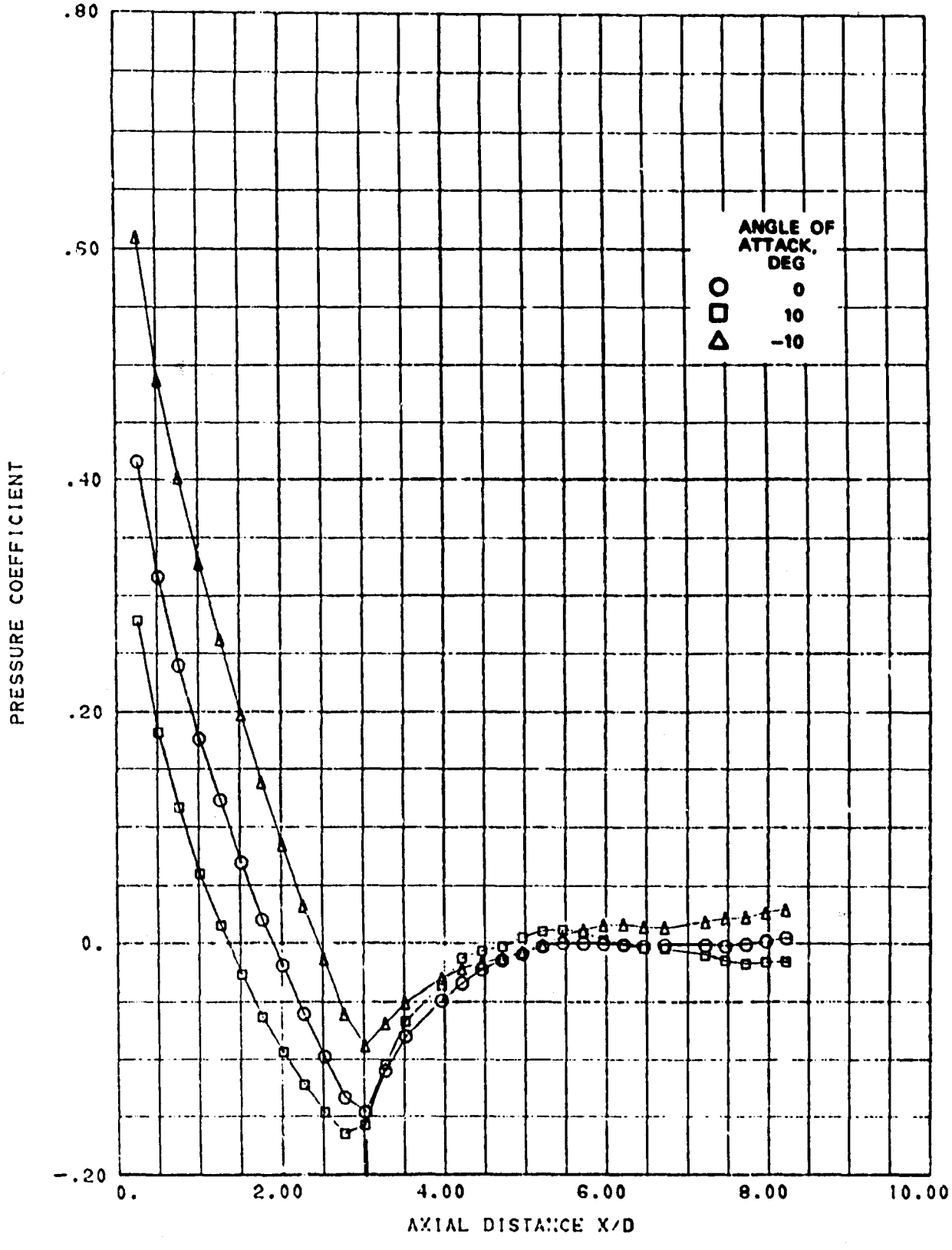

FIG. A-56. Longitudinal Pressure Distribution; Nose B, Mach 1.1, Roll Angle 15 Degrees.

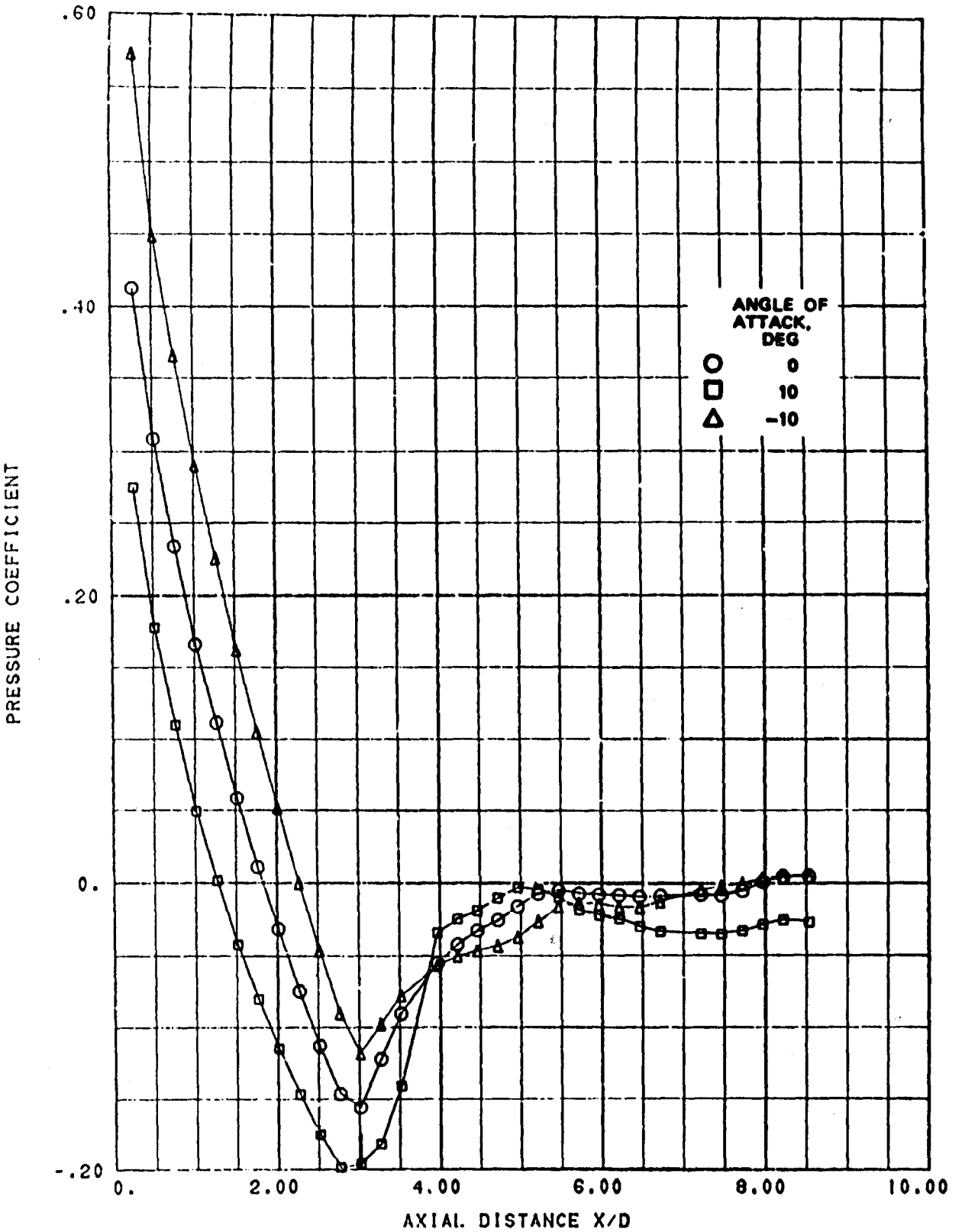

FIG. A-57. Longitudinal Pressure Distribution; Nose B, Mach 1.1, Roll Angle 30 Degrees.

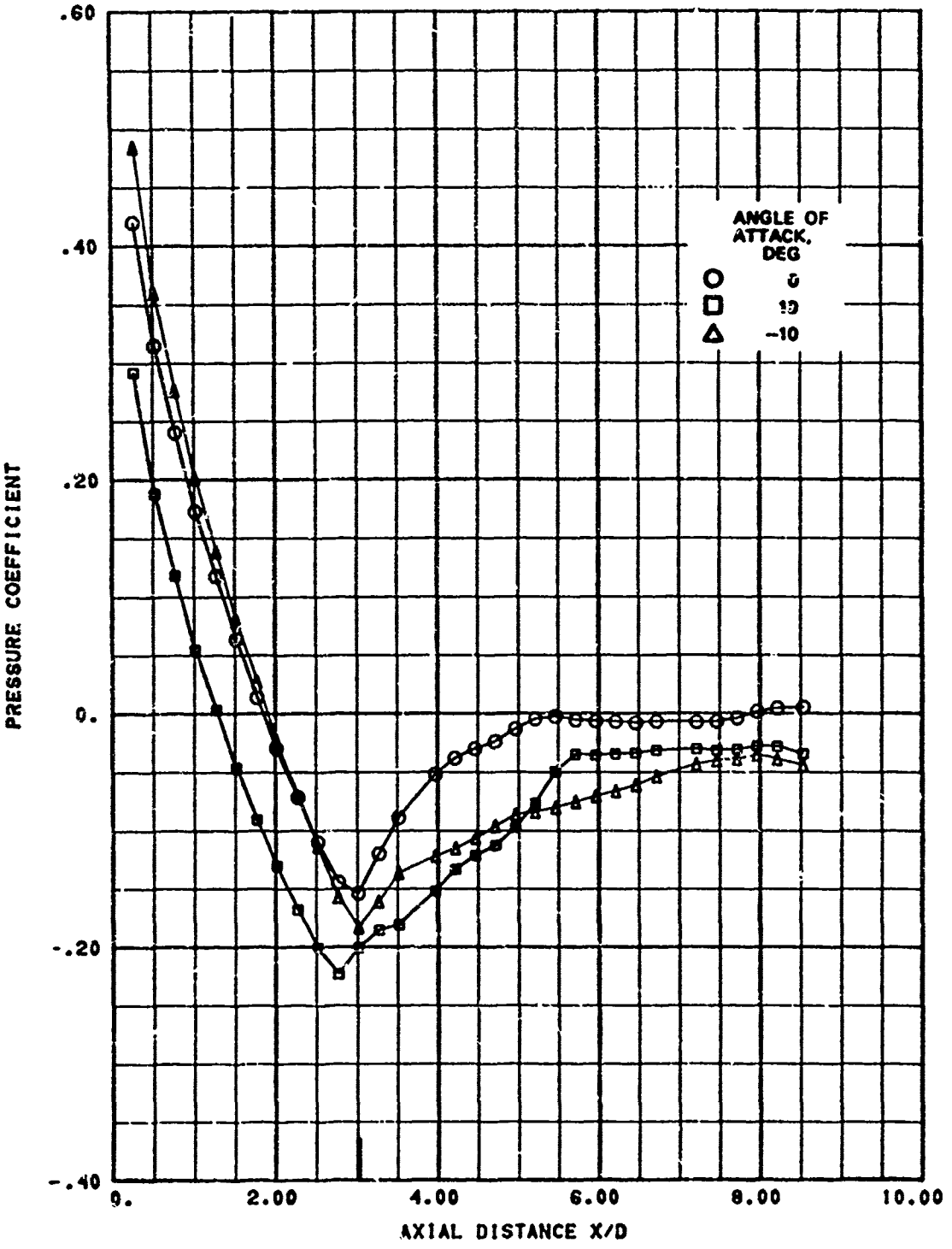

FIG. A-58. Longitudinal Pressure Distribution; Nose B, Mach 1.1, Roll Angle 60 Degrees.

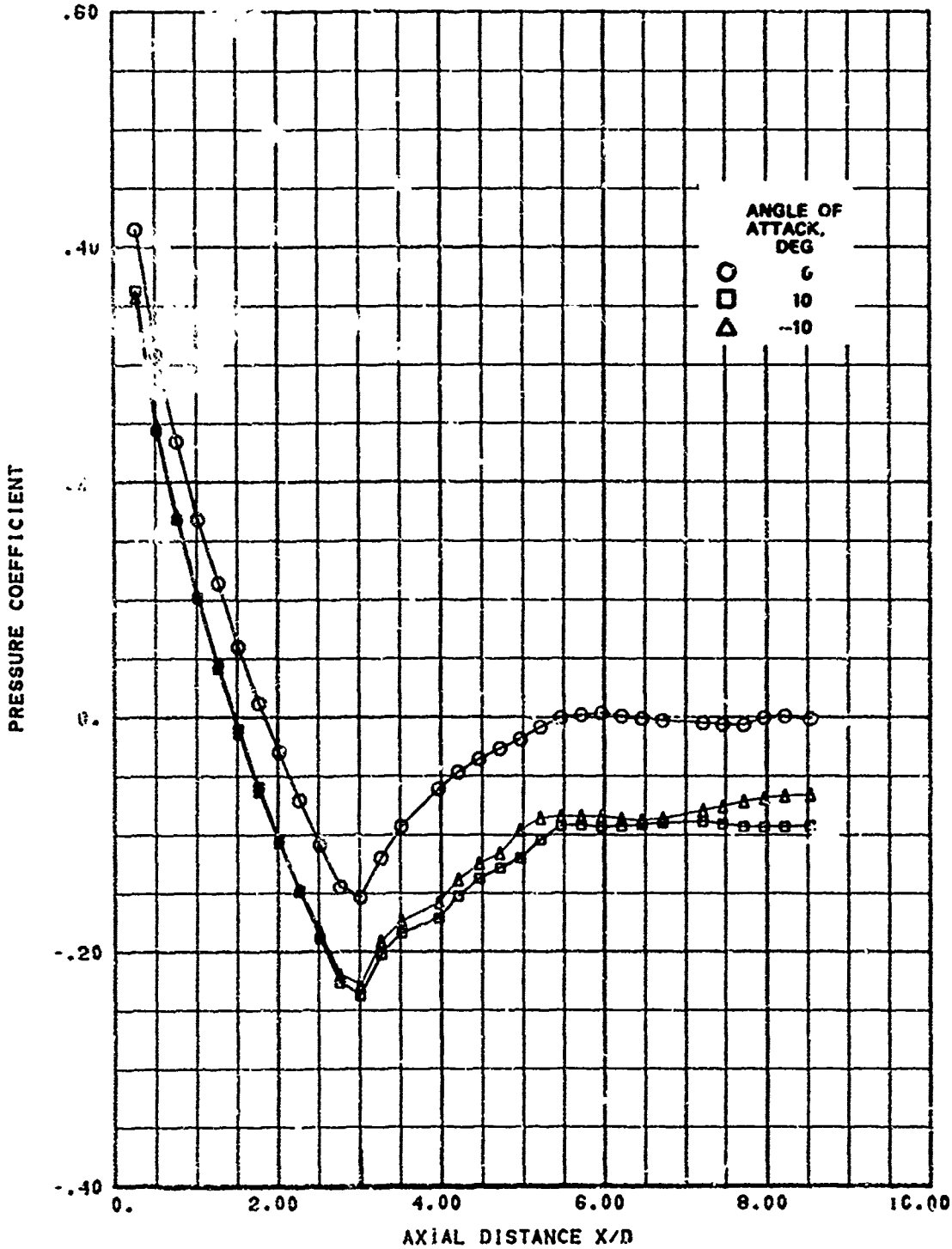

FIG. A-59. Longitudinal Pressure Distribution; Nose B, Mach 1.1, Roll Angle 90 Degrees.

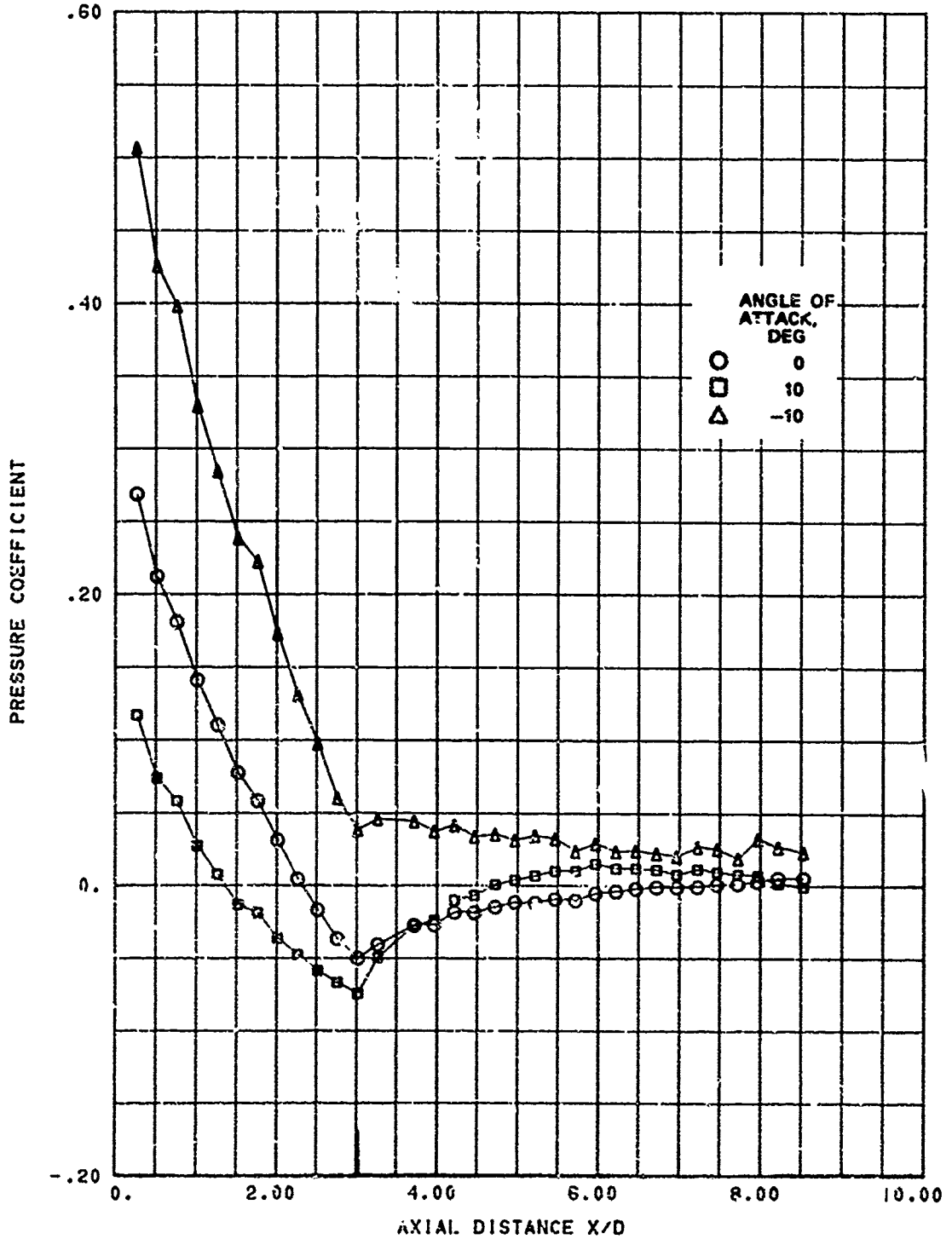

FIG. A-60. Longitudinal Pressure Distribution; Nose B, Mach 2.02, Roll Angle 0 Degrees.

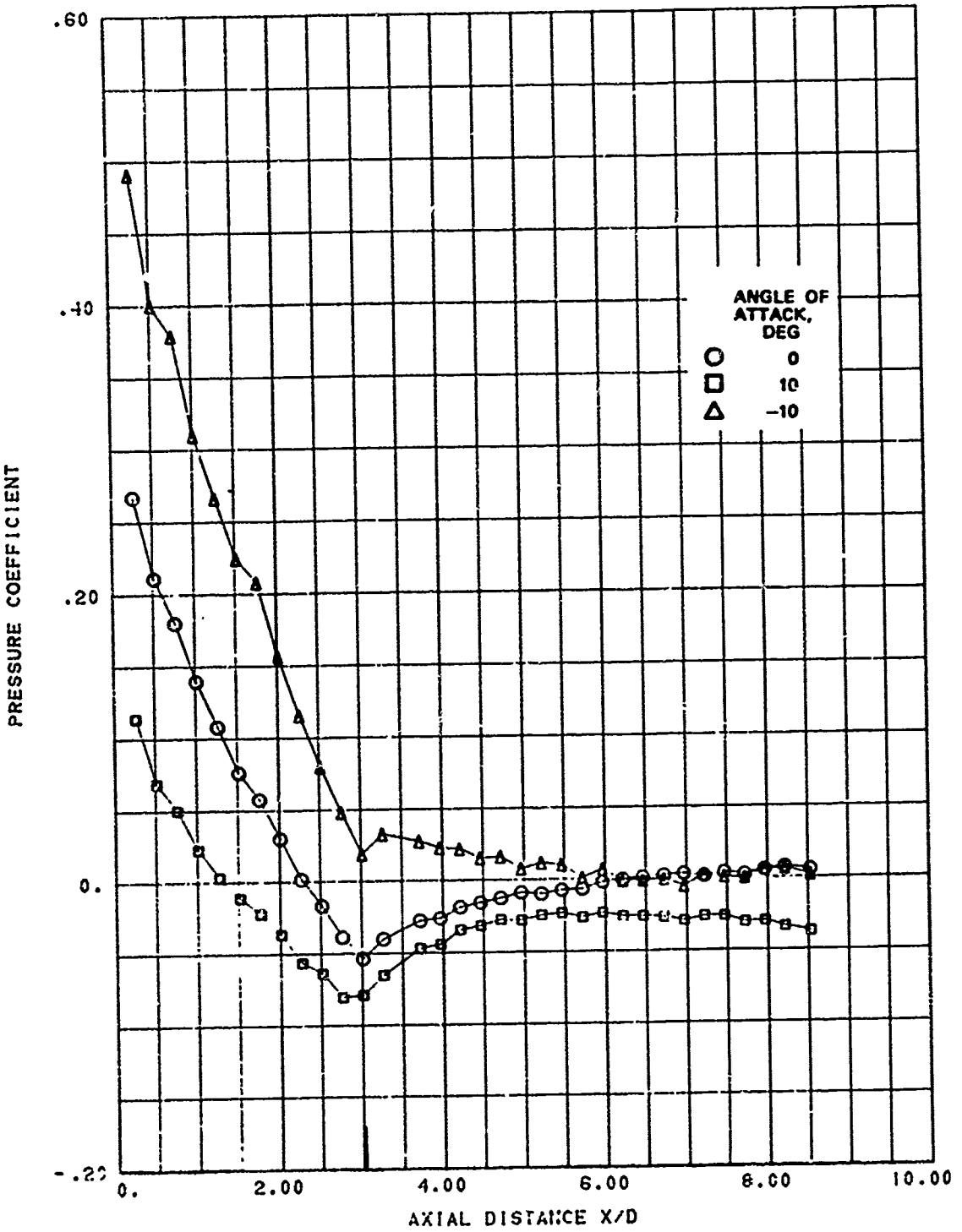

FIG. A-61. Longitudinal Pressure Distribution; Nose B, Mach 2.02, Roll Angle 15 Degrees.

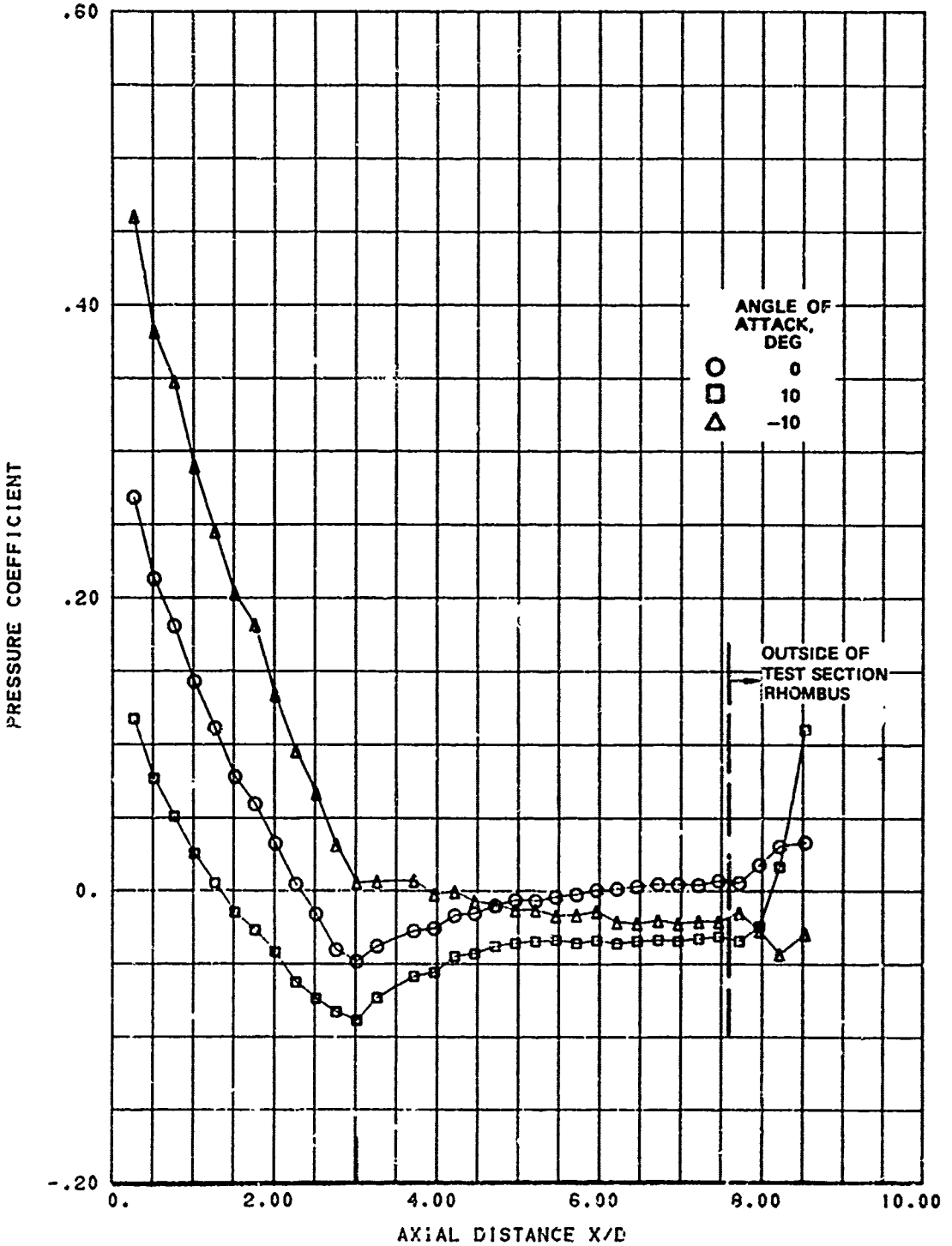

FIG. A-62. Longitudinal Pressure Distribution; Nose B, Mach 2.02, Roll Angle 30 Degrees.

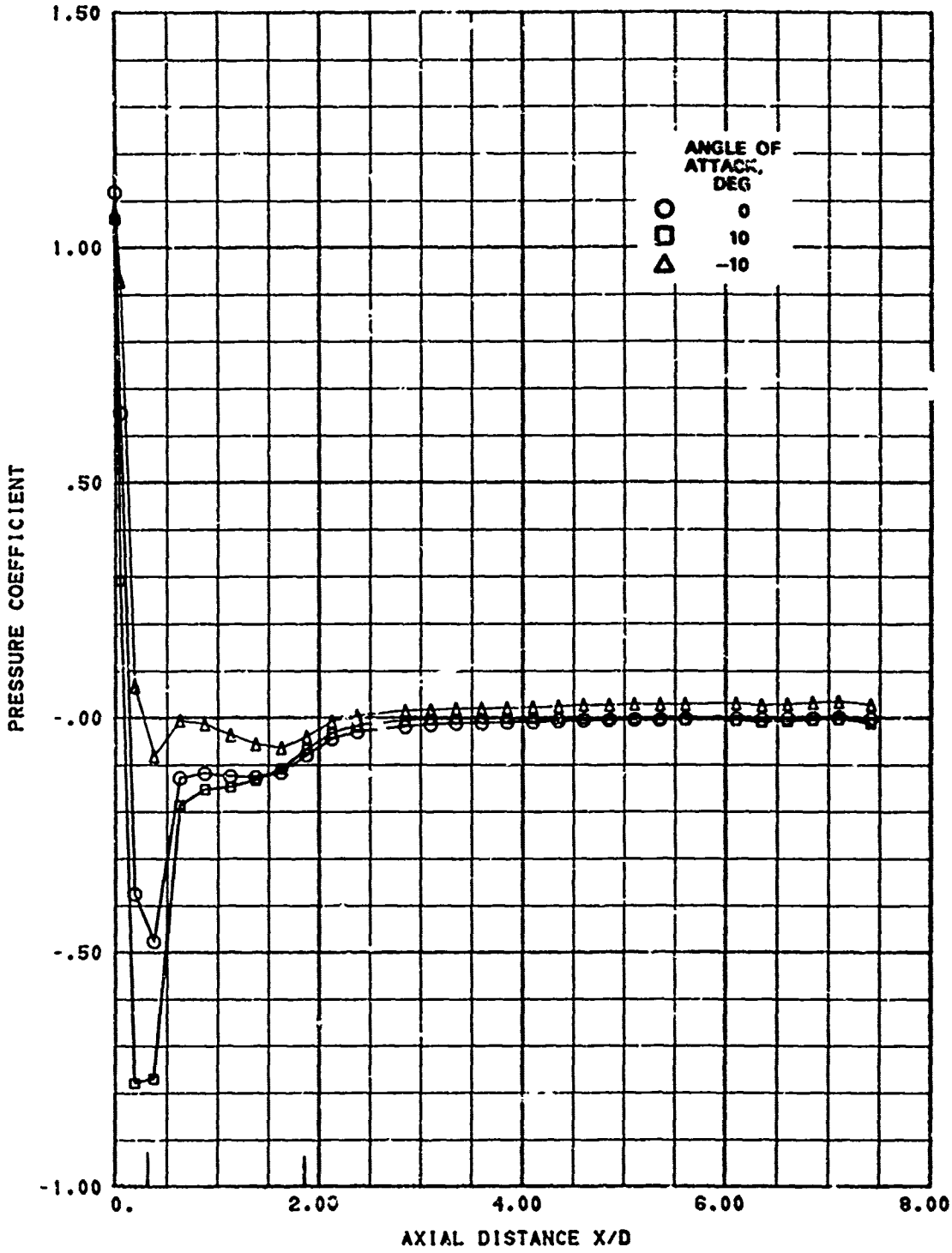

FIG. A-63. Longitudinal Pressure Distribution; Nose C, Mach 0.7, Roll Angle 0 Degrees.

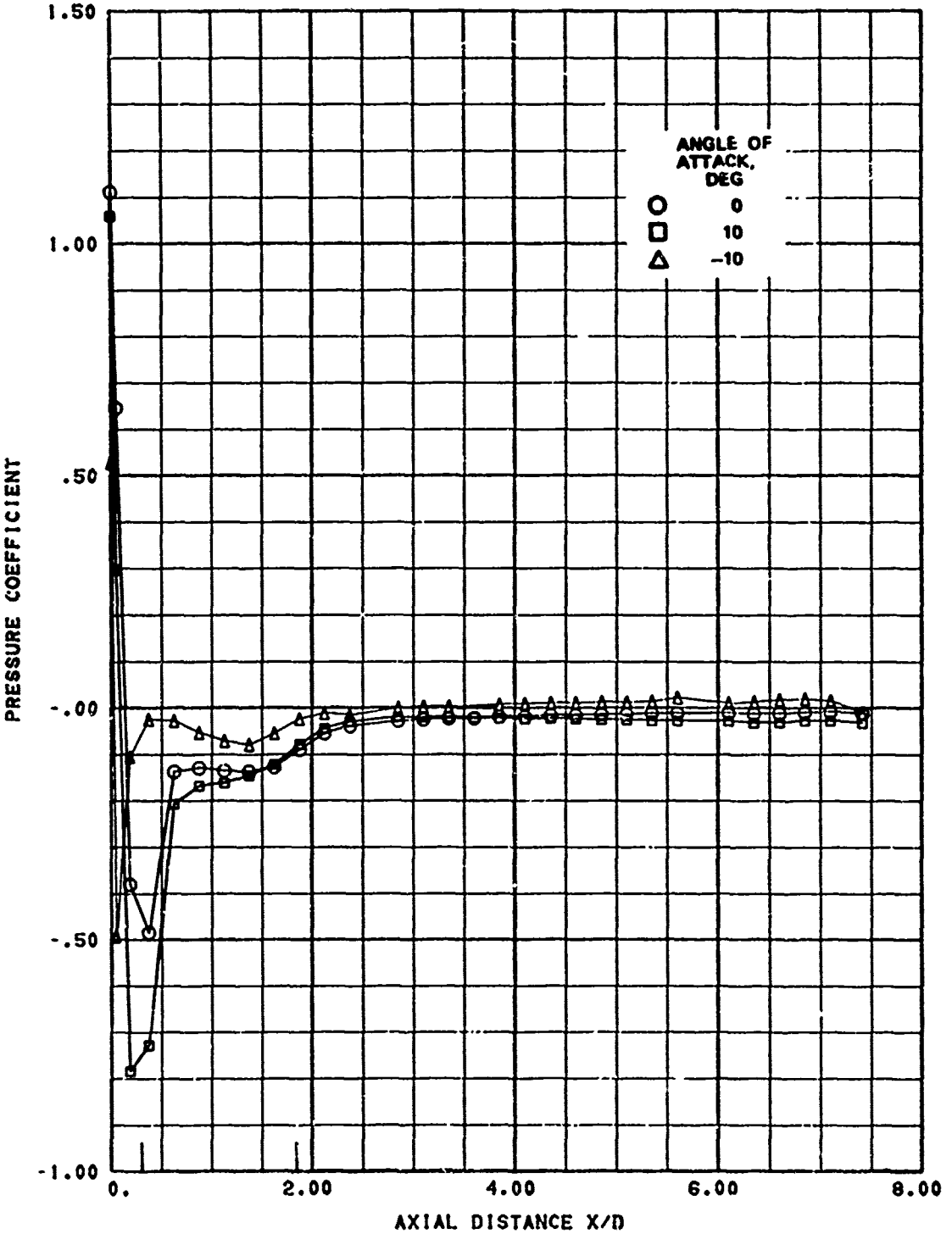

FIG. A-64. Longitudinal Pressure Distribution; Nose C, Mach 0.7, Roll Angle 15 Degrees.

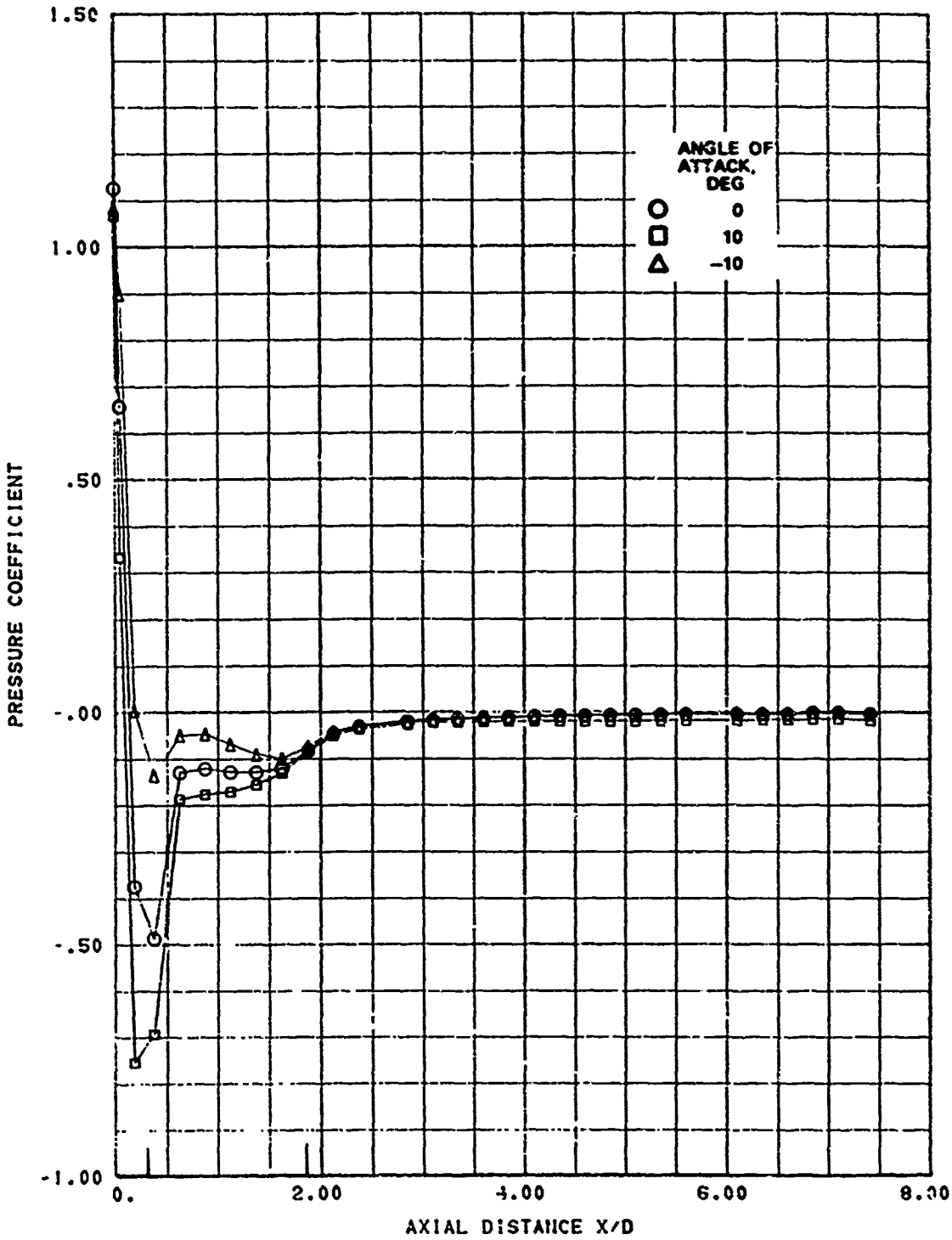

FIG. A-65. Longitudinal Pressure Distribution; Nose C, Mach 0.7, Roll Angle 30 Degrees.

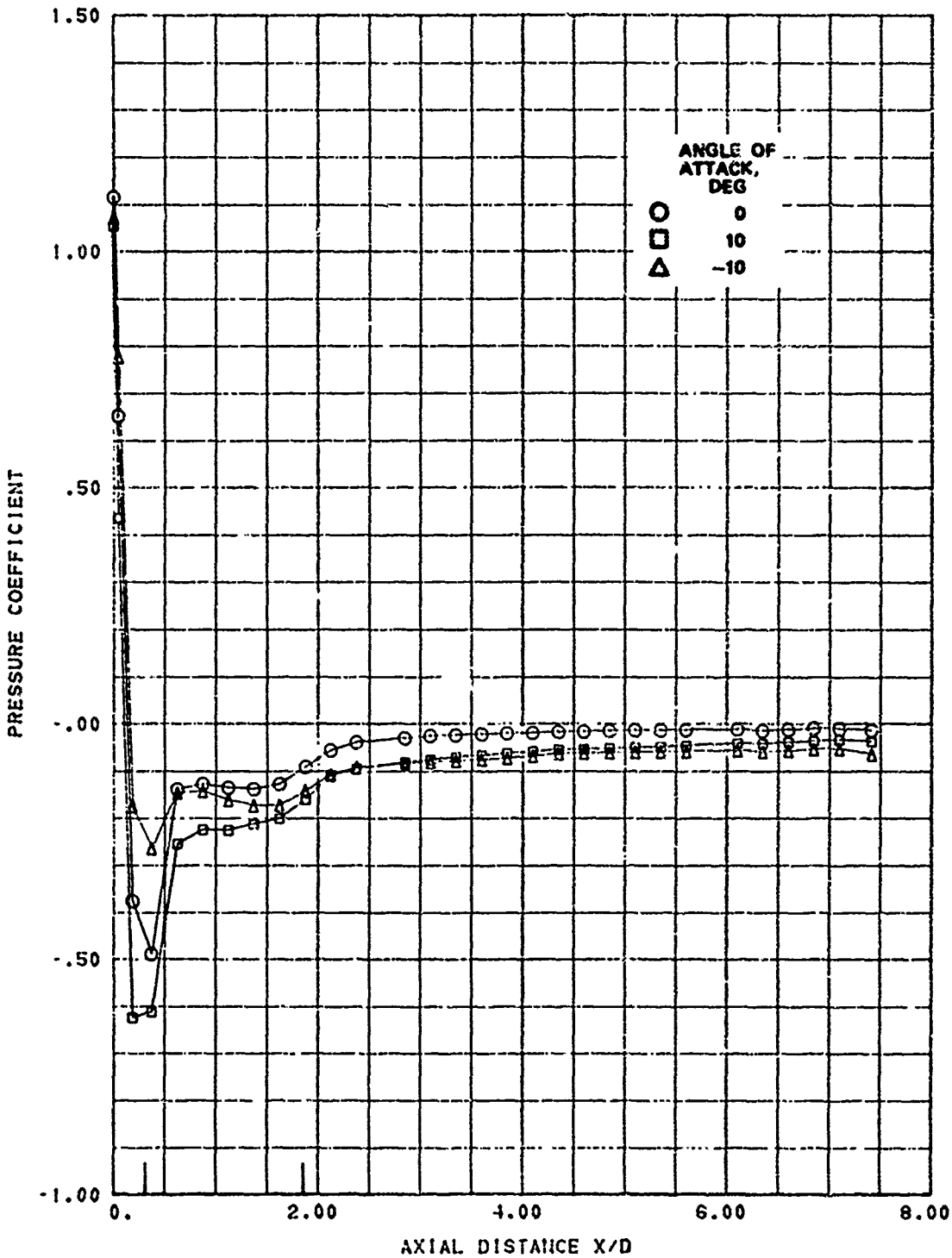

FIG. A-66. Longitudinal Pressure Distribution; Nose C, Mach 0.7, Roll Angle 60 Degrees.

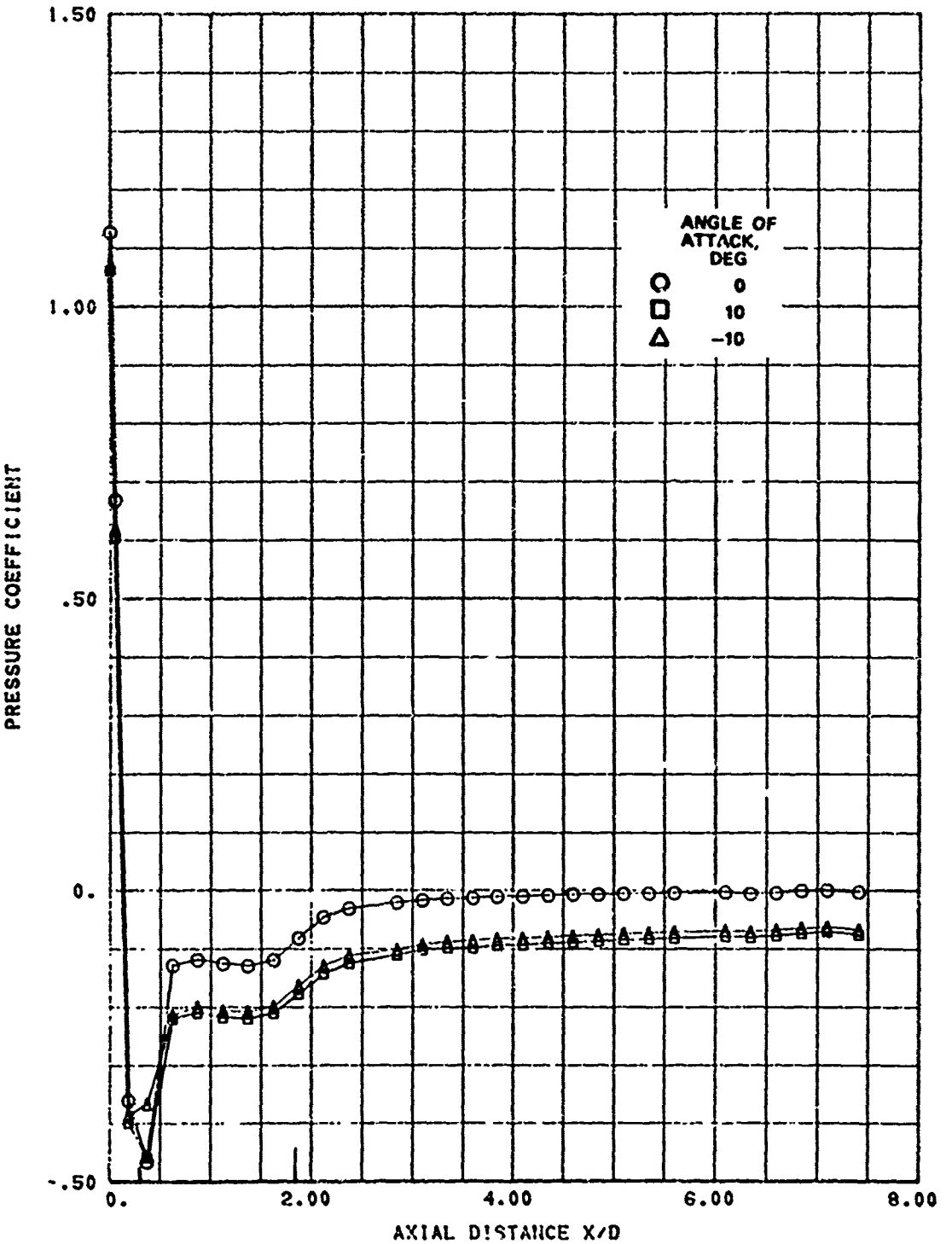

FIG. A-67. [illegible]nal Pressure Distribution; Nose C, Mach 0.7, Roll Angle 90 [illegible]

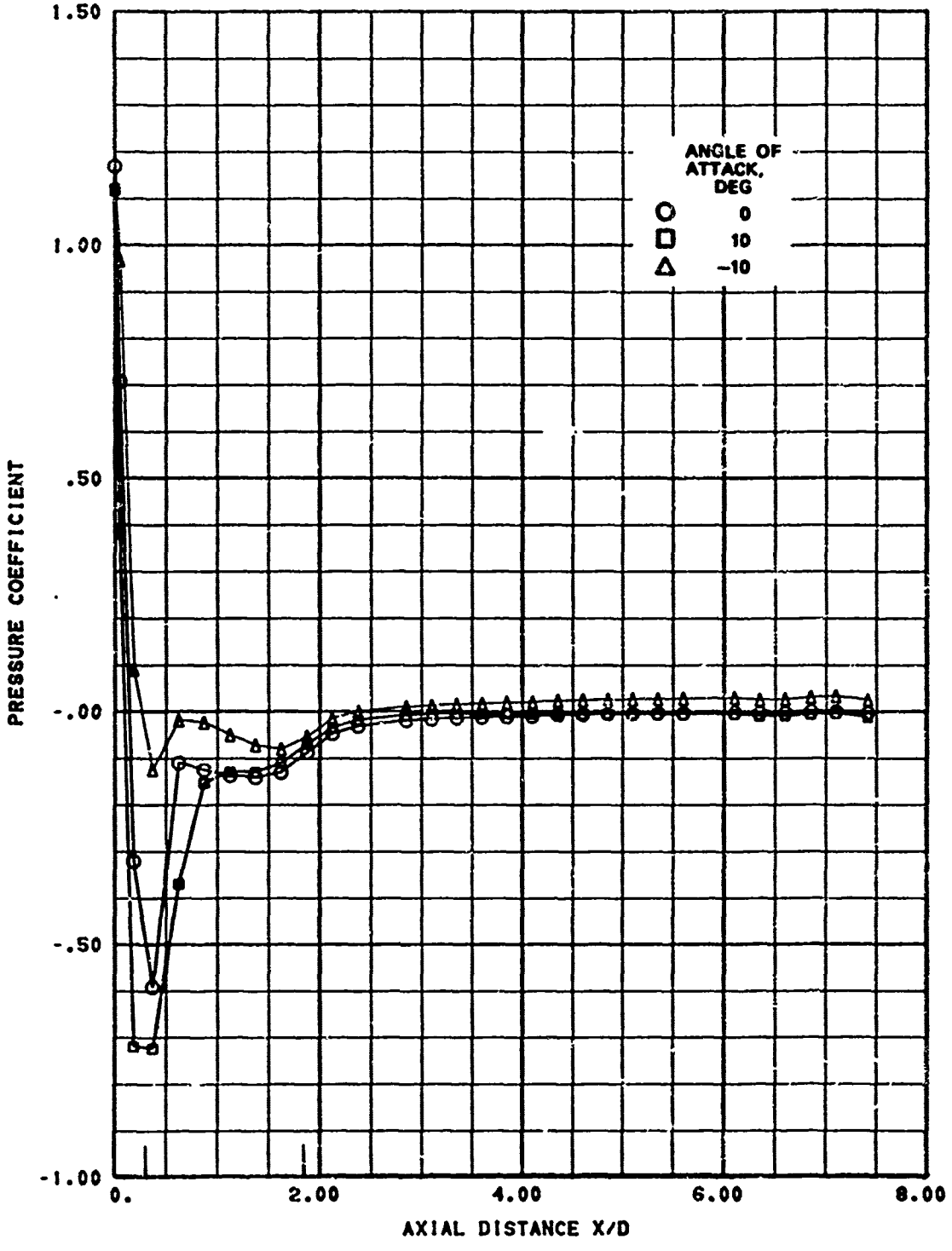

FIG. A-68. Longitudinal Pressure Distribution; Nose C, Mach 0.8, Roll Angle 0 Degrees.

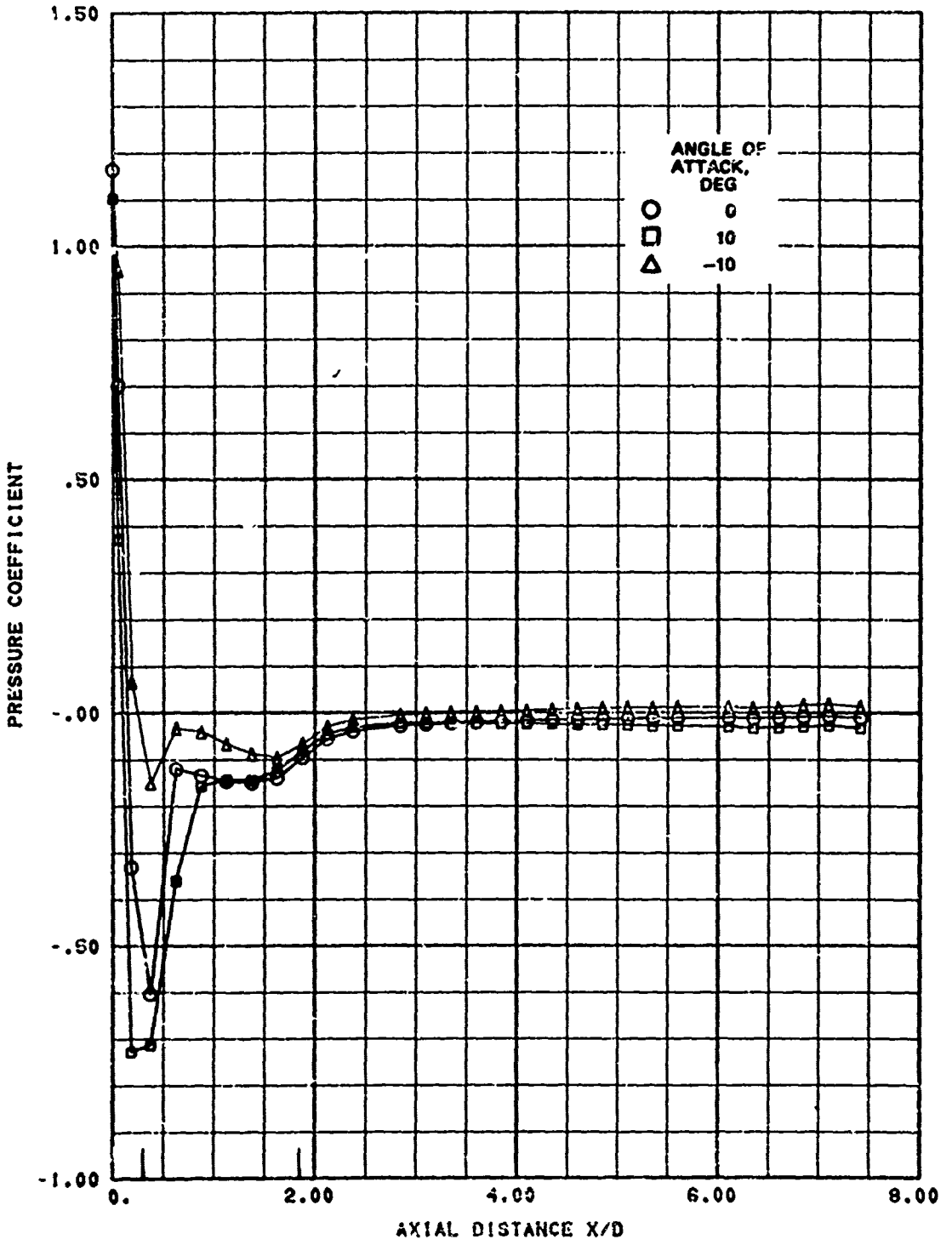

FIG. A-69. Longitudinal Pressure Distribution; Nose C, Mach 0.8, Roll Angle 15 Degrees.

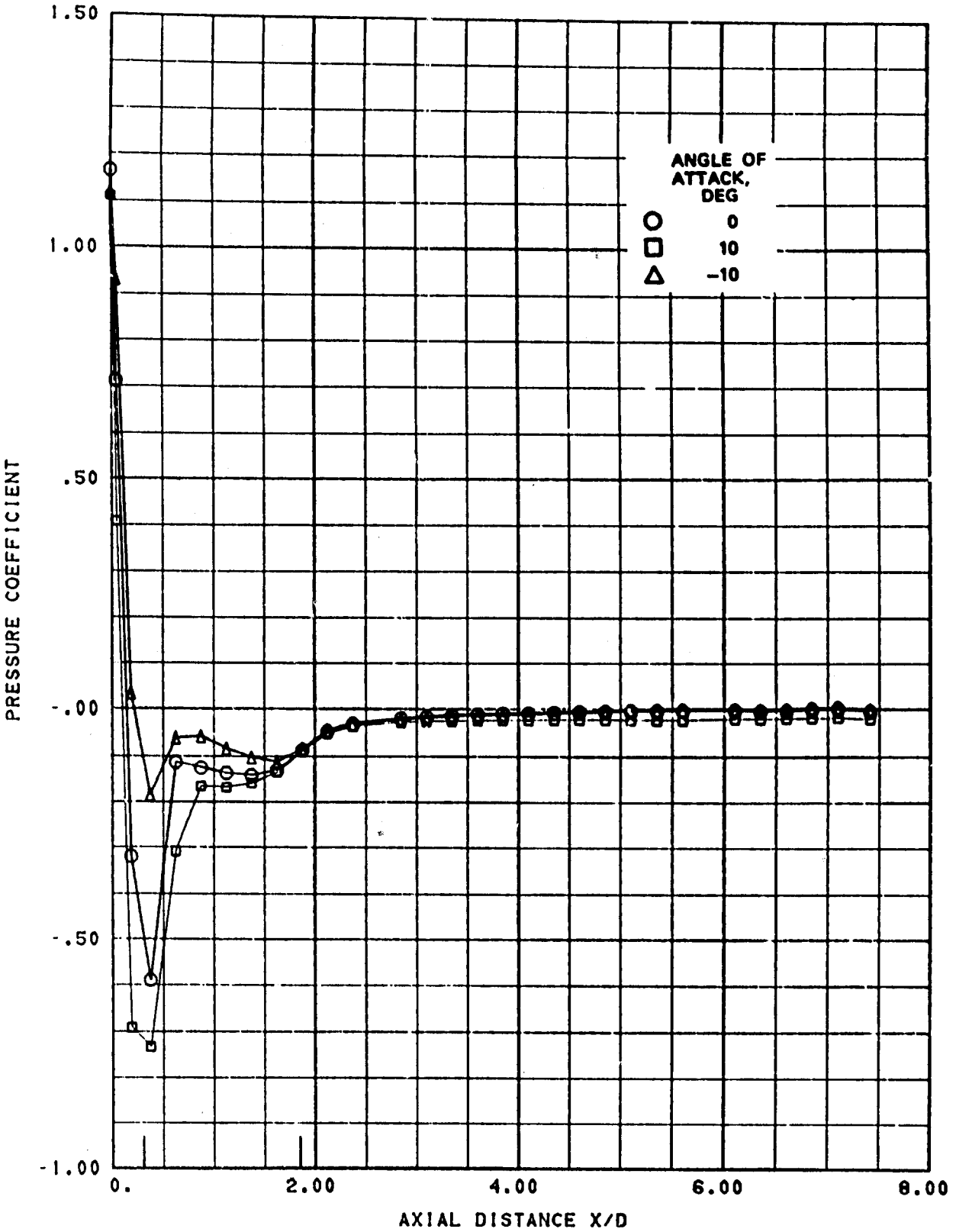

FIG. A-70. Longitudinal Pressure Distribution; Nose C, Mach 0.8, Roll Angle 30 Degrees.

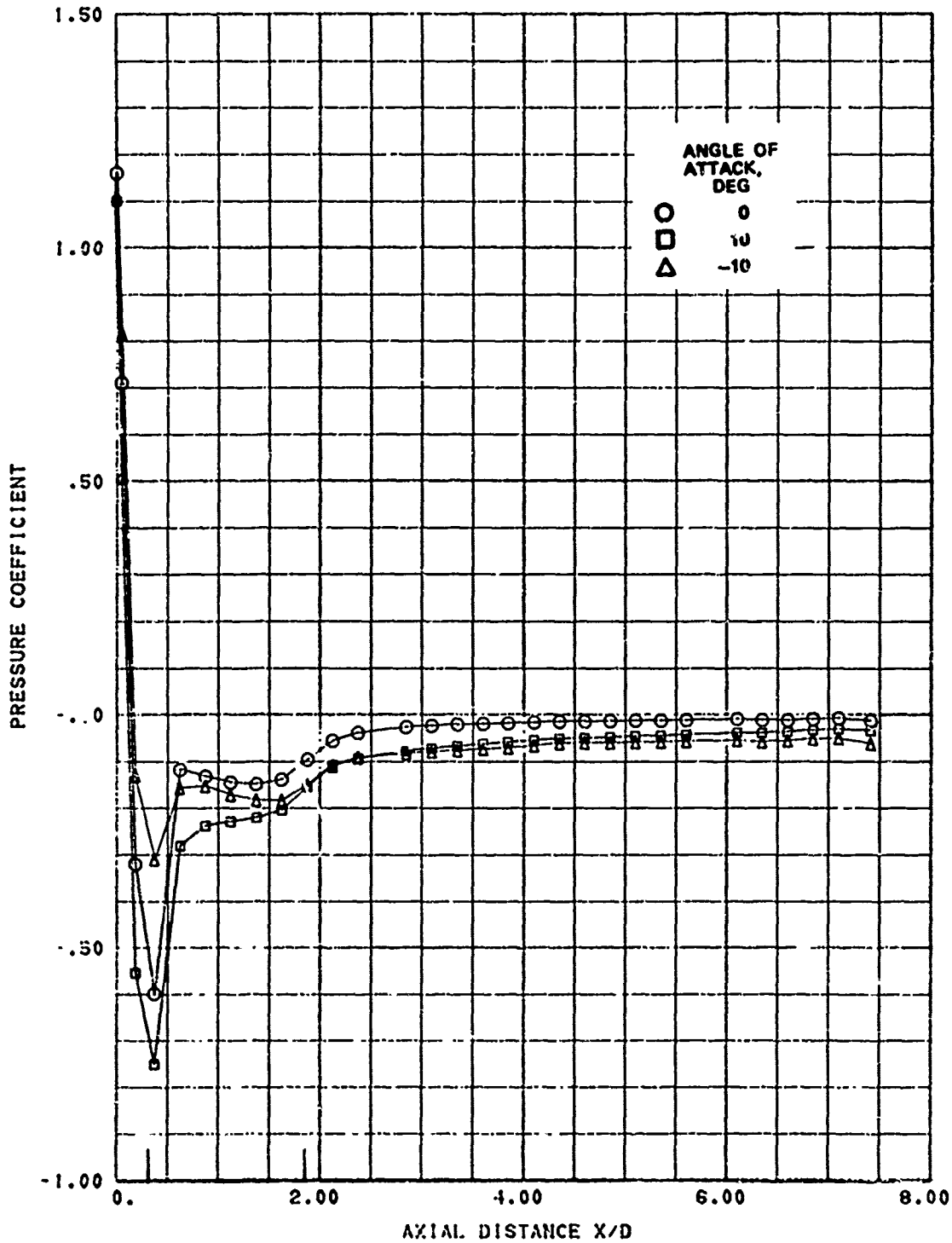

FIG. A-71. Longitudinal Pressure Distribution; Nose C, Mach 0.8, Roll Angle 60 Degrees.

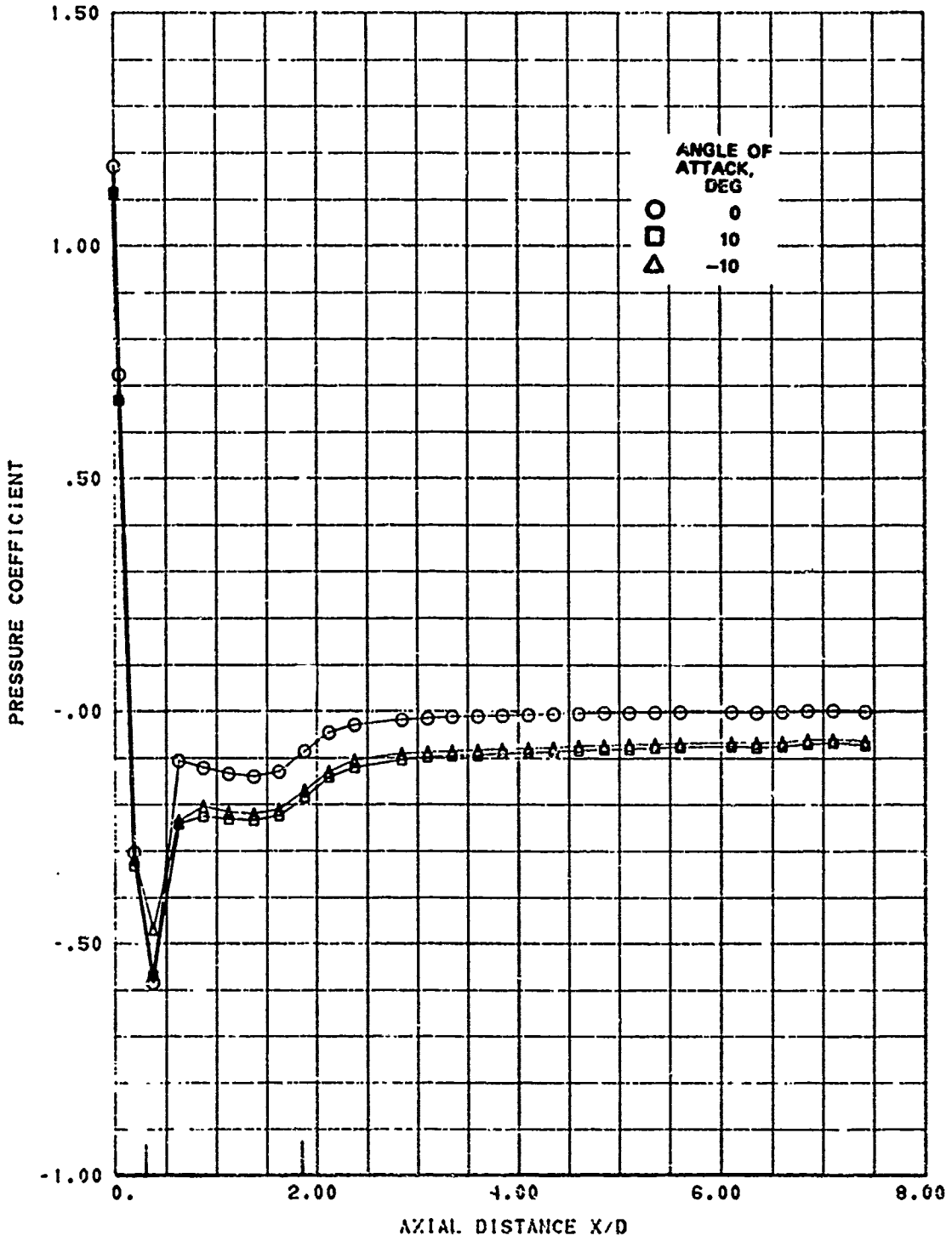

FIG. A-72. Longitudinal Pressure Distribution; Nose C, Mach 0.8, Roll Angle 90 Degrees.

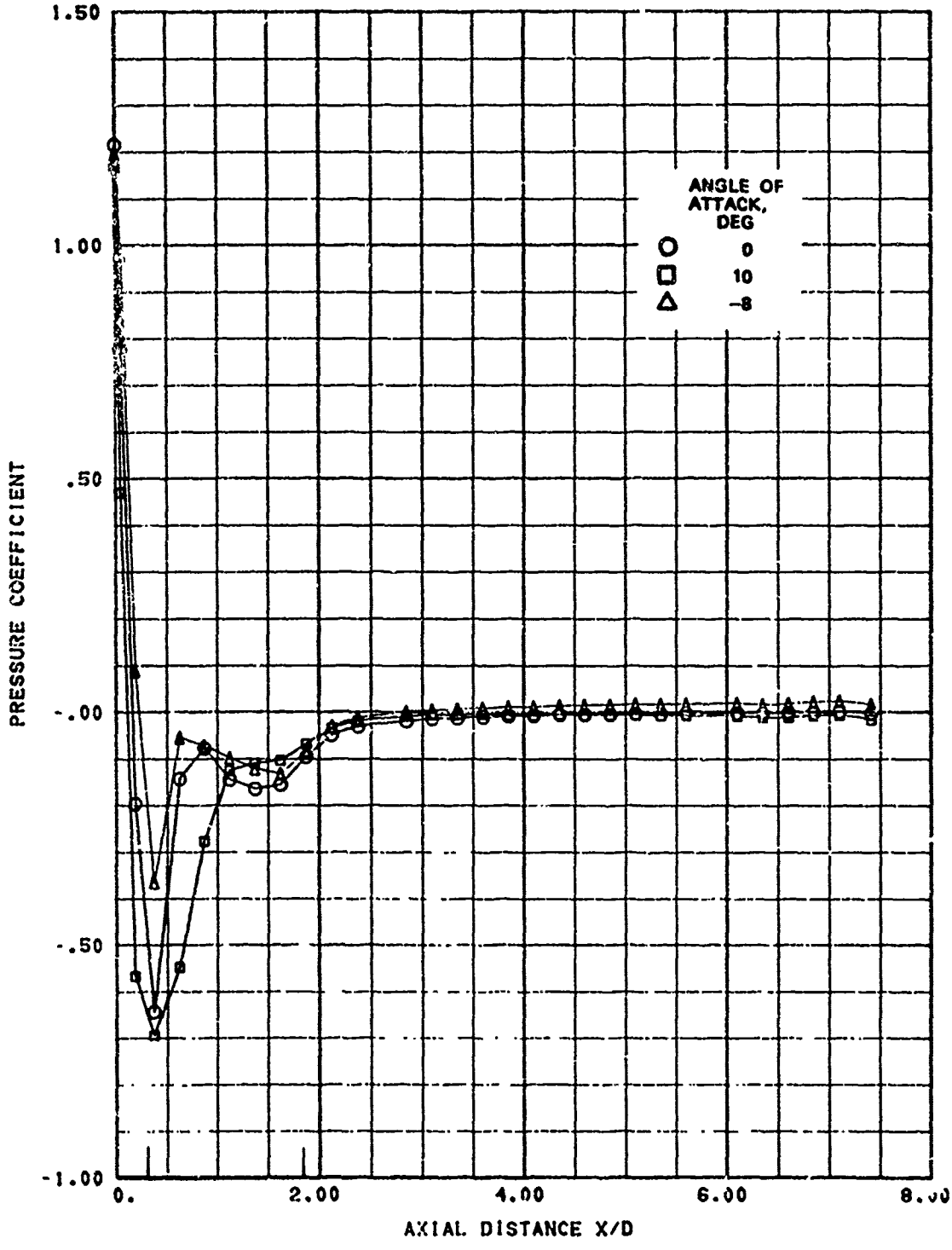

FIG. A-73. Longitudinal Pressure Distribution; Nose C, Mach 0.9, Roll Angle 0 Degrees.

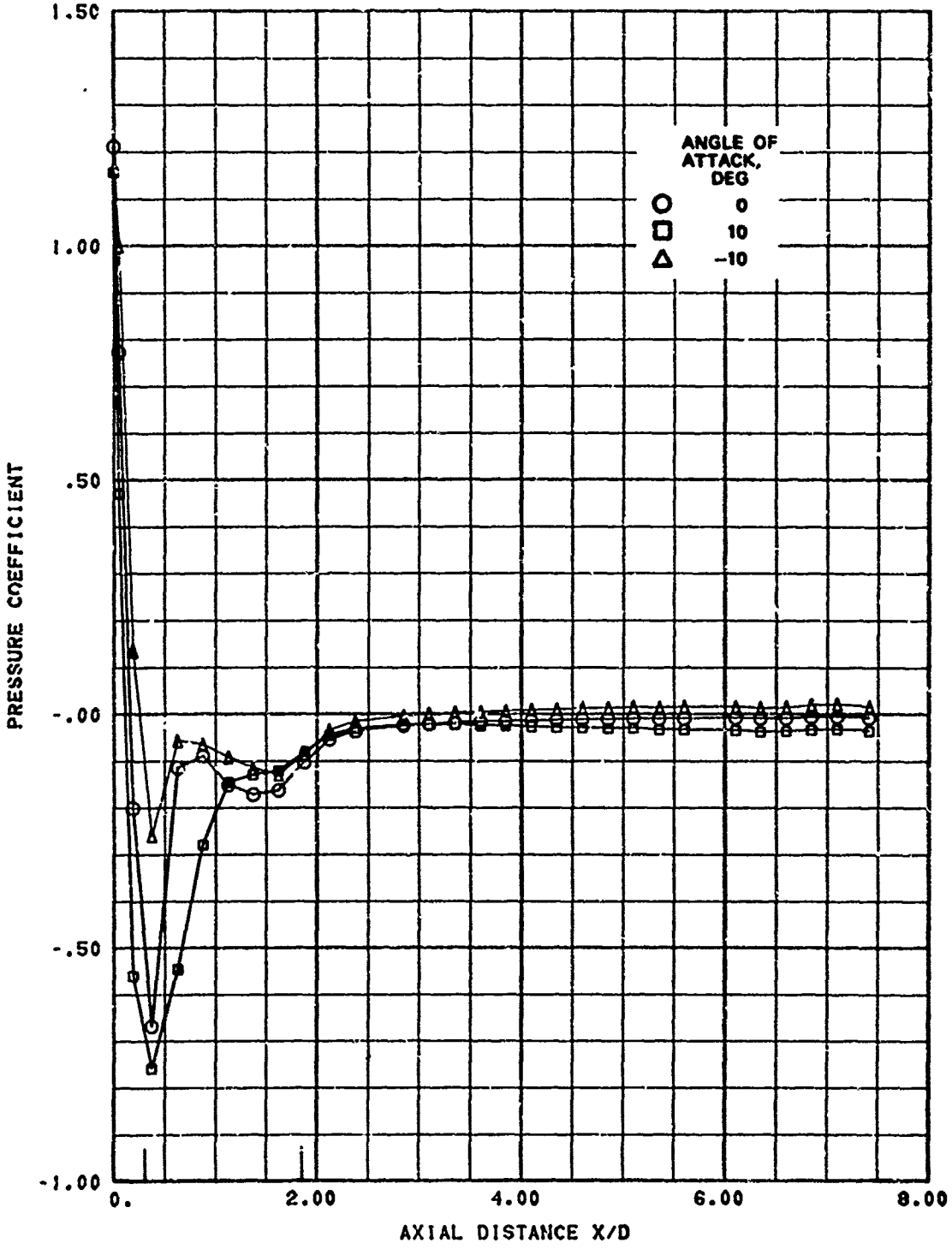

FIG. A-74. Longitudinal Pressure Distribution; Nose C, Mach 0.9, Roll Angle 15 Degrees.

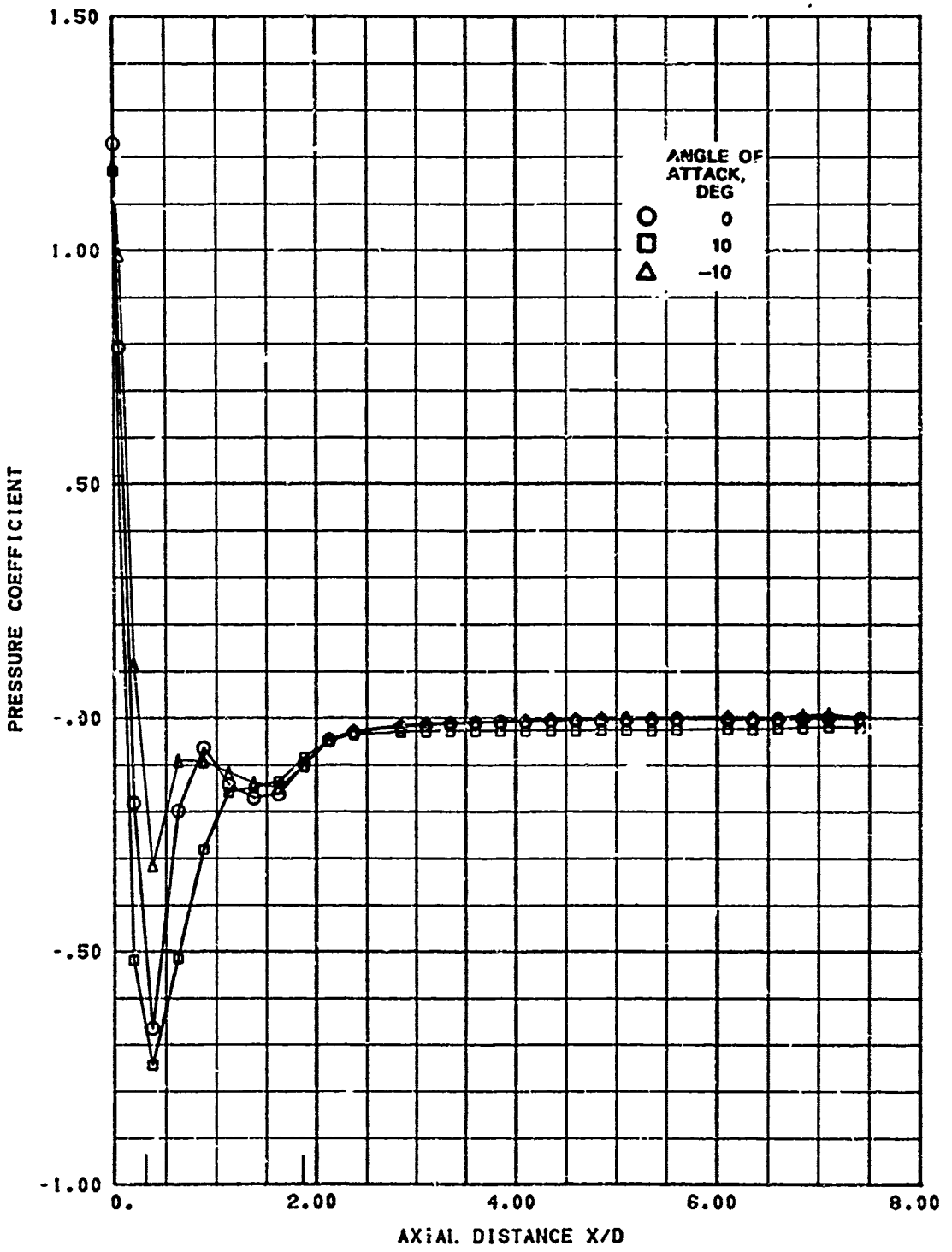

FIG. A-75. Longitudinal Pressure Distribution; Nose C, Mach 0.9, Roll Angle 30 Degrees.

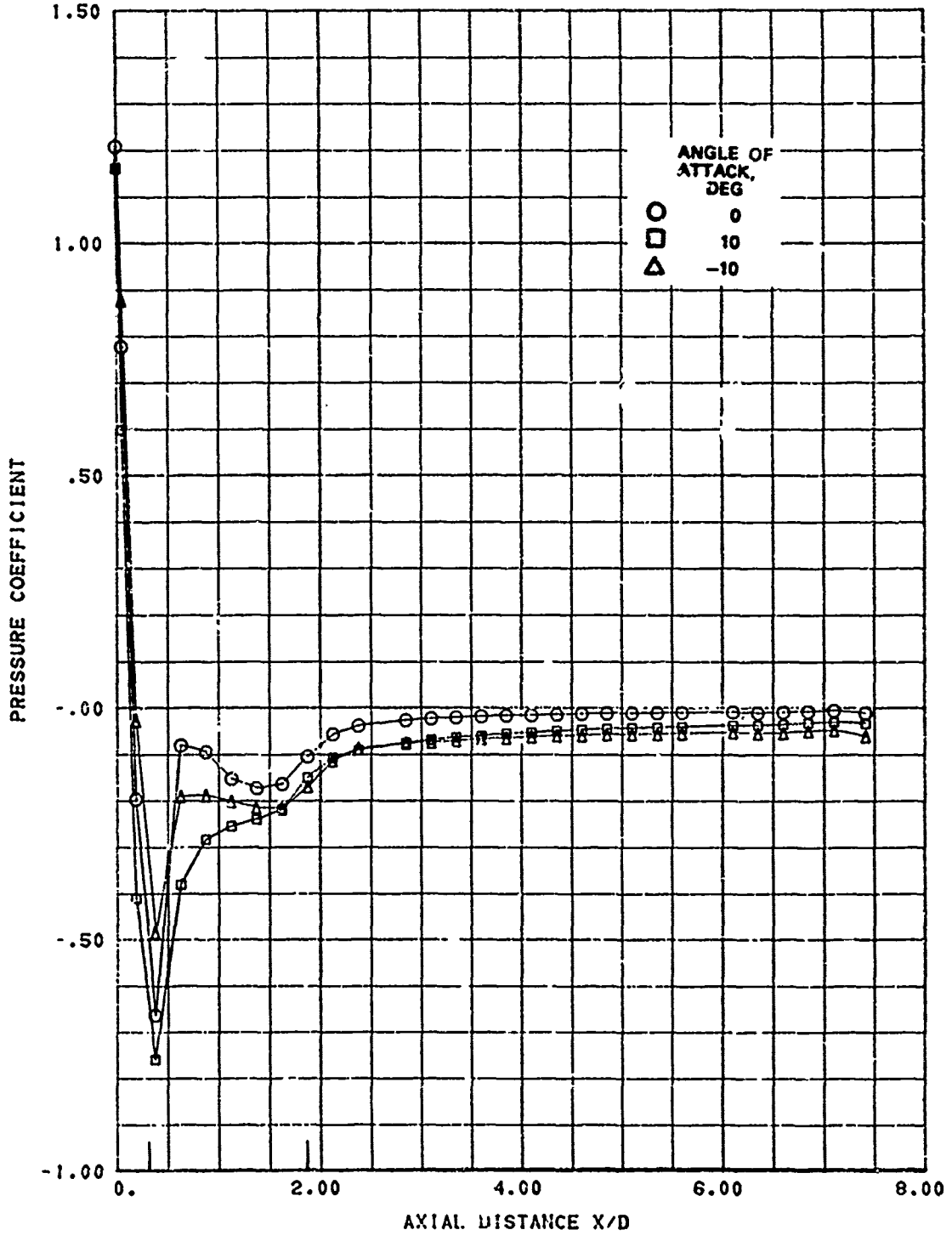

FIG. A-76. Longitudinal Pressure Distribution; Nose C, Mach 0.9, Roll Angle 60 Degrees.

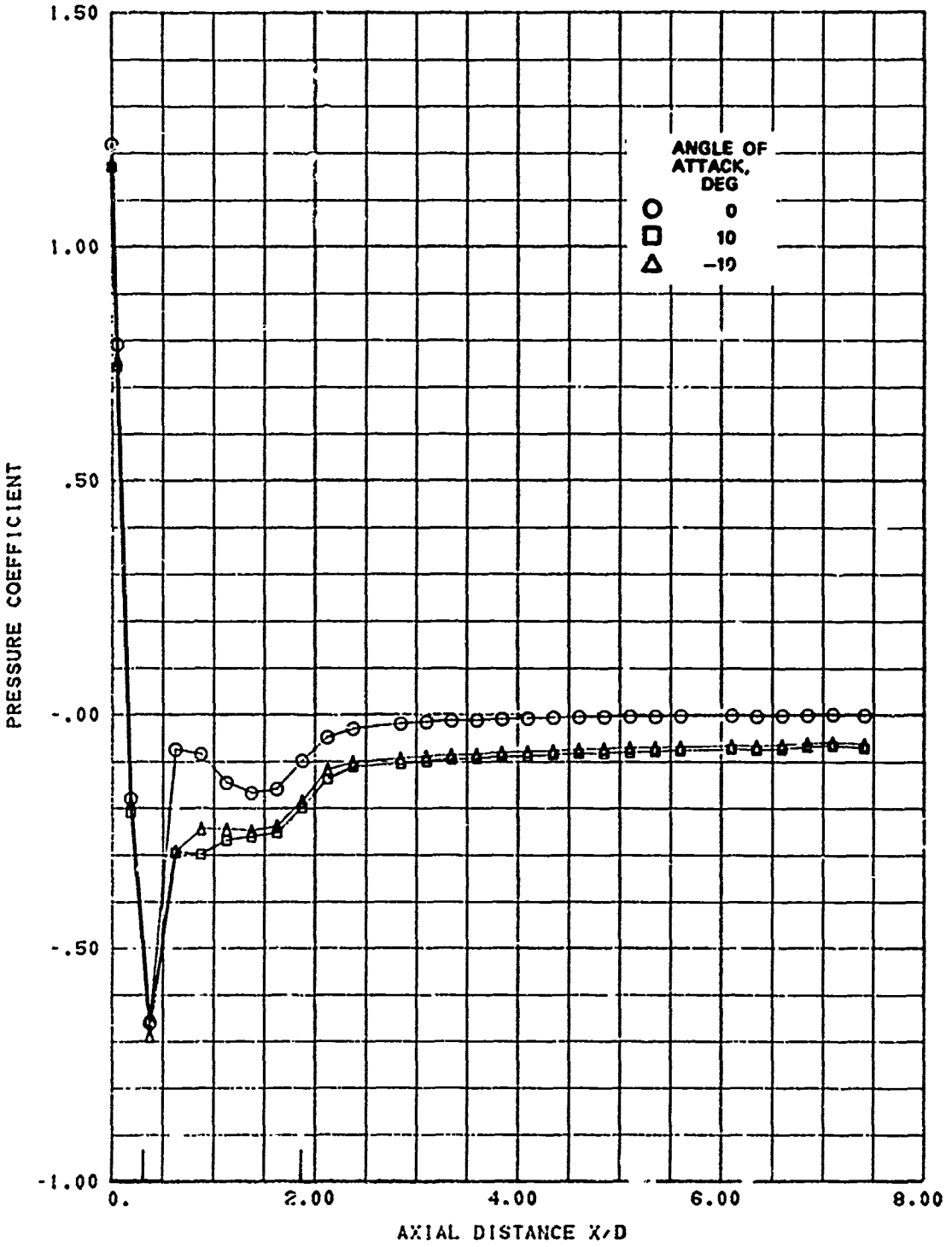

FIG. A-77. Longitudinal Pressure Distribution; Nose C, Mach 0.9, Roll Angle 90 Degrees.

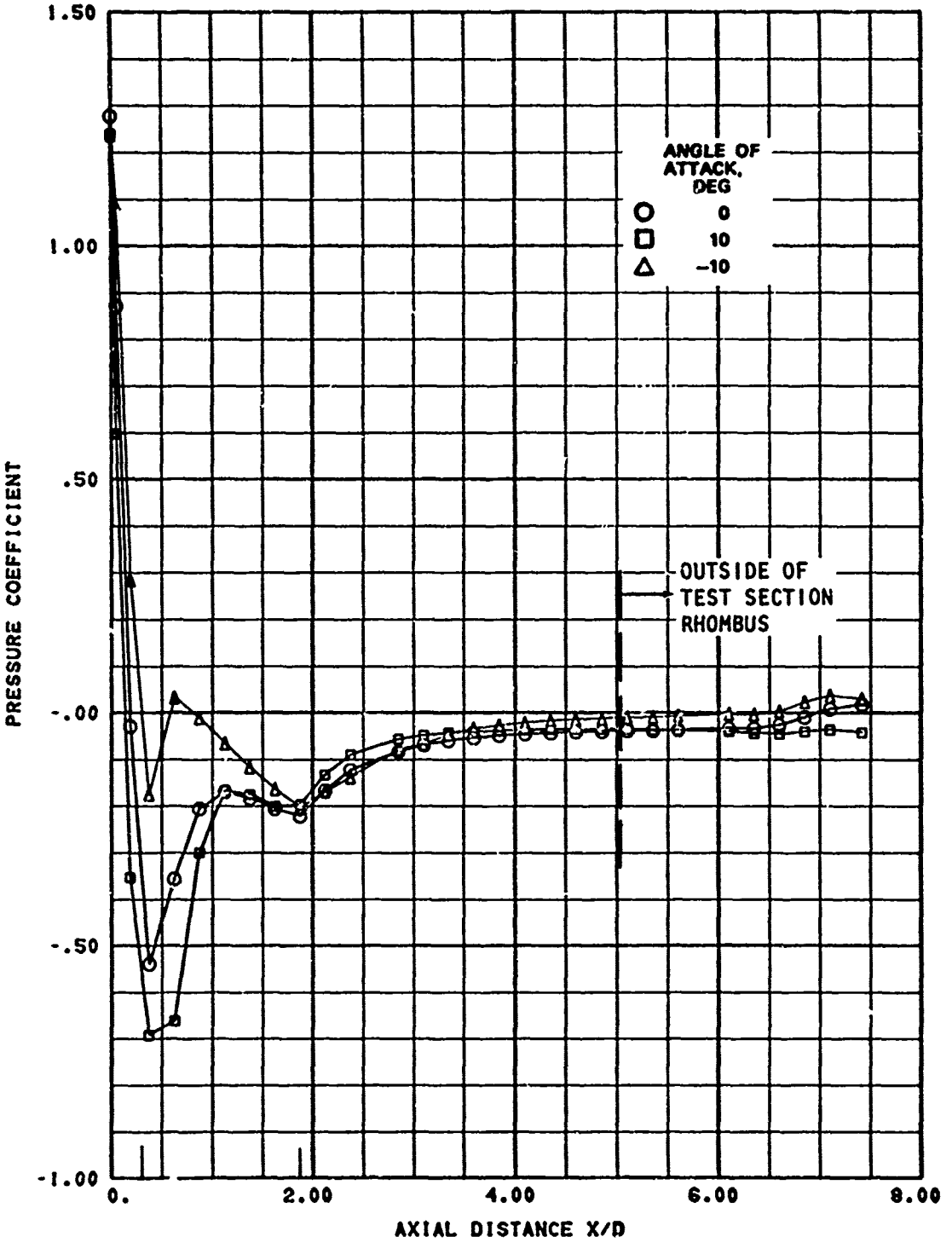

FIG. A-78. Longitudinal Pressure Distribution; Nose C, Mach 1.0, Roll Angle 0 Degrees.

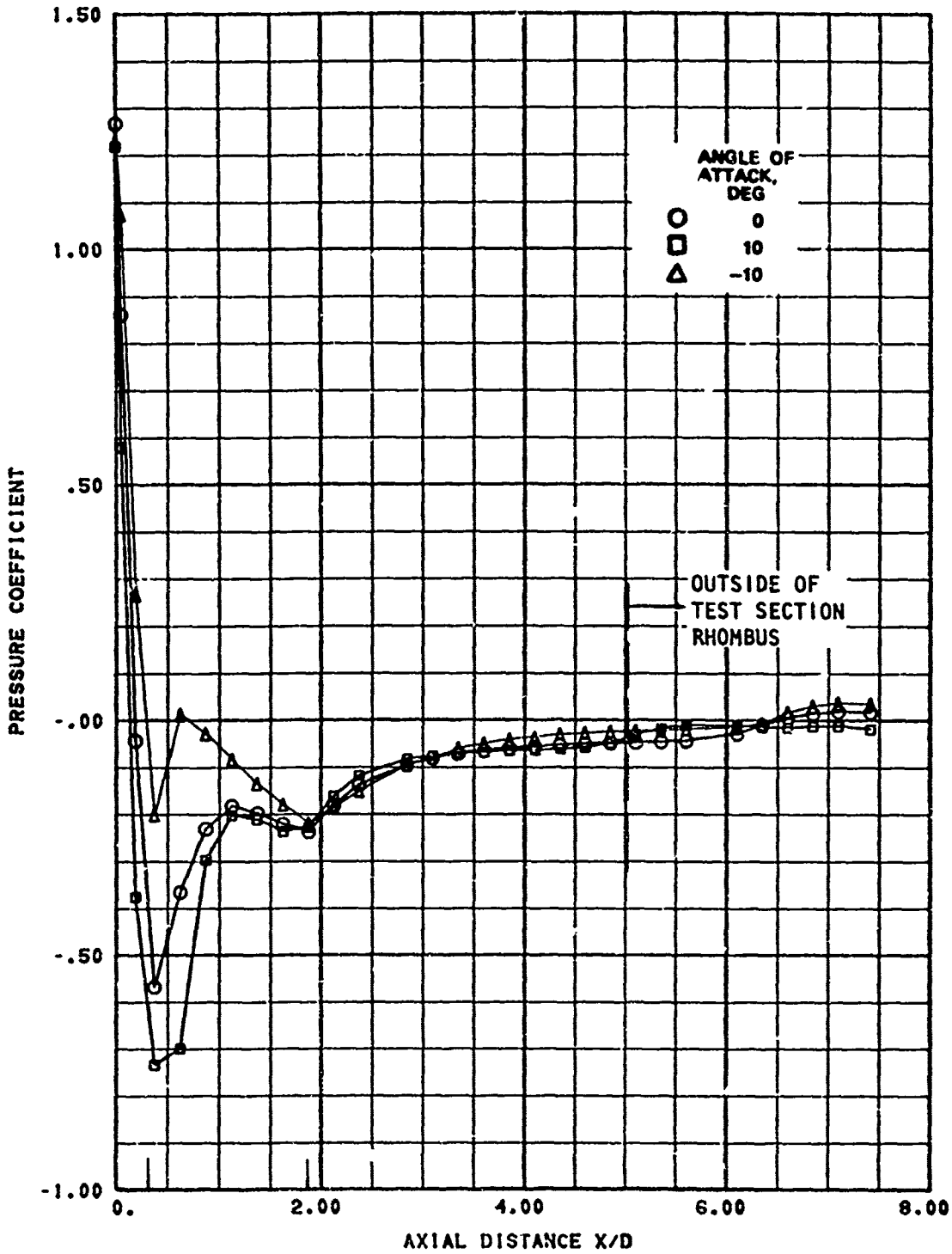

FIG. A-79. Longitudinal Pressure Distribution; Nose C, Mach 1.0, Roll Angle 15 Degrees.

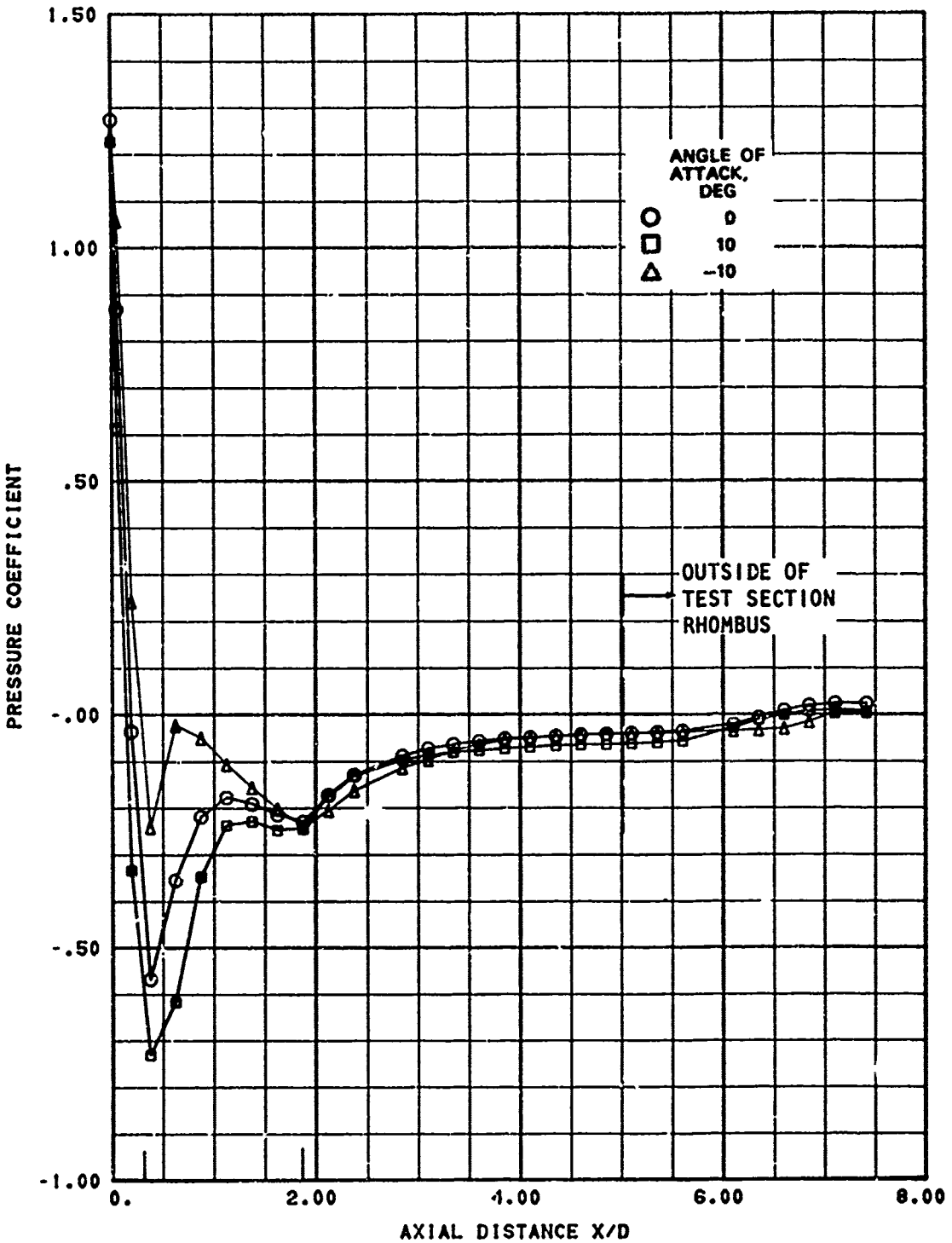

FIG. A-80. Longitudinal Pressure Distribution; Nose C, Mach 1.0, Roll Angle 30 Degrees.

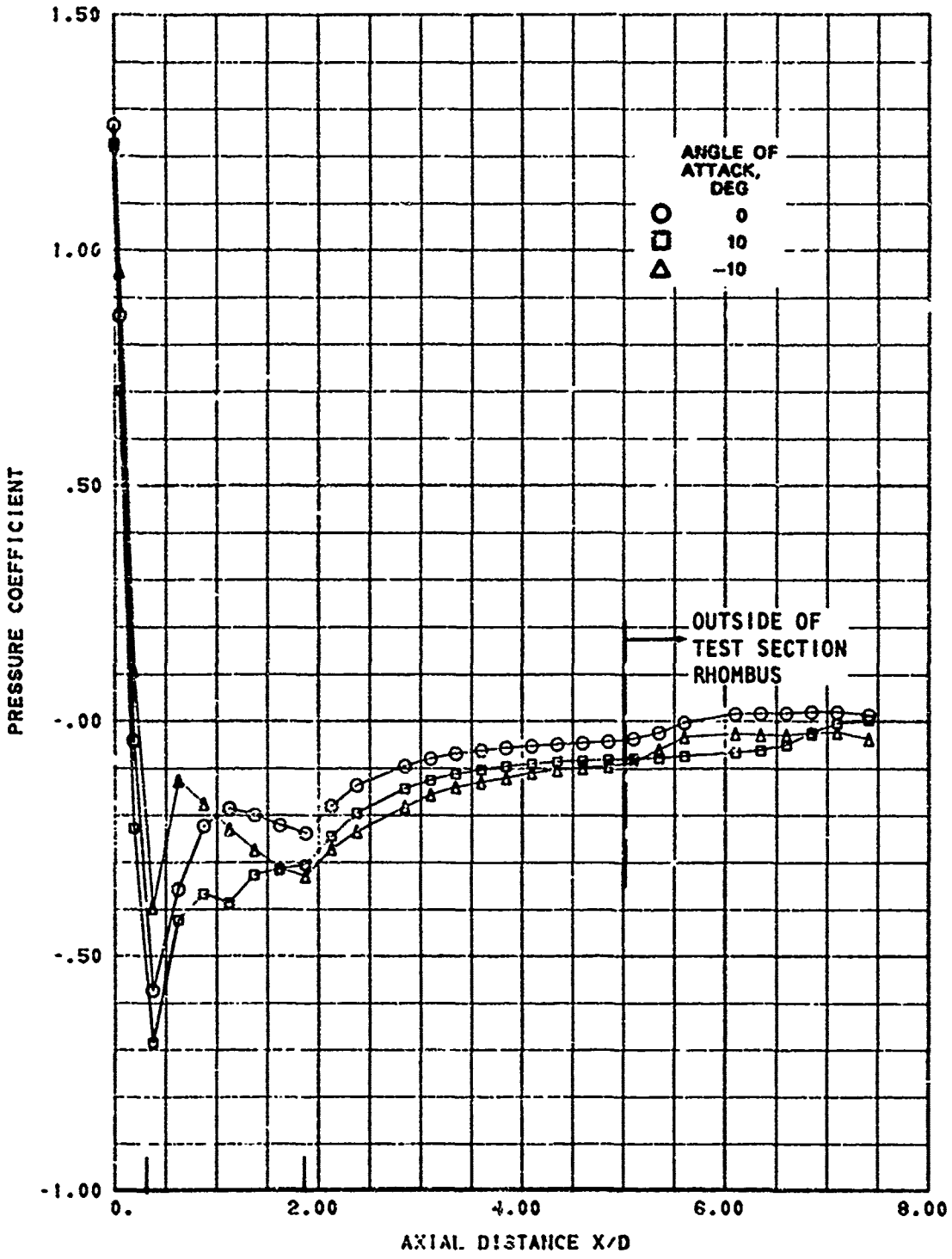

FIG. A-81. Longitudinal Pressure Distribution; Nose C, Mach 1.0, Roll Angle 60 Degrees.

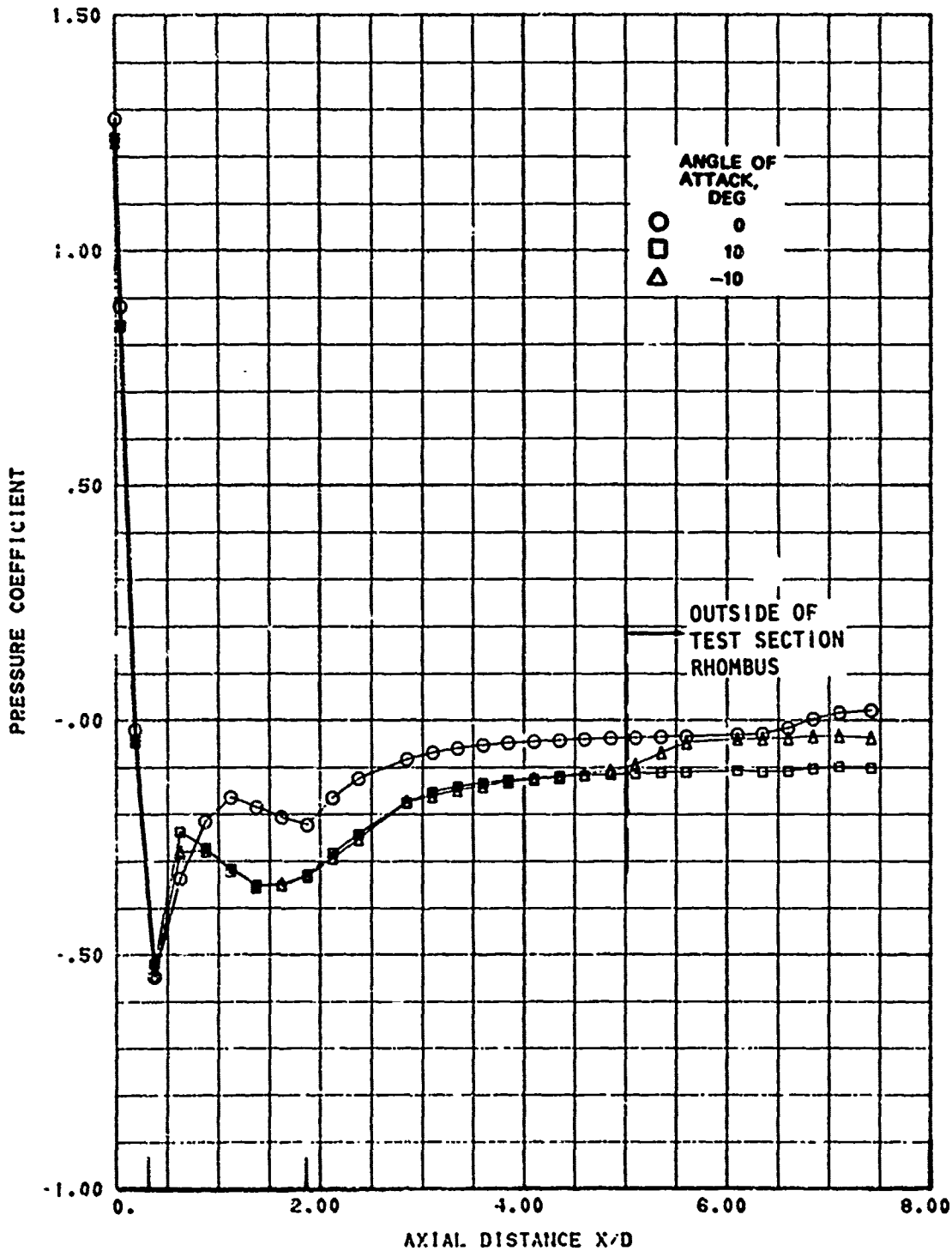

FIG. A-82. Longitudinal Pressure Distribution; Nose C, Mach 1.0, Roll Angle 90 Degrees.

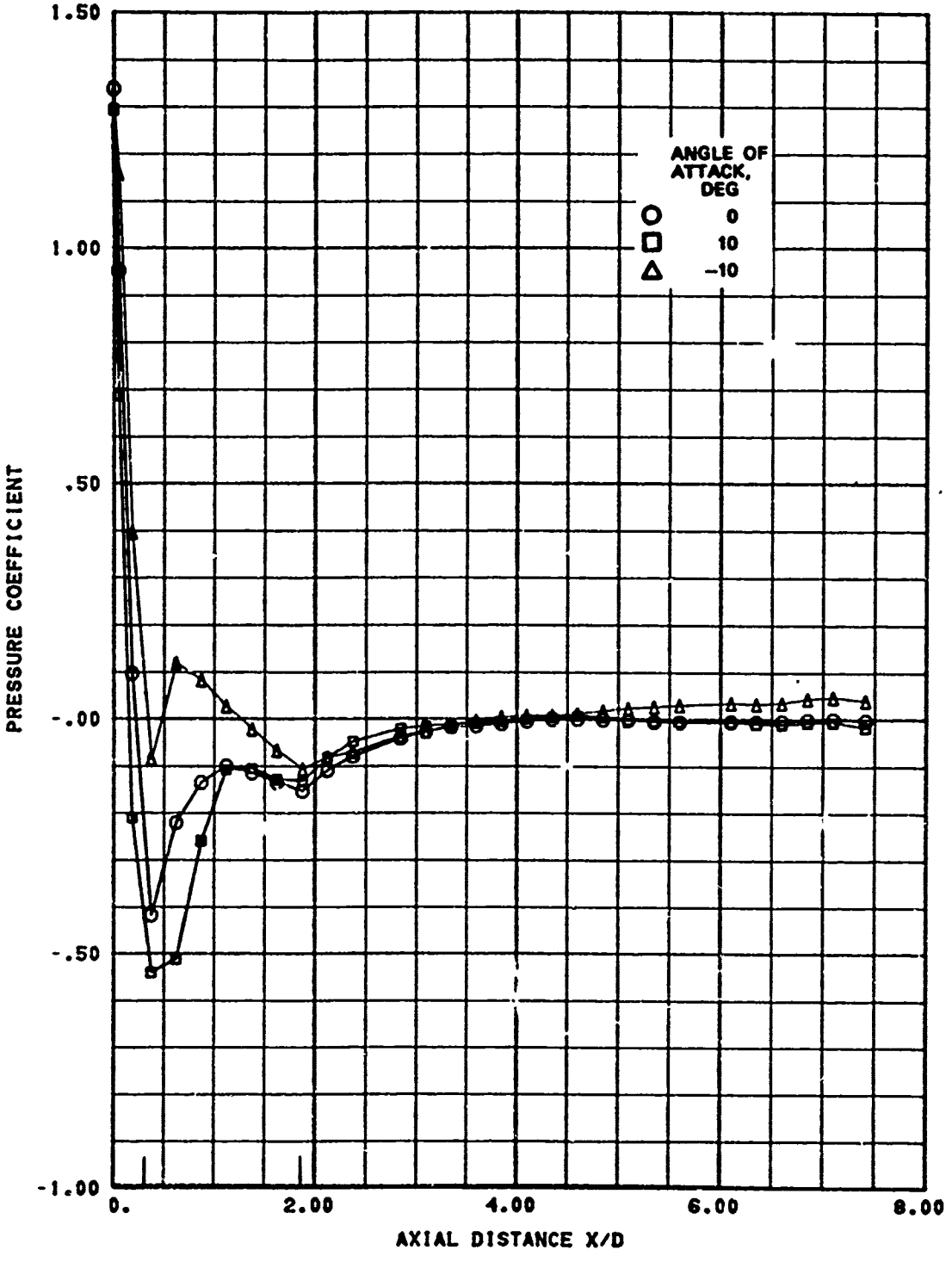

FIG. A-83. Longitudinal Pressure Distribution; Nose C, Mach 1.1, Roll Angle 0 Degrees.

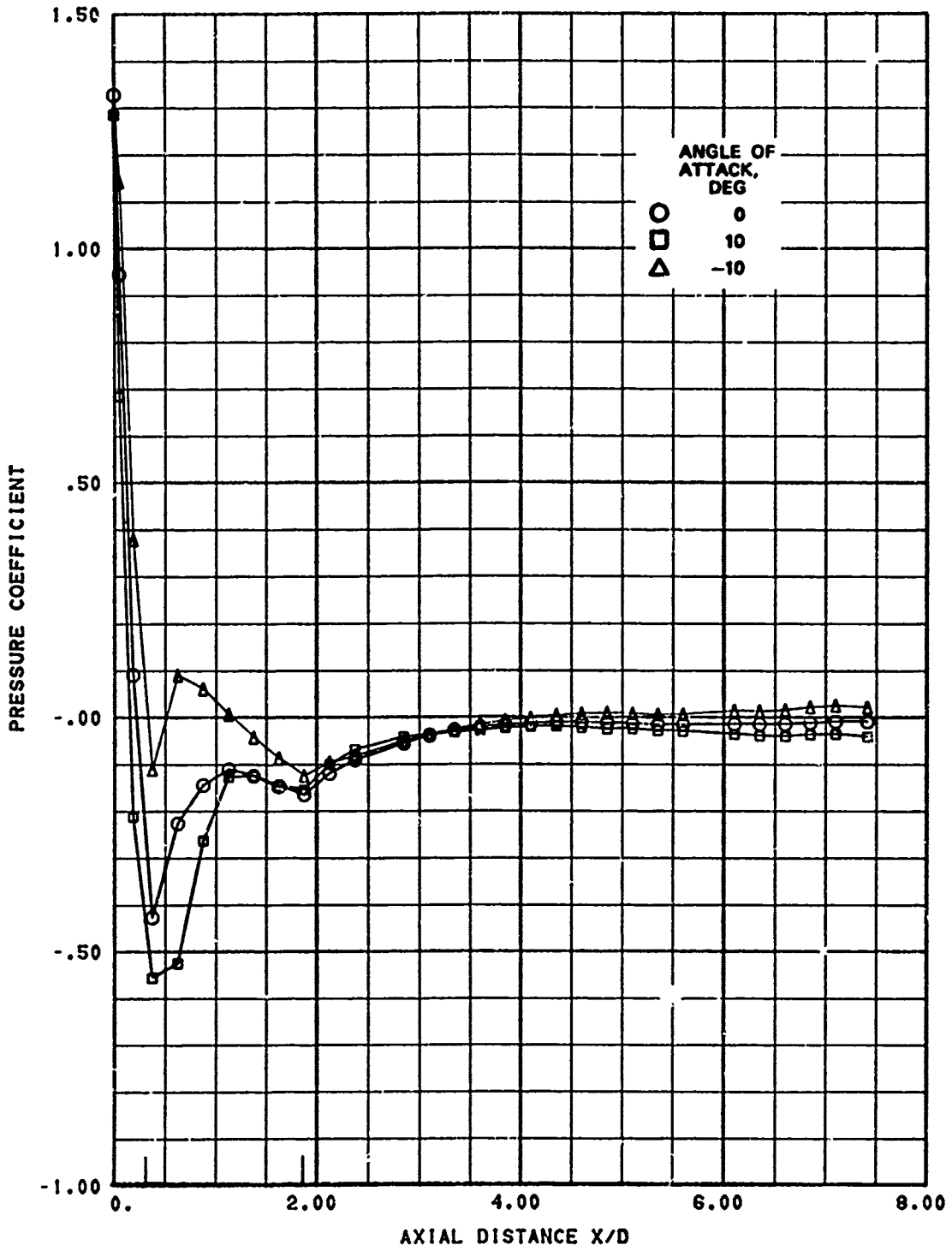

FIG. A-84. Longitudinal Pressure Distribution; Nose C, Mach 1.1, Roll Angle 15 Degrees.

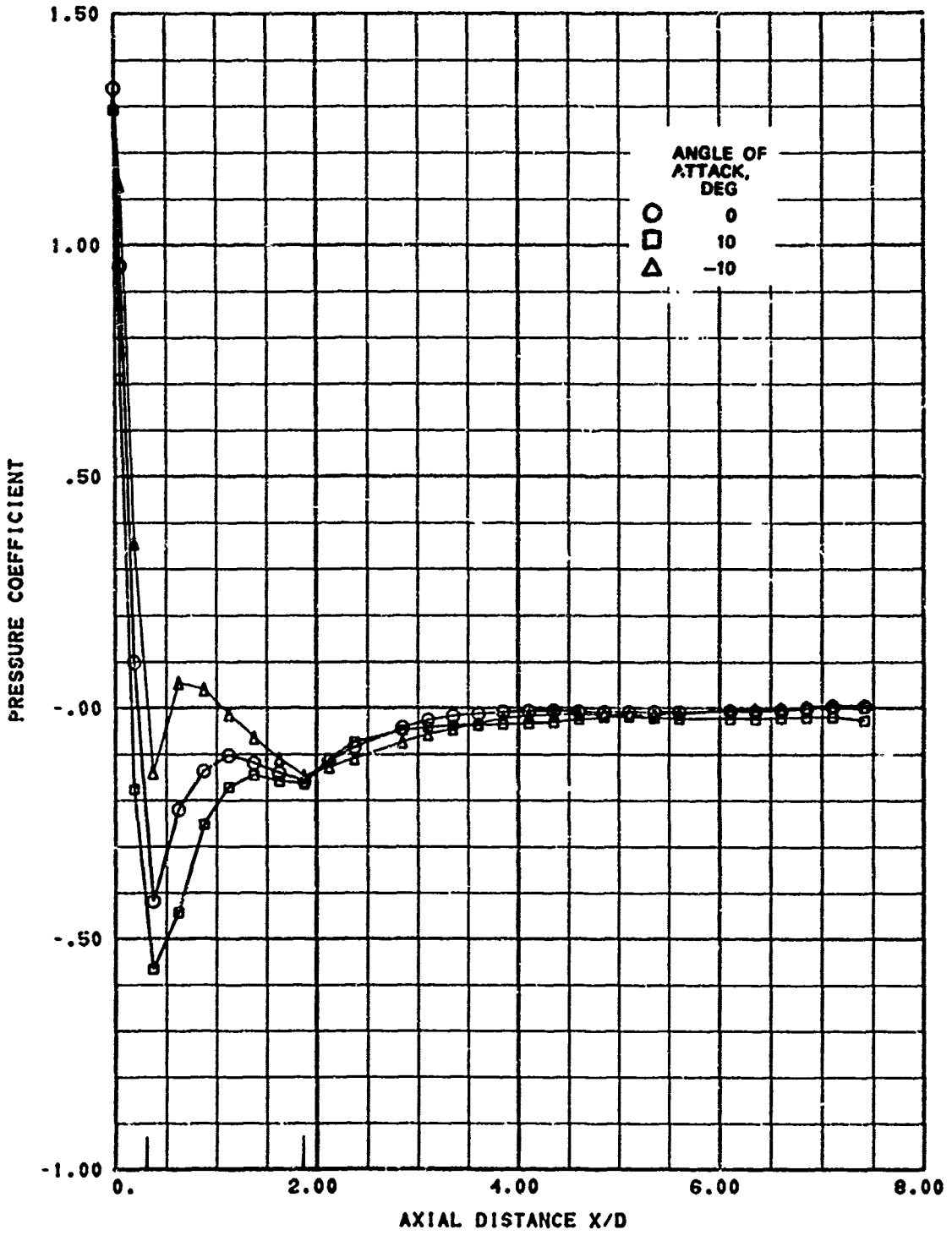

FIG. A-85. Longitudinal Pressure Distribution; Nose C, Mach 1.1, Roll Angle 30 Degrees.

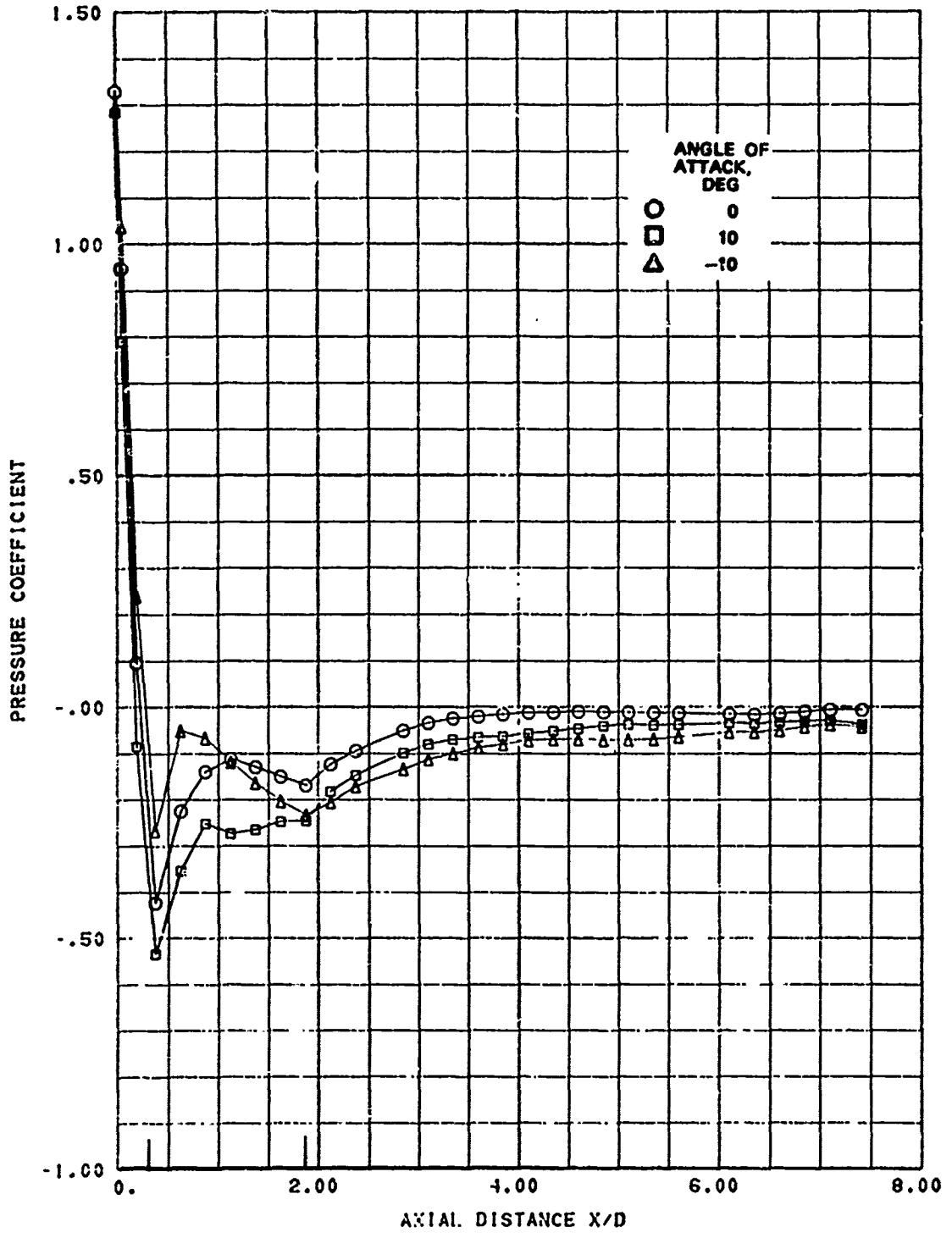

FIG. A-86. Longitudinal Pressure Distribution; Nose C, Mach 1.1, Roll Angle 60 Degrees.

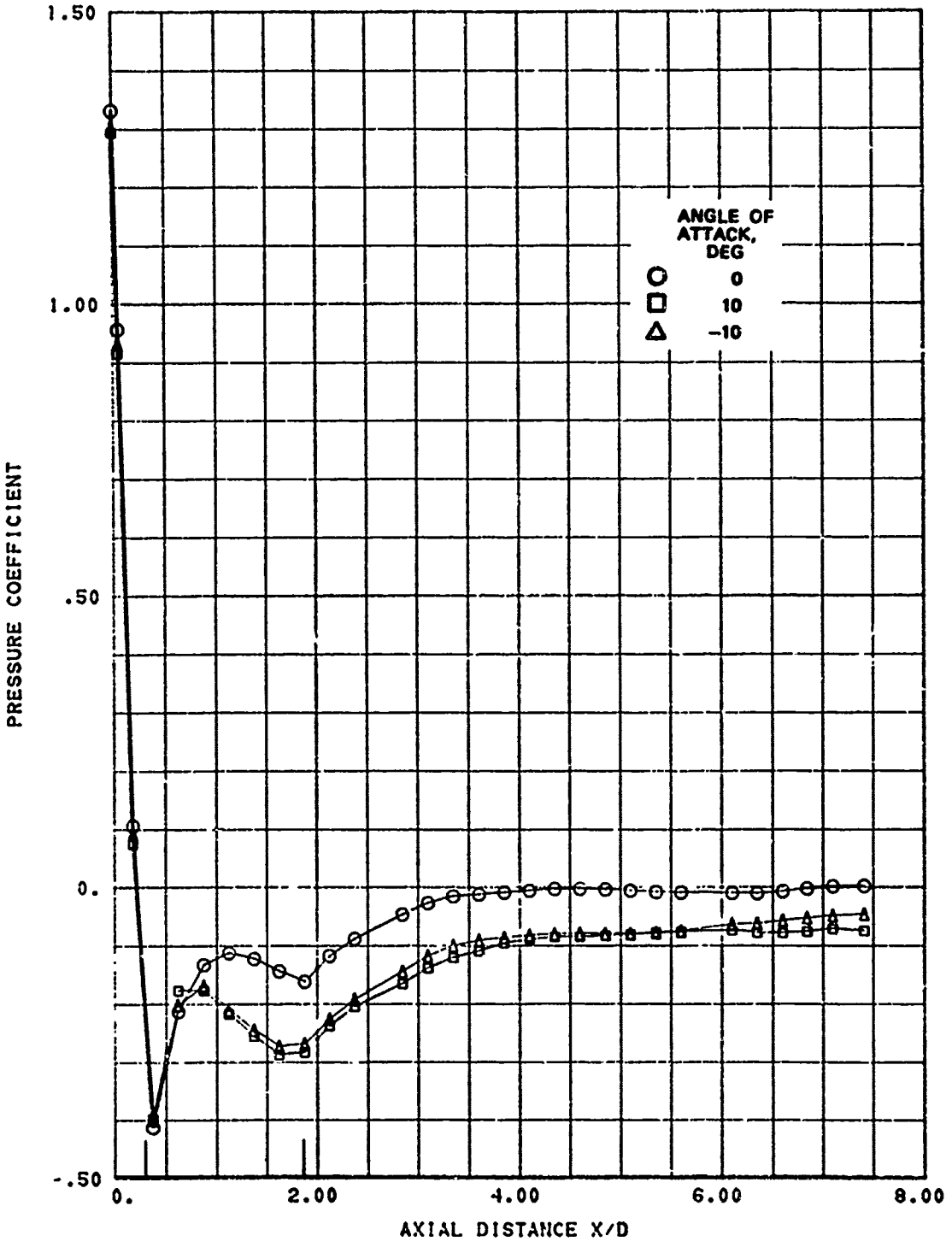

FIG. A-87. Longitudinal Pressure Distribution; Nose C, Mach 1.1, Roll Angle 90 Degrees.

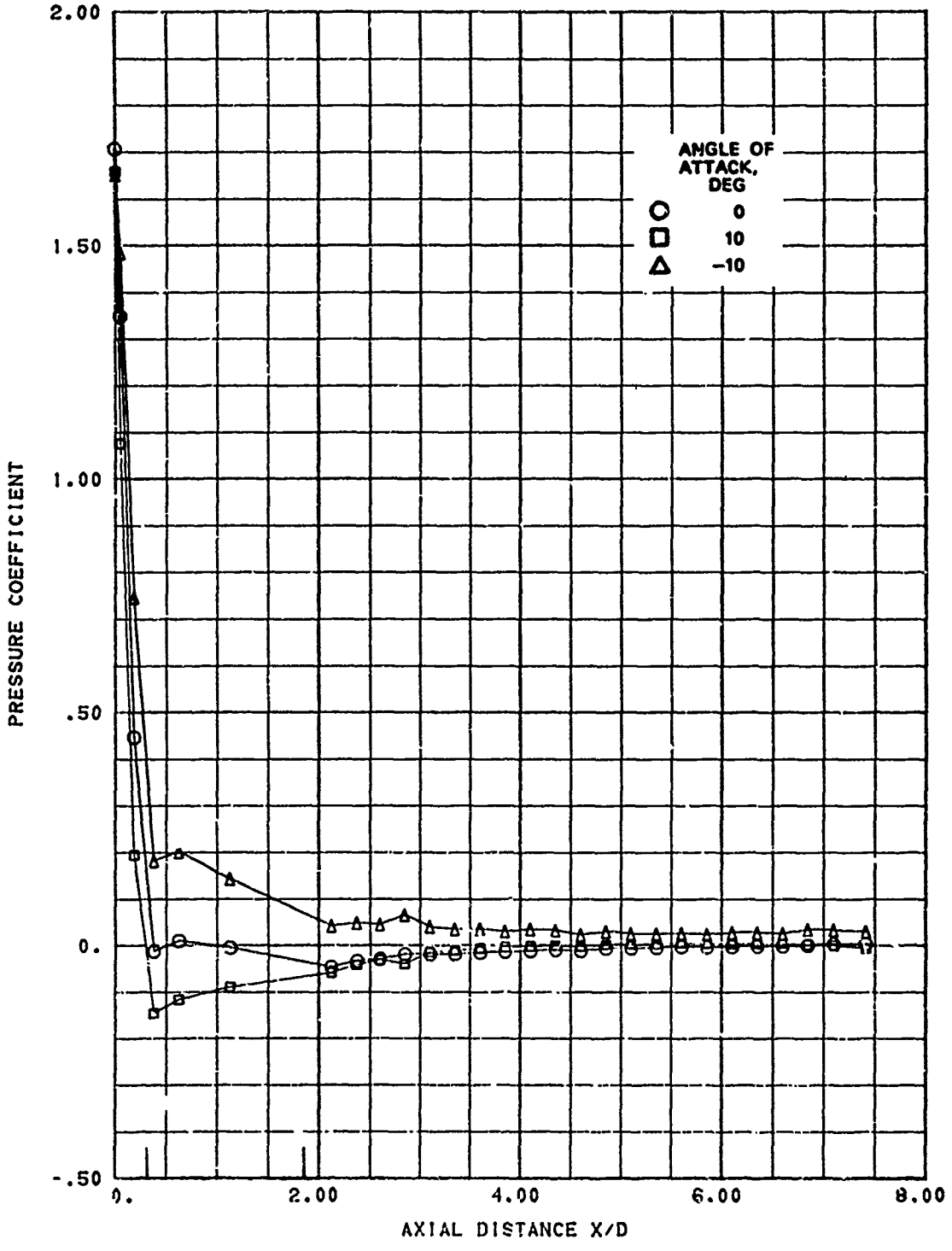

FIG. A-88. Longitudinal Pressure Distribution; Nose C, Mach 2.02, Roll Angle 0 Degrees.

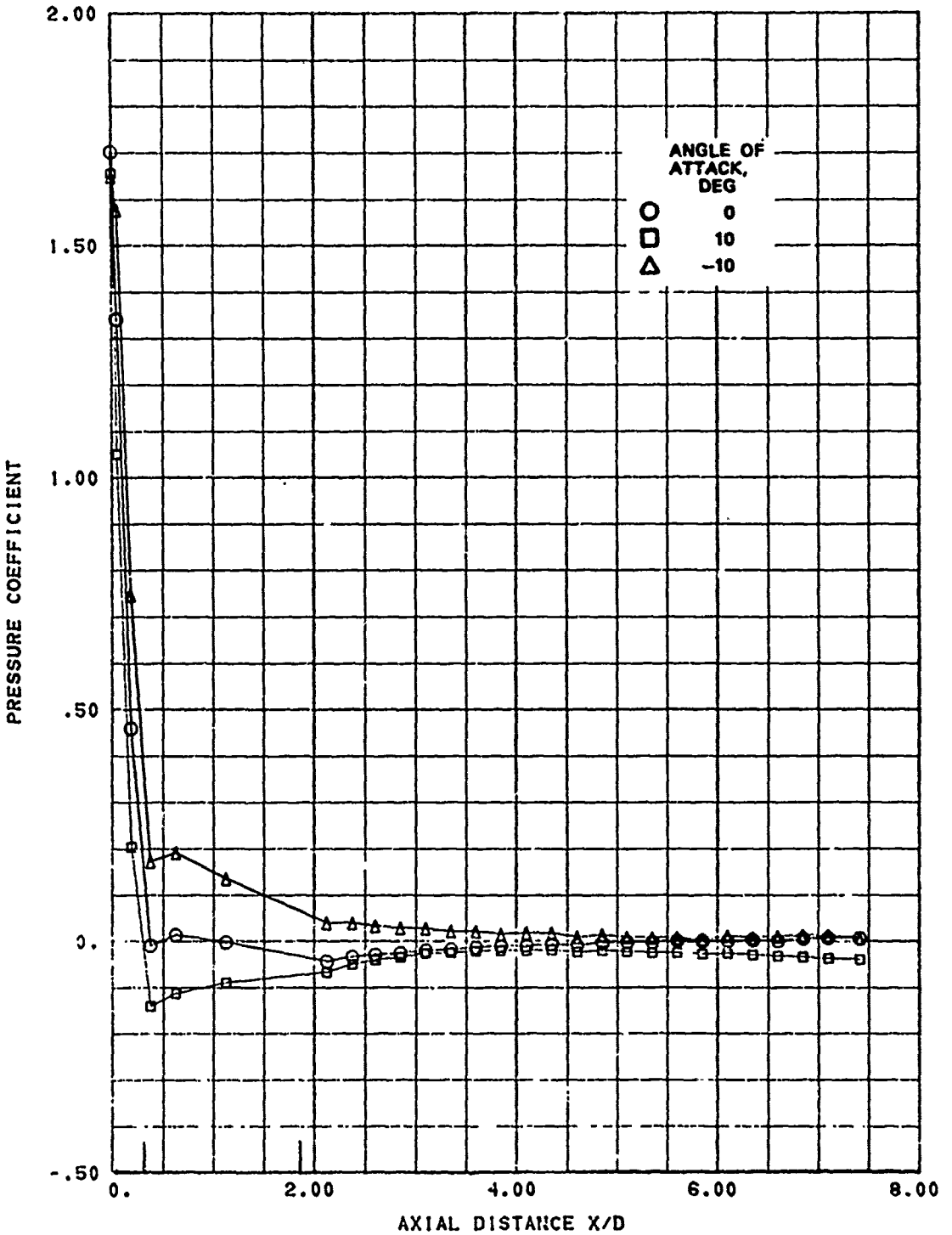

FIG. A-89. Longitudinal Pressure Distribution; Nose C, Mach 2.02, Roll Angle 15 Degrees.

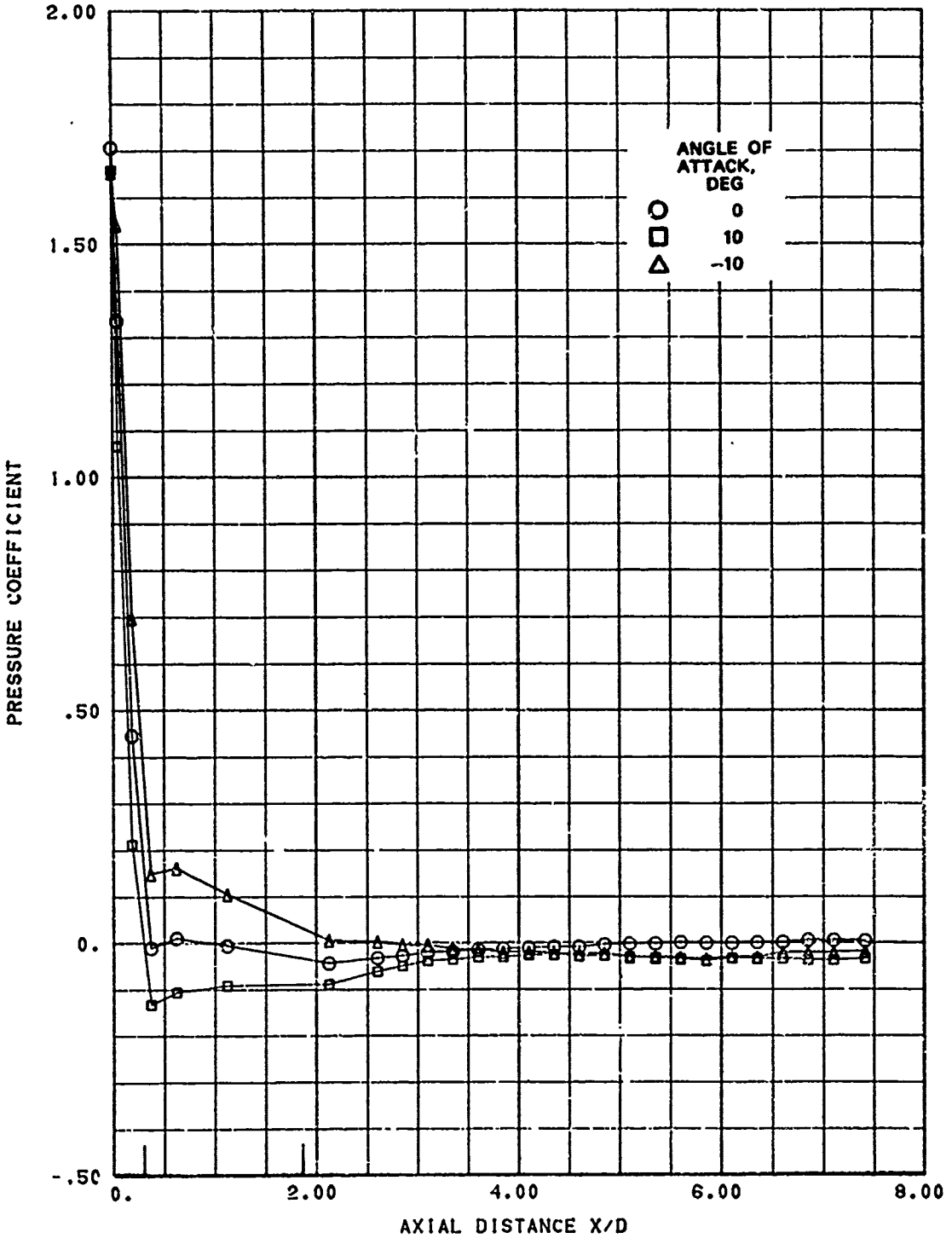

FIG. A-90. Longitudinal Pressure Distribution; Nose C, Mach 2.02, Roll Angle 30 Degrees.